

Ultrafast Coherent Control and Multidimensional Spectroscopy at the Nanoscale

Dissertation

Christian Strüber

**Lehrstuhl für Molekül- und Oberflächenphysik
Fakultät für Physik
Universität Bielefeld**

supervised by
Prof. Dr. W. Pfeiffer

Referees
Prof. Dr. W. Pfeiffer
Prof. Dr. T. Huser

January 7, 2014

"Atoms are like people. Get lots of them together, never know what they'll do."

Neal Stephenson, *Zodiac* [1]

Publications

Scientific publications presented in this thesis which have already been published:

In scientific journals and proceedings:

A cooperation of scientists from Bielefeld, Kaiserslautern, and Würzburg has contributed to the following joint publications. The author lists of these publications is by agreement sorted alphabetically and does not indicate the specific contribution of each author to the published data and text.

- [2] Aeschlimann, M, Bauer, M, Bayer, D, Brixner, T, Cunovic, S, Dimler, F, Fischer, A, Pfeiffer, W, Rohmer, M, Schneider, C, Steeb, F, Strüber, C, & Voronine, D. V. (2010) Spatiotemporal control of nanooptical excitations. *Proceedings of the National Academy of Sciences of the United States of America* **107**, 5329–5333
- [3] Aeschlimann, M, Brixner, T, Cunovic, S, Fischer, A, Melchior, P, Pfeiffer, W, Rohmer, M, Schneider, C, Strüber, C, Tuchscherer, P, & Voronine, D. V. (2012) Nano-optical control of hot-spot field superenhancement on a corrugated silver surface. *IEEE Journal of Selected Topics in Quantum Electronics* **18**, 275–282
- [4] Aeschlimann, M, Brixner, T, Fischer, A, Kramer, C, Melchior, P, Pfeiffer, W, Schneider, C, Strüber, C, Tuchscherer, P, & Voronine, D. V. (2011) Coherent two-dimensional nanoscopy. *Science* **333**, 1723–1726
- [5] Aeschlimann, M, Bauer, M, Bayer, D, Brixner, T, Cunovic, S, Fischer, A, Melchior, P, Pfeiffer, W, Rohmer, M, Schneider, C, Strüber, C, Tuchscherer, P, & Voronine, D. V. (2012) Optimal open-loop near-field control of plasmonic nanostructures. *New Journal of Physics* **14**
- [6] Aeschlimann, M, Bauer, M, Bayer, D, Brixner, T, Cunovic, S, Dimler, F, Fischer, A, Pfeiffer, W, Rohmer, M, Schneider, C, Steeb, F, Strüber, C, & Voronine, D. V. (2009) in *Ultrafast Phenomena XVI*, Springer Series in Chemical Physics, eds. Corkum, P, Silvestri, S, Nelson, K. A, Riedle, E, & Schoenlein, R. W. (Springer Berlin Heidelberg) No. 92, pp. 705–707
- [7] Aeschlimann, M, Bauer, M, Bayer, D, Brixner, T, Cunovic, S, Fischer, A, Melchior, P, Pfeiffer, W, Rohmer, W, Schneider, C, Strüber, C, Tuchscherer, P, & Voronine, D. V. (2010) *Deterministic control of subwavelength field localization in plasmonic nanoantennas*, Proc. 17th Int. Conference, Ultrafast Phenomena XVII eds. Chergui, M, Jonas, D. M, Riedle, E, Schoenlein, R. W, & Taylor, A. J. p. 667
- [8] Aeschlimann, M, Bauer, M, Bayer, D, Brixner, T, Cunovic, S, Fischer, A, Melchior, P, Pfeiffer, W, Rohmer, M, Schneider, C, Strüber, C, Tuchscherer, P, & Voronine, D. V. (2010)

Deterministic Control of Subwavelength Field Localization in Plasmonic Nanoantennas, OSA Technical Digest (CD). (Optical Society of America), p. WA2

At international conferences as presenting author:

- Strüber, C, Aeschlimann, M, Bauer, M, Bayer, D, Brixner, T, Cunovic, S, Dimler, F, Fischer, A, Pfeiffer, W, Rohmer, M, Schneider, C, Steeb, F, and Voronine, D.V., *Subwavelength spatio-temporal control of ultrafast nano-optical fields*, Ultrafast Surface Dynamics 6, Kloster Banz, Germany (2008)
- Strüber, C, Aeschlimann, M, Bauer, M, Bayer, D, Brixner, T, Cunovic, S, Dimler, F, Fischer, A, García de Abajo, F.J., Myroshnychenko, V, Pfeiffer, W, Rohmer, M, Schneider, C, Steeb, F, Voronine, D.V., *Simultaneous spatial and temporal control of the local excitation of a nanostructure using polarization shaped laser pulses*, Nanometa, Seefeld, Austria (2009)
- Strüber, C, Aeschlimann, M, Bauer, M, Bayer, D, Brixner, T, Cunovic, S, Dimler, F, Fischer, A, Pfeiffer, W, Rohmer, M, Schneider, C, Steeb, F, and Voronine, D.V., *Analysis Tools for Spatial and Temporal Control of Plasmonic Excitations at Metal Nanostructures*, O 27.70, DPG Spring Meeting, Dresden, Germany (2009)
- Strüber, C, Aeschlimann, M, Bauer, M, Bayer, D, Brixner, T, Cunovic, S, Fischer, A, Melchior, P, Pfeiffer, W, Rohmer, M, Schneider, C, Tuchscherer, P and Voronine, D.V., *Deterministic control of nanooptical excitations in plasmonic nanostructures*, 2nd International Workshop on Ultrafast Nanooptics, Bad Dürkheim, Germany (2010)
- Strüber, C, Aeschlimann, M, Brixner, T, Cunovic, S, Fischer, A, Kramer, C, Melchior, P, Pfeiffer, W, Schneider, C, Tuchscherer, P, and Voronine, D.V., *Nanooptical control of hot-spot field superenhancement and long-lived coherences on a corrugated silver surface*, O 66.4, DPG Spring Meeting, Dresden, Germany (2011)
- Strüber, C, Aeschlimann, M, Brixner, T, Fischer, A, Kramer, C, Melchior, P, Pfeiffer, W, Schneider, C, Tuchscherer, P, and Voronine, D.V., *Hybridization of dark and bright modes leading to longlived plasmonic coherences on a corrugated silver surface*, O 52.6, DPG Spring Meeting, Berlin, Germany (2012)
- Strüber, C, Aeschlimann, M, Brixner, T, Fischer, A, Kramer, C, Melchior, P, Schneider, C, Tuchscherer, P, Voronine, D.V., and Pfeiffer, W, *Hybridization of dark and bright modes leading to long-lived plasmonic coherences on a corrugated silver surface*, 17th SAOT Workshop - Microchip Plasmonics, Erlangen, Germany (2012)
- Strüber, C, Aeschlimann, M, Birlo, M, Brixner, T, Differt, D, Hensen, M, Kramer, C, Lükermann, F, Melchior, P, Piecuch, M, Pfeiffer, W, Stiebig, H, Thielen, P, *Localization of photonic modes in thin film solar cells*, 3rd International Workshop on Ultrafast Nanooptics, Bad Dürkheim, Germany (2013)

Additional scientific publications not presented in this thesis:

In scientific journals and proceedings:

- Differt, D, García de Abajo, F.J., Pfeiffer, W, Strüber, C, and Voronine, D.V., *Nanocal-ization of Ultrashort Time-Reversed Pulses in Random Nanoparticle Assemblies*, Ultrafast Phenomena XVII (Jonas, D, Riedle, E, Schoenlein, R, Eds.)(Oxford University Press, Ox-ford), p. 272

At international conferences:

- Strüber, C, Differt, D, García de Abajo, F.J., Pfeiffer, W, and Voronine, D.V., *Nanocal-ization of Ultrashort Time-Reversed Laser Pulses in Random Nanoparticle Assemblies*, 2nd International Workshop on Ultrafast Nanooptics, Bad Dürkheim, Germany (2010)
- Hensen, M, Strüber, C, and Pfeiffer, W, *Frequency comb stabilization with zero phase slip frequency for high repetition rate carrier envelope sensitive experiments*, Q 15.70, DPG Spring Meeting, Dresden, Germany (2011)
- Soleymanzadeh, B, Strüber, C, Stiebig, H, and Pfeiffer, W, *Femtosecond laser induced recrystallization and ablation of hydrogenated amorphous silicon films*, DS 34.1, DPG Spring Meeting, Dresden, Germany (2011)
- Differt, D, Garcia de Abajo, F.J., Strüber, C, Voronine, D.V., and Pfeiffer, W, *Spa-tiotemporal nanofocusing in random nanostructures achieved by time-reversal, adaptive optimization, and optimal open-loop control of ultrashort laser pulses*, O 41.6, DPG Spring Meeting, Dresden, Germany (2011)
- Sander, C, Merschjohann, F, Neb, S, Bartz, P, Strüber, C, Hensen, M, Müller, N, Pfeiffer, W, and Heinzmann, U, *Carrier-Envelope-Phase Effects on High Harmonic Spectra and Photoelectron Spectra of Neon*, K 4.8, DPG Spring Meeting, Stuttgart, Germany (2012)
- Soleymanzadeh, B, Neumann, C, Strüber, C, Hensen, M, Prunici, P, Gondorf, A, Stiebig, H, and Pfeiffer, W, *Femtosecond laser pulse interaction with hydrogenated amorphous silicon (a-Si:H) thin films*, K 8.5, DPG Spring Meeting, Stuttgart, Germany (2012)
- Birlo, M, Differt, D, Lükermann, F, Strüber, C, Stiebig, H, and Pfeiffer, W, *Light trapping in thin-film solar cells characterized by fs-laser pulse backscattering*, O 74.2, DPG Spring Meeting, Berlin, Germany (2012)
- Hensen, M, Aeschlimann, M, Birlo, M, Brixner, T, Differt, D, Fischer, A, Kramer, C, Melchior, P, Pfeiffer, W, Piecuch, M, Schneider, C, Stiebig, H, Strüber, C, and Thielen, P, *Light trapping in thin-film silicon solar cells investigated by spectral interference and time-resolved PEEM*, 17th SAOT Workshop - Microchip Plasmonics, Erlangen, Germany (2012)

Preface

The work discussed in this thesis is part of a cooperative project between the groups of Walter Pfeiffer, Martin Aeschlimann and Tobias Brixner in Bielefeld, Kaiserslautern, and Würzburg, respectively. This cooperation contributes with the project *Simultaneous spatial and temporal control* to the priority program *SPP 1391 on Ultrafast Nanooptics* of the *DFG*. The experiments and new developed concepts concerning coherent spectroscopy on the nanoscale have been discussed in several joint publications and contributions to international conferences. Since the author lists of these publications by tradition is sorted alphabetically and not all journals requested a statement concerning the specific contribution of each author to the published data and text, a brief notification is added at the beginning of the experimental chapters.

The experimental setup combines time-resolved photoemission electron microscopy (TR-PEEM) with a femtosecond polarization pulse shaper and pulse characterization devices. The basic laser equipment and the PEEM was provided by Martin Aeschlimann's group in Kaiserslautern. The polarization pulse shaper and the spectral interferometry setup originate from Würzburg as well as the basic software routines that allow for a simultaneous operation of the complete hardware. However, modifications of the software were implemented during the project to adapt for the particular tasks connected with coherent control on the nanoscale and coherent 2D nanoscopy. Here, substantial contributions were made by the groups in Würzburg and Bielefeld. Parts of the evaluation software were implemented during the experiments in Kaiserslautern, but most routines were developed in Bielefeld and Würzburg in the evaluation process.

This thesis is divided in six main chapters:

- Chapter 1 is based on literature and introduces concepts of the generation and characterization of polarization-shaped femtosecond laser pulses. Furthermore, plasmonic excitations and nanoscopic devices are discussed and an overview over photoemission electron microscopy is given.
- Chapter 2 describes a coherent control experiment on gold nanostructures that demonstrates the applicability of deterministic control rules for achieving sub-diffraction localization of optical excitation. The experiments were performed in a cooperative effort in Kaiserslautern.
- Chapter 3 deals with an experiment for achieving spatial and temporal resolution in the detection of nanooptical excitation at a silver nanostructure by means of time-resolved two-photon photoemission microscopy. The experiments were performed in a cooperative effort in Kaiserslautern.
- Chapter 4 introduces the basic concepts of coherent 2D nanoscopy, which is a nonlinear spectroscopy technique with subwavelength spatial resolution related to coherent two-dimensional optical spectroscopy (see Appendix D) that detects photoemission signals instead of optical radiation. 2D nanoscopy is applicable for the investigation of quantum

system with distinct energy levels and coherence lifetimes, but it also examines the local spectral response function of strongly dephasing systems such as metallic nanostructured samples with high spatial resolution. In the later case adaptations to the theoretical concepts are necessary which are also described in Chapter 4. Fourier transform time domain simulations allow for the calculation of 2D nanoscopy spectra for arbitrary linear response functions and excitation conditions. These simulations are the basis for evaluation routines that quantitatively retrieve spectroscopic information from experimentally obtained 2D nanoscopy spectra.

- Chapter 5 presents the results of several experiments and simulations investigating localized plasmonic excitations on a corrugated silver surface. Concepts of coherent control were applied in adaptive optimizations of the pulse shapes and in pulse parameter scans. A first demonstration of coherent 2D nanoscopy is discussed. The results of a two-pulse nanoscopy experiment indicate the hybridization of plasmonic modes on the corrugated silver film. The experiments were performed in a cooperative effort in Kaiserslautern.
- Chapter 6 presents experimental investigations of photon management in hydrogenated amorphous silicon thin-film solar cells. Basic characterization measurements and laser pulse scattering experiments on these devices were performed and evaluated in Bielefeld. The 2D nanoscopy experiments were performed in a cooperative effort in Kaiserslautern. The combined findings emphasize that the enhanced absorption in nanotextured thin-film solar cells is attributed to localized photonic modes.

In the Appendix a brief description of the employed pulse characterization techniques are given (Appendix A). Additionally, methods for drift correction in PEEM data are discussed (Appendix B), which are necessary, for successful adaptive optimizations and 2D nanoscopy experiments with high spatial resolution. Appendix C deals with mathematical details on excitation pathways in single-color pump-probe experiments. Appendix D gives a brief overview on the description of coherent optical two-dimensional spectroscopy in literature. Mathematical details concerning the local photoemission rate in 2D nanoscopy are presented in Appendix E. Appendix F contains a brief mathematical discussion of the response function of a Lorentz oscillators, which approximatively describes the spectral and temporal properties of a damped harmonic oscillator.

Contents

Publications	i
Preface	v
Introduction	1
1. Basic Theoretical and Experimental Concepts	5
1.1. Description and Representation of Polarization-Shaped Laser Pulses	5
1.1.1. Temporal and Spectral Description of Femtosecond Laser Pulses	6
1.1.2. Spatial Propagation of Light in Dispersive Media	9
1.1.3. Elliptical Pulse Parameter	10
1.2. Concepts of Laser Pulse Shaping	13
1.2.1. Polarization Pulse Shaper Setup	13
1.2.2. Methods for Amplitude, Phase and Polarization Pulse Shaping	15
1.2.3. Adaptive Techniques for Pulse Shaping	18
1.3. Optical Near-Fields and Optical Nanoantennas	20
1.3.1. Localization of Light below the Diffraction Limit	20
1.3.2. Propagating Surface Plasmon Polaritons	21
1.3.3. Localized Surface Plasmon Resonances	23
1.3.4. Nanoantennas and Coupling of Plasmonic Modes	27
1.3.5. Spatial and Temporal Control Mechanisms	28
1.4. Time-Resolved Photoemission Electron Microscopy	31
1.4.1. Time-resolved Photoemission Spectroscopy	31
1.4.2. PEEM – PhotoEmission Electron Microscopy	33
1.4.3. Multiphoton Photoemission from Nanoscaled Systems	38
2. Optimal Open-Loop Near-Field Control of Plasmonic Nanostructures	41
2.1. Introduction	41
2.2. Experimental Setup and Sample Characterization	43
2.3. Open-Loop Control of Nanoplasmonic Excitations	48
2.4. Conclusion	51
3. Spatially and Temporally Resolved Control of Nanooptical Excitations	53
3.1. Introduction	54
3.2. Experimental Setup and Sample Characterization	58
3.3. Ultrafast Nanoscale Excitation Switching	60
3.4. Conclusion	62

4. Principles of Coherent 2D Nanoscopy	63
4.1. Bringing Nonlinear Spectroscopy to the Nanoscale	63
4.2. Principles of Coherent 2D Nanoscopy	71
4.2.1. Liouville Space Description of 2D Nanoscopy	72
4.2.2. 2D Nanoscopy in Strongly Dephasing Systems	75
4.2.3. 2D Nanoscopy for Single Harmonic Oscillators in Strongly Dephasing Systems	80
4.2.4. Phase Cycling	83
4.3. Simulation of Coherent 2D Nanoscopy	84
4.3.1. Fourier Transform Time Domain Simulations	85
4.3.2. Influence of Limited Excitation Bandwidth and Above Threshold Nonlinearities on 2D Nanoscopy Spectra	96
4.3.3. Fast Data Evaluation Routine for 2D Nanoscopy Measurements	98
5. Hybridization of Dark and Bright Plasmonic Modes	103
5.1. Experimental Setup and Sample Characterization	103
5.2. Optical Near-Field Control of Hot Spot Photoemission on Silver	106
5.2.1. Near-field Superenhancement	106
5.2.2. Sub-Diffraction Control of Photoemission Hot spots	108
5.2.3. Reproducibility of Adaptive Optimizations	110
5.2.4. Multidimensional Pulse Parameter Scans	111
5.2.5. Conclusion	114
5.3. Coherent 2D Nanoscopy on a Corrugated Silver Surface	114
5.4. Hybridization of Plasmonic Modes on a Corrugated Ag Surface	118
5.4.1. Experimental Results and Representation by Delay-Phase-Plots	119
5.4.2. Hybridization Model for Coupled Plasmon Modes	123
5.4.3. Evaluation of Two-Pulse Nanoscopy Experiment	126
5.4.4. Conclusion and Outlook	129
6. Localization of Photonic Modes in Thin-Film Solar Cells	131
6.1. Hydrogenated Amorphous Silicon Thin-Film Solar Cells	132
6.1.1. Thin-Film Solar Cells	132
6.1.2. Photon Management in Thin-Film Solar Cells	134
6.2. Sample Characterization	136
6.2.1. Sample Designs and Structural Properties	136
6.2.2. Linear Absorption Spectroscopy	138
6.2.3. Ultrafast Backscattering Spectroscopy Experiments	139
6.3. 2D Nanoscopy on Nanotextured Thin-Film a-Si:H	143
6.3.1. Nonlinear Hot Spot Electron Emission from Nanotextured a-Si:H	143
6.3.2. Thermionic Emission from Photonic Mode Heated Hot Spots	144
6.3.3. 2D Nanoscopy on Nanotextured Thin-Film a-Si:H	149
6.4. Conclusion	154
Summary and Outlook	157

A. Laser Pulse Characterization	161
A.1. Experimental Pulse Characterization	161
A.1.1. Second-Harmonic FROG	161
A.1.2. Dual-Channel Spectral Interferometry	164
A.2. Jones-Matrix Formalism	167
A.3. Jones-Matrix as Pulse Characterization Tool	168
B. Drift Correction of PEEM Data	171
C. Excitation Pathways for Single Color Pump-Probe Experiments	177
D. Principles of Optical Coherent 2D Spectroscopy	179
D.1. Representation of Mixed Quantum Mechanic States with the Density Matrix . . .	179
D.2. Response Function Formalism in Liouville Space	182
D.3. Liouville Pathways for Third Order Polarization	184
D.4. Optical 2D Spectroscopy in Experiments	186
E. 2D Nanoscopy: Mathematical Details	189
E.1. Local Photoemission Rate for $n = 4$ in Explicit Notation	189
E.2. Partial Photoemission Rate for Lorentz Oscillator Response Function	191
F. Lorentz Oscillator	193
List of Figures	195
Bibliography	199
Acknowledgements	229

Introduction

The observation and control of ultrafast processes on the nanoscale has become of interest recently as a consequence of developments on the fields of generating [9–11] and shaping [12–14] ultrashort laser pulses, nonlinear optical spectroscopy [15], nanooptics [16] and plasmonics [17]. Novel plasmonic devices are highly relevant for present and future applications for example in chip technology as high-speed interconnects [18–22], as localized coherent source of optical radiation and plasmonic excitations [23, 24], as well as for sensors and in solar cells [25]. Additionally, plasmonic devices employed as optical antennas couple strongly to individual single quantum systems [26–28], e.g. atoms and molecules, and localized plasmonic resonances on nanostructured metal surfaces are strongly enhancing molecular Raman spectroscopy signals [29–34]. Light-matter-interaction in plasmonic systems occurs and decays within femtoseconds and confines electric fields to spatial dimensions considerably smaller than the optical wavelength [20]. Thus, it is a challenging, but necessary task to develop instruments which are able to simultaneously resolve dynamics on these time and length scales.

The development and advancement of techniques which are sensitive to objects and processes that are too small, too far away, too fast or too weak to be recognized by direct observation with the bare eye has always been an essential and successful part of physical research. The magnified imaging of small objects employing single lenses can be considered as a starting point for optical microscopy [35]. Later, optical instruments were improved by using combinations of different lenses or curved mirrors. The increased spatial resolution of optical microscopes enabled to investigate biological tissue leading to the discovery of eukaryotic cells [36] and bacteria [37]. Despite further advancement of the instruments, it was discovered in the 19th century that an improvement of the resolution of conventional optical microscopes beyond the diffraction limit is not possible [38].

Optical spectroscopy techniques were initially probing static spectral properties of matter, e.g. absorption [39, 40] and emission spectra, obtaining information on linear light-matter interactions. Using ultrafast laser technology optical spectroscopy methods have become extremely precise in determining the exact energy of detected photons [41] as well as in measuring dynamics with high temporal resolution [11, 42]. Ultrafast optical spectroscopy involves preparing the investigated system with a *pump* pulse driving it off its thermal equilibrium state and probing the properties of the excited system with a delayed *probe* pulse [15, 43, 44]. Recently, *coherent optical two-dimensional (2D) spectroscopy* [15, 45–50] as an analog to two-dimensional spectroscopy of nuclear magnetic resonances [51] has become an important tool for the investigation of coupled molecular systems. The fully coherent excitation and detection scheme allows for separating contributions to the optical response from different excitation pathways, since the excitation and detection frequencies are represented on two independent spectral axes [15, 47, 50]. In optical 2D spectroscopy electronic and vibrational coupling in quantum systems appears as cross diagonal peaks and homogeneous and inhomogeneous broadening of resonant peaks are distinguished [15, 47, 50]. Utilizing femtosecond laser pulses the investigation and manipulation of

molecular systems is achieved on the timescales of the underlying electronic processes [10, 52, 53]. Femtosecond pulse shaping employs the high degrees of freedom provided by the high spectral bandwidth of femtosecond laser pulses and enables the *coherent control* over molecular dynamics and chemical reactions [44, 54–57]. However, these optical far-field methods all suffer from the diffraction limit of optical microscopy according to Abbe [38]. As a consequence, the interaction volume of the radiation with the sample is much larger than the typical dimensions of a single quantum system, e.g. a molecule, and the optical signal is averaged over an ensemble of such systems. Employing highly diluted samples, in which the density of quantum systems is reduced, and using tight optical focusing single molecule experiments have been demonstrated [58, 59]. Nevertheless, the optical resolution is still diffraction-limited and the investigated quantum systems are not embedded in a functional environment.

In the last two decades optical far-field methods have been developed that are able to break the optical diffraction limit by means of nonlinear confocal fluorescence microscopy [60]. In contrast to conventional optical microscopy, the term *far-field optical nanoscopy* is used to emphasize the high spatial resolution which is applied for example in the investigation of biological samples [60]. An important breakthrough was the invention of stimulated-emission-depletion (STED) microscopy in which fluorescent molecules mark the positions of proteins, membranes and other cell components [61]. Recently, other methods also demonstrated a resolution of few tens of nanometer e.g. PALM/STORM [62–65] and SSIM [66]. The use of fluorescent molecules provides high position sensitivity but prohibits a further spectroscopic investigation of the sample. Thus, techniques that do not rely on creating a far-field focus of optical radiation are necessary to gain spectroscopic information on sub-diffraction length scales.

Scanning probe microscopy achieves a high lateral resolution by scanning a nanoscaled tip over the sample surface and monitoring, depending on the particular method, different kinds of signals e.g. the tunneling current between probe and conducting samples (STM) [67, 68] and atomic forces between probe and sample (AFM) [69]. With near-field scanning optical microscopy (NSOM/SNOM) it is also possible to achieve resolutions beyond the diffraction limit, while still investigating an optical interaction with the sample [16, 27, 28, 70–72]. Optical near-fields are solutions of Maxwell's equations in the vicinity of interfaces which are much stronger confined in spatial dimensions than far-field radiation [16]. An appropriate choice of excitation and detection conditions even allows for temporal resolved SNOM [73–75].

Because of the small electron wavelength, electron microscopy techniques such as transmission electron microscopy (TEM) and scanning electron microscopy (SEM) suffer considerably less from diffraction and are able to achieve sub-nanometer resolution [76–78]. *Photoemission electron microscopy* (PEEM) maps the spatial distribution of electrons emitted from a sample which is illuminated by radiation [79, 80]. In multiphoton PEEM, i.e. the photoemission process involves more than one photon, the local photoemission yield from nanoscopic systems reflects the optical near-field distribution as a response to the excitation with ultrashort laser pulses [81]. Hence, multiphoton PEEM detects, similar to SNOM, electric fields which are confined to regions smaller than the optical diffraction limit. In contrast to SNOM, PEEM enables the simultaneous data acquisition in an extended spatial region. Furthermore, no probe tip has to be placed in the vicinity of the sample avoiding any unwanted interaction of excitation source and sample. Additional to the high spatial resolution, a time-resolved detection of the photoemission yield has been demonstrated by employing two femtosecond laser pulses with variable delay as pump and probe excitations [82]. Time-resolved PEEM (TR-PEEM), therefore, is a promising detection method for an ultrafast spectroscopy technique below the diffraction limit.

This thesis examines the three major experimental aspects which are necessary for the achievement of ultrafast spatiotemporal spectroscopy on the nanoscale by combination of coherent control of optical near-fields and time-resolved PEEM:

- Localization of optical near-fields acting as pump and probe excitations in space and time
- Spatial and temporal detection of the generated local photoemission yield
- Retrieval of spectroscopic information from localized delay-dependent photoemission data

Localization of optical near-fields acting as pump and probe excitations

By theoretical considerations it was shown that the localization of optical near-fields in the vicinity of a nanostructure can be manipulated, in analogy to coherent control of molecular systems [44, 54–56], by specifically tailored femtosecond laser pulse shapes [83, 84]. Furthermore, it was demonstrated in other theoretical publications that polarization pulse shaping enables the coherent control of spatial and temporal localization of optical near-fields [85, 86]. Two important coherent control mechanisms were identified: spatial control is achieved by adapting the polarization state of each frequency component and the spectral phase of the laser pulses is crucial for temporal control [86, 87]. The experimental scheme proposed in [85] uses localized optical near-fields in the vicinity of a nanostructure as pump and probe excitations, which are separated in space and in time, to investigate charge and energy transfer processes between quantum systems.

By combining femtosecond polarization pulse shaping with PEEM it was demonstrated experimentally that concepts of coherent control can indeed be applied for tailoring optical near-fields at different positions in nanoscopic systems [88]. In order to find optimal pulse shapes for localizing optical near-fields adaptive optimizations are employed because of the potentially complex local response of nanostructured samples to the incident laser pulses. These adaptive optimizations reliably find the global optimum of the applicable pulse shapes. However, the involved optimization procedure is tedious and measures to reduce the necessity of closed-loop optimizations can speed up further investigations of the system. In Chapter 2 an experimental demonstration of a universal rule for the coherent control of the local field intensity in nanostructured systems is presented [5, 87]. The utilization of the control rule allows for the open-loop switching between optimal pulse shapes generating opposite localized surface plasmon resonance distributions at a nanostructure.

Spatial and temporal detection of localized photoemission yield

In previous demonstrations of coherent control of optical near-fields the complete time-integrated photoemission yield at certain spatial positions was evaluated [88]. The resulting pulse shapes often showed a complex evolution of polarization states [88]. Accordingly, even though spatial localization of the optical fields was achieved, no information on the temporal evolution of the near-field was gathered. In a pump-probe experiment, however, also the control over the temporal evolution of the local fields is necessary. Chapter 3 presents a single-color pump-probe technique that achieves the simultaneous spatial and temporal resolved detection of near-fields at a nanostructure excited by polarization shaped laser pulses via TR-PEEM [2]. These experiments demonstrate that a sequence of localized optical excitations spatially separated on sub-diffraction length scale and temporally separated on femtosecond time scale are generated and detected

within a nanoscopic environment. Therefore, time-resolved PEEM combined with polarization pulse shaping indeed probes the local response of the nanosystem in space and time.

Retrieval of spectroscopic information from localized TR-PEEM data

In a next step TR-PEEM is combined with concepts of two-dimensional optical spectroscopy to gain full spectral information of a nanoscopic system [15, 45, 89]. This new investigation technique is named *coherent two-dimensional nanoscopy* (2D nanoscopy), since it obtains two-dimensional spectra of localized excitations with a resolution well below the optical diffraction limit of the excitation laser pulses [4]. In analogy to optical 2D spectroscopy a series of pulses excites the sample by inducing coherent electronic transitions into excited population states. Instead of detecting the material polarization via coherently emitted optical signal, 2D nanoscopy probes the local yield of photoemitted electrons in dependence of the relative delays and phases between the pulses in the excitation pulse sequences. Despite these differences the theoretical description of 2D nanoscopy, which is discussed in Chapter 4, is based on conventional optical 2D spectroscopy and exhibits many similarities in the resulting formalism. In principle, 2D nanoscopy determines the coherent excitation of electrons into population states, but it can also be extended towards the investigation of local electric fields in systems with fast electronic dephasing processes.

Employing the ultrafast coherent control and 2D nanoscopy techniques discussed and demonstrated in Chapter 1–4 two complex nanophotonic structures are studied, i.e. a corrugated silver surface (Chapter 5) and nanotextured absorber layers as they are used in thin-film solar cells for efficiency enhancement (Chapter 6).

The dominant multiphoton photoemission from corrugated silver films is connected to strongly localized photoemission hot spots, which are candidates for enabling surface enhanced spectroscopy [29–34]. By means of ultrafast coherent control experiments [3] as well as in the first experimental implementation of 2D nanoscopy [4] it is demonstrated that at several of these hot spots the local coherence lifetimes exceptionally exceed the expected short-lived behavior of localized plasmonic resonances. In a coherent two-pulse experiment the delay- and phase-dependent photoemission data from such a hot spot is analyzed. The retrieved local response function exhibits spectral features that indicate a coupling between two plasmonic modes. These observations are explained by hybridization of localized plasmonic modes with long-lived surface plasmon polariton modes.

The small thickness of the absorber layer and the reduced absorption coefficient of hydrogenated amorphous silicon (a-Si:H) at near-infrared optical wavelength limits the total absorption in a-Si:H thin-film solar cells [90, 91]. Light trapping in disordered scattering structures plays an important role in photon management strategies implemented in thin-film photovoltaic devices. In Chapter 6 coherent 2D nanoscopy is utilized to investigate the connection between absorption enhancement in nanotextured a-Si:H thin-film solar cells and the localization of photonic modes within the absorber layer [92]. The increased nonlinear order of the electron emission yield with respect to the pulse fluence is explained by an ultrafast thermionic emission process [93–95] driven by localized photonic modes. The spatial resolved detection of the local spectral properties via 2D nanoscopy allows to identify photoemission signals originating from individual photonic modes.

1. Basic Theoretical and Experimental Concepts

This chapter deals with the basic concepts concerning femtosecond laser pulses and time-resolved photoemission electron microscopy. A mathematical description of polarization-shaped laser pulses is presented in Section 1.1. First, a general introduction in the properties of ultrashort laser pulses is given. Afterwards, representations of the polarization state are discussed. Femtosecond laser pulse shaping enables tailoring the spectral phase and amplitude of laser pulses and is used for near-field control and to generate pulse sequences with high interferometric stability (Section 1.2). Plasmonic excitations at the surface of metals and in nanoscopic objects lead to a strong confinement and enhancement of electric fields at surfaces. Thus, interesting properties and applications arise which are discussed in Section 1.3. Combining femtosecond laser pulses with photoemission electron microscopy permits the time-resolved detection of optical near-fields with a spatial resolution beyond the optical diffraction limit (Section 1.4).

1.1. Description and Representation of Polarization-Shaped Laser Pulses

Ultrashort laser pulses can be considered in the limit of classical waves, i.e. large photon numbers, as coherent superposition of monochromatic waves. The mathematical descriptions in time domain and frequency domain are connected by Fourier transformation. The fixed phase relation between the frequency components determines, together with the shape of the spectrum, the temporal properties of the laser pulse. In the following section the mathematical descriptions for linearly polarized laser pulses is briefly presented based on literature [11, 44, 96].

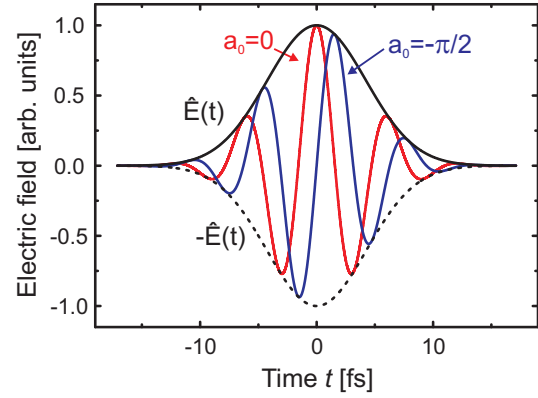
During the propagation electric fields are affected by the medium via absorption of light energy and dispersion. Basic aspects of propagation of light through dispersive media are discussed in Section 1.1.2.

Light is a transverse electromagnetic wave. Field oscillations are allowed in every orientation normal to the propagation direction. Thus, the electric field vector lies on a two-dimensional plane and needs a representation with two independent basis vectors \mathbf{e}_1 and \mathbf{e}_2 .

$$\mathbf{E}(t) = E_1(t)\mathbf{e}_1 + E_2(t)\mathbf{e}_2 = \begin{pmatrix} E_1(t) \\ E_2(t) \end{pmatrix} \quad (1.1)$$

Most conveniently, \mathbf{e}_1 and \mathbf{e}_2 are orthogonal and normalized, i.e. $\mathbf{e}_1\mathbf{e}_2 = 0$ and $\mathbf{e}_1\mathbf{e}_1 = \mathbf{e}_2\mathbf{e}_2 = 1$. Such basis vectors are, for example, those of the Cartesian coordinate system $(\mathbf{e}_x, \mathbf{e}_y, \mathbf{e}_z)$, where \mathbf{e}_z denotes the direction of propagation and $\mathbf{e}_1 = \mathbf{e}_x$ and $\mathbf{e}_2 = \mathbf{e}_y$ point in horizontal and vertical direction, respectively. However, all sets of basis vectors rotated around \mathbf{e}_z are equally valid, e.g. $\mathbf{e}_1 = \sqrt{2}(\mathbf{e}_x + \mathbf{e}_y)$ and $\mathbf{e}_2 = \sqrt{2}(\mathbf{e}_x - \mathbf{e}_y)$ for a rotation angle of 45° . According to Eq. (1.1), the

Figure 1.1: A femtosecond laser pulse with carrier frequency $\omega_0 = 1$ rad/fs (wavelength: $\lambda = 1.89 \mu\text{m}$, photon energy: $\hbar\omega_0 = 0.65$ eV). The Gaussian-shaped envelope $\hat{E}(t)$ is centered at $t_0 = 0$ fs and has a full width at half maximum of 10 fs. The solid red line indicates the electric field of an unchirped laser pulse without carrier-envelope phase offset ($a_0 = 0$). The blue line shows a laser pulse with identical parameters but a carrier envelope phase set to $a_0 = -\pi/2$.



electric field vector $\mathbf{E}(t)$ is the superposition of both field components. In general its orientation varies through a pulse because $E_1(t)$ and $E_2(t)$ are complex quantities. A representation which does reflect the orientation and ellipticity of the momentary polarization state is achieved with a transformation to elliptical pulse parameters that is introduced in Section 1.1.3.

1.1.1. Temporal and Spectral Description of Femtosecond Laser Pulses

At a fixed point in space, the temporal evolution of an arbitrary electric field component $E(t)$ of a femtosecond laser pulse can be described as

$$E(t) = \hat{E}(t) \cos(\phi(t)) , \quad (1.2)$$

where $\hat{E}(t)$ is the temporal amplitude or envelope and $\phi(t)$ is the temporal phase. A Taylor expansion of $\phi(t)$ around the center of the pulse at t_0 yields

$$\phi(t) = \sum_{j=0}^{\infty} \frac{a_j}{j!} (t - t_0)^j = \omega_0 t + \tilde{a}_0 + \overbrace{\sum_{j=2}^{\infty} \frac{a_j}{j!} (t - t_0)^j}^{=\varphi(t)} \quad (1.3)$$

$$\text{with } \tilde{a}_0 = a_0 - \omega_0 t_0 \text{ and } a_j = \left. \frac{\partial^j \phi(t)}{\partial t^j} \right|_{t=t_0} .$$

The linear term $\omega_0 t$ contains information on the carrier frequency ω_0 , which is the average oscillation frequency of the electric field. In $\varphi(t)$ the temporal modulation of the phase is expressed. Therefore, $\varphi(t)$ describes the phase of the laser pulse observed in the *rotating frame*, i.e. compared to a systems which oscillates with the center frequency ω_0 [97]. The constant term \tilde{a}_0 is the absolute phase. Since a_0 describes the shift of the fast carrier oscillations with respect to the center of the electric field envelope $\hat{E}(t)$ (see Figure 1.1), it is also called carrier-envelope phase (CEP) [10, 98, 99]. It becomes increasingly important the shorter the laser pulses are because it determines the maximal electric field strength within the pulse. In the few-cycle regime control over the CEP enables the creation of isolated attosecond pulses in the HHG in noble gases [100, 101]. Using these attosecond pulses electric field oscillations of a laser pulse are made visible in attosecond-streaking experiments [42, 102, 103]. Also with non-amplified laser pulses from an CEP-stabilized laser cavity CEP effects in the photoemission from solids, e.g. tungsten tips,

have been demonstrated [104, 105]. Furthermore, phase-stabilized lasers offer the possibility to perform extremely precise optical spectroscopy experiments [41]. In this thesis, the employed pulse length is too long for observing CEP related effects. However, considering the vectorial nature of polarization-shaped laser pulses, the phase difference between both polarization components becomes crucial. Relative CEP offsets play also an important role in the pulse sequences used for coherent 2D nanoscopy (see Chapters 4, 5 and 6) [4].

If higher order terms of the temporal phase modulation $\varphi(t)$ have non-zero values, the laser pulse is *chirped*. A chirp leads to a change of the instantaneous frequency $\omega(t)$ which is defined as

$$\omega(t) = \frac{d\phi(t)}{dt} = \omega_0 + \frac{d\varphi(t)}{dt} = \omega_0 + \sum_{j=2}^{\infty} \frac{a_j}{(j-1)!} (t-t_0)^{j-1}. \quad (1.4)$$

Thus, a_2 , a_3 and a_4 determine the linear, quadratic and cubic temporal derivative of $\omega(t)$, respectively. If a chirp is introduced into a pulse with constant $\varphi(t)$, e.g. via the propagation through a glass substrate, the temporal pulse envelope is elongated and distorted. Further details on the effect of dispersion on the pulse shape will be presented in Section 1.1.2.

The electric field is equivalently expressed in time- and frequency-domain as it is shown in Eq. (1.5). The spectral representation is obtained by Fourier transform of the temporal electric field. Starting with electric fields defined in frequency-domain the temporal electric field is recovered by the inverse Fourier transform [106].

$$E(\omega) = \mathcal{F}\{E(t)\} = \frac{1}{\sqrt{2\pi}} \int_{-\infty}^{\infty} E(t) e^{-i\omega t} dt \quad (1.5)$$

$$E(t) = \mathcal{F}^{-1}\{E(\omega)\} = \frac{1}{\sqrt{2\pi}} \int_{-\infty}^{\infty} E(\omega) e^{i\omega t} d\omega \quad (1.6)$$

As the temporal field in Eq. (1.2) is defined as a real-valued quantity for the spectral representation the Hermitian condition

$$E(\omega) = E^*(-\omega) \quad (1.7)$$

is fulfilled, where the complex conjugate is indicated by the asterisk. Thus, already the positive frequency part of the complex spectral electric field

$$E^+(\omega) = \begin{cases} E(\omega) & \text{if } \omega \geq 0, \\ 0 & \text{if } \omega < 0 \end{cases} \quad (1.8)$$

gives the complete information on the temporal electric field. The spectral electric field $E^+(\omega)$ is factorized into a real- and positive-valued and spectral amplitude $\hat{E}(\omega)$ and a complex-valued term containing the spectral phase $\varphi(\omega)$:

$$E^+(\omega) = \hat{E}(\omega) e^{-i\varphi(\omega)} \quad (1.9)$$

$\hat{E}(\omega)$ denotes the amplitude of the monochromatic wave components which contribute to the laser pulse and $\varphi(\omega)$ determines how these components interfere. Spectral amplitude $\hat{E}(\omega)$ and

temporal envelope $\hat{E}(t)$ do not build a Fourier transform pair, since $\hat{E}(\omega)$ is centered at the carrier frequency ω_0 . The spectral phase $\varphi(\omega)$ can also be written as a Taylor expansion. A linear spectral phase leads to a shift of the pulse in time domain according to the shift theorem of Fourier transformation [106]. A second order contribution to $\varphi(\omega)$ introduces a linear chirp in time domain and broadens the temporal pulse envelope. Higher order spectral phases also affect the pulse envelope and lead to complex and asymmetrically shaped pulses. Thus, manipulating the spectral amplitude and phase gives access to tailoring the temporal properties of the femtosecond laser pulse as it is described further in Section 1.2.

The temporal electric field $E^+(t)$ which is given by the inverse Fourier transform of $E^+(\omega)$

$$E^+(t) = \frac{1}{\sqrt{2\pi}} \int_0^{\infty} E(\omega) e^{i\omega t} d\omega = \frac{1}{\sqrt{2\pi}} \int_{-\infty}^{\infty} E^+(\omega) e^{i\omega t} d\omega, \quad (1.10)$$

is a complex-valued representation and, therefore, is used for mathematical operations in a more general and often simpler fashion than the real-valued $E(t)$. Also the complex electric field can be expressed in a factorized notation:

$$E^+(t) = \hat{E}(t) e^{i\phi(t)} = \tilde{E}^+(t) e^{i\omega_0 t}, \quad (1.11)$$

where $\tilde{E}^+(t)$ denotes the complex temporal envelope containing the phase modulations φ_t . The Fourier transform of $E^+(t)$ yields again $E^+(\omega)$ and Fourier transform of the complex envelope $\tilde{E}^+(t)$ yields the spectral field shifted to the zero frequency position $E^+(\omega + \omega_0)$. Accordingly, $E^-(t)$ contains the information of the negative frequencies and is the complex conjugate of $E^+(t)$. Since the spectral electric field $E(\omega)$ can be separated into

$$E(\omega) = E^+(\omega) + E^-(\omega) \quad (1.12)$$

and the Fourier transformation is linear, the analogous relation holds for the temporal electric field $E(t)$:

$$E(t) = E^+(t) + E^-(t) = 2\text{Re}\{E^+(t)\}. \quad (1.13)$$

The temporal intensity $I(t)$ denotes the temporal evolution of the energy flux associated with the propagation of the electric field [11]:

$$I(t) = 2\varepsilon_0 c n E^+(t) E^-(t) = \frac{1}{2} \varepsilon_0 c n \hat{E}^2(t). \quad (1.14)$$

Hence, $I(t)$ is proportional to the squared field envelope $\hat{E}(t)$. Here, the additional factors are the vacuum dielectric constant ε_0 , the vacuum velocity of light c and the index of refraction n of the medium in which the intensity is measured. The spectral intensity is defined similarly

$$I(\omega) = 2\varepsilon_0 c n E^+(\omega) E^-(\omega) = \frac{1}{2} \varepsilon_0 c n \hat{E}^2(\omega). \quad (1.15)$$

For the sake of simplicity the prefactors will be omitted in the derivations in this thesis. The total energy flux F , which is also called linear flux or fluence, is equal in the temporal and spectral

representations satisfying Parseval's theorem [107]:

$$F = \int_{-\infty}^{\infty} I(t)dt = \int_{-\infty}^{\infty} I(\omega)d\omega. \quad (1.16)$$

The temporal duration τ_P and the spectral bandwidth $\Delta\omega$ of a laser pulse are determined by the corresponding intensity distributions $I(t)$ and $I(\omega)$, respectively. Several definitions for τ_P and $\Delta\omega$ are customary [11]. In this thesis the full width at half maximum (FWHM) of the intensity $I(t)$ and $I(\omega)$ are used:

$$\tau_P = \text{FWHM}\{I(t)\} \quad \text{and} \quad \Delta\omega = \text{FWHM}\{I(\omega)\}. \quad (1.17)$$

These definitions can only be applied to simple pulse shapes e.g. Gaussian-shaped pulses, Sech pulse shapes and Lorentzian pulse shapes [11]. Since the temporal and spectral representations of the electric field are connected via Fourier transformation, there is a relation between the duration τ_P of a laser pulse with the corresponding spectral bandwidth $\Delta\omega$ [11]. The so called time-bandwidth product has to be bigger than a pulse-shape-dependent constant c_B :

$$\tau_P\Delta\omega \geq c_B. \quad (1.18)$$

The time-bandwidth product constant for Gaussian pulses is $c_B = 4 \ln 2$. For a Gaussian spectrum a pulse with minimal duration according to the spectral bandwidth is called bandwidth-limited, transform-limited, or Fourier-limited and cannot contain any phase modulations of second or higher order. Complex pulses with strongly modulated intensities the mean square deviation, which is identical with the second order moment of the distribution, is a better estimate for the pulse length, but it is insufficient to completely characterize the pulse [11].

1.1.2. Spatial Propagation of Light in Dispersive Media

In the previous section ultrashort electric field pulses at a fixed spatial positions were discussed. However, light is an electromagnetic wave and its spatial and temporal properties are classically described by Maxwell's equations. To satisfy Maxwell's equations, the electric field $\mathbf{E}(\mathbf{r}, t)$ has to be a solution of the inhomogeneous wave equation

$$\Delta\mathbf{E}(\mathbf{r}, t) - \mu_0\varepsilon_0 \frac{\partial^2}{\partial t^2}\mathbf{E}(\mathbf{r}, t) = \mu_0 \frac{\partial^2}{\partial t^2}\mathbf{P}(\mathbf{r}, t), \quad (1.19)$$

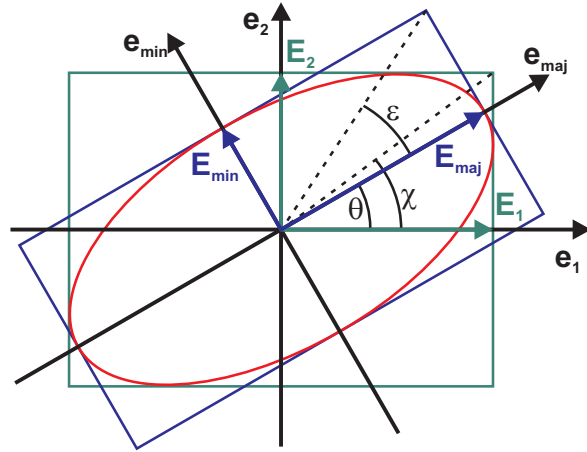
which determines the interaction of $\mathbf{E}(\mathbf{r}, t)$ with non-magnetic matter. The material polarization $\mathbf{P}(\mathbf{r}, t)$ denotes the displacement of positive and negative charge carriers as a response of the medium to the electric field. Reciprocally, the polarization acts as the source for the electric field. In general the polarization comprises also terms which depend in a nonlinear fashion on the electric field and can be expanded accordingly

$$\mathbf{P}(\mathbf{r}, t) = \sum_n \mathbf{P}^{(n)}(\mathbf{r}, t) \quad (1.20)$$

By Fourier transforming Eq. (1.19) the temporal derivatives are replaced by multiplication with $i\omega$ and the equation further simplifies to

$$\Delta\mathbf{E}(\mathbf{r}, \omega) - \omega^2\mu_0 [\varepsilon_0\mathbf{E}(\mathbf{r}, \omega) + \mathbf{P}(\mathbf{r}, \omega)] = 0 \quad (1.21)$$

Figure 1.2: Coordinate system for elliptic representation of polarized light. The ellipse-inherent coordinate system (\mathbf{e}_{maj} , \mathbf{e}_{min}) is rotated by the orientation angle θ with respect to the Cartesian coordinate system (\mathbf{e}_1 , \mathbf{e}_2). The ellipticity ε of the light-polarization ellipse is determined by the ratio of the electric fields E_{maj} and E_{min} along the major and minor principal axis. The corresponding angle between E_1 and E_2 is χ . Adapted from Brixner [109–111].



In a uniform isotropic linear medium the polarization contains only the linear term $\mathbf{P}(\omega) = \varepsilon_0(\varepsilon_r(\omega) - 1)\mathbf{E}(\omega)$. The dielectric function $\varepsilon_r(\omega)$ in general varies with the frequency and is connected with the linear refractive index by $n(\omega) = \sqrt{\varepsilon_r(\omega)}$. Another helpful relation is $\mu_0\varepsilon_0 = 1/c^2$ leading to solutions for this equation given by

$$\mathbf{E}(\mathbf{r}, \omega) = \mathbf{E}(0, \omega)e^{i\mathbf{k}(\omega)\mathbf{r}}, \quad (1.22)$$

where $\mathbf{k}(\omega) = \omega n(\omega)/c \cdot \mathbf{e}_k$ is the wave vector of the electromagnetic wave propagating towards the direction of the normalized vector \mathbf{e}_k . In a material without absorption ($n(\omega) = \text{Re}\{n(\omega)\} > 1$) the propagation of the electric field is fully described by the accumulation of spectral phase $\varphi(\mathbf{r}, \omega) = \varphi(0, \omega) + \mathbf{k}(\omega)\mathbf{r}$. Since the refractive index in dispersive media $\varepsilon_r(\omega)$ in generally changes with the frequency, $\mathbf{k}(\omega)$ deviates from a linear increase with ω . Consequently, the spectral phase accumulates higher-order contributions to its Taylor expansion. After propagation to position \mathbf{r} , the linear phase term causes a *group delay* $\text{GD} = |\mathbf{r}|/n(\omega)c$ indicating the temporal shift of the pulse envelope. The quadratic *group delay dispersion* (GDD) denotes the temporal displacement, which a small-bandwidth wave packet at frequency ω gains during the propagation with respect to the central frequency ω_0 . GDD leads to a broadening of the pulse envelope and a linear increase or decrease of the instantaneous frequency $\omega(t)$. Thus, it is connected to the temporal phase coefficient a_2 . The *third order dispersion* (TOD) causes asymmetrical pulse envelopes with oscillation at the leading or trailing edge, depending on the sign of the TOD.

In a birefringent medium the dielectric function is anisotropic and, therefore, can differ along the directions of the electric field basis vectors. Accordingly, the propagation of the electric field polarization components through this medium is associated with different accumulated phases. As a consequence, the polarization state of the electric field changes during the propagation. The polarization state is also affected by interfaces between media with differing dielectric functions, e.g. the reflexion at a metal surface leads to a relative phase shift of the polarization components. A description of the propagation of light through media with nonlinear contributions $\mathbf{P}^{(n)}(\mathbf{r}, t)$ to the material polarization can be found in [11, 44, 57, 108].

1.1.3. Elliptical Pulse Parameter

Combining Eq. (1.1) with the definitions of Section 1.1.1, the electric field of a polarization-shaped laser pulse at a fixed position in space is fully described by the superposition of two

orthogonal field components perpendicular to the propagation direction:

$$\begin{aligned}\mathbf{E}(t) &= \begin{pmatrix} E_1(t) \\ E_2(t) \end{pmatrix} = \begin{pmatrix} \hat{E}_1(t) \cos(\omega_0 t + \varphi_1(t)) \\ \hat{E}_2(t) \cos(\omega_0 t + \varphi_2(t)) \end{pmatrix} \\ &= \hat{E}_1(t) \cos(\omega_0 t + \varphi_1(t)) \mathbf{e}_1 + \hat{E}_2(t) \cos(\omega_0 t + \varphi_2(t)) \mathbf{e}_2\end{aligned}\quad (1.23)$$

Often, a representation of polarization-shaped laser pulses with elliptical pulse parameters is more intuitive. The discussion of this representation within this section is based on literature [109–112]. It is valid within the slowly varying envelope approximation (SVEA), i.e. the evolution of the field envelope $\hat{E}(t)$ is considered to be small on the time scale of the oscillation period $T_P = 2\pi/\omega(t)$. Then, the motion of the electric field vector $\mathbf{E}(t)$ follows an ellipse which is characterized by the angle of ellipticity $\varepsilon(t)$ and the orientation angle $\theta(t)$ between the major principal axis \mathbf{e}_{maj} of the ellipse and \mathbf{e}_1 in the Cartesian coordinate system. The geometric relations between those quantities are shown in Fig 1.2. The orientation angle $\theta(t)$ and the ellipticity $\varepsilon(t)$ define the momentary polarization state. The auxiliary angle

$$\chi(t) = \arctan \left(\frac{\hat{E}_2(t)}{\hat{E}_1(t)} \right) \in [0, \pi/2], \quad (1.24)$$

which is given by the ratio of the temporal envelopes in Cartesian coordinates $\hat{E}_1(t)$ and $\hat{E}_2(t)$, and the phase modulation difference

$$\Phi(t) = \varphi_2(t) - \varphi_1(t) \in [-\pi, \pi] \quad (1.25)$$

simplify the calculation of $\varepsilon(t)$ and $\theta(t)$ from linear coordinate system parameters. The square brackets indicate the definition intervals of the quantities. For complex notation of the electric field $\chi(t)$ and $\Phi(t)$ are both connected to the ratio of the complex field components via

$$\frac{E_2^+(t)}{E_1^+(t)} = \frac{\hat{E}_2(t) e^{-\varphi_2(t)}}{\hat{E}_1(t) e^{-\varphi_1(t)}} = \tan \chi(t) e^{-\Phi(t)}. \quad (1.26)$$

The orientation angle $\theta(t)$ is by convention restricted to the interval $[-\pi/2, \pi/2]$. Thus, the major principal axis is always in the first or fourth quadrant of the Cartesian coordinate system. It can be written as

$$\theta(t) = \begin{cases} \tilde{\theta}(t) & \in [-\pi/4, \pi/4] & \text{if } \chi(t) \leq \pi/4 \\ \tilde{\theta}(t) + \pi/2 & \in [\pi/4, \pi/2] & \text{if } \chi(t) > \pi/4 \wedge \tilde{\theta}(t) < 0 \\ \tilde{\theta}(t) - \pi/2 & \in [-\pi/2, -\pi/4] & \text{if } \chi(t) > \pi/4 \wedge \tilde{\theta}(t) \geq 0 \end{cases} \quad (1.27)$$

where

$$\tilde{\theta}(t) = \frac{1}{2} \arctan [\tan(2\chi(t)) \cos(\Phi(t))] \in [-\pi/4, \pi/4]. \quad (1.28)$$

From Eq. (1.28) an interesting property of the elliptical representation is deduced. Since the linear coordinate system is in principle arbitrarily chosen, at a certain instant it can be rotated to match the orientation of the principal axes. This causes $\tilde{\theta}(t)$ to become zero. As the auxiliary

angle $\chi(t)$ exhibits an arbitrary value between 0 and $\pi/2$, $\cos(\Phi(t))$ has to be zero. This is the case only for phase differences of $\Phi(t) = -\pi/2$ and $\Phi(t) = \pi/2$. Consequently, the field components along the principal axes of the ellipse have a fixed phase difference of $\pm\pi/2$. The sign is determined by the sign of the ellipticity $\varepsilon(t)$. For the ellipticity it can be shown that

$$\varepsilon(t) = \frac{1}{2} \arcsin [\sin(2\chi(t)) \sin(\Phi(t))] \in [-\pi/4, \pi/4]. \quad (1.29)$$

If the angle of ellipticity $\varepsilon(t)$ is zero, the polarization state is linear. In this case the minor principal amplitude $\hat{E}_{min}(t)$ becomes zero and the polarization oscillates in the direction specified by θ . For non-zero values of $\varepsilon(t)$ the electric field vector rotates along the polarization ellipse. In case of a positive ellipticity ($\varepsilon(t) > 0$) the sense of rotation is momentarily left and negative values of $\varepsilon(t)$ indicate momentarily right elliptically polarized light state. The convention for right- and left-handedness is given by the movement of the electric field vector on a plane perpendicular to the propagation and observed from negative propagation direction. In the special case of $|\varepsilon(t)| = \pi/4$ the polarization state is called circular and both principal axes have the same size. As a consequence, the orientation angle θ does not affect the polarization state. However, the left and right circular polarization states are not identical but orthogonal. They form a pair of basis vectors which also enables a complete representation of the electrical field [96].

In the elliptical representation the angles $\theta(t)$ and $\varepsilon(t)$ determine the polarization state, but for a full description of the electric field two additional real-valued quantities are necessary. In the linear coordinate system such a set is $\{I_1(t), I_2(t), \varphi_1(t), \varphi_2(t)\}$, with $I_1(t)$ and $I_2(t)$ calculated from the amplitudes according to Eq. (1.14). The total intensity defined by

$$I(t) = [\hat{E}_1(t)]^2 + [\hat{E}_2(t)]^2 = [\hat{E}_{maj}(t)]^2 + [\hat{E}_{min}(t)]^2 \quad (1.30)$$

and the total phase

$$\varphi(t) = \varphi_1(t) + \text{sign}[\theta(t)\varepsilon(t)] \arccos \left[\frac{\sqrt{I(t)}}{\hat{E}_1(t)} \cos \theta(t) \cos \varepsilon(t) \right] \quad (1.31)$$

give combined with $\theta(t)$ and $\varepsilon(t)$ sufficient information for a full representation of the electric field [109–111]. The zero position of the total phase is always located on that point on the polarization ellipse, where the electric field vector points in the direction of the major principal axis (\mathbf{e}_{maj}). Hence, it moves according to the ellipse-inherent coordinate system. Due to the use of the arccosine function the total phase $\varphi(t)$ might contain phase jumps of $\pm\pi$, which have to be removed in order to obtain a continuous phase function. If $|\varepsilon(t)| = \pi/4$, Eq. (1.31) contracts to $\varphi(t) = \varphi_1(t) + \text{sign}[\theta(t)\varepsilon(t)]\theta(t)$. Thus, for circular polarization the value of the orientation angle $\theta(t)$ does only affect the phase $\varphi(t)$ by an offset. In case of linear polarization Eq. (1.31) directly yields: $\varphi(t) = \varphi_1(t)$.

In analogy to Eq. (1.4) the momentary oscillation frequency is given by the temporal derivative of the phase

$$\omega(t) = \omega_0 + \frac{d\varphi(t)}{dt}. \quad (1.32)$$

Hence, the intensity $I(t)$ and phase $\varphi(t)$ determine the momentary size and frequency of the polarization ellipse.

The elliptical pulse parameters are useful in the representation of polarization-shaped laser pulses. However, individually plotting the four necessary quantities that fully characterize the polarization state (e.g. $\{\theta, \varepsilon, I, \varphi\}$) in spectral or temporal domain often yields unintuitive graphs that needs further interpretation. In this thesis mainly two alternative representations are used: plots of the Poincaré surface [111–113] and quasi-3D representations [110] (see Figure 2.7). Quasi-3D representations show the momentary polarization ellipses at discrete temporal positions and provide information on the polarization state and the intensity via the shape, orientation and size of the polarization ellipse [110]. The coloring of the ellipses encode the momentary frequency. The sense of rotation of the polarization state is not distinguishable in this representation. The momentary polarization state defined by $\theta(t)$ and $\varepsilon(t)$ can be indicated by points on the so-called Poincaré surface, which is the surface of a sphere and the spherical angles of longitude and latitude are determined by $2\theta(t)$ and $2\varepsilon(t)$, respectively [111–113]. The projection of the Poincaré surface onto a plane enables a simplified representation. However, the trajectories on this planar Poincaré surface still reflect the periodic boundary conditions of the sphere [111, 112]. The color and the color saturation of the plotted data points can indicate the momentary frequency and intensity.

1.2. Concepts of Laser Pulse Shaping

Laser pulse shaping is of high importance for broadband coherent control as well as for multidimensional spectroscopy on the nanoscale because it enables the specific generation of complex pulse shapes [56, 114] and pulse sequences with high interferometric stability [49, 115]. By dispersing the frequency components of the laser pulse, e.g. by a grating, the components are spatially separated and individually tailored with a spatial light modulator (SLM) [116, 117] utilizing the relations between spectral and temporal pulse properties discussed in Section 1.1. The pulse shaper implemented in the experiments that are discussed in this thesis employs a liquid crystal display (LCD) as spatial light modulator in the Fourier plane of a zero-dispersion 4f-compressor [12, 13, 109, 118, 119]. Liquid crystal display based pulse shaper achieve a high spectral resolution and are able to tailor many degrees of freedom simultaneously. So called vector-field synthesizer have been designed and tested which provide full control over the spectral amplitudes, phases and polarization states of the shaped laser pulses [14, 120]. Thus, within device specific limits, arbitrarily shaped ultrashort laser pulses are generated.

In this section the basic concepts of the polarization pulse shaper design are introduced (see Section 1.2.1). It is discussed how amplitude and phase shaping as well as polarization shaping are implemented (Sections 1.2.2). Pulse shaper offer a high flexibility of achievable pulse shapes. However, the huge accessible parameter space complicates the identification of the optimal pulse shape for a specific problem. Adaptive optimization experiments can find the optimal pulse much faster than a multidimensional scan of all parameters. The optimization technique used in the coherent control experiments in this thesis is presented in Section 1.2.3. It utilizes an evolutionary algorithm that detects the optimal pulse parameter similarly to the biological evolution process.

1.2.1. Polarization Pulse Shaper Setup

Basically, a polarization pulse shaper consists of a 4f zero-dispersion compressor with a liquid crystal display placed in the Fourier plane between the two gratings. This is presented schemati-

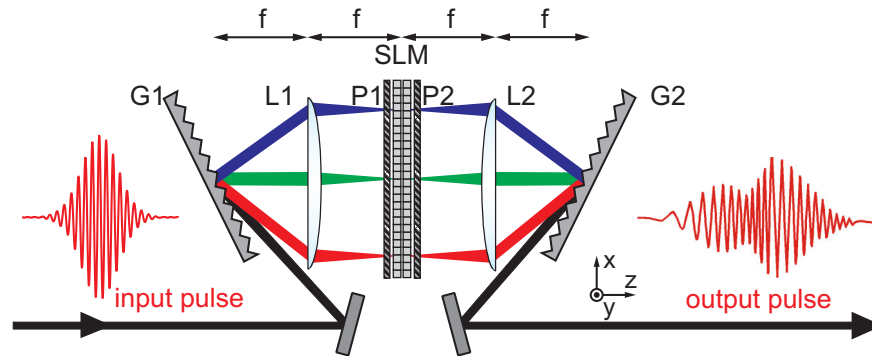


Figure 1.3.: Schematic of polarization pulse shaper setup. The two plano-cylindrical lenses (L1 and L2) with focal length f and the two identical gratings (G1 and G2) form a $4f$ zero dispersion compressor. Ultrashort laser pulses (black arrow) are spatially dispersed at G1 and focused by lens L1 onto the Fourier plane. A LCD modulates the properties of the individual frequency components, which are collimated by L2 and recombined by G2. The two polarizers P1 and P2 (hatched rectangles) determine the polarization component that is modulated by the double-layer LCD (arrays of gray squares) acting as SLM and whether polarization pulse shaping or combined amplitude and phase shaping is performed. For polarization pulse shaping the polarizer P2 is left out of the setup. In case of amplitude and phase shaping P2 determines the output polarization. Modified from [109].

cally in Figure 1.3. The incident laser pulses are dispersed by the first grating in its frequency components. Two plano-cylindrical lenses (L1 and L2) are positioned at a distance of the focal length f to the gratings (G1 and G2, respectively) and with a separation of $2f$ to each other. Consequently, L1 focuses the frequency components at different positions of the Fourier plane, where the spatial light modulator is located, and L2 collimates the beams transmitted by the SLM pixels and directs them to the identical spot on the second grating (G2). The frequency components are recombined after a propagation distance of $4f$ between both gratings and leave the pulse shaper with a temporal structure given by the settings of the SLM. The implemented spatial light modulator (Cambridge Research & Instrumentation SLM-256-NIR) consists of two liquid crystal display layers. Each layer contains a linear arrays of 128 pixels which is individually addressed by a control voltage. In front of the SLM the polarizer P1 defines the linear input polarization direction. The second polarizer (P2) is inserted into the setup for amplitude and phase shaping instead of polarization pulse shaping.

A schematic illustration of one of the LCD layers of the SLM is presented in Figure 1.4. The layer comprises two glass plates in the x - y -plane coated on the inside with indium-tin-oxide (ITO), which is transparent for near-infrared radiation and electrically conducting. The interspace between the plates contains liquid crystal molecules in the nematic phase [122–124]. The preferential orientation of the molecules is fixed to the y direction by a special coating of the glass plates. Without applied voltage the liquid crystal molecules within a pixel orient in the preferential direction and the anisotropic polarizability of the molecules leads to a birefringence, i.e. the refractive indices $n_x(\omega)$ and $n_y(\omega)$ for x or y polarized field components differ. In the presence of an electric field in z direction the molecules rotate along the x axis causing a voltage-dependent refractive index $n_y(\omega)$ for the y polarized component. The pixels are addressed individually by a controller (Cambridge Research & Instrumentation SLM-ELT-256) that applies voltages U between 0 V and 10 V. Depending on U the phase retardation introduced by the pixel is written

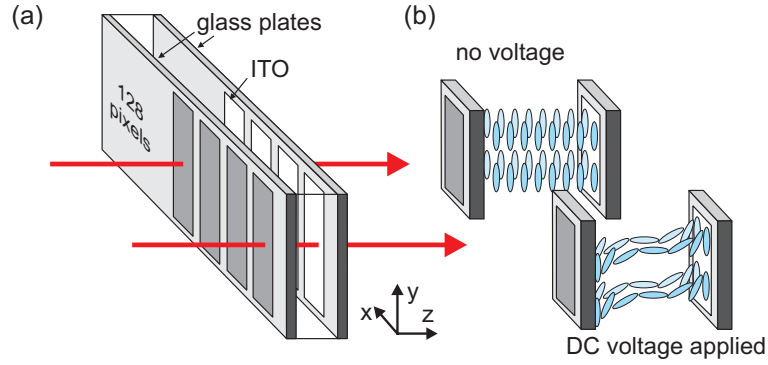


Figure 1.4.: Liquid crystal display (LCD) setup (a) and orientation of liquid crystal molecules within a pixel of the LCD with and without applied voltage (b). (a) The used spatial light modulator (Cambridge Research & Instrumentation SLM-256-NIR) contains two LCD layers. The displayed LCD layer consists of two glass plates coated on the inside with ITO. The 128 pixels are $97 \mu\text{m}$ wide and 2 mm high and displaced in x direction by $100 \mu\text{m}$ leaving a gap of $3 \mu\text{m}$ between the pixels. (b) The liquid crystal molecules within a pixel orient along the preferential y direction when no voltage is applied to the electrodes of the pixel. With applied voltage the molecules twist towards the z direction. Adapted from [109, 121].

as

$$\Delta\phi(U, \omega) = \frac{\omega d}{c} [n_y(\omega)(U, \omega) - n_y(\omega)(0 V, \omega)] , \quad (1.33)$$

where $n_y(\omega)(0 V, \omega)$ is the refractive index without applied voltage and d denotes the length of the pixel. The phase retardation $\Delta\phi(U, \omega)$ depends in a nonlinear fashion from the applied voltage U and the light frequency ω at the pixel. Thus, prior to an experiment two major calibration steps have to be performed by measuring the center frequencies of each LCD pixel and determining the introduced phase retardation for the complete voltage range. The maximal phase range achievable with a pixel is approximately 6π . This is sufficient, as phase modulations creating a phase difference between two pixels which is bigger than this limit are wrapped back into the shapeable interval by introducing jumps of $\pm 2\pi$. Further details of the polarization shaper setup are given in [109, 110, 121, 125, 126] In the following section it will be discussed how the control of the applied phase retardations in a two-layer LCD allows amplitude and phase shaping of linearly polarized pulses or polarization pulse shaping.

1.2.2. Methods for Amplitude, Phase and Polarization Pulse Shaping

The SLM of the polarization pulse shaper provides an adjustable birefringence via the orientation of the liquid crystal molecules. To achieve independent control over the phase retardation of two perpendicular polarization components, a LCD double-layer with orthogonal orientations has to be used. By orienting the preferential directions rotated by 45° and -45° with respect to polarizer P1, which defines the input polarization direction, the amplitudes of the tailored components are distributed equally. Thus, in contrast to Figure 1.4b, the adjustable extra-ordinary axes are on the two orthogonal diagonals between x and y direction. To change the polarization state, the phase shifts introduced by the two subsequent LCD pixels have to be different. This is visualized in Figure 1.5. Here, the horizontal (x) input polarization (blue) is decomposed into the electric field components along the LCD directions 1 (red) and 2 (green) with identical phases ($\varphi_1 = \varphi_2$).

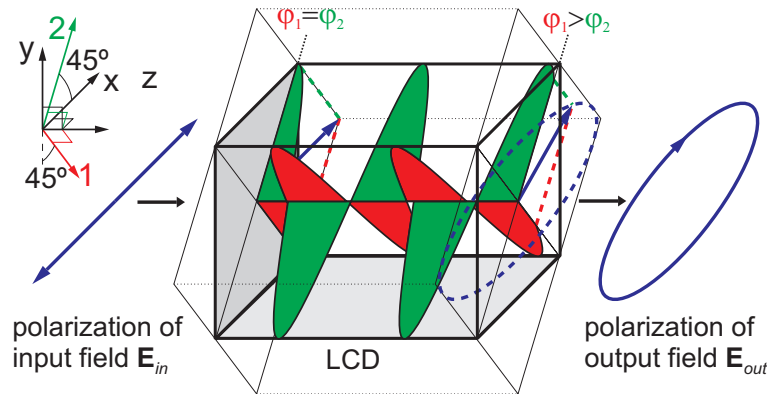


Figure 1.5.: Schematic illustration of polarization pulse shaping by a two-layer LCD. The extra-ordinary axes of the LCD layers (1 and 2) are oriented rotated by 45° with respect to the horizontally (x) polarized input electric field \mathbf{E}_{in} . The projections of the polarization components along the axes are depicted in green for layer 1 and in red for layer 2. Horizontal polarization is associated with identical phases $\varphi_1 = \varphi_2$. Adjustable birefringence along the layer axes causes phase shifts $\Delta\phi_1$ and $\Delta\phi_2$ which are added to the original phases of the respective field components. Accordingly, if $\Delta\phi_1 > \Delta\phi_2$ as it is indicated, the polarization phases are out of phase ($\varphi_1 > \varphi_2$) after the LCD. The output polarization in general is elliptically polarized. Details are given by Eq. (1.36). Modified from Brixner [110].

For sake of simplicity the detailed structure of the LCD is not shown. Different optical path length for both polarizations cause a phase difference after the LCD which leads, according to the considerations in Chapter 1.1, to a change of the polarization state.

The output electric field $\mathbf{E}_{out}(\omega)$ leaving the pulse shaper in z -direction can be described conveniently with the Jones-matrix formalism presented in Appendix A.2 [127]. Due to the fixed orientation of polarizer P1, the input electric field $\mathbf{E}_{in}(\omega)$ is completely horizontal polarized. The Jones-matrix of the polarization pulse shaper display $J^{(LCD)}(\omega)$ is determined by rotating the coordinate system from the laboratory frame (x, y) to the orientation of the LCD axes (1, 2) by multiplication with the rotation matrix $R(45^\circ)$ (see Eq. (A.23)). Then, the first layer of the LCD acts on the polarization component along direction 1 by introducing an additional phase $\Delta\phi_1(\omega)$ and, accordingly, the second layer by introducing an additional phase $\Delta\phi_2(\omega)$ for the second polarization component. Ideally, no cross-diagonal terms occur in the Jones-matrix. Afterwards, the coordinate system is rotated back into the laboratory frame using the inverse rotation matrix $R(-45^\circ)$ (see Eq. (A.23)) and the Jones matrix denotes the transfer of the incoming electric field $\mathbf{E}_{in}(\omega)$ through the pulse shaper. Multiplication of the Jones matrix with the input field $\mathbf{E}_{in}(\omega)$ yields the output electric field $\mathbf{E}_{out}(\omega)$ via:

$$\begin{aligned} \mathbf{E}_{out}(\omega) &= J^{(LCD)}(\omega)\mathbf{E}_{in}(\omega) \\ &= R(-45^\circ) \begin{pmatrix} e^{-i\Delta\phi_1(\omega)} & 0 \\ 0 & e^{-i\Delta\phi_2(\omega)} \end{pmatrix} R(45^\circ)\mathbf{E}_{in}(\omega) \end{aligned} \quad (1.34)$$

Using the definition of the rotation matrices in Eq. (A.23) and substituting $\mathbf{E}_{in}(\omega) = E_{x,in}(\omega)\mathbf{e}_x$ this equation is reshaped towards,

$$\mathbf{E}_{out} = e^{\frac{\Delta\phi_1 + \Delta\phi_2}{2i}} \begin{pmatrix} \cos\left(\frac{\Delta\phi_1 - \Delta\phi_2}{2}\right) & -i \sin\left(\frac{\Delta\phi_1 - \Delta\phi_2}{2}\right) \\ -i \sin\left(\frac{\Delta\phi_1 - \Delta\phi_2}{2}\right) & \cos\left(\frac{\Delta\phi_1 - \Delta\phi_2}{2}\right) \end{pmatrix} \begin{pmatrix} E_{x,in} \\ 0 \end{pmatrix} \quad (1.35)$$

$$= E_{x,in} e^{\frac{\Delta\phi_1 + \Delta\phi_2}{2i}} \begin{pmatrix} \cos\left(\frac{\Delta\phi_1 - \Delta\phi_2}{2}\right) \\ -i \sin\left(\frac{\Delta\phi_1 - \Delta\phi_2}{2}\right) \end{pmatrix}, \quad (1.36)$$

where the frequency-dependence of the quantities was omitted for the sake of a compact notation. Nevertheless, the outgoing electric field has to be calculated for each frequency component individually. Consequently, the outgoing electric field is determined by the sum $\Delta\phi_1(\omega) + \Delta\phi_2(\omega)$ and the difference $\Delta\phi_1(\omega) - \Delta\phi_2(\omega)$ of the phases applied by the LCD. An identical increase of $\Delta\phi_1(\omega)$ and $\Delta\phi_2(\omega)$ changes the spectral phase but does not affect the polarization state of $\mathbf{E}_{out}(\omega)$. In contrast, opposite LCD phases $\Delta\phi_1(\omega) = -\Delta\phi_2(\omega)$ do not introduce an additional spectral phase, but lead to a variation of the polarization state. With a two-layer LCD display effectively only two of the four parameters necessary for full control over the electric field are accessible. Hence, it is not possible to adjust the intensity transmitted by the LCD. Additionally, because of the trigonometric relation between the horizontal and vertical field amplitudes not all polarization states can be accessed. Nevertheless, the generation of horizontal and vertical field orientations as well as circular polarizations for both senses of rotation is possible within experimental limitations given by the Jones matrix of the complete setup (see Appendix A.3).

By inserting polarizer P2 after the LCD the operation mode of the pulse shaper changes from polarization shaping to amplitude and phase shaping. Now, the outgoing electric field is projected onto the polarization component defined by P2. If P2 transmits horizontal polarization, Eq. (1.36) simplifies to

$$E_{x,out}(\omega) = E_{x,in}(\omega) e^{\frac{\Delta\phi_1(\omega) + \Delta\phi_2(\omega)}{2i}} \cos\left(\frac{\Delta\phi_1(\omega) - \Delta\phi_2(\omega)}{2}\right). \quad (1.37)$$

Therefore, the shaped electric field amplitude depends on the difference of the phase retardations in the two LCD layers, whereas the spectral phase is given by their sum. For a known input pulse spectrum $E_{x,in}(\omega)$ the spectral phase of the output pulse is given by $\varphi_{x,out}(\omega) = \varphi_{x,in}(\omega) + [\Delta\phi_1(\omega) + \Delta\phi_2(\omega)]/2$. The spectral amplitude can only be attenuated by the pulse shaper. Thus, the generation of particular shapes of the amplitude spectrum which differ strongly from the input spectrum is connected to a distinct loss of total laser power.

Recently, concepts for full vector field synthesizer have been developed and tested [14, 120]. These pulse shapers are able to control a complete set of parameters and thereby determining the electric field vector at each spectral and temporal position. Ninck *et al.* have demonstrated that a phase stable superposition of amplitude and phase shaped laser pulses with perpendicular polarizations is feasible within a single pulse shaper with 4f-compressor design [14]. In the vector-field synthesizer the beams of two orthogonal polarization components are separated by a polarization beam splitter and hit the dispersive grating with different angle of incidence. Consequently, the beams are located at different parts of the LCD and are shaped individually. Both beams are recombined at the polarization beam splitter, where effectively two perpendicularly polarized laser pulses shaped in amplitude and phase generate the desired pulse. Another design was demonstrated by [120] employing a stack of four LCD arrays in the Fourier plane of the 4f-compressor.

1.2.3. Adaptive Techniques for Pulse Shaping

The shape of femtosecond laser pulses has been demonstrated to affect the efficiency and selectivity of photoassisted molecular reactions [56, 114, 128] and nonlinear processes e.g. high harmonic generation in a gas target [129]. The pulse shape also has a strong impact on the localized excitation of nanostructures [83–85, 88, 130]. With a pulse shaper a high number of degrees of freedom can be accessed. In the specific case discussed in Section 1.2.1 256 spectral parameters are modulated with the SLM. The identification of the optimal pulse shape in this multi-dimensional parameter space requires search strategies that find the optimal set of parameters for the specific task. Open-loop optimization strategies are used, if the response function of the investigated system is known or if the optimal pulse shape is accessible via suitable theoretical considerations or experiments [87, 131–133]. If the response of the system is unknown, the parameter space has to be searched in a closed-loop investigation, i.e. by evaluation of the signals generated after excitation with pulse shapes representing points in the parameter space and deduction of the optimal pulse shape from these results. The number of possible pulse shaper settings, i.e. the total number of points in the parameter space of the polarization pulse shaper described in Section 1.2.1, is huge. By considering the full dynamic range of the voltage steps of each pixel it is estimated to be $(2^{12})^{256} = 10^{925}$ [111]. Even with a sparse distribution of sampling points per SLM pixel the total number of combinations remains enormous. Thus, search strategies based on adaptive learning algorithms have to be applied that go beyond a multi-dimensional scan of all parameters. In the closed-loop optimization experiments presented in this thesis an evolutionary algorithm is employed finding the optimal parameters in an adaptive routine analog to the biological evolution process [134–137].

The selection of replicative units, i.e. genes, by their capability to replicate while interacting with a complex environment is the driving force in the biological evolution [137]. In a population of individuals whose ability to survive and reproduce is determined by their genetic information, those individuals with the highest fitness transfer their genes to the next generation more efficiently. As a consequence, the genes of the fittest individuals will gain a higher share of the gene pool of the population and finally will eliminate all other gene combinations, if the environmental conditions remain fixed.

The evolutionary algorithm mimics the natural evolution process by treating each pulse shape as an individual. The set of parameters determining the spectral phase corresponds to the genetic information. Here, several different representations are possible, e.g. the chirp-basis which determines the applied spectral phase by the coefficients of its Taylor expansion, the van-Neumann-basis [138, 139] or the pixel basis which simply states the spectral phase for each wavelength bin. An appropriate choice of the employed representation can already contribute to a further reduction of degrees of freedom. A schematic example for the algorithm is presented in Figure 1.6. In the selection process the fitness of the individuals is evaluated according to a feedback signal obtained from an experiment or simulation. The fittest individuals of this generation are selected. All other individuals are rejected and their genes are not used in the reproduction process, which generates the individual for the next generation of the algorithm. The reproduction is partly achieved by cloning, mutation and crossover. Cloning simply transfers the selected individual into the pool of the next generation without further changes. Mutation randomly varies parts of the genetic information of one of the selected individuals. Crossover involves the combination of the genes of two individuals by replacing a linear array of genes at a

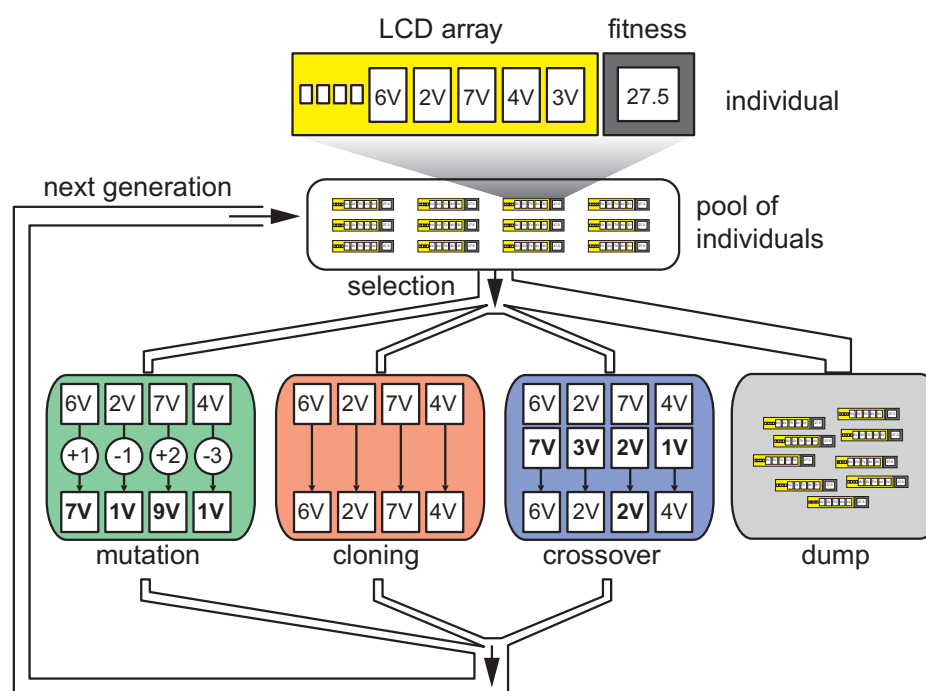


Figure 1.6.: Graphical representation of evolutionary algorithm used for adaptive optimizations of laser pulse parameters. An iteration of the algorithm starts with ordering the individuals according to their fitness values. The genes of the individuals contain the information of the pulse shape. They are coefficients of a selectable basis that determines the spectral phase settings that are applied by a set of voltages for the LCD. Whereas the biggest part of the population is rejected in the selection process, the fittest individuals are reproduced without change of genetic information (cloning), with random changes of genetic information (mutation) and by mixing genes of different individuals (crossover). The reproduction process creates the population for the next iteration of the algorithm comprising the same number of individuals as prior to the selection. Taken from Brixner [109].

random position in the first individual by the corresponding gene values of the second individual. After the reproduction, the new generation of individuals is tested by the experiment or simulation and a new cycle of evaluation, selection and reproduction follows. The evolutionary algorithm is stopped when convergence is reached. Then, the gene pool is dominated by a particular gene combination and the algorithm cannot find a comparably adapted individual via mutation. Instable experimental conditions or an insufficient definition of a fitness function might prevent the convergence. In the first case, the determined fitness values are affected by uncertainties or systematic deviations introduced of the data acquisition leading to disturbances of the selection and reproduction processes. In the latter case, the fitness function might not lead to the intended optimization goal, because trivial or unwanted solutions are favored. Then, a fitness function has to be chosen which more precisely enables the identification of optimal individuals. Experimental implementation of adaptive optimizations will be presented in Chapters 2 and 5.2. There, the localization of near-field at gold nanoprisms and on a corrugated silver film are demonstrated, respectively.

1.3. Optical Near-Fields and Optical Nanoantennas

In this section an overview over the most important properties of optical near-fields and nanoscopic systems are presented. Optical near-fields can be confined within one, two or even all three spatial dimensions to sizes smaller than the optical diffraction limit (Section 1.3.1). Hence, the application of near-fields provides means of improving the resolution of optical investigation techniques and applications down to a small fraction of the wavelength. Prominent examples of nano-optical excitations are propagating surface plasmon polaritons and localized plasmonic resonances (Sections 1.3.2 and 1.3.3). Coupling of plasmonic modes creates nanoscopic devices with intriguing functionalities (Section 1.3.4). Nanoscopic objects interact with the radiation from the far-field as well as with optical near-fields. They are utilized as antennas for manipulating and controlling near-fields by adjusting the geometry of the nanoantennas to the particular task (Section 1.3.4). An alternative approach is the coherent control of nanoscopic systems by means of polarization pulse shaping. This technique achieves the selective localization of near-fields in the vicinity of nanostructures by manipulating the far-field properties of the laser pulses. In Section 1.3.5 mechanisms for the spatial and temporal control of near-fields via polarization pulse shaping are discussed.

1.3.1. Localization of Light below the Diffraction Limit

The resolution of conventional optical microscopes is limited by diffraction [38, 140]. The diffraction limit is defined as the minimal spatial confinement of light that is achieved by superimposing plane waves. In analogy to the time-bandwidth-product the product of the spatial localization Δx and wavevector spread Δk_x can be written as

$$\Delta x \Delta k_x \geq c_k , \quad (1.38)$$

because the position-space is connected to the wavevector-space via Fourier transformation [16]. Here, the constant c_k arises from the focusing conditions. Consequently, a strong confinement of the spatial position is only achieved if the wavevector distribution is broad. The dispersion relation

$$\hbar\omega = \hbar c |\mathbf{k}| \quad (1.39)$$

determines the length of the wavevector of light for a given frequency ω , where \hbar denotes Planck's constant divided by 2π . The absolute value of \mathbf{k} is also connected to the x , y and z components via

$$|\mathbf{k}| = \frac{2\pi}{\lambda} = \sqrt{k_x^2 + k_y^2 + k_z^2} . \quad (1.40)$$

Possible wavevectors are located on the surface of a sphere centered at the zero position in the wavevector space. The focus of plane waves propagating in positive z direction contains at most one half of the sphere. Hence, the maximal spread in the k_x component in free space is given by length of the wavevector [16], so that Eq. (1.38) is rewritten as

$$\Delta x \geq \frac{\lambda}{2\pi c_k} . \quad (1.41)$$

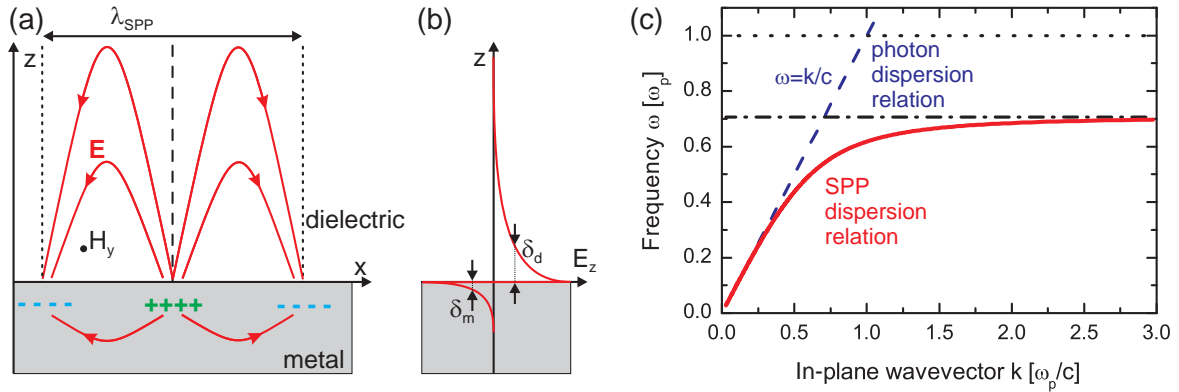


Figure 1.7.: Basic properties of surface plasmon polaritons (SPP). (a) Schematic representation of the electric charges (+ and -) and electric fields (red lines) associated with a surface plasmon polariton mode. The gray shaded space represents metal and the white space above is filled with a dielectric medium. The wavelength of the SPP is indicated by λ_{SPP} . (b) Distribution of the z component of the electric field (E_z) with distance from the surface z . The penetration depths into the metal δ_m is lower than in case of the dielectric δ_d . (c) Dispersion relation of SPP mode according to Eqs. (1.43) and (1.44) for a dissipation constant $\Gamma = 3 \cdot 10^{-5} \omega_p$ of the metal and air as dielectric medium. The dispersion relation of light propagating parallel to the surface is shown as dashed blue line and the plasma frequency ω_p and the surface plasma frequency $\omega_p/\sqrt{2}$ are highlighted by dotted horizontal lines.

This expression is similar to Abbe's diffraction limit and specifies the maximal resolution in a free space focus. To achieve a higher spread Δk_x , the maximal value of k_x has to be increased above $|\mathbf{k}|$. This is only possible according to Eq. (1.40) if at least one of the components k_y or k_z is purely imaginary. For simplification k_y is considered to be zero leading to an imaginary k_z . The z component of the electric field

$$E_z(z, \omega) = E_z(0, \omega) e^{ik_z z} = E_z(0, \omega) e^{-|k_z|z} \quad (1.42)$$

becomes an evanescent wave following a decaying exponential function in the positive z direction. However, in negative z direction the electric field increases exponentially without any limit, violating normalization conditions. Thus, in free space evanescent waves are forbidden. However, at a surface with suitable change of the refractive index the infinite increase of the electric field can be avoided. Thus, a confinement beyond Eq. (1.41) is possible for evanescent waves.

1.3.2. Propagating Surface Plasmon Polaritons

Surface plasmon polaritons (SPPs) are propagating electromagnetic modes at the interface of a metal [141–143] or graphene [144–146] to a dielectric medium. The most important properties of surface plasmon polaritons are presented schematically in Figure 1.7. The two half spaces, one containing a dielectric medium and the other containing a metal, in Fig. 1.7a and b are separated by a horizontal interface. The SPP is the combination of collective oscillations of the free electron gas in the metal and an electric field bound to the interface by the interaction with the charges. Thus, on a planar surface SPPs cannot escape but propagate until their energy is absorbed by the conductive matter. The main electric field component is perpendicular to the surface. The magnetic field has a component which is oriented parallel to the surface (in y direction) and perpendicular to the propagation direction (x) of the plasmon. These conditions are derived from

Maxwell's equation [17]. The z component of the electric field decays exponentially into both materials, but the penetration depths into the metal δ_m is lower than in case of the dielectric δ_d and the sign of E_z changes at the interface. This evanescent electric field is called *near-field* of the surface plasmon polariton.

The propagation of a surface plasmon polariton is determined by the wavevector which is given by [17, 143]:

$$k_{SPP}(\omega) = \frac{\omega}{c} \sqrt{\frac{\varepsilon_m(\omega)\varepsilon_d(\omega)}{\varepsilon_m(\omega) + \varepsilon_d(\omega)}}, \quad (1.43)$$

where the dielectric functions of the metal and the dielectric medium are denoted as $\varepsilon_m(\omega)$ and $\varepsilon_d(\omega)$, respectively, and k_{SPP} is the wavevector component in propagation direction. Analog to optical waves, the real part of the k_{SPP} determines the wavelength, whereas the imaginary part describes the losses during the propagation along the interface which limit the typical propagation length to several tens of micrometer [143].

Specifically, k_{SPP} depends on the dielectric functions of the materials at the interface. In case of the metal $\varepsilon_m(\omega)$ is commonly approximated by a Drude model, describing an ideal electron gas [17, 147]:

$$\varepsilon_m(\omega) = 1 - \frac{\omega_p^2}{\omega^2 + i\Gamma\omega}. \quad (1.44)$$

The plasma frequency ω_p and the collision rate Γ then fully define the optical response of the metal. For such an idealized metal the dispersion relation, i.e. the dependence of the frequency on the wavevector, is presented in 1.7c for SPPs at the metal air interface. The dispersion relation for photons propagating along the surface in vacuum, is depicted by a dashed blue line along $\omega = ck$. The SPP dispersion relation approaches the photon dispersion relation for small wavevectors, but it does not cross it. If the light beam has an angle with respect to the surface, the in-plane wavevector component of the photons is reduced and the resulting dispersion relation for the given angle lies between the photon dispersion relation and the vertical axis. Therefore, for a given frequency the momentum of the SPP is always larger than that of a photon. Consequently, a direct excitation of SPPs by far-field illumination is forbidden at a flat metal-dielectric interface because of this momentum mismatch. For the same reason the decay of surface plasmon polaritons via emission of a photon is likewise impossible without a further break of symmetry. The horizontal dotted lines indicate the plasma frequency ω_p and the surface plasma frequency $\omega_p/\sqrt{2}$, which the SPP dispersion relation approaches asymptotically for high wavevectors. In case of gold and silver the plasma frequency is approximately $\omega_p \approx 13.7$ rad/fs ($\hbar\omega_p \approx 9.0$ eV) [147]. Thus, in the energy regime of near-infrared photons (1.55 eV $\approx 0.17\omega_p$) the dispersion relation of the SPP is still close to the photon dispersion relation.

Concepts for introducing an interaction between photons and SPPs are based on gratings written on the interface acting as coupling device [148–150] and evanescent waves which are generated by total internal reflection at the interface of dielectrics, e.g. glass prisms [151, 152]. The diffraction at a grating leads to the transfer of momentum compensating the differences in the dispersion relations. As it is discussed in Section 1.3.1, evanescent waves achieve enhanced lateral wavevector components compared to free photons of the same frequency because of the exponential decay of the near-field perpendicular to the interface. Thus, the momentum mismatch is avoided and the evanescent waves couple to SPPs. Still, even simpler structures like edges and

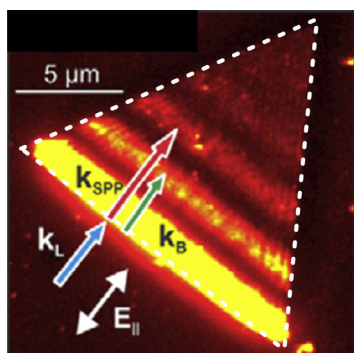


Figure 1.8: Propagation of SPPs imaged by PEEM. Multiphoton PEEM image of triangular Ag nanoisland (white dotted lines) upon excitation with near-infrared laser pulse in grazing incidence geometry. At the nanotriangle edge facing the incident light SPPs are generated by the electric field perpendicular to the edge orientation. The beating between propagating surface plasmon polariton field and the excitation laser pulse is visible in the photoemission distribution. Arrows indicate wavevectors of plasmons (red), laser (blue) and of beat signal (green). Adapted from [155].

grooves in the metal surface are employed to launch SPPs when illuminated with light [153–155]. Additionally, SNOM provides the possibility to couple confined optical far-field modes to the near-field [16, 74, 75, 156, 157].

Surface plasmon polaritons can be studied with photoemission electron microscopy (PEEM), which is further described in Section 1.4 [154, 155, 158, 159]. An example is presented in Figure 1.8, which was taken from [155]. At the edges of the silver island SPP waves are launched. The coupling efficiency depends on the orientation of the polarization vector to the edges of the nanostructure [159]. The observed photoemission patterns are given by the beating of the SPP wave with the excitation laser pulse generating a moiré pattern. Thus, the periodicity of the signal does reflect the true SPP wavelength only indirectly, if the incidence angle of the excitation pulse is not normal to the sample surface. The employment of a normal incidence PEEM geometry allows for a moiré-free detection (see Section 1.4.2) [159]. The propagation directions of the SPPs launched at the nanostructure edges are determined by Snellius' law [155]. It has been further demonstrated that the propagation of surface plasmon polaritons can be guided and manipulated via nanoplasmonic devices for example by V-shaped grooves cut into a metal surface [160] and two-dimensional Fresnel zone plates [154]. Recently, a confocal microscopy combined with spectral interferometry has been developed that determines the dispersion and group velocity of propagating plasmons in nanowaveguides [161, 162].

1.3.3. Localized Surface Plasmon Resonances

Localized surface plasmon resonances (LSP) are collective oscillations of charge carriers which do not propagate along the metal dielectric interface but remain stationary because they are bound to nanoparticles or nanovoids with dimensions considerably smaller than the wavelength. Localized plasmon resonances have a wide range of applications [163]. The employment of colloidal gold particle for coloring glasses is a technique which has been developed already in the antique. The Lycurgus Cup dating from 5th to 4th century B.C. as a famous example transmits red wavelengths and appears green in reflection, due to the presence of strongly scattering gold nanoparticles. Colloidal metal particles have been studied in the last centuries because of their strong scattering and absorption properties [163–165]. At the beginning of last century Mie found solutions of Maxwell's equation which are able to reproduce the extinction spectra of colloidal metal particles and proposed a complete electro-dynamical theory to explain the size-dependent scattering color of colloidal particles by expansion of the contributing fields in the respective vector harmonics [166]. In the last decades it has been demonstrated that the enhancement of the local fields in

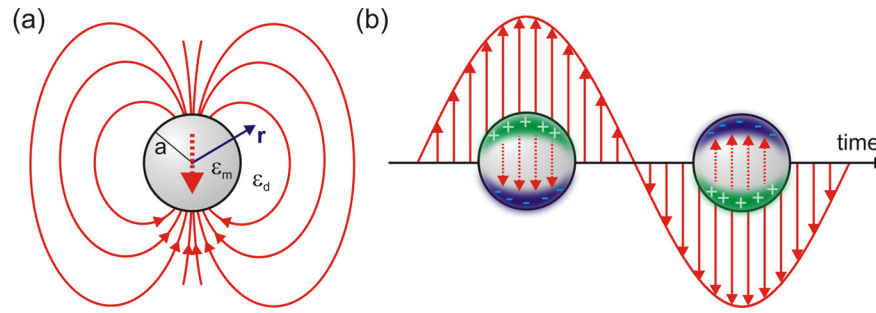


Figure 1.9.: Localized plasmonic resonance in a spherical nanoparticle. (a) Spherical metal nanoparticle with radius a and dielectric function $\varepsilon_m(\omega)$ in an isotropic dielectric medium with $\varepsilon_d(\omega)$. An induced dipole represented by the internal field within the particle (dotted arrow) induces the classical dipole field in the dielectric medium determining the local electric field for each spatial position \mathbf{r} . (b) Schematic representation of the response of the nanosphere to the external electric field (red solid line, and arrows). The polarization is connected to spatial separation of positive (green) and negative (blue) charges. The induced internal field (dotted arrows) reduces the total electric field within the metal sphere.

the vicinity of nanoparticles can be used for sensors [167, 168], in surface plasmon optical devices [18], for achieving optical nonlinearities [169] and for the improvement of photovoltaic devices [25, 170]. An other important application is surface enhanced Raman scattering (SERS) [33], which benefits from the local plasmon resonance by an increase of the single molecular signal strength of several orders of magnitude [31, 32].

In an applied external field the electrons in a nanoparticle are displaced with respect to the atomic lattice. The strength of the electronic polarization, i.e. the separation of positive and negative electrical charges within the particle, depends on the external field amplitude, the materials and the shape of the particle. Figure 1.9a illustrates schematically the electric fields created by an electric dipole within the sphere and outside of the sphere. Inside the sphere the electric field is homogeneously connecting the spatially displaced positive and negative charge distributions. Outside, the electric field corresponds to the field of a point dipole.

The polarization of the sphere follows the driving electric field. This is depicted in Figure 1.9b for the case of a fast electronic response compared to the incoming electric field oscillations, i.e. below the resonance frequency of the particle. The electric field created by the induced polarization reduces the driving electric field in the metal. Outside the particle the dipole field interferes constructively with the external field. If the frequency of the external field is increased and approaches the resonance frequency of the localized surface plasmon, the phase between induced polarization and external field changes and the maximal polarization occurs at the zero positions of the incident field oscillations.

To calculate the localized surface plasmon resonance for a nanoscopic object, its response to the external field has to be calculated. In the quasi-static limit the incident electric field is considered to have a constant intensity and a constant phase over the complete particle. This assumption enables the approximative calculation of the nanoparticles response to the quasi-static field. The polarizability $\alpha(\omega)$ determines the dipole moment $\mathbf{p}(\omega)$ induced by the applied electric field $\mathbf{E}(\omega)$ via

$$\mathbf{p}(\omega) = \varepsilon_0 \varepsilon_d(\omega) \alpha(\omega) \mathbf{E}(\omega) . \quad (1.45)$$

In general $\mathbf{a}(\omega)$ is a tensor reflecting the particle geometry and composition. For a small metal nanosphere with radius $a \ll \lambda$ the polarizability $\mathbf{a}(\omega)$ is written in the quasi-static case as a product of a scalar function $\alpha(\omega)$ with the identity matrix $\mathbb{1}$. Thus, the polarizability $\mathbf{a}(\omega) = \alpha(\omega)\mathbb{1}$ becomes direction independent and the scalar polarizability function for the sphere yields [17]:

$$\alpha(\omega) = 4\pi a^3 \frac{\varepsilon_m(\omega) - \varepsilon_d(\omega)}{\varepsilon_m(\omega) + 2\varepsilon_d(\omega)}, \quad (1.46)$$

where $\varepsilon_m(\omega)$ and $\varepsilon_d(\omega)$ are the dielectric function of the metal and the surrounding dielectric medium, respectively. The plasmon resonance occurs when the polarizability becomes maximal. In Eq. (1.46) the maximum is reached for

$$\text{Re}(\varepsilon_m(\omega)) = -2\varepsilon_d(\omega), \quad (1.47)$$

if the imaginary part of $\varepsilon_m(\omega)$ is changing weakly around the resonance position. The amplitude and width of the resonance are mainly determined by the imaginary part of $\varepsilon_m(\omega)$ as the dielectric function $\varepsilon_d(\omega)$ is real. Hence, the resonance frequency is strongly affected by the particle properties as well as the surrounding material.

Outside of the nanoparticle the local electric field $\mathbf{E}_{loc}(\mathbf{r}, \omega)$ combines the contribution of the applied electric field $\mathbf{E}(\mathbf{r}, \omega)$ and the dipolar field generated by the particle. For a particle in the origin of the coordinate system and $\mathbf{r} = r \cdot \mathbf{e}_r$ the local field is given by [17]:

$$\mathbf{E}_{loc}(\mathbf{r}, \omega) = \mathbf{E}(\mathbf{r}, \omega) + \frac{3\mathbf{e}_r(\mathbf{e}_r \cdot \mathbf{p}(\omega)) - \mathbf{p}(\omega)}{4\pi\varepsilon_0\varepsilon_d(\omega)} \frac{1}{r^3}. \quad (1.48)$$

Implicitly \mathbf{e}_r depends on the spatial position \mathbf{r} , as it always points away from the origin. Equation (1.48) only contains the near-field of the dipole. The electric field of an oscillating dipole is additionally described by an intermediate and far-field radiation zone decaying with $1/r^2$ and $1/r$, respectively. [17, 96]. However, in the vicinity of the particle the $1/r^3$ -term dominates. Substitution of the polarization vector by an isotropic polarizability $\mathbf{a}(\omega) = \alpha(\omega)\mathbb{1}$ into Eq. (1.48) and factorization yields

$$\mathbf{E}_{loc}(\mathbf{r}, \omega) = \overbrace{\left[\mathbb{1} + \frac{3\mathbf{e}_r(\mathbf{e}_r \cdot \mathbf{a}(\omega)) - \mathbf{a}(\omega)}{4\pi r^3} \right]}^{\mathcal{A}(\mathbf{r}, \omega)} \mathbf{E}(\mathbf{r}, \omega) \quad (1.49)$$

$$= \left[\mathbb{1} + \alpha(\omega) \frac{3\mathbf{e}_r(\mathbf{e}_r \cdot \mathbb{1}) - \mathbb{1}}{4\pi r^3} \right] \mathbf{E}(\mathbf{r}, \omega). \quad (1.50)$$

The local electric field, therefore, is the product of the incident electric field and the term denoted as $\mathcal{A}(\mathbf{r}, \omega)$. This quantity is the local response function, which is in a most general approach also a tensor, since it is based on the polarizability of the microscopic environment of each spatial position \mathbf{r} . The local optical response function of a nanosystem is determined by the geometry of the nanostructure and the focusing conditions. It is independent of the particular pulse shape

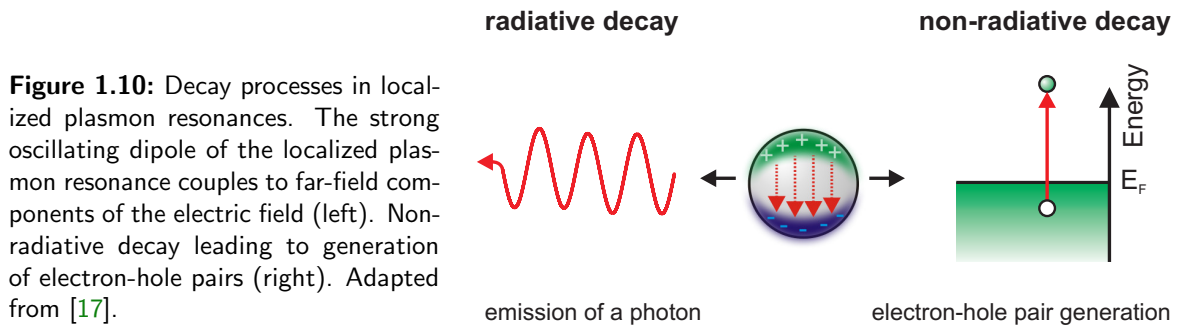


Figure 1.10: Decay processes in localized plasmon resonances. The strong oscillating dipole of the localized plasmon resonance couples to far-field components of the electric field (left). Non-radiative decay leading to generation of electron-hole pairs (right). Adapted from [17].

of the electric field as it includes the linear response of the system. Hence, for each polarization component $\mathbf{E}^{(i)}(\mathbf{r}, \omega)$ in the far-field

$$\mathbf{A}^{(i)}(\mathbf{r}, \omega) = \begin{pmatrix} A_x^{(i)}(\mathbf{r}, \omega) \\ A_y^{(i)}(\mathbf{r}, \omega) \\ A_z^{(i)}(\mathbf{r}, \omega) \end{pmatrix} \quad (1.51)$$

determines the amplitude and phase of the excited local field components in x , y , and z direction. The quasi-static approach, for which good agreement with measured scattering and absorption properties of nanoparticles is observed, is not accurate for particle dimensions on the order of the wavelength. In Eq. (1.46) the radius a of the nanosphere only affects the polarizability as a constant prefactor, but a size-dependence of the plasmon resonance frequency and spectral width has been shown experimentally [171, 172]. Evidently, the polarizability is a size-dependent quantity and the resonance frequency decreases with the particle size.

The spectral bandwidth of the localized plasmon resonance is determined by the strength of plasmon decay processes [17]. The creation of electron-hole pairs by absorption of the electric field of the plasmon reaching into the metal reduces the energy stored in the plasmonic mode and enhances the internal energy of the electronic system (see Fig. 1.10). In a Drude-type metal only intraband transitions are possible. In real metals e.g. gold and silver interband transitions are allowed for sufficiently high excitation frequencies [173, 174]. The relaxation of the excited electrons takes place in secondary processes [175]. If the excited electrons gain sufficient energy to leave the material in a photoemission process, they are accessible for detection mechanisms like photoelectron spectrometry and microscopy. Photoemission from nanoscaled systems is highly relevant for the experiments presented in this thesis and will be discussed in more detail in Section 1.4. Another important decay channel unaccounted for in the above equations is the radiative damping, i.e. the conversion of the collective electronic oscillations into photons. Since the polarizability of nanoparticles is high, the coupling of localized plasmons to the far-field is strong. Both decay channels contribute to the inelastic decay, i.e. the loss of plasmonic energy, characterized by the inelastic decay time T_1 via

$$\frac{1}{T_1} = \frac{1}{T_{nr}} + \frac{1}{T_{rad}}, \quad (1.52)$$

where T_{nr} and T_{rad} denotes the non-radiative and radiative decay time, respectively. Elastic processes lead to a dephasing of the collective electronic motion by elastic scattering events and are denoted by the pure dephasing time T_2^* . The elastic and inelastic decay process determine

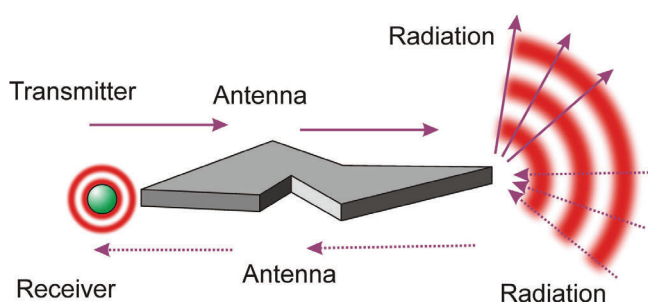


Figure 1.11: Optical nanoantennas for coupling near-field and far-field. Optical nanoantennas enhance the transmission of radiation from a localized emitter into the far-field (upper arrows) and from the far-field to a localized receiver (lower arrows). Figure adapted from [28].

the homogeneous linewidth Γ_{hom} of the localized plasmonic resonance, which is connected to the dephasing time T_2 , via

$$\frac{\Gamma_{hom}}{2} = \frac{1}{T_2} = \frac{1}{2T_1} + \frac{1}{T_2^*}. \quad (1.53)$$

Due to the strong coupling of the localized plasmon resonance to the far-field as well as the high absorption of electric fields at optical wavelengths in metals, the contributions of pure dephasing are relatively small and the dephasing time is directly connected to the inelastic decay via $T_2 = 2T_1$ [17]. In optical spectroscopy measurements the linewidth and dephasing times as well as the resonance energy of localized plasmon resonances in spherical gold nanoparticles has been determined [172]. The observed dephasing time T_2 for particles diameters of 100 nm and smaller does not exceed 10 fs. Gold particles with resonance frequency in the near infrared regime are 150 nm in size or bigger and feature even shorter plasmon lifetimes.

1.3.4. Nanoantennas and Coupling of Plasmonic Modes

Nanoscale objects interact with the radiation from the far-field as well as with optical near-fields of nanoscale objects in their vicinity. They can be utilized as optical antennas as an analog to antennas in the radiowave regime [26, 28, 176–178]. In Figure 1.11 the antenna concept is schematically shown. An antenna acts as transducer between free-space radiation and localized energy, e.g. stored in a localized quantum systems. By reciprocity the receiving and transmitting functionalities are connected. Nanoantennas allow for the manipulation and control of near-fields by adjusting the geometry of the nanoantennas to the particular task, e.g. antennas for single molecule detection [27] and antennas for broadband field enhancements used for high harmonic generation [169].

The scaling of well known antenna designs from the radiowave regime into the optical regime has several difficulties. First, the fabrication process on the nanoscale is tedious and has become feasible following a top down approach just in the last decades by techniques as electron-beam lithography [179–181], electron-beam induced deposition [182, 183], nanoimprint lithography [184, 185] or focused ion-beam milling [26, 186–189]. Chemical synthesis of nanoparticles pursuing a bottom-up strategy provides particles with controllable size distributions and composition, but has the disadvantage that the particles are dispersed in a solvent while being stabilized by organic ligands [163]. To utilize such a colloidal particle as an antenna requires to isolate and attach the particle to a device or sample [190, 191]. Second, at optical frequencies the penetration of radiation into metals cannot be neglected. Due to the finite electron density the electronic

response is delayed with respect to the driving field. Consequently, the electron gas responds to an effective wavelength λ_{eff} which is typically a factor of 2-6 shorter than the incident free space wavelength λ [28, 178]. Thus, a $\lambda/2$ dipole antenna, e.g. a rod of gold with 5 nm radius, has a length of $\lambda_{\text{eff}}/2 \approx \lambda/10$ [178].

The efficiency of an optical antenna as a transducer between a local quantum system and the far-field depends on the coupling to the quantum system. Coupling of localized modes can also occur between excitations in nanoparticles. Nanosized Yagi-Uda antennas tailoring the direction of emission into the far-field [192] and nanoparticle chain waveguides supporting propagating plasmon modes [87, 193, 194] are examples for achieving new functionalities by coupling of localized plasmonic resonances. The strength and the type of coupling are strongly determined by the geometric properties. The coupling between the plasmonic modes depends strongly on the spatial and spectral mode overlap. For small interparticle distances, i.e. much smaller than the wavelength, the coupling is dominated by interactions of the near-field of one particle with the charge density distribution in the other particles [17].

Coupling of localized plasmonic resonances leads to hybridization of modes, i.e. the single particle excitation cannot be treated independently, but the collective response of all contributing particles has to be considered. This leads to the generation of new plasmonic modes with shifted resonance frequencies [195, 196]. Hybridization of plasmonic modes generates Fano-type resonances, if a strongly damped mode is coupled to a mode with reduced decay rate e.g. a quadrupolar mode that does not radiate into the electric far-field [197–199].

1.3.5. Spatial and Temporal Control Mechanisms

Optical nanoantennas have to be designed, fabricated and positioned within limited margins of tolerance to efficiently enhance the coupling between localized emitters or receivers and the electric far-field. A more flexible approach to utilize nanoantennas and nanostructured samples is the coherent control [54–56, 83, 84] of nanoscopic systems by means of polarization pulse shaping [85, 86, 88, 200]. This technique achieves the selective localization of near-fields in the vicinity of nanostructures by manipulating the far-field properties of the laser pulses such as the polarization state and the spectral phase.

In a nanoscopic sample with structure sizes well below the diffraction limit also the optical response function is modulated on the corresponding length scale. Accordingly, by controlling the interference of near-field modes the spatial distribution the electric fields is tailored on sub-wavelength length scale. The control mechanism is based on adjusting the polarization state of each frequency component, utilizing that the local response of the near-field is sensitive to the incident polarization. The confinement of the near-field to the nanostructure and the field enhancement enable to localize strong electric fields at selectable positions on the nanostructured surface [86]. The broadband spectral response of nanoparticles, furthermore, enables the creation of ultrafast excitations of the optical near-field. The interference of the spectral components is determined by the spectral phase of the local response function. Controlling the phase of the optical far-field pulses, therefore, allows for manipulating the spatial and temporal properties of the nanooptical excitations [86].

The local response function of the nanosystem to a given linear polarization component was introduced in Eq. (1.51). Generally, the far-field consists of two independent polarization

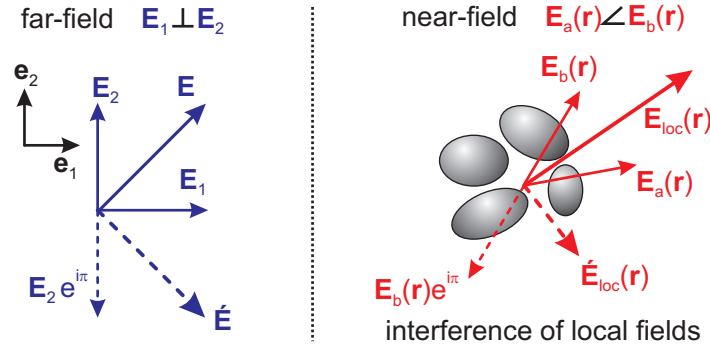


Figure 1.12.: Spatial control of near-fields by constructive and destructive interference of local field components. In the far-field (left, blue arrows) the electric fields \mathbf{E} and $\tilde{\mathbf{E}}$ are created by superposition of field component \mathbf{E}_1 and \mathbf{E}_2 . In case of $\tilde{\mathbf{E}}$ a shift by π in for the second field component is introduced, changing the direction of the resulting electric field vector, but not the intensity, as \mathbf{E}_1 and \mathbf{E}_2 are perpendicular. In the near-field (right, red arrows) of a nanostructure the angle between the local fields $\mathbf{E}_a(\mathbf{r})$ and $\mathbf{E}_b(\mathbf{r})$ depends on the local response function at position \mathbf{r} and in principle is arbitrary. The local intensity is phase-dependent creating a strong field $\mathbf{E}_{loc}(\mathbf{r})$ for the interference of $\mathbf{E}_a(\mathbf{r})$ and $\mathbf{E}_b(\mathbf{r})$ and only a weak field $\tilde{\mathbf{E}}_{loc}(\mathbf{r})$ for $\mathbf{E}_a(\mathbf{r})$ and $\mathbf{E}_b(\mathbf{r})e^{i\pi}$. Adapted from [86].

components denoted here as 1 and 2. The resulting local electric field is calculated via the coherent superposition of the local fields $\mathbf{E}_a(\mathbf{r}, \omega)$ and $\mathbf{E}_b(\mathbf{r}, \omega)$ which are generated by the respective polarization components $\mathbf{E}_1(\omega)$ and $\mathbf{E}_2(\omega)$ of the incident light [85]:

$$\mathbf{E}_{loc}(\mathbf{r}, \omega) = \mathcal{A}(\omega) \begin{pmatrix} \hat{E}_1(\omega) e^{-i\varphi_1(\omega)} \\ \hat{E}_2(\omega) e^{-i\varphi_2(\omega)} \end{pmatrix} \quad (1.54)$$

$$= \underbrace{\begin{pmatrix} A_x^{(1)}(\mathbf{r}, \omega) \\ A_y^{(1)}(\mathbf{r}, \omega) \\ A_z^{(1)}(\mathbf{r}, \omega) \end{pmatrix}}_{=\mathbf{E}_a(\mathbf{r}, \omega)} \hat{E}_1(\omega) e^{-i\varphi_1(\omega)} + \underbrace{\begin{pmatrix} A_x^{(2)}(\mathbf{r}, \omega) \\ A_y^{(2)}(\mathbf{r}, \omega) \\ A_z^{(2)}(\mathbf{r}, \omega) \end{pmatrix}}_{=\mathbf{E}_b(\mathbf{r}, \omega)} \hat{E}_2(\omega) e^{-i\varphi_2(\omega)}. \quad (1.55)$$

This equation is reshaped using the complex envelope notation for the components $\tilde{\mathbf{E}}_a(\mathbf{r}, \omega)$ and $\tilde{\mathbf{E}}_b(\mathbf{r}, \omega)$ yielding

$$\mathbf{E}_{loc}(\mathbf{r}, \omega) = \left[\tilde{\mathbf{E}}_a(\mathbf{r}, \omega) + \tilde{\mathbf{E}}_b(\mathbf{r}, \omega) e^{-i\Phi(\omega)} \right] e^{-i\varphi_1(\omega)}, \quad (1.56)$$

where $\Phi(\omega) = \varphi_1(\omega) - \varphi_2(\omega)$ determines the relative phase between the polarization components in the far-field. Thus, $\Phi(\omega)$ is the frequency space equivalent of the elliptical pulse parameter $\Phi(t)$ (see Eq. (1.25)) affecting the ellipticity $\varepsilon(\omega)$ and $\theta(\omega)$ of the far-field polarization ellipse for each frequency. The complex local field envelopes $\tilde{\mathbf{E}}_a(\mathbf{r}, \omega)$ and $\tilde{\mathbf{E}}_b(\mathbf{r}, \omega)$ implicitly include a local spectral phase modulation given by the complex local response function $\mathcal{A}(\omega)$. The interference term within the parenthesis determines the spectral intensity of the local electric field. Furthermore, it contains information on the local spectral phase for an excitation with a pulse without phase modulations in the first far-field polarization component, i.e. $\varphi_1(\omega) = 0$. Such phase modulations cannot change the spectral intensities for the individual frequencies, but varying $\varphi_1(\omega)$ affects the temporal structure of $\mathbf{E}_{loc}(\mathbf{r}, t)$.

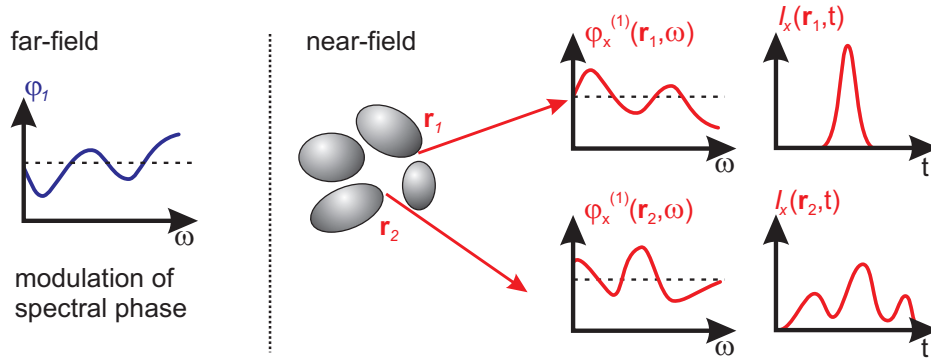


Figure 1.13.: Spectral phase control at a nanostructure. Tailoring the spectral phase $\varphi_1(\omega)$ in the electric far-field is used to compensate the phase of the local response function in the vicinity of a nanostructure. In this example the applied phase is the negative local spectral phase of the x component at position \mathbf{r}_1 , i.e. $\varphi_1(\omega) = -\varphi_x^{(1)}(\mathbf{r}_1, \omega)$. Consequently, the local field intensity $I_x(\mathbf{r}_1, t)$ in time domain is high at \mathbf{r}_1 , whereas at \mathbf{r}_2 a distorted pulse structure is observed in $I_x(\mathbf{r}_2, t)$ because of the non-matching spectral phase $\varphi_x^{(1)}(\mathbf{r}_2, \omega)$. Adapted from [86].

Based on Equation (1.56) a scheme for spatial control of the local electric field distribution at nanoparticles can be identified. Figure 1.12 presents schematically the basic idea. The far-field components are orthogonal. Hence, a change of the relative phase difference $\Phi(\omega)$ affects the polarization state, but it does not lead to modulation of the intensity by interference. The example in Figure 1.12 highlights that by changing the sign of the second polarization component, i.e. inverting the field direction via introducing a phase offset of π , the direction of the new electric field vector $\hat{\mathbf{E}}$ has changed direction, but is identical in amplitude as the initial electric field \mathbf{E} . The near-fields $\mathbf{E}_a(\mathbf{r})$ and $\mathbf{E}_b(\mathbf{r})$ presented by red arrows in Figure 1.12 are not orthogonal anymore, because local anisotropies of the polarizability influence the local response function. The generated local fields, therefore, point in arbitrary directions. Thus, the phase difference $\Phi(\omega)$ determines the interference of the local fields $\mathbf{E}_a(\mathbf{r}, \omega)$ and $\mathbf{E}_b(\mathbf{r}, \omega)$. A change of the sign of one far-field component switches from constructive to destructive interference. To control the spatial field distribution in the vicinity of the nanostructure, the spectral intensities $I_1(\omega)$ and $I_2(\omega)$ as well as the spectral phase difference $\Phi(\omega)$ have to be adjusted individually for each frequency component of the far-field.

The temporal structure of the local electric field can be described analogously to ultrashort laser pulses by a field amplitude and a temporal phase, which are associated to the spectral phase and amplitude by Fourier transformation. Hence, the shortest event in the near-field are achieved with an unmodulated spectral phase. In frequency domain, the local electric field is the product of incident spectral far-field and the local response function (see Eq. (1.54)). Thus, the spectral phase modulations of the laser pulse and the spectral phase of the local response add up. In Figure 1.13 an example only considering the component of the electric field in x direction is presented. If the chirp of the laser pulse precompensates the modulations of the local spectral phase at position \mathbf{r}_1 , local pulse compression occurs leading to a strong peak in the time-dependent local intensity. Consequently, if nonlinear processes are involved, the signal from this position is strong. Simultaneously, at a different position the same spectral phase $\varphi_1(\omega)$ of the incident field might lead to even stronger temporal distortions of the pulse. A nonlinear signal from position \mathbf{r}_2 would

be considerably lower. By application of an incident field with adapted spectral phase $\varphi_1(\omega)$ the local electric field pulses at \mathbf{r}_2 or any other position can be compressed.

Spectral phase control has been demonstrated in theoretical calculations by tailoring localized plasmonic excitations of a V-shaped nanostructure [83, 84]. Another example, which will be discussed in more detail in the introduction of Chapter 2, is the optimization of the local linear flux in plasmonic chain waveguides [87]. An idea connected to local pulse compression is localization of excitations by time-reversal, which has been successfully demonstrated in acoustics and for electromagnetic waves [133, 201, 202]. Theoretical calculations have shown the feasibility of the time-reversal approach also for nanoscaled systems [132].

1.4. Time-Resolved Photoemission Electron Microscopy

A photoemission electron microscope (PEEM) detects electrons which are emitted from the surface of the sample after excitation with light [203–205]. PEEM is not limited by the wavelength or the type of the optical excitation source. Since the wavelength of the detected electrons is merely a few nanometer for low energy electrons and even shorter for electrons with higher kinetic energies, the smaller amount of diffraction allows highly resolved photoemission imaging [206–208].

In the following a brief introduction into time-resolved photoemission spectroscopy is given (Section 1.4.1). Afterwards, the photoemission electron microscope is discussed (Section 1.4.2). The most important properties of the PEEM setups employed for the experiments in this thesis are also presented there. The final section of this chapter treats multiphoton photoemission processes from nanoscaled systems.

1.4.1. Time-resolved Photoemission Spectroscopy

The PEEM detects electrons which are emitted from the surface of the sample after an excitation by light. In this photoemission process light quanta are absorbed by the matter and electrons are emitted into the vacuum. The photoemission as a fundamental quantum electronic effect has been intensively studied for over one hundred years. Photoemission was first observed by Hertz [209] and Hallwachs [210] investigating the discharging of metal plates by ultraviolet light. The first quantitative studies of the photoelectric effect were performed in equilibrated systems by measuring the electric potential of a metal plate caused by the irradiation with light [211, 212]. These experiments provided crucial information on the quantization of light. Einstein identified the energy quantization $E = h\nu = \hbar\omega$ used by Planck [213] as the energy of a photon with frequency ω [212]. Accordingly, the maximal kinetic energy of photoelectrons after the absorption of a photon is given by [212]:

$$E_{kin}^{max} = \hbar\omega - \Delta E . \quad (1.57)$$

The parameter ΔE leads to a reduction of the maximal kinetic electron energy. Electrons at the Fermi energy E_F perceive ΔE to be equal to the work function E_W , which is specific for the material and the surface properties of the investigated sample and describes the energetic difference of Fermi energy and vacuum energy E_{vac} [214]. If the photoemitted electrons originate from an electronic state with energy below E_F , the binding energy E_B further reduces the final kinetic energy. Fig. 1.14 presents different types of photoemission processes involving one or two photons. If the photon energy is smaller than the energy ΔE , photoemission cannot take

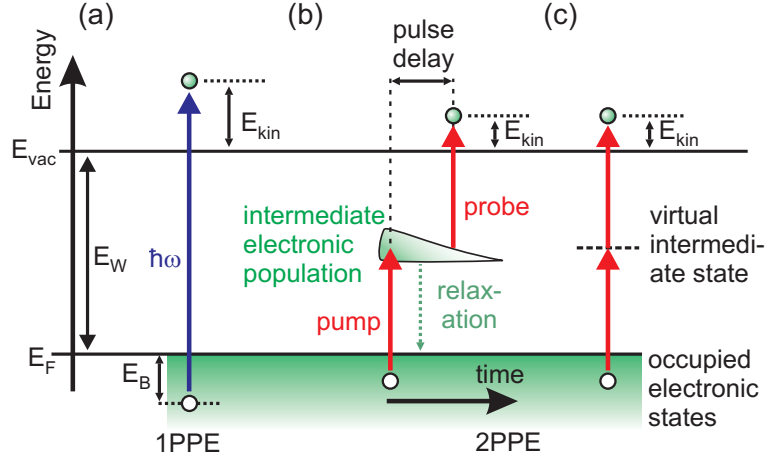


Figure 1.14.: Schematic illustration of one-photon photoemission (1PPE) (a) and two-photon photoemission (2PPE) via an intermediate electronic population (b) and a virtual state (c). (a) In the 1PPE process the final kinetic energy of the photoelectron is given by the photon energy $\hbar\omega$ reduced by the work function E_W and the binding energy of the electron E_B . (b) If the photon energy is not sufficient to overcome E_W and E_B , more than one photon needs to be absorbed to generate photoemission. In 2PPE electronic populations are excited in unoccupied electronic states above the Fermi energy E_F . From there the intermediate electronic population relaxes in energy and decays back into equilibrium state without further optical excitation. If a second photon is absorbed, an electron gains a total energy above the vacuum energy E_{vac} and leaves the sample. By separating the pump and probe excitation step using two pulses separated by a temporal pulse delay the relaxation dynamics of the sample are investigated by time-resolved photoemission spectroscopy. (c) Even in case of no available electronic states 2PPE occurs via virtual intermediate states.

place in a one-photon photoemission (1PPE) process, since the electron energy remains below the vacuum energy E_{vac} . Nevertheless, by successive absorption of several photons electrons are first excited into electronic states between E_F and E_{vac} and finally gain sufficient energy to leave the material. Considering N absorbed photons with individual frequency ω_n and Eq. (1.57) transforms to

$$E_{kin}^{max} = \left(\sum_{n=1}^N \hbar\omega_n \right) - E_W - E_B . \quad (1.58)$$

The electronic states substantially above the Fermi energy are unoccupied for thermal equilibrium conditions. They have a limited lifetime due to electron-electron inelastic scattering processes [175]. Other scattering processes such as electron-phonon and electron-imperfection interactions have minor importance [175, 215]. Thus, these excited states decay within a few femtoseconds in metals. If the electron in the excited state is excited by another photon before relaxation, it reaches higher energetic states in the solid. If the electron energy is above the vacuum energy E_{vac} , the electron can leave the sample. However, the emission probability is limited by inelastic scattering during the propagation towards the surface [216]. Hence, electrons close to the surface and with a momentum in the direction of the surface have a higher emission probability than electrons with identical energy which are located deeper inside the material or have a momentum vector pointing into the material. Consequently, the photoemitted electrons contain information which is mainly determined by the surface of the sample.

The two-photon photoemission (2PPE) process is possible, even if no real intermediate state exists [217]. Then the photons are absorbed simultaneously and the emission process is described as photoemission via a virtual intermediate state with a lifetime $\tau_{virt} = 0$. The photoemission yield $Y(I)$ is connected to the field intensity I via a power function

$$Y(I) \propto I^N, \quad (1.59)$$

where the exponent is determined by the number of absorbed photons N [217–220]. Thus, the photocurrent of the two-photon photoemission scales with the fourth power of the amplitude of the electric field envelope and the square of the intensity, respectively. If the work function E_W of the material is bigger than twice the photon energy, photoemission is still possible via multi-photon photoemission (MPPE) involving three or more photons.

In time-resolved two-photon photoemission (TR-2PPE) experiments a pair of ultrashort laser pulses with a variable time-delay is employed [221, 222]. By scanning the relative delay between the pulses the temporal dynamics of the electronic system are measured. The first pulse (pump) generates a population of excited electrons which is probed by the second pulse (probe). The photoemission strength then depends on the lifetime of the electronic population and the pulse delay. Hence, with time-resolved two-photon photoemission (TR-2PPE) the lifetime τ of the excited electrons between Fermi energy and vacuum energy is investigated. In consistence with theoretical calculations the experimentally obtained electron lifetime in metals scales with the electron energy [175, 223–225]:

$$\tau(E) \sim \frac{1}{(E - E_F)^2}. \quad (1.60)$$

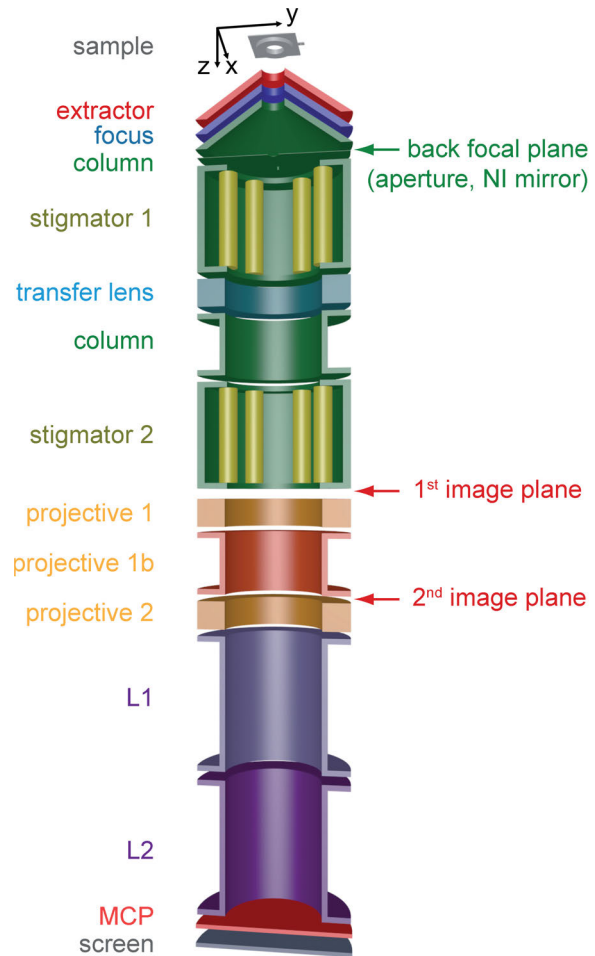
In the accessible energy range after absorption of a photon at 800 nm wavelength the electron lifetime $\tau(E)$ is a few tens of a femtosecond or even shorter.

Several time-resolved photoemission spectroscopy techniques have been developed in the last decades which are adapted in their specific excitation and detection schemes to their respective task. Interferometric time-resolved photoemission spectroscopy enables to investigate lifetimes of coherent processes [226, 227]. With two-color experiments employing a pump or probe pulse with high photon energy it feasible to monitor structural and electronic changes in matter by measuring electrons excited from states below the Fermi energy. Using pulsed extreme ultra violet (XUV) or soft X ray sources even core electron levels are reached [228, 229]. In the limit of amplified few-cycle laser the generation of isolated XUV pulses with attosecond duration in a gas target has been demonstrated [100, 101, 230]. These XUV pulses are employed in attosecond-streaking experiments to investigate the photoemission process in gases and solid matter on the timescale of the electronic motion around the atomic nucleus [42, 102, 103, 229].

1.4.2. PEEM – PhotoEmission Electron Microscopy

Over the last 80 years, several types of electron microscopes have emerged [76–80]. The transmission electron microscope (TEM) offers an extremely high spatial resolution [77, 231–233]. With scanning electron microscopy extended objects with complex shape and surface structure can be investigated [78, 234]. Photoemission electron microscopes detect electrons which are emitted from a surface upon illumination with light, i.e. photoelectrons [76, 79, 80]. First demonstrations of imaging cathode surfaces using photoemission were performed by Brüche [203] as well as Knoll

Figure 1.15: Schematic of photoemission electron microscope (PEEM) for the example of the *Focus NI-PEEM*. Voltages between sample (gray), extractor (red), focus (blue) and column (green) focus the extracted photoelectrons onto the back focal plane (green) and create an image on the first image plane (red). In the *Focus NI-PEEM* setup two particular components are included: a small rhodium mirror in the objective lens system positioned close to the electron beam enables normal incidence (NI) illumination and the transfer lens (light blue) allows for detecting the wavevector distribution of the photoelectrons providing a signal similar to ARPES. Projectives (orange) further expand the electron image mapped onto a multi-channel plate (MCP, red) after a drift distance (L1 and L2). The enhanced electron signal from the MCP is detected by a spatial resolved electron detector. A combination of fluorescence screen and CCD camera as well as a delay-line detector (DLD) can be employed. The DLD offers simultaneous spatial yield and kinetic energy detection. Adapted from [159].



and Ruska [204]. Multiphoton PEEM is a tool for the investigation of localized surface plasmons at nanostructures, since the field enhancement at the nanostructure has an eminent effect on the photoemission yield [81, 235]. Another important development is the time-resolved two-photon photoemission electron microscopy [82]. TR-PEEM allows the laterally-resolved monitoring of ultrafast dynamics in nanostructured samples using PEEM by excitation with ultrafast laser pulse pairs with adjustable temporal delay.

The experiments presented in this thesis were performed with two PEEM setups from *Focus GmbH*. The *Focus IS-PEEM* [236–239] was utilized for the experiments discussed in Chapter 2, 3 and 5. For the 2D nanoscopy experiments in Chapter 6 an advanced PEEM setup was employed that is based on the *Focus IS-PEEM* and shares most of the basic design, but includes some new features e.g. the possibility to map the momentum distribution of the photoelectrons similar to ARPES [240, 241] and to achieve an incidence angle of the excitation laser pulses which is close to the surface normal of the sample. According to the latter option this new setup will be referred to as *Focus NI-PEEM*. The concept of normal incidence (NI) illumination used by the *Focus NI-PEEM* has already been demonstrated with a PEEM setup for EUV radiation [242–244].

A PEEM consists of a series of electrostatic lenses along a common optical axis normal to the surface of the sample [159]. The electrostatic fields within the lens system extract the

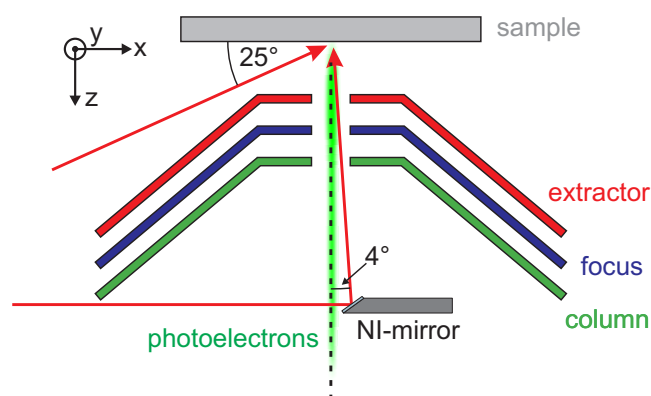
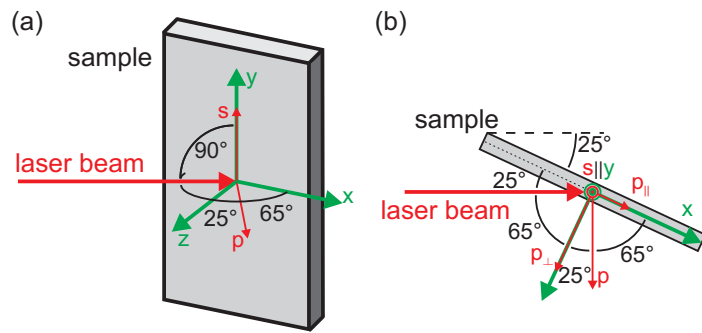


Figure 1.16.: Grazing and normal incidence illumination geometries in *Focus NI-PEEM*. The objective lens system consists of sample and extractor, focus and column electrode. In conventional grazing incidence PEEM mode the incidence angle of the incoming light is limited by the geometry of the conical extractor electrode. In the *Focus IS-PEEM* only the incidence angle of 65° is realized. In the newly developed *Focus NI-PEEM* normal-incidence illumination is optionally achieved by steering the laser beam through an aperture in the objective lens system onto a movable rhodium mirror positioned in the back focal plane close to the focused electron beam. The resulting angle of incidence is 4° .

photoemitted electrons from the sample and project the image of the sample onto the detecting devices. The most important components are depicted schematically in Figure 1.15. Topmost, the sample itself is one out of four major components of the objective lens system in which it acts as a cathode. The other parts are called extractor, focus and column electrode. Photoemitted electrons from the sample are accelerated towards the extractor by a high voltage between sample and extractor. Focus and column electrode map the photoemission distribution on the first image plane. The quality of the image strongly improves with the extractor voltage. However, not all samples endure the high electric fields associated with extractor voltages of 10 kV or higher. Then, blurring of the image might occur or in worst case an electrical breakdown, which is a danger to the PEEM system. In the back focal plane a contrast aperture allows for selection of spatial frequencies. The *Focus NI-PEEM* setup includes a small rhodium mirror which can be positioned close to the electron beam to achieve normal incidence illumination [159, 245]. The stigmators compensate for spatial aberrations. Two projective lenses magnify the image the photoelectrons generate at a multi-channel plate (MCP) of the detector system. The MCP amplifies the electron yield which is then detected by a combination of fluorescence screen and CCD camera or by a delay-line detector (DLD). The DLD also offers the possibility of time-of-flight mapping of photoemitted electrons (TOF-PEEM) allowing the detection the electron kinetic energy distribution at each spatial pixel [246, 247]. Basically, the delay line detector consists of two meshes of meandering wires with orthogonal orientations [248]. In these wires an electronic impulse is launched by the electron bunch created in the MCP upon the arrival of an individual photoelectron. The arrival times of the electronic impulses at the ends of the wires are analyzed and yield information on the impact time and position. For a given drift length defined by L1 and L2 and by comparison with a trigger signal generated by the laser pulse the drift velocity and the corresponding kinetic energy are retrieved.

In conventional PEEM setups an illumination under normal-incidence is prohibited by the electron optics and the electron detection system, which on the one hand blocks the laser beam and on

Figure 1.17: Geometric conditions at PEEM sample for an incidence angle of 65° shown as side view (a) and top view (b). The s polarization component is parallel to the vertical (y) surface vector of the sample. The p component points partially (p_{\parallel}) along the horizontal surface vector x and also has a strong normal component p_{\perp} .



the other hand would strongly be disturbed in their functionality by additional components within or close to the electron path through the microscope. Thus, in case of the *Focus IS-PEEM* the light beam has to be guided outside of the electron optics as it is shown in Figure 1.16. The geometry of the conical extractor electrode, therefore, limits the adjustable angle of incidence to approximately 65° with respect to the surface normal of the sample. Normal incidence illumination is achieved in the *Focus NI-PEEM* by careful modification of the objective lens system. Through a small hole in the objective lens system the laser is guided onto a rhodium mirror positioned close to the electron beam (see Fig. 1.16). Since the electron beam diameter is small at this position and the dimension of the mirror are merely $(2 \text{ mm})^2$, a disturbance by the mirror is avoided. The slight offset of the mirror from the electron optical axis causes a deviation from normal incidence by 4° . Rhodium was used as a material for the mirror because it is inert and robust while providing a high reflectivity for s and p polarization over a broad spectral range. A detailed discussion of the rhodium mirror properties can be found in [245].

The geometric conditions connected with an incidence angle of 65° between laser pulses and the PEEM sample are schematically shown in Figure 1.17. Since the s-polarized electric field component is perpendicular to the plane of incidence, its projection onto the sample is independent from the incidence angle. Thus, the s-polarized field component always points along the vertical (y) surface vector. For p polarization, however, a strong out-of-plane component p_{\perp} is present at the sample. This often complicates the interpretation of the PEEM image because the photoemission yield excited by the p_{\perp} -component dominates the contributions of the in-plane components [159]. Additionally, the grazing incidence rotates the phase fronts with respect to the sample leading to retardation effects that affect time-resolved measurements [159]. In case of perfect normal incidence the p and s polarization components become equivalent. The former p polarization component points parallel to the horizontal surface vector x and the out-of-plane component p_{\perp} is suppressed. Accordingly, the electric field vector is always in-plane independently from the momentary polarization state. Due to the small remaining angle of incidence the distinction between s and p polarization component is still applicable for the normal incidence illumination in the *Focus NI-PEEM*. A comparison of near-normal incidence illumination and grazing incidence illumination in the excitation and detection of SPPs is given by [159].

The lateral resolution of photoemission electron microscopes depends on several conditions [249–252]. The point spread function of the PEEM is affected by chromatic and spheric aberrations of the electrostatic lens system. Another limitation is given by the diffraction of electrons at the contrast aperture of the microscope [159]. Since the incident light is typically focused to excitation spot dimensions larger than the field of view, the incident optical intensity is almost homogeneous in the investigated area. Nanometer feature sizes in the photoemission distribution

only occur, if the sample itself creates the contrast in the photoemission signal.

Contrast mechanisms are for example material contrast and topographical contrast. Material contrast is achieved, if the different electronic structure of two areas of different materials on the sample leads to distinct work functions $E_{W,1}$ and $E_{W,2}$ or to a different photon absorption cross section. The highest material contrast occurs, if the photon energy is between the work functions of the materials, i.e. $E_{W,1} < h\nu < E_{W,2}$. Thus, a linear photoemission process takes place only in the material denoted with index 1, whereas for the second material a two-photon photoemission is necessary. The probability for the nonlinear process is much smaller, especially in the low excitation energy regime and for incoherent or continuous wave radiation. Consequently, the photoemission yield from the first material is dominant. Also the surface topography influences the spatial resolution [249]. Image contrast is also caused by anisotropies of the sample e.g. the orientation of ferromagnetic domains associated with different densities of electronic states for the two opposing spin populations. For different magnetization directions the resulting photoemission yield exhibits a contrast depending on the orientation of the polarization direction [253]. As the electric potential is identical on the conducting sample surface, the electric field between sample and extractor is distorted in regions where the surface is structured. Consequently, the photoelectrons are deflected on their way to the detector and even for surfaces with homogeneous material composition the PEEM images contain structural information. The most important contrast mechanism for the experiments in this thesis is caused by the near-field enhancement of resonant nanoscopic objects [81]. The high local electric field strength at the surface leads to an increased local photoemission yield. This effect becomes most prominent in multi-photon photoemission processes. A detailed discussion of this mechanism is given in Section 1.4.3.

To demonstrate the spatial resolution of the *Focus IS-PEEM* used for the experiments discussed in Chapter 2, 3 and 5, a gold nanostructure was investigated upon ultraviolet (UV) continuous-wave illumination and in case of excitation by femtosecond laser pulses. The results have already been shown in the supplementary information in [4]. The nanostructure was fabricated with focused ion-beam milling to generate a sharp edge. The employed UV lamp provided photon energies above the work function of gold with a low temporal photon flux density at the sample position. The excitation is, therefore, uniformly linear and the obtained resolution is a good estimate for the resolution of the PEEM. The PEEM image for UV illumination is presented in Figure 1.18a. The steepest gradient in the photoemission distribution is found perpendicular to the edge of the nanostructure. Thus, the data along a cut indicated by a red line is evaluated by fitting a sigmoidal function. Figure 1.18b shows the data points (squares) together with the best fit result (red) and the spatial resolution according to a 16%–84% criterion. The width of the edge in the PEEM image is 57.6 nm. However, this does not reflect the best resolution of the PEEM, because the edge does not perfectly follow a step function. Furthermore, the topography contrast by electric fields at the edge leads to a broadening of the photoelectron distribution compared to an instantaneous change of contrast on a flat surface.

The excitation of a nanostructure with ultrashort laser pulses with photon energies below the work function generates multiphoton photoemission (see Fig. 1.14). The spatial resolution for multiphoton PEEM is determined in an experiment comprising excitation with transform-limited laser pulses at 798 nm center wavelength, which are the reference pulses for all experiments described in the following chapters. In the multiphoton PEEM image of the nanostructure (see Fig. 1.18c) again the data along a cut (red) are selected for evaluation. Here, using the identical fit function as before a resolution of 52.5 nm was estimated (see Fig. 1.18d). Hence, it is concluded that also with multiphoton excitation PEEM images with high spatial resolution were

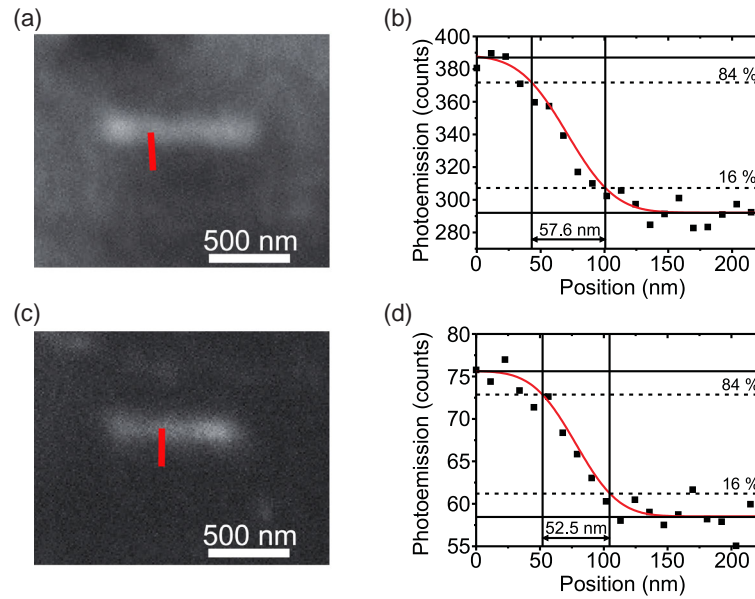


Figure 1.18.: Resolution of PEEM setup determined for single photon PEEM and multiphoton PEEM. (a) PEEM image of a gold nanostructure which was fabricated by focused ion-beam milling for incoherent excitation by ultraviolet light. Data points on cut indicated by red line are evaluated in (b). (b) Data points (squares) and best sigmoidal fit (red) providing a resolution of 57.6 nm according to a 16%–84% criterion (c) Multiphoton PEEM image of identical nanostructure for excitation with ultrashort near-infrared laser pulses. (d) Data points (squares) along red line in (c) and best sigmoidal fit (red) providing a resolution of 52.5 nm according to a 16%–84% criterion. Taken from from supplementary information in [4].

recorded. Comparison with other experiments shows that with the same type of device even better spatial resolutions of approximately 25 nm are possible [254]. With recently developed PEEM setups it is even possible to approach 2 nm resolution [208].

1.4.3. Multiphoton Photoemission from Nanoscaled Systems

In Section 1.3.3 it was already discussed that plasmonic resonances are able to cause strongly enhanced localized electric fields at the vicinity of nanoscopic objects. The local response function $\mathcal{A}(\mathbf{r}, \omega)$ determines the particular near-field distribution for a given incident electric field $\mathbf{E}(\mathbf{r}, \omega)$. On the other hand, for a given local response function control mechanisms (see Section 1.3.5) provide access to the local electric field distribution by tailoring the far-field properties of the excitation laser pulses. This section contains a brief consideration on the impact of local field enhancement on the multiphoton photoemission from nanostructures.

Figure 1.19 illustrates the multiphoton photoemission process at a nanoparticle. In this simplified picture only one field component is used for excitation and the tensorial properties of the local response are neglected for the sake of simplicity. Nevertheless, an extension towards the full representation of the electric fields and response function as discussed in Section 1.3.3 is feasible. The incident far-field $E_p(\mathbf{r}, t)$ excites a localized plasmonic mode. The temporal response function $A(\mathbf{r}, t)$ of the nanostructure is connected to the spectral response function $A(\mathbf{r}, \omega)$ via Fourier transformation. Thus, it is determined by the geometry and the dielectric function of the particle as

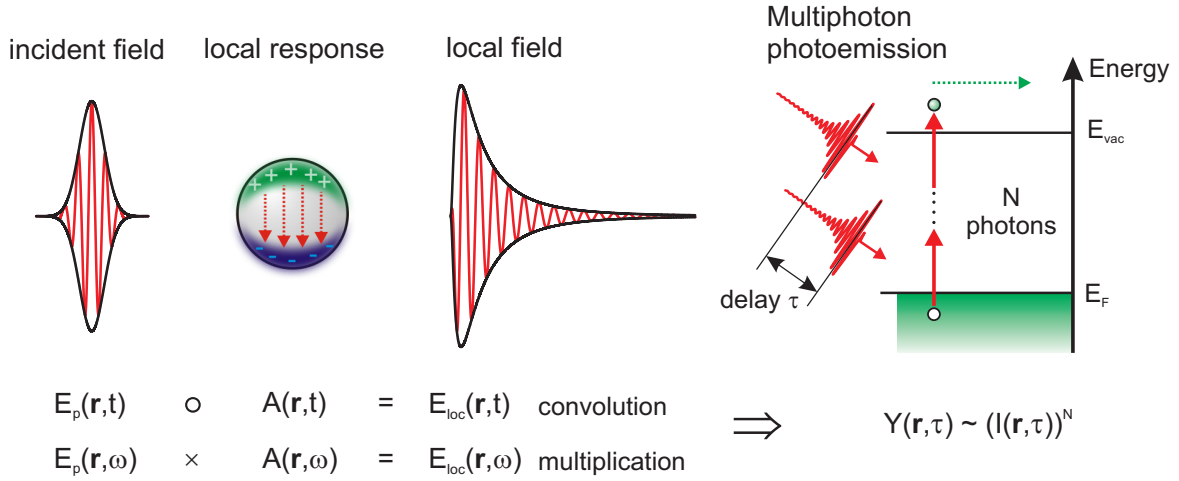


Figure 1.19.: Photoemission driven by local optical field in the vicinity of a nanoparticle. The metallic nanoparticle is excited by an incident pulse $E_p(\mathbf{r}, t)$. The localized plasmonic excitation of the particle modifies the local electric field E_{loc} according to the local response function. In time domain $E_{loc}(\mathbf{r}, t)$ is given by a convolution of electric far-field and local response function. In spectral domain $E_{loc}(\mathbf{r}, \omega)$ is given by multiplication. The multiphoton photoemission process is driven by the local optical field. The resulting photoemission yield Y is proportional to the N -th power of the temporal intensity, where N denotes the number of absorbed photons. By using a sequence of laser pulses with a variable delay τ the local electric field is probed with temporal resolution. Adapted from [255].

well as the dielectric function the surrounding medium. The modification of the incident electric field is expressed in time domain as convolution of $E_p(\mathbf{r}, t)$ and $A(\mathbf{r}, t)$. More conveniently, the spectral notation is used, where the local field $E_{loc}(\mathbf{r}, \omega)$ is calculated by multiplication of $E_p(\mathbf{r}, \omega)$ and $A(\mathbf{r}, \omega)$. Consequently, the temporal local field can also be expressed via Fourier transformation of the spectral field:

$$E_{loc}(\mathbf{r}, t) = \mathcal{F}^{-1}\{E_p(\mathbf{r}, \omega)A(\mathbf{r}, \omega)\} . \quad (1.61)$$

The local photoemission rate $\mathcal{P}(\mathbf{r}, t)$ is approximatively treated by a model for plasmon-assisted multiphoton photoemission introduced by Merschdorf [227]. In this model the dephasing of intermediate electronic states is assumed to take place instantaneously due to the high bandwidth of the available electronic states above the Fermi energy in metals. As a consequence, the photoemission probability is given by a transition rate that is proportional to the N -th power of the local electric field intensity:

$$\mathcal{P}(\mathbf{r}, t) \propto (I_{loc}(\mathbf{r}, t))^N = (E_{loc}^+(\mathbf{r}, t)E_{loc}^-(\mathbf{r}, t))^N . \quad (1.62)$$

From Eq. (1.62) it is obvious that an enhancement of the local electric field $E_{loc}(\mathbf{r}, t)$ increases the local photoemission probability. In the two-photon ($N = 2$) and multiphoton ($N \geq 2$) regime even small local variations of the field strength lead to a strong contrast of $\mathcal{P}(\mathbf{r}, t)$. By integrating over the local photoemission probability $\mathcal{P}(\mathbf{r}, t)$ the local photoemission yield $Y^{(n)}(\mathbf{r})$

is calculated:

$$Y^{(n)}(\mathbf{r}) \propto \int_{-\infty}^{\infty} [\mathcal{F}^{-1}\{E_p(\mathbf{r}, \omega)A(\mathbf{r}, \omega)\}]^n dt . \quad (1.63)$$

Here, the index n denotes the number of electric field terms that are involved. This notation for the photoemission yield is motivated by the perturbative treatment in the description of 2D nanoscopy (see Chapter 4.2.1) and is used in Chapter 3–6. The number of interactions with the electric field is twice the number of absorbed photons, i.e. $2N = n$. In multiphoton PEEM experiments it has been demonstrated that the local field enhancement at nanostructures causes a strongly localized photoemission [81, 256]. Thus, with nonlinear PEEM it is possible to observe optical near-fields with a spatial resolution that is sufficient to map the confinement of localized plasmonic modes. Using the local photoemission yield as feedback it is even possible to adaptively control the optical near-fields at nanostructures [88]. Upon excitation of the nanosystem with a sequence of laser pulses with variable delay a time-resolved detection of the local photoemission enables the investigation of radiative and nonradiative inelastic decay processes [255]. This is also depicted in Figure 1.19. The delay τ between the excitation pulses changes the local field intensity and leads to a delay-dependent yield $Y^{(n)}(\mathbf{r}, \tau)$.

In Chapter 3 time-resolved detection of optical near-fields via two-photon photoemission demonstrates spatiotemporal control of nanooptical excitations. On femtosecond timescale a change of the nanoscopic excitation pattern is generated using polarization-shaped laser pulses and detected by a pump-probe experiment. Also for the 2D nanoscopy experiments discussed in Chapter 5 and Chapter 6 the transition rate model for multiphoton photoemission is applicable. Thus, 2D nanoscopy in samples with fast electronic dephasing provides information on the local response function of the nanosystem. Further details to the influence of strong dephasing on this newly developed spectroscopy method are discussed in Chapter 4.2.2.

2. Optimal Open-Loop Near-Field Control of Plasmonic Nanostructures

This chapter presents experiments on optimal open-loop control of optical near-fields. The experimental application of an analytically derived control rule for nano-optical excitations is demonstrated. Optimal spatial near-field localization in gold nanoprisms is achieved by adaptive optimization of polarization-shaped laser pulses. Afterwards, open-loop excitation switching is realized by applying a π -shift to the relative phase between two polarization components of the pulses. Adaptive and optimal open-loop control lead to the same near-field excitation and finds very similar optimal pulse shapes.

The experiments in this chapter include the coherent control of a nanostructure via polarization pulse shaping and the characterization of the optimal pulse shapes. I took active part in both of these experimental tasks with a focus on the application of the genetic algorithm. I developed solutions for supporting a fast and reliable convergence of the optimizations despite experimental restrictions such as a drift of the sample position (Appendix B) and fluctuations in the local photoemission signal. In the experimental pulse characterization I had an assisting contribution. The analysis of the pulse shapes was performed by Philip Tuchscherer. All evaluations of the PEEM data presented in this thesis or elsewhere [5, 126] were done by me. The PEEM, the laser setup and the investigated nanostructures were provided by Martin Aeschlimann's group and the polarization pulse shaper was provided by Tobias Brixner's group. The paper was written in a cooperative effort [5].

2.1. Introduction

In a theoretical study by Tuchscherer *et al.* [87] the feasibility to coherently control the propagation of plasmons in a y-shaped chain of nanoparticles has been investigated (see Fig. 2.1). The design of the chain waveguide was inspired by theoretical work by Sukharev *et al.* [194]. The nanoparticle chain is excited by polarization-shaped laser pulses that are focused to a particular position at one end of the structure. Hence, the plasmonic excitations propagate from the excitation spot into the other parts of the branching waveguide. A fitness function was defined that increases with the local linear flux $F(\mathbf{r}_1)$, i.e. the integral over the local electric field intensity (see Eq. (1.16)), at a position \mathbf{r}_1 in one arm of the waveguide structure and decreases with the local linear flux $F(\mathbf{r}_2)$ in the other arm [87]. In analytic calculations it was demonstrated that the propagation direction in the branching waveguide structure can be controlled by adjusting the spectral amplitudes and the phase difference between the polarization components. This influenced the polarization state of each frequency component to yield maximal linear flux at \mathbf{r}_1 or \mathbf{r}_2 utilizing the control mechanism of local mode interference described in Section 1.3.5. Since the control of the linear flux was observed to depend only on the polarization state, only the phase difference between both polarization components $\Phi(\omega) = \varphi_1(\omega) - \varphi_2(\omega)$ is a relevant parameter for spatial control.

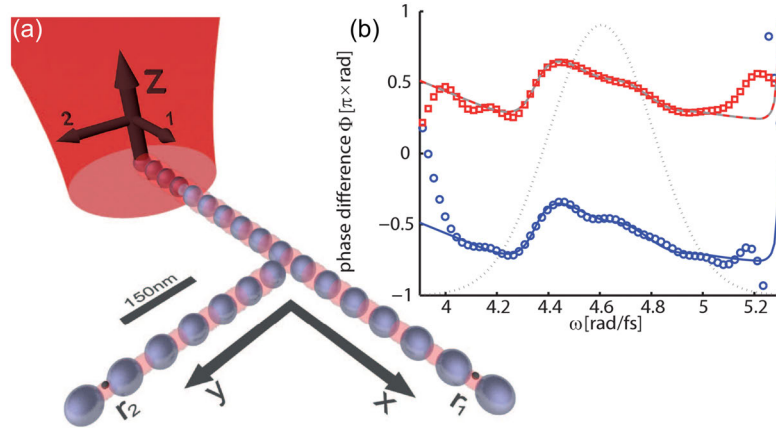


Figure 2.1.: Analytic control of plasmonic nanostructures. (a) Schematic of simulated nanoplasmic waveguide excited by ultrashort laser pulse at one arm of the y-shaped chain of nanoparticles. The excitation propagates towards \mathbf{r}_1 and \mathbf{r}_2 depending on the pulse properties. The spatial control of the linear flux is achieved by choosing the relative phase difference $\Phi(\omega)$ affecting the polarization state of each frequency. (b) Phase differences $\Phi_{max}(\omega)$ for analytic maximization (blue solid line) and $\Phi_{min}(\omega)$ for minimization (red dashed line) of the linear flux difference $F(\mathbf{r}_1) - F(\mathbf{r}_2)$. Additionally, adaptively optimized phases (blue circles and red squares, respectively) are presented. The thin black dotted line indicates the spectral amplitude of the simulated pulses. The spectral evolution of the phase differences for both optimization goals are identical but displaced by an offset of π displayed by the black arrow. Taken from [87].

An important relation for the phase differences $\Phi_{max}(\omega)$ and $\Phi_{min}(\omega)$ yielding the maximum and the minimum signals was found to be

$$\Phi_{max}(\omega) - \Phi_{min}(\omega) = \pi . \quad (2.1)$$

Hence, the optimal polarization states differ by a relative phase shift of π between the phases $\varphi_1(\omega)$ and $\varphi_2(\omega)$ of the polarization components [87]. This gives immediate access to the optimal phase difference for minimization, as soon as $\Phi_{max}(\omega)$ has been retrieved analytically or adaptively for example in an experiment. The same is valid for Φ_{max} in case of known $\Phi_{min}(\omega)$. Hence, the pulse shape for the optimal switching of the excitation contrast is determined by an open-loop approach and does not have to be retrieved by further closed-loop optimizations. The optimization results for $\Phi(\omega)$ are plotted in the diagram in Figure 2.1 as blue solid and dashed red lines for maximization and minimization of the linear flux difference $F(\mathbf{r}_1) - F(\mathbf{r}_2)$, respectively. The analytically calculated optimal pulse parameters were confirmed by an adaptive optimization employing an evolutionary algorithm as discussed in Section 1.2.3. The identified global optima (open symbols) were identical to the analytic approach in the overlap with the excitation spectrum. Significant deviations occurred in both cases only for spectral position with low intensity.

The remaining degrees of freedom of the spectral phase parameter were utilized for temporal control, e.g. pulse compression for achieving high nonlinear signals. At the desired spatial position temporal compression of the near-field was performed by compensating the modulations of the local spectral phase while keeping $\Phi(\omega)$ constant [87].

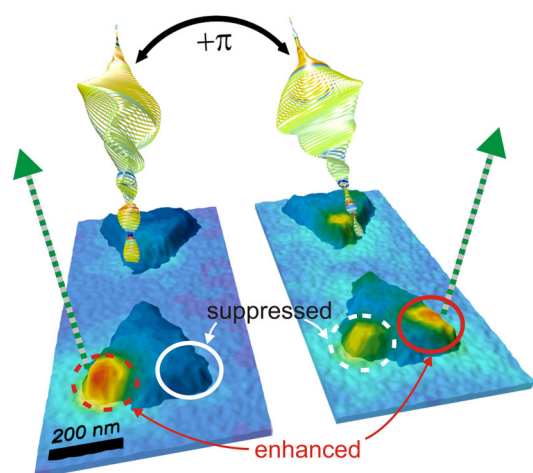


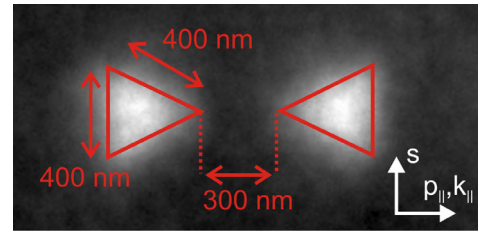
Figure 2.2: Concept of optimal open-loop control of plasmonic nanostructures. The photoemission distribution indicated by a false-color plot is also shown in Fig. 2.7. The spatially resolved photoemission yield symbolized by green arrows is the feedback signal for the optimization of polarization-shaped laser pulses depicted as quasi-3D representations. In a first step (left) near-fields are localized and enhanced by adaptive optimization at one position of the nanostructure (red dashed circle) and suppressed at a second position (white solid circle). The retrieved phase and polarization information is used to directly generate the pulse shape (right) that enhances the photoemission from the formerly suppressed position (red solid circle). Both optimal pulse shapes differ only by an offset of π in the phase difference of both polarization components. The control rule holds in both directions and works for both starting locations.

The basic experimental concept for the demonstration of optimal open-loop control by employing the theoretically derived control rule (Eq. (2.1)) is presented in Fig. 2.2. The schematic picture shows an artistic 3D height profile representing the topography of the investigated gold nanostructure consisting of two equilateral triangular nanoprisms with facing corners. The measured local photoemission yield (see Fig. 2.7c and d) is indicated by a false-color plot mapped onto the surface. The excitation of the gold nanostructure is localized and enhanced by adaptive polarization pulse shaping at one corner of the antenna (dashed circle) and suppressed at the opposite corner (white solid circle). After successful optimization, the phase difference $\Phi(\omega) = \varphi_1(\omega) - \varphi_2(\omega)$ determines the optimal polarization state of each frequency component. Furthermore, $\varphi_1(\omega)$ and $\varphi_2(\omega)$ are optimized to compress the local temporal near-field at this corner of the nanoprism via constructive superposition of all frequency contributions. After shifting the phase difference $\Phi(\omega)$ by π , i.e. adding π to one of the polarization components, the new pulse shape creates a strong optical near-field at the opposite corner (red solid circle). By proving that the open-loop pulse shape is optimal for the inverse optimization goal by comparison with adaptive optimization results, it is demonstrated that optimal open-loop control indeed finds the correct spectral phases for high contrast excitation switching on the nanoscale. In this chapter the details and the results of the corresponding experiments are discussed.

2.2. Experimental Setup and Sample Characterization

The sample featured arrays of gold nanostructures on an ITO/glass substrate and was prepared by Daniela Bayer using electron beam lithography in the facilities of the Nano-Bio Center at the University of Kaiserslautern [239, 257]. Each nanostructure consists of a pair of triangular nanoprisms with facing corners. Nanostructures with differently sized nanoprisms and varying gaps between the nanoprisms were fabricated. A PEEM image of the nanostructure which is employed in the experiments is presented in Fig. 2.3. The one-photon-photoemission excited by the incoherent UV radiation of a mercury gas discharge lamp is evenly distributed over the nanostructure. The nanoprisms were 40 nm in height and the edges forming the triangle had the

Figure 2.3: UV-PEEM image of gold nanostructure used for optimal open-loop control with outlines highlighted by red lines. The nanostructure consists of two equilateral triangular nanoprisms with 400 nm edge elongation and 40 nm height. The nanoprisms are separated by a 300 nm gap. The directions of the wavevector projected on surface (k_{\parallel}) and of the polarization components (s , p_{\parallel}) in case of laser pulse illumination are indicated by white arrows.



identical length of 400 nm. The gap between the nanoprisms was 300 nm.

The setup of the control experiment is presented in Figure 2.4. A Ti:Sapphire laser oscillator (*Newport Spectra-Physics Tsunami*, repetition rate: 80 MHz, center wavelength: 795 nm, temporal FWHM: 30 fs, pulse energy: 9nJ) generates horizontally polarized near infrared laser pulses. An active beam stabilization system (*TEM Messtechnik Beamlok 4D*) ensures the exact positioning of the beam in the optical setup. A beam splitter in front of the polarization pulse shaper partially reflects the laser pulses. The reflected part of each pulse is frequency-doubled in a second harmonic generation process in a 300 μm BBO crystal and employed as a probe pulse. Accordingly, the photon energy of the probe pulse is doubled from 1.55 eV for the fundamental pulses to 3.1 eV. The transmitted part of the pulse propagates through the polarization pulse shaper, where it is shaped by applying voltages to the pixels of the liquid crystal display. The polarization-shaped pump pulse and the frequency doubled probe pulse are focused weakly by the same lens and overlap on the sample located in the UHV chamber of the photoemission electron microscope (PEEM) under a small angle of less than 1° . The spot size on the sample is adjusted by changing the spatial position of the lens in beam direction. Typically, a spot size of 70 μm was used in the following experiments. The temporal overlap of the pulses is achieved by setting the delay stage in the probe arm. Chirp in the probe pulse is compensated for by a prism compensator, which is not shown in the schematic picture, resulting in 30 fs duration of the 398 nm pulses.

As characterization tools for the polarization-shaped laser pulses FROG [258–261] and dual-channel interferometry [262–264] were employed (see Appendix A). With FROG the laser pulses from the pulse shaper with unmodulated phases were measured. In a first spectral interferometry measurement the FROG phase was used to determine the reference pulse of the polarization pulse shaper setup. The newly characterized reference pulse is used in dual-channel interferometry measurements to retrieve the spectral amplitude and spectral phase of the pulses from the polarization pulse shaper. The position at which the pulses diagnostics were located, was close to the last mirrors that couples the beam into the PEEM. A duplicate of the entrance window of the vacuum chamber was used to introduce the same amount of chirp in the characterized beam as in the beam propagating into the PEEM chamber. Accordingly, the deviations between measured pulse shapes and pulse shapes at the position of the sample are considered to be small. The pulse duration of the unshaped laser pulses was determined to be 50 fs which is above the achievable duration of the laser system. A reason for the elongation is spectral narrowing caused by the limited bandwidth of the pulse shaper. The employed photoemission microscope was the *Focus IS-PEEM* presented in Chapter 1.4.2. Thus, the incidence angle of the beams on the sample was 65° .

Deposition of Cs onto the sample reduced the work function of the gold surface below 4.6 eV

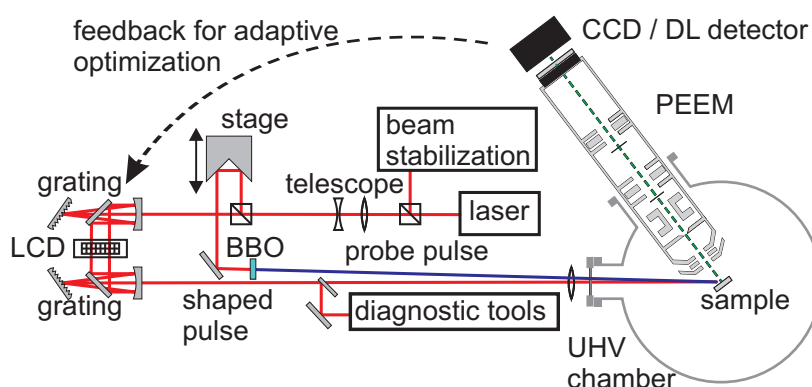


Figure 2.4.: Experimental setup for demonstration of optimal open-loop control of plasmonic nanostructures. The 30 fs laser pulses of a Ti:Sapphire oscillator with 80MHz repetition rate at 795nm center wavelength are actively beam stabilized in front of a beam splitter. A part of the beam propagates through the polarization pulse shaper. Here, the spectral phases of the polarization components are modified independently. The polarization-shaped pulses are focused onto the sample under an incidence angle of 65° and act as pump for the nanoscopic excitation. Not included in this figure is the low intense reference beam that is split from the beam before the first grating of the pulse shaper and recombined with the shaped beam at the exit of the pulse shaper. The other beam originating from the first beam splitter is frequency-doubled in a second harmonic generation process in a $300 \mu\text{m}$ BBO crystal and then overlapped with the pump beam on the sample. The incidence angle deviates by about 1° with respect to the probe beam. The photoemission pattern emitted from the sample is recorded with a CCD detector and provides the feedback for adaptive optimizations.

permitting two-photon photoemission for the combined absorption of one 800 nm and one 400 nm photon. The intensities of pump and probe pulse are adjusted for optimal two-color two-photon photoemission yield from the sample. In the overlap of pump and probe pulse the signal is enhanced by a factor of three compared to the static background of two-photon photoemission from the probe pulse and three-photon photoemission from the pump pulse. The two-photon photoemission distribution generated only by the 400 nm probe pulse is homogeneous, i.e. the complete nanostructure is uniformly excited. In the two-color excitation process the intermediate state is either populated by the pump or the probe pulse. In both cases the observed emission pattern is proportional to the local electric field intensity generated by the polarization-shaped pump laser pulse. Thus, although a nonlinear method is used, the linear response of the nanoprisms at the pump wavelength is investigated.

The gap size of the investigated structure is too large to introduce a coupling between the two nanoprisms. Thus, the nanostructure responds to laser excitation like independent nanoprisms with different orientation. Equivalently, the nanostructure shows simultaneously the local excitation created for two directions of incidence at an identical nanoprism. The near-field distribution at a nanoprism is in case of normal incidence determined by the orientation of the polarization vector with respect to the edges of the triangle. A field vector parallel to the nanoprism edge generates strong field enhancement in the corners of this edge are achieved [165]. Contrary, a polarization perpendicular to the edge causes weak near-field enhancement along this edge and a strong enhancement at the opposite corner [265].

In order to estimate the local electric field distribution at the nanostructure for the non-normal incidence geometry finite difference time domain (FDTD) simulations of a model system are

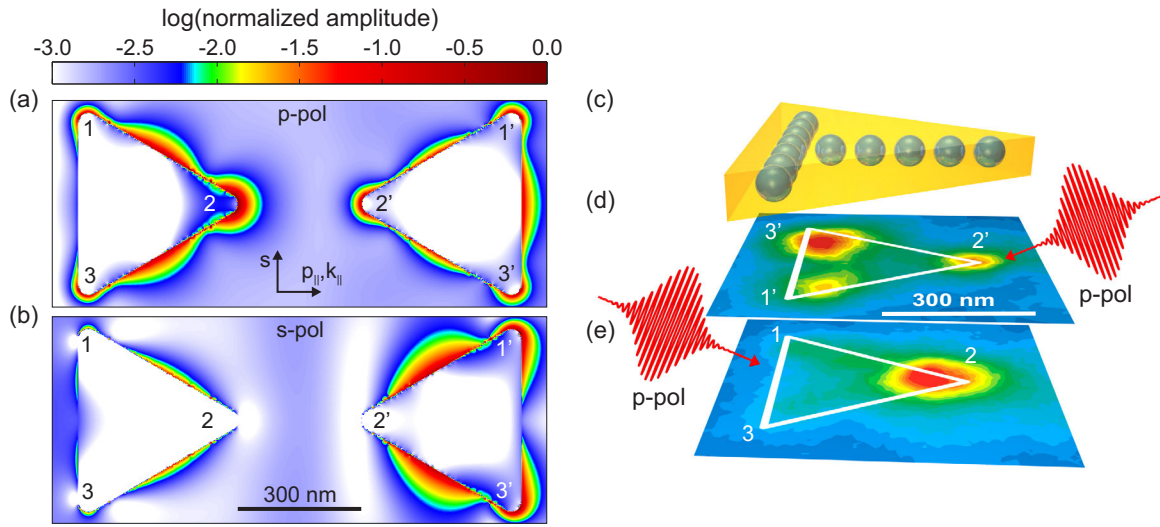


Figure 2.5.: Dependence of gold nanoprism near-field distribution on wavevector and polarization direction. (a, b) FDTD simulations of local electric field amplitudes at triangular nanoprisms at a height of 38 nm above the substrate. The nanoprisms are excited by plane-wave radiation at 800 nm wavelength and with an incidence angle of 65° with respect to the surface normal. The wavevector component parallel to the surface \mathbf{k}_{\parallel} , and the polarization directions \mathbf{s} and \mathbf{p}_{\parallel} are indicated. Corners of nanoprisms are marked by numbers. (a) Excitation with p-polarized laser pulses. (b) Excitation with s-polarized laser pulses. (c) Schematic illustration of equilateral gold nanoprism with 400 nm side length and 40 nm height overlapped with the plasmonic nanoparticle chain waveguide structure investigated in [194]. (d) Two-color two-photon PEEM image of gold nanoprism upon excitation by a transform limited p-polarized pump pulse at 1.6 eV and a 3.1 eV s-polarized probe pulse coming from the right. The angle of incidence was 65° . (e) PEEM image under similar conditions as in (b), but illumination from the left. (c–e) Adapted from [5].

performed. FDTD is an established numerical technique for finding approximate solutions of differential equations [266–268]. Among other usage FDTD has been successfully applied for calculating optical excitations in nanoscopic systems [269, 270]. In the simulations described here a commercially available software (*FDTD Solutions, Lumerical*) is employed. The simulated dielectric function gold is adjusted to fit data from [271]. The results of the FDTD simulations for p- and s-polarized laser pulses are presented in Figure 2.5a and b, respectively. The corners of the nanoprisms are denoted as 1, 2, 3 (left nanoprism) and 1', 2', 3' (right nanoprism).

The dominant excitation of the left nanoprism in Figure 2.5a is located at corner 2, which is pointing away from the incident radiation, whereas at the edge facing the radiation very weak signals are observed. At the right nanoprism in Figure 2.5a, which is rotated by 180° , the excitation pattern is not simply retrieved by rotation. Strong local fields are observed in all three corners with slightly higher field strength in the corners 1' and 3', which are opposite to the incoming wave. The two-color two-photon PEEM images for p-polarized near-infrared pulses presented in Figure 2.5d and e qualitatively agree with the simulation results. For a nanoprism orientation with one corner pointing towards the incident light (right nanoprism in Fig. 2.5a, Fig. 2.5d) an excitation of all three corners (1', 2', 3') is visible. The photoemission distribution exhibits an asymmetry between corners 1' and 3'. This is an indication for slightly asymmetric conditions at the sample e.g. the orientation of the nanoprism towards the laser beam or small structural imperfections leading to differences in the local electric field at the corners. As the

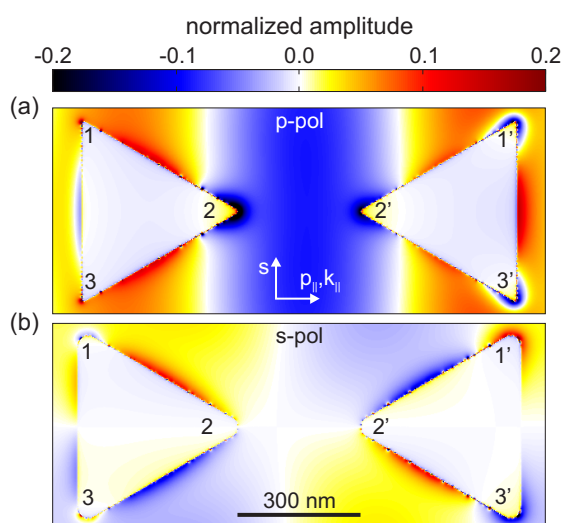


Figure 2.6: Distribution of electric field component E_z at gold nanoprisms simulated by FDTD at identical excitation conditions as in Fig. 2.5. (a) Imaginary part of E_z for p-polarized excitation pulses. The corners 1' and 3' exhibit identical values of E_z . (b) Real part of E_z for s-polarized excitation pulses. E_z has different signs at corners 1' and 3'.

photoemission signal depends on the intensity, differences in the local electric fields are further enhanced. The dominant feature for the rotated geometry (left nanoprism in Fig. 2.5a, Fig. 2.5e) clearly is located on the corner opposite to the incident field (2).

For s-polarized laser pulses (see Fig. 2.5b) a very weak excitation of the left nanoprism is visible. Highest field amplitudes are located along the edges of the triangular nanoprism. The inverted orientation of the right nanoprism leads to a much stronger coupling to the far-field. High electric fields are achieved at the corners 1' and 3'. Hence, for both polarization components it is obvious that the non-normal incidence leads to wavevector-dependent local field distributions. Theoretical demonstrations of nano-optical switching in branched plasmonic nanoparticle waveguides as they are depicted schematically in 2.5c as well exhibit that the direction of the incident fields controls the direction of the propagating modes and the resulting near-field distribution [87, 193]. In case of the nanoprisms investigated here, the orientation of the wavevector determines which spatial positions are effectively accessible by a coherent control strategy. In the left nanoprism the local field is strongly enhanced at corner 2, if excited by p-polarized radiation. However, s-polarization does not achieve strong local fields and a coherent superposition of both field distributions would not lead to significant changes of the local field intensity. At the right nanoprism the situation differs significantly. Here, both far-field components generate intense local fields at corners 1' and 3' and, therefore, coherent control of the local excitation via the polarization components is feasible.

To estimate whether a localization of the electric field in one of the corners is achievable while the excitation at the opposite corner is suppressed, phase-dependent signals have to be evaluated. The electric field component E_z , which is normal to the surface of the substrate, is depicted in Figure 2.6. The obtained field distribution closely follows the overall amplitude distributions presented in Figure 2.5. For p-polarized radiation the field distribution is symmetric, so identically oriented out-of-plane components E_z are generated at these corners. In case of s-polarized excitation E_z has an antisymmetric distribution with respect to the horizontal line through corners 2 and 2'. Accordingly, at the corners 1' and 3' it has identical amplitude but different signs. The s-polarized component is pointing completely in-plane. Nevertheless, it generates the out-of-plane electric field component because the displaced charges in corners 1' and 3' act as sources for the local field. Since E_z significantly determines the local photoemission yield [159], a coherent superposition of

the electric fields distributions excited by p- and s-polarized light can enhance the photoemission from corner 1' and suppress corner 3' and vice versa depending on the relative phase difference between the far-field polarization components. Whereas in Figure 2.6a the imaginary part of E_z is shown, in Figure 2.6b the real part is depicted. Thus, the local field distributions implicitly are presented for a relative phase difference of $\pi/2$ as it would be the case for excitation by circular polarized far-field radiation. In this case the local fields at corner 3' interfere constructively and the highest excitation is achieved there. However, the circular polarization state is not optimal for the localization at this corner, since the local field enhancement differs for both polarization components. The local electric field of the s component is larger by a factor of approximately 1.3. Because of the normalization of the plots, this cannot be inferred directly from Figures 2.5 and 2.6. Nevertheless, this indicates that an elliptical polarization state is more effective for coherent control, especially in the suppression of the local field in the corner.

Similar results have also been obtained in a study by Melchior *et al.* using finite integral methods for calculating the response of such a type of nanostructure and employing the identified polarization control mechanism in an experiment by interferometric superposition of bandwidth-limited pulses with s and p polarization [239, 257]. There, however, the optical delay between the perpendicularly polarized pulses influenced the polarization state of the complete laser pulse. In contrast, the setup employed here enables to independently adjust the polarization state and the spectral phase of each frequency component. This offers the possibility to optimize the local linear flux by means of the polarization control mechanism as well as spectral phase control mechanism which have been discussed in Chapter 1.3.5. To evaluate which pulse shapes are optimal for a high contrast switching of the local excitation in the nanoprism, a systematic examination of different pulse shapes has to be performed. The corresponding experiment based on adaptive optimizations is presented in the following section.

2.3. Open-Loop Control of Nanoplasmonic Excitations

The experimental demonstration of open-loop control of nanoplasmonic excitations required in a first step the adaptive optimization of pulse shapes. The optimization goal was the achievement of an enhanced local photoemission yield in one region of interest (ROI 1) around corner 1' while the photoemission from ROI 2 located at corner 3' was suppressed. In a second step it was demonstrated that the analytically derived control rule switches the excitation distribution and enhance the local yield in ROI 2. In a subsequent optimization with the inverse optimization goal it was verified that, indeed, the optimal pulse shapes for the switched photoemission distribution are provided by the control rule and again adding π to the relative phase difference $\Phi(\omega)$ achieved the optimal pulse for the first optimization goal.

For adaptive optimizations the obtained PEEM images generated by each individual pulse shape were analyzed by a computer based evaluation routine which performs spatial drift correction in the obtained PEEM data and evaluates regions of interest according to a fitness function. The fitness values of each individual were used as a feedback for the evolutionary algorithm that is described in Chapter 1.2. The pulse shaper was set to polarization pulse shaping which involves an independent tailoring of the spectral phases of two perpendicular polarization components. Both spectral phases $\varphi_1(\omega)$ and $\varphi_2(\omega)$ were parameterized by an individual set of coefficients of the sixth-order Taylor expansion. However, the absolute phase of one of the components remained

fixed. Accordingly, 11 parameters determined the genes of an individual of the evolutionary algorithm. Each generation consisted of 40 individuals. Convergence of the adaptive learning loop was reached typically after 20 to 40 generations.

Figure 2.7 presents the results of two adaptive optimizations followed by two optimal open-loop control experiments. The first adaptive control experiment optimized the ratio of the photoemission in corners 1' and 3' of the nanoprism. Figure 2.7c shows the regions of interest and the achieved adaptively optimized photoemission distribution. The optimization goal was defined by the fitness function

$$f_{\text{Mean}}^{\text{Max}}(\text{ROI 1}, \text{ROI 2}) = \text{Max}(\text{ROI 1})/\text{Mean}(\text{ROI 2}) . \quad (2.2)$$

The Max-function finds the pixel with the highest photoemission yield in the ROI and evaluates the average yield within the 7×7 pixels including the maximum pixel in the center. The Mean-function determines the average of all pixels in the region of interest. The evolution of the fitness of the best individual in each generation is presented as red circles in Figure 2.7g together with the corresponding reference fitness obtained with unshaped laser pulses. Whereas the fitness for the reference pulses showed some small fluctuations, a significant change of the fitness was only observed for the optimized pulse shapes. The starting population was generated by a random choice of gene values i.e. a random distribution of pulse shapes. By chance the best individuals had a fitness equal to the reference pulse. The choice of the fitness function and the positioning of the ROIs ensured a reference fitness above 1, which is the fitness value in case of very low photoemission in both ROIs. Thus, bandwidth limited pulses, creating a significantly strong but unspecific photoemission distribution, are preferred by the optimization routine to complex pulse shapes which suppress the total photoemission signal. For this reason the employed fitness functions $f_{\text{Mean}}^{\text{Max}}$ provides a fast convergence and additionally favors a high total photoemission yield. Over the initial 20 generations in the closed-loop process continuous improvements were made. Then, the fitness saturates as the fittest gene sequence asserts itself in the pool of individuals. By mutations and crossing of almost identical individuals only a small increase of the fitness is achieved. The optimal pulse shape obtained by this first optimization is shown by a quasi-3D representation in Fig. 2.7a. The pulse characterization for each pulse in this chapter was performed using dual-channel spectral interferometry.

In the photoemission image (see Fig. 2.7c) a strong emission in ROI1 and almost no yield from the lower corner was observed. Optimal open-loop control uses the information which is implicitly encoded in the spectral phase of the optimized pulse for achieving a switching of the local excitation. After applying the control rule for optimal switching contrast, i.e. shifting the relative spectral phase between the polarization components by π , the new pulse shape was determined as depicted in Fig. 2.7b. This open-loop control step, as expected, changed the photoemission distribution towards the lower corner of the nanoprism (see Fig. 2.7d). The strongest emission was now located in ROI2, but there was still some considerable yield in ROI 1. To verify that the optimal open-loop control scheme found the global optimum for the reversed fitness function, also the adaptive optimization for

$$f_{\text{Mean}}^{\text{Max}}(\text{ROI 2}, \text{ROI 1}) = \text{Max}(\text{ROI 2})/\text{Mean}(\text{ROI 1}) \quad (2.3)$$

was performed. The choice of the ROI sizes and positions differed from the previous optimization. However, since the Max-function searches for the maximum yield in the ROI, changes in the exact ROI definition do not affect significantly the adaptive optimization. The results of the

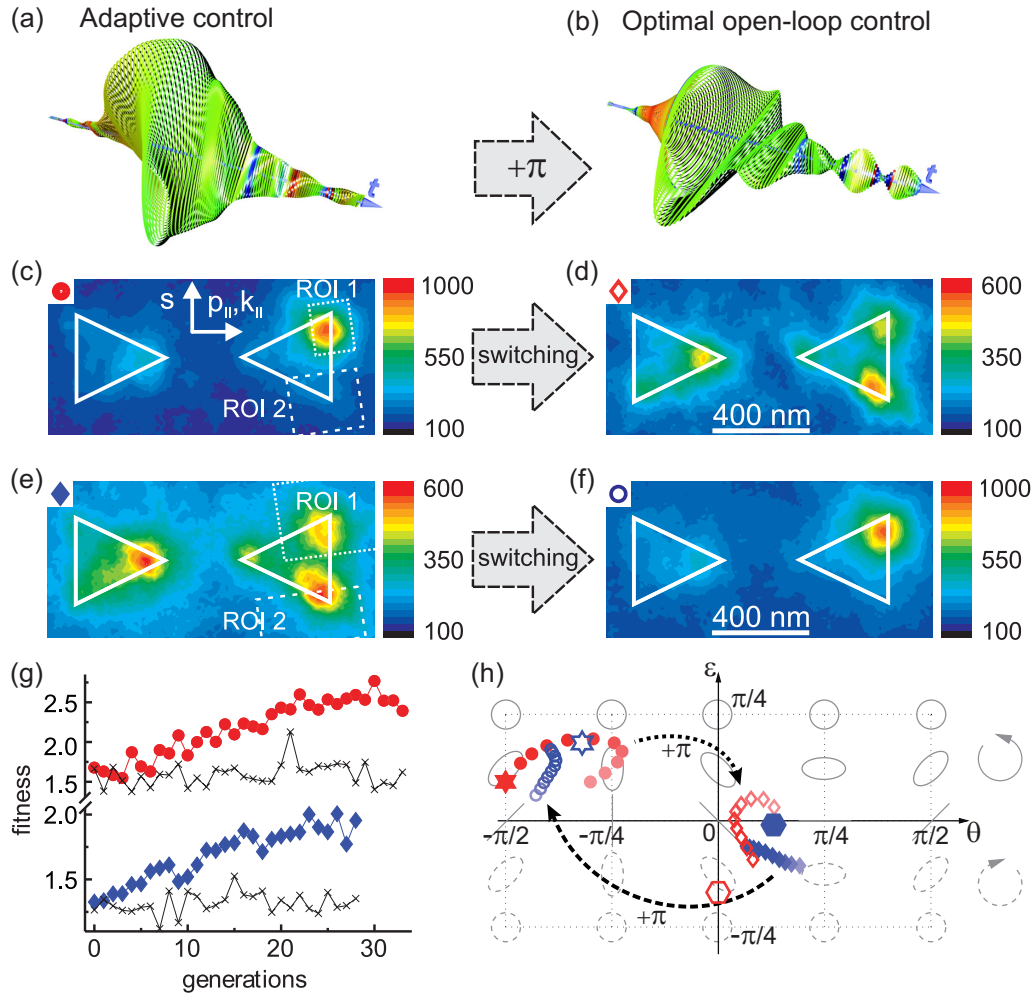


Figure 2.7.: Adaptive (left) versus optimal open-loop control (right) of the photoemission distribution at a nanoprism. (a) Optimal pulse shape after adaptive enhancement of the photoemission ratio between ROI 1 and ROI 2 presented in (c). (b) Application of control rule provided altered pulse shape for achieving a high localized yield at the lower corner (ROI2) of the nanoprism. (c,d) PEEM images for optimal pulse shape of adaptive optimization (a) and optimal open-loop control (b). The projections of the laser wave vector and the polarization components are indicated as arrows in (c). (e) PEEM image with ROIs after adaptive optimization of photoemission yield in the lower corner of the nanoprism. (f) Application of control rule exhibiting strong excitation of the upper corner. During the optimizations and for (c)–(f) a transform-limited s-polarized pulse at 398 nm center wavelength was used as a probe pulse. (g) Evolution of fitness during adaptive optimizations presented in (c) (red circles) and (e) (blue diamonds) and reference fitness (black crosses) of the corresponding generation. (h) Representation of pulse shapes found adaptively (filled symbols) and by the optimal open-loop control rule (open symbols) on the Poincaré surface. The plots cover the time interval from -30 fs to 30 fs in which the overlap with the frequency double probe pulse occurs. The normalized electric field strength is displayed by the symbol shading. The stars and hexagons indicate the polarization state for maximum overlap with the probe pulse (at 0 fs) in a repeated experiment with identical optimization goals. A perfect inversion of the trajectories with respect to the center (0, 0) of the Poincaré surface was not achieved by the relative phase shift by π . Deviations are caused by limitations of the pulse shaper and the optical setup. Adapted from [5].

adaptation process are presented in Fig. 2.7e. Here, a photoemission distribution that closely resembles the open-loop result were found as a global optimum. Again, the coexcitation of photoemission in ROI 1 could not be suppressed completely. An application of the control rule to the optimal pulse of this second optimization switches the emission pattern back towards an isolated excitation of the upper corner. Thus, the spatial excitation obtained by open-loop control in both cases reproduces the adaptive results of the same optimization goal. Clearly, this demonstrates experimentally the theoretically derived control rule.

For a further investigation and comparison of the pulse shapes the evolution of the polarization state within the pulses is shown in Figure 2.7h as trajectories on the Poincaré surface [111]. The gray ellipses indicate the polarization state at particular positions. The linear polarization states are located along the horizontal axis, i.e. for $\varepsilon = 0$. The orientation along the first LCD layer of the SLM is set to $\theta = 0$. Circular polarization are located at the upper and lower boundary of the plot ($|\varepsilon| = \pi/4$). The left-handed polarization states (solid lines) are in the upper half of the plot. The symbols in this plots are the same as indicated in the photoemission images in Figure 2.7c–f. Ten time bins per pulse indicate the temporal steps from -30 fs to 30 fs, which is the time interval in which pump and probe pulse overlap. The symbol shading represents the normalized electric field strength of the temporal step, where highest saturation means highest intensity. Optimal open-loop pulses (open symbols) and adaptively optimized pulses (solid symbols) with identical optimization goal are located at the same regions on the Poincaré surface providing evidence that the open-loop control achieves the global optimum for the excitation switching as theoretically predicted. The optimal pulse shapes for enhancing the signal in ROI 1 have a positive ellipticity φ , whereas the localization in ROI 2 is achieved with almost linearly polarized pulses. This asymmetry reflects deviations of the real nanostructure from the ideal triangular shape for which a symmetric behavior is expected. A good repeatability of the control experiments is concluded from the results of a repeated run of the experiment. In Fig. 2.7h the stars (enhancement of ROI 1) and hexagons (enhancement of ROI 2) represent the polarization states of the corresponding optimal pulses of the open-loop optimizations (open symbols) and the adaptive optimizations (solid symbols). To facilitate the recognition, only a single symbol for zero delay between pump and probe pulse is plotted per pulse. Again, the pulse parameter are localized in the same region on the Poincaré surface with deviations that are presumably caused by experimental uncertainties, reproducing the results of the initial experimental run. A shift of the relative phase by π leads in the ideal case to an inversion of the pulse parameter with respect to the center (0, 0) of the Poincaré surface. The inversion which is observed in Fig. 2.7h obviously exhibits imperfections that are attributed to the frequency-dependent Jones-matrix of the setup causing pulse modifications upon propagation through the pulse shaper and the remaining optical elements. Nevertheless, the imperfect Jones matrix influences the pulse shapes obtained by adaptive optimization as well as the open-loop control. Hence, the control rule still provides the optimal phase settings for the given experimental conditions.

2.4. Conclusion

In this chapter the applicability of the theoretically derived control rule for optimal open-loop excitation switching was demonstrated for localized plasmonic near-fields at a gold nanoprisim. The two-color two-photon photoemission scheme enabled the detection of a signal that is proportional

to the local linear flux $F(\mathbf{r})$, i.e. the integrated local field intensity, as it is discussed in [87]. Implicitly, the experiments are performed time-resolved, since the photoemission signal is strongly enhanced in the overlap of pump pulse and probe pulse. Thus, the closed-loop and open-loop polarization pulse shaping tailors the spatial and temporal properties of the local electric field at the nanostructure simultaneously. Hence, the applied coherent control scheme goes beyond the spatial control of nanooptical fields that was demonstrated in [88]. A related experiment achieving spatiotemporal control of optical near-fields via polarization pulse shaping is published in [2].

The investigated control rule follows from analytic considerations which are more general [87]. Thus, also in other nanoscopic systems the optimal pulse shapes for two opposite optimization goals are connected by a spectral phase difference of π . This relation can be exploited even without a pulse shaper setup, since simpler optical elements, e.g. half-wave plates or Mach-Zehnder interferometers with crossed polarization directions as in [257], also provide the necessary phase shift in one polarization component. Nevertheless, to investigate the local response of the nanostructure and to create the optimal pulse shape for arbitrary nanoscopic excitations a polarization pulse shaper is beneficial as polarization and spectral phase control mechanisms can be employed.

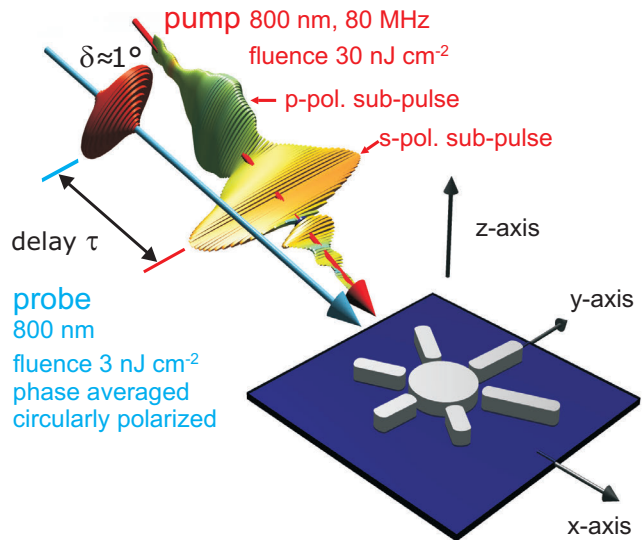
3. Spatially and Temporally Resolved Control of Nanooptical Excitations

The experimental implementation of time-resolved photoemission microscopy as a feedback for coherent control gives access to detect and control the localization of optical near-fields not only in space but also in time [2]. In a previous publication of Aeschlimann *et al.* coherent control of optical near-fields at an artificial nanostructure was demonstrated using polarization pulse shaping in combination with PEEM [88]. The optimal pulse shapes found adaptively by an evolutionary algorithm were reconstructed from the spectral phase and amplitude determined by dual-channel spectral interferometry and Jones-Matrix calculations (see Appendix A). The reconstructed temporal pulse shapes often showed complex behavior of the intensity as well as the polarization state. To investigate how such complex pulse shapes affect the temporal evolution of the local electric field at a nanostructure, an ultrafast spatial-resolved detection method is necessary.

The experiment discussed in this chapter demonstrates the simultaneous control over spatial and temporal degrees of freedom of electromagnetic excitations in the vicinity of a nanostructure [2]. Using polarization pulse-shaping the excitation pulse is tailored to achieve an ultrafast nanoscale excitation switching process, i.e. nanooptical fields at two different locations of a nanostructure are excited with femtosecond temporal separation. In an incoherently performed single-color pump-probe experiment the temporal evolution of the near-field-induced local excitation is investigated with means of TR-PEEM on sub-diffraction length scale and on a femtosecond time scale. A compact mathematical relation for the delay-dependent time-integrated photoemission signal is deduced employing the concept that the local electric field at the nanostructure drives the two-photon photoemission process. This derivation demonstrates that the local excitation created by the pump pulse is mapped, whereas the probe pulse acts as a temporal gate which selects the investigated temporal position.

This chapter puts an emphasis on the detection scheme for ultrafast excitation switching. In a joint publication [2] also a demonstration of simultaneous coherent control in spatial and temporal degrees of freedom was discussed. In the preparation of the experiments I took part in the assemblage of the optical setup and alignment of the hardware components, e.g. PEEM, polarization pulse shaper and pulse characterization devices. Furthermore, I developed software routines for controlling the hardware and the direct data evaluation embedded in the measurement process. I contributed to the experiments by planning and executing the data acquisition process with the combined experimental setup, while the individual hardware components were maintained by other members of the cooperation. Except for the pulse characterization, the data evaluation during and after the experimental session was mainly performed by me.

Figure 3.1: Generation and detection scheme for ultrafast excitation switching. By scanning the delay τ between the polarization-shaped pump (red arrow) and circularly polarized probe (blue arrow) laser pulses the temporal evolution of the spatially localized excitation is detected via time-resolved PEEM. There is a small offset of $\delta \approx 1^\circ$ in the angle of incidence between pump and probe that has no significant effect on the measurement. A fast dither (± 2 fs) suppresses coherent effects in this single color experiment. Adapted from [2].



3.1. Introduction

Fig. 3.1 depicts the basic idea of the space- and time-resolved experiment at an artificial sun-shaped Ag nanostructure [2]. Two laser pulses are employed which are denoted as pump and probe pulse. The pulses are depicted in a quasi-3D-representation [110]. The polarization-shaped femtosecond pump laser pulse creates a time- and space-dependent excitation pattern in a nanostructure, which is then monitored via time-resolved two-photon photoemission electron microscopy detecting the delay-dependent enhancement of the local photoemission yield in the overlap with the probe pulse. The pump laser pulse shape, the local optical response of the nanostructure and the coherent and inelastic lifetime of the electronic excitation in the material determine the transient spatial distribution of photoexcited electrons.

The pump pulse shown in Fig. 3.1 is not a result of an adaptive optimization but has been intentionally designed. The laser spectrum is split into a long wavelength (≥ 796 nm) and short wavelength part (< 796 nm), which are shaped independently. By application of a phase difference $\Phi(t) = \pi$ between the LCD layers of the polarization pulse shaper the red spectral components are set to linear polarization in vertical (y) direction, which is perpendicular to the plane of incidence. A phase difference of $\Phi(t) = 0$ for the short wavelength components generates linear polarization along the horizontal plane defined by x and z . The directions are defined according to Fig. 1.17. Additionally to creating perpendicular polarization states, the red and blue subpulses are separated by 200 fs by a different choice of the respective linear spectral phases. The shaped pulses are characterized via dual-channel spectral interferometry using an independently determined reference pulse. The quasi-3D-representation illustrates that the pump pulse consists, as intended, of two parts with perpendicular polarizations. The preceding s-polarized pump subpulse is mainly exciting the local dipoles in y -direction. The p-polarized subpulse exhibits a field component with electric field along the x -direction (see Fig. 1.17). Thus, different local dipoles in the sun-shaped nanostructure are addressed. The fluence (see Eq. (1.16)) of the pump-pulse is $F_{pump} = 30 \text{ nJ cm}^{-2}$.

The probe pulse is a bandwidth-limited laser pulse with circular polarization with comparatively low fluence ($F_{probe} = 3 \text{ nJ cm}^{-2}$). A circularly polarized pulse is chosen to avoid effects of a

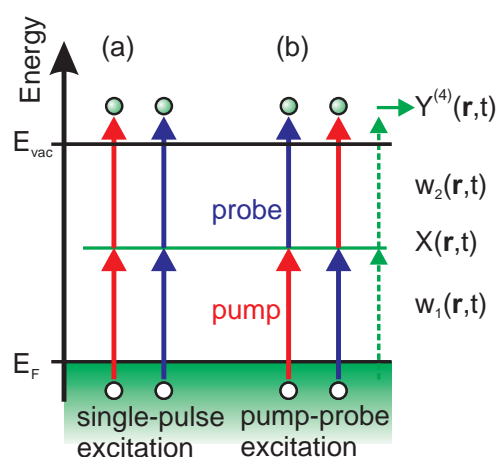


Figure 3.2: Excitation scheme for two-photon photoemission with single-color pump and probe pulses. (a) By single pulse excitation the photoemission is created only by interaction of electrons with single pump (red) or probe (blue) pulses. (b) In the temporal overlap of both pulses an additional excitation pathway occurs. Electrons are excited into intermediate states by either the pump or the probe pulse and are transferred into continuum states above the vacuum energy by the remaining pulse. This mixed-pulse excitation is delay-dependent. Local excitation rates $w_1(\mathbf{r}, t)$ and $w_2(\mathbf{r}, t)$ denote the probability of electron excitation into the intermediate-state population $X(\mathbf{r}, t)$ and into continuum states above E_{vac} leading to the photoemission signal $Y^{(4)}(\mathbf{r}, t)$.

preferential polarization direction. By scanning the delay τ between both pulses spatially and simultaneously temporally resolved cross-correlation measurements of the nanooptical excitation pattern are performed. Optical interference between pump and probe pulses is averaged out by a fast dither ($\pm 2\text{fs}$) of the temporal delay using a piezo-driven delay stage. For varying τ photoemission patterns are detected by the photoemission electron microscope. Doping with Cs reduced the work function $E_W = E_{vac} - E_F$ of the silver sample below the threshold for two-photon photoemission. As the polarization state and the momentary frequency do not change during the probe pulse, the photoemission distribution is expected to vary in the total yield but to be stationary in its shape. Hence, delay-dependent variations of the photoemission yield are associated with the temporal evolution of the local excitation created by the polarization-shaped pump pulse. Long-term drifts of the sample positions are canceled by the drift correction scheme explained in Appendix B with the probe pulse creating the reference signal.

The ultrafast spatial-resolved detection of the localized optical near-fields in a pump-probe scheme necessarily requires that the local photoemission signal changes with the delay of the second pulse. In Figure 3.2 the delay-dependent contributions to the photoemission are identified. If both pulses have a large temporal separation, only the single pulse excitation processes create a delay-independent background signal (see Fig. 3.2a). In or close to the pulse overlap additional photoemission pathways involving the interaction with the electric fields of both pulses are possible (see Fig. 3.2b). For these mixed-pulse excitations either the pump or the probe pulse is responsible for creating a population in the intermediate states, which is then photoexcited by the remaining pulse. As the population in intermediate electronic states in metals decays rapidly, it closely follows the evolution of the local electric field of the pulses. Accordingly, the strength of the final excitation step is dependent on the delay between the pulses.

In the following a mathematical description of the photoemission yield associated with the excitation by pump and probe pulse is derived [2]. The excitation of electrons in the metal nanostructure by the local field is most generally described by a sum over scalar products between the local field and the local transition dipole moments. The local electric field in time domain $\mathbf{E}_{loc}(\mathbf{r}, t)$ is defined according to the derivations in Chapter 1.3 and will be abbreviated by $\mathbf{E}(\mathbf{r}, t)$. A full quantum-mechanical treatment of the optical excitation of electronic population would require an individual dipole moment with a particular magnitude and orientation for every possible combination of initial and final states. However, it is assumed in an approximate treatment that

the excitation into the intermediate state as well as the excitation into the continuum state can be represented each by one dominating local dipole moment \mathbf{p}_1 and \mathbf{p}_2 , respectively. Then, the local excitation rates $w_1(\mathbf{r}, t)$ and $w_2(\mathbf{r}, t)$ are given by

$$w_j(\mathbf{r}, t) = a |\mathbf{p}_j \mathbf{E}(\mathbf{r}, t)|^2 = a p_j^2 E_j^+(\mathbf{r}, t) E_j^-(\mathbf{r}, t) \quad (3.1)$$

where $E_j^\pm(\mathbf{r}, t)$ denotes the projection of the local electric field onto the j -th local dipole moment \mathbf{p}_j in the complex field representation discussed in Chapter 1.1. The proportionality factor a is omitted in the following. The local electric field already includes the effects of the nanoscopic environment. Implicitly, the local response function for all polarization components is evaluated leading to phenomena like local mode interference and local pulse compression as discussed in Chapter 1.3.5.

Since metals provide a continuum of intermediate states, electronic coherences are considered to be extremely short-lived [223, 224, 227]. In an approximative treatment the dephasing is considered to be instantaneous [227]. The temporal evolution of the intermediate-state population $X(\mathbf{r}, t)$ is then described by the convolution of the local excitation rate $w_1(\mathbf{r}, t)$ with the electronic relaxation function $R(\mathbf{r}, t)$.

$$X(\mathbf{r}, t) = \int_{-\infty}^{\infty} w_1(\mathbf{r}, t') R(\mathbf{r}, t - t') dt' = p_1^2 [E_1^+(\mathbf{r}, t) E_1^-(\mathbf{r}, t)] \circ R(\mathbf{r}, t) \quad (3.2)$$

The open circle represents the convolution. The electronic relaxation from the intermediate state $R(\mathbf{r}, t - t')$ is a local property of the system and depends explicitly on the spatial coordinate. Spatial transport of electronic population in the intermediate state would lead to a nonlocal relaxation behavior, i.e. the population history in adjacent locations influences the relaxation process at position \mathbf{r} . In a simple approach the relaxation is treated as a one-sided exponential decay with a typical time constant given by the energy relaxation lifetime of the intermediate state.

To establish a time-resolved two-photon photoemission experiment, the intermediate-state population is probed by an additional excitation pulse into continuum states above the vacuum energy creating a photoelectron emission $Y^{(4)}(\mathbf{r})$ from the surface. This second excitation step is given by the time-integrated product of intermediate-state population $X(\mathbf{r}, t)$ (Eq. (3.2)) and photoemission excitation rate $w_2(\mathbf{r}, t)$ for the intermediate state.

$$\begin{aligned} Y^{(4)}(\mathbf{r}) &= \int_{-\infty}^{\infty} X(\mathbf{r}, t) p_2^2 [E_2^+(\mathbf{r}, t) E_2^-(\mathbf{r}, t)] dt \\ &= \int_{-\infty}^{\infty} \{ p_1^2 [E_1^+(\mathbf{r}, t) E_1^-(\mathbf{r}, t)] \circ R(\mathbf{r}, t) \} p_2^2 [E_2^+(\mathbf{r}, t) E_2^-(\mathbf{r}, t)] dt \end{aligned} \quad (3.3)$$

Here, the subscript $i = 1, 2$ identifies the excitation step. In order to describe a two-pulse experiment the local electric field is written as a superposition $\mathbf{E}(\mathbf{r}, t) = \mathbf{E}_\alpha(\mathbf{r}, t) + \mathbf{E}_\beta(\mathbf{r}, t - \tau)$ of the local fields excited by the pump and probe pulse labeled by the additional indices α and β , respectively. The temporal delay τ between the pulses is associated with the temporal position of the maxima of the pulse envelopes, but in principle $\mathbf{E}_\alpha(\mathbf{r}, t)$ and $\mathbf{E}_\beta(\mathbf{r}, t - \tau)$ might have

arbitrary shapes. In the experimental scheme presented in this chapter the pump pulse consists of a series of pulses with varying polarization states and the probe pulse is a transform limited pulse. As a result of the superposition, the local photoemission is expressed in the form of a local cross-correlation signal

$$\begin{aligned}
Y^{(4)}(\mathbf{r}, \tau) &= \int_{-\infty}^{\infty} \left\{ p_1^2 \left[\left(E_{\alpha,1}^+(\mathbf{r}, t) + E_{\beta,1}^+(\mathbf{r}, t - \tau) \right) \left(E_{\alpha,1}^-(\mathbf{r}, t) + E_{\beta,1}^-(\mathbf{r}, t - \tau) \right) \right] \circ R(\mathbf{r}, t) \right\} \\
&\quad p_2^2 \left[\left(E_{\alpha,2}^+(\mathbf{r}, t) + E_{\beta,2}^+(\mathbf{r}, t - \tau) \right) \left(E_{\alpha,2}^-(\mathbf{r}, t) + E_{\beta,2}^-(\mathbf{r}, t - \tau) \right) \right] dt \\
&= p_1^2 p_2^2 \int_{-\infty}^{\infty} \int_{-\infty}^{\infty} R(\mathbf{r}, t - t') F(\mathbf{r}, t, t', \tau) dt' dt .
\end{aligned} \tag{3.4}$$

To simplify the following derivations the commutativity of the convolution was exploited so that the relaxation function $R(\mathbf{r}, t - t')$ now depends of $t - t'$ before integration. In the two-dimensional integral the product of the electric fields is represented by $F(\mathbf{r}, t, t', \tau)$ which sums up all the terms that result from the multiplication. Details of $F(\mathbf{r}, t, t', \tau)$ are discussed in the Appendix C. Most of the terms of $F(\mathbf{r}, t, t', \tau)$ are neglected because of the fast dither of ± 2 fs introduced between the pump pulse and probe pulse. The local photoemission is then given by a delay-independent photoemission background term $Y_{stat}^{(4)}(\mathbf{r})$ and two contributions $Y_{seq}^{(4)}(\mathbf{r}, \tau)$ and $Y_{coh}^{(4)}$ which contain temporal information:

$$Y^{(4)}(\mathbf{r}, \tau) = Y_{stat}^{(4)}(\mathbf{r}) + Y_{seq}^{(4)}(\mathbf{r}, \tau) + Y_{coh}^{(4)}(\mathbf{r}, \tau) . \tag{3.5}$$

The term $Y_{stat}^{(4)}(\mathbf{r})$ describes those photoemission processes which are driven exclusively either by the pump pulse or the probe pulse and, therefore, do not depend on the delay between both pulses. A sequential excitation in which one pulse is responsible for creating the population in the intermediate state and the other pulse excites electrons from the intermediate states into the continuum above the vacuum energy is denoted as $Y_{seq}^{(4)}(\mathbf{r}, \tau)$. In the excitation process responsible for the last term $Y_{coh}^{(4)}(\mathbf{r}, \tau)$ each excitation step contains an interaction with the electric fields of pump and probe pulse.

A further assumption helps simplifying the cross-correlation signal. The energy relaxation lifetime of polycrystalline silver films is estimated to be about 10 fs for intermediate state electrons 1.5 eV above the Fermi energy [224]. This is considerably below the temporal resolution of the experiment of about 40 fs, which is mainly determined by the duration of the probe pulse (see Fig. 3.1). Thus, $R(\mathbf{r}, t - t')$ is approximated by the Dirac delta function in time domain $\delta(t)$. The time-invariant contribution to the cross-correlation signal is then given by

$$Y_{stat}^{(4)}(\mathbf{r}) = p_1^2(\mathbf{r}) p_2^2(\mathbf{r}) \int_{-\infty}^{\infty} I_{\alpha,1}(\mathbf{r}, t) I_{\alpha,2}(\mathbf{r}, t) + I_{\beta,1}(\mathbf{r}, t) I_{\beta,2}(\mathbf{r}, t) dt , \tag{3.6}$$

where the intensities are calculated via $I_{i,j}(\mathbf{r}, t) = E_{i,j}^+(\mathbf{r}, t - \tau) E_{i,j}^-(\mathbf{r}, t)$.

$$Y_{seq}^{(4)}(\mathbf{r}, \tau) = p_1^2(\mathbf{r})p_2^2(\mathbf{r}) \int_{-\infty}^{\infty} I_{\alpha,1}(\mathbf{r}, t)I_{\beta,2}(\mathbf{r}, t - \tau) + I_{\beta,1}(\mathbf{r}, t - \tau)I_{\alpha,2}(\mathbf{r}, t) dt \quad (3.7)$$

$$Y_{coh}^{(4)}(\mathbf{r}, \tau) = p_1^2(\mathbf{r})p_2^2(\mathbf{r}) \int_{-\infty}^{\infty} E_{\alpha,1}^+(\mathbf{r}, t)E_{\beta,1}^-(\mathbf{r}, t - \tau)E_{\beta,2}^+(\mathbf{r}, t - \tau)E_{\alpha,2}^-(\mathbf{r}, t) \\ + E_{\beta,1}^+(\mathbf{r}, t - \tau)E_{\alpha,1}^-(\mathbf{r}, t)E_{\alpha,2}^+(\mathbf{r}, t)E_{\beta,2}^-(\mathbf{r}, t - \tau) dt \quad (3.8)$$

If the excitation dipoles $\mathbf{p}_1^2(\mathbf{r})$ $\mathbf{p}_2^2(\mathbf{r})$ are oriented parallel the electric fields $E_{j,1}$ and $E_{j,2}$ become equal, which causes $Y_{seq}^{(4)}(\mathbf{r}, \tau)$ and $Y_{coh}^{(4)}(\mathbf{r}, \tau)$ to be identical. This assumption is motivated by the polycrystalline material. With

$$Y^{(4)}(\mathbf{r}, \tau) = p_1^2(\mathbf{r})p_2^2(\mathbf{r}) \int_{-\infty}^{\infty} I_{\alpha}^2(\mathbf{r}, t) + I_{\beta}^2(\mathbf{r}, t) + 4I_{\alpha}(\mathbf{r}, t)I_{\beta}(\mathbf{r}, t - \tau) dt \quad (3.9)$$

the obtained photoemission signal acts analog to an intensity correlation between two ultrashort laser pulses. However, the photoemission yield is a local quantity and strongly connected to near-field interference and the local response at the investigated position \mathbf{r} .

Ultimately, for probe pulses with durations in the few cycle regime, which approach the electronic relaxation time, also the probe pulse is treated as an infinitesimally short excitation. Then, for the delay-dependent contribution to the cross-correlation simply follows

$$Y^{(4)}(\mathbf{r}, \tau) \propto 4p_1^2(\mathbf{r})p_2^2(\mathbf{r})I_{\alpha}(\mathbf{r}, \tau). \quad (3.10)$$

The cross-correlation signal now is proportional to the intensity of the local electric field of the pump pulse projected onto the dipole moments $p_1(\mathbf{r})$ and $p_2(\mathbf{r})$ of the excitation. However, in the experiment discussed here the pulse length of the probe pulse is considerably larger. The fast dither which cancels out the coherence between pump and probe beam, causes an additional uncertainty in the relative delay of approximately ± 2 fs which is negligible.

3.2. Experimental Setup and Sample Characterization

The experimental setup for demonstration of spatial and temporal control of nanooptical excitations is in most components identical to the setup described in the previous chapter (see Fig. 2.4). Differences occur in the probe pulse arm, which does not involve a SHG process. Accordingly both pulses have center frequencies of 798 nm. By a quarter-wave plate in the probe arm, the polarization of the probe pulse is adjusted to a circular polarization state. A fast dither of ± 2 fs is introduced by driven mechanical oscillations at a folding mirror. The fluences of pump (30 nJ cm^{-2}) and probe pulse (3 nJ cm^{-2}) are chosen to yield a strong pump-probe effect of about the same magnitude as the background emission.

The specific shape of the pump pulse (see Fig. 3.1) is realized by employing two almost perpendicularly oriented subpulses. In previously performed test measurements indeed a strong dependence

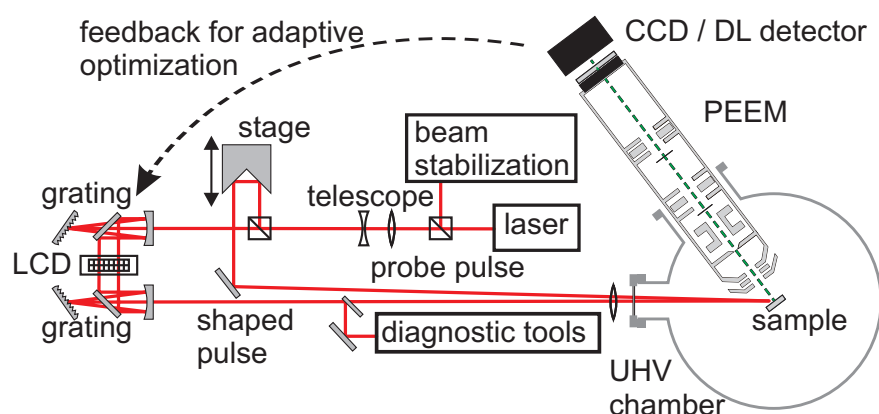


Figure 3.3.: Experimental setup for demonstration of spatial and temporal control of nano-optical excitations. The laser system and the pump arm is identical to the experiments presented in Chapter 2 (see Fig. 2.4). The transform-limited probe pulse is set to circular polarization by a quarter-wave plate (not shown), but remains at 798 nm center wavelength.

of the local photoemission distribution from the polarization state was observed. Additionally, the analytic solutions for optimal near-field control of plasmonic nanostructures derived in [87] demonstrated that strong spatial contrast of near-field excitations are achieved for a shift of the relative phase difference of π between the two polarization components. In the pump pulse this control rule is followed by applying a phase difference of π at the two LCD layers for the red spectral components and identical phases for the blue part of the spectrum. If the difference in the center frequencies of the subpulses is small compared to the nanostructure response, the excitation patterns created by the subpulses are expected to exhibit strong differences. Thus, the control rule which has been tested for adaptively optimized pulse in the previous chapter, is used for pulse shapes with a priori unknown local excitation.

The investigated sample is an array of sun-shaped silver nanostructures on an indium tin oxide layer on glass. Figure 3.4a shows a scanning electron microscope (SEM) image of such a nanostructure. It has a height of 40 nm and a varying arm length from 115 nm to 225 nm. The circular disc in the center has a diameter of 200 nm. One of the structures is selected for the following experiments. In the one-photon PEEM image (Fig. 3.4b) obtained for illumination with incoherent ultraviolet light the geometry of the selected nanostructure is visible. To achieve two-photon photoemission with near-infrared laser pulses, the surface of the sample has been dosed with Cs to reduce the work function just below the two-photon photoemission threshold. The two-photon photoemission distributions generated in a single pulse excitation process of pump pulse (Fig. 3.4c) and probe pulse (Fig. 3.4d) are very similar. During the acquisition the other beam was blocked. The sum of these signals reflects the time-independent background $Y_{stat}^{(4)}(\mathbf{r})$ Eq. (3.6) and is measured separately for each delay step and subtracted from the time-resolved PEEM patterns. Saturation effects in the two-photon photoemission process are excluded because the experiment is performed in the limit of weak excitations for the given fluences. Even taking into account field enhancement effects the fraction of excited electrons remains below 10^{-3} . The strong likeness of the photoemission patterns of the single pulses could not be expected a priori as the pump and probe pulses differ significantly in several properties. Whereas the probe pulse is transform-limited and with a constant polarization state, the pump pulse is much more complex featuring a temporal separation of the polarization components by

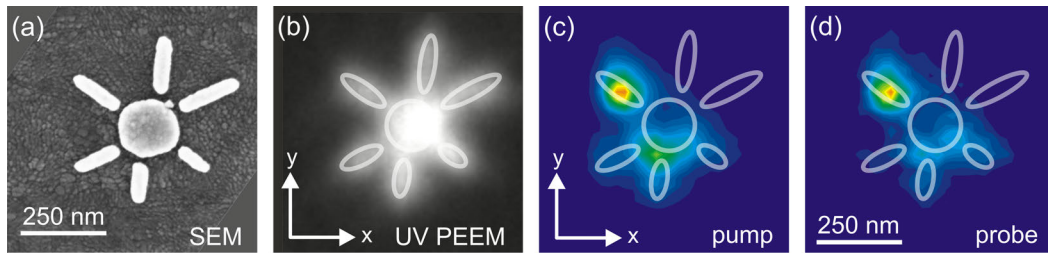


Figure 3.4.: Characterization of sun-shaped Ag nanostructure with SEM, i.e. scanning electron microscopy, (a), one-photon photoemission upon incoherent UV illumination (b) and two-photon photoemission for excitation with pump (c) and probe (d) pulse. (a) The structure consists of a circular disk 200 nm in diameter surrounded by six arms with lengths increasing clockwise from 115 nm to 225 nm starting with the arm pointing towards the lower right corner of the image. (b) With one-photon PEEM the basic structural properties of the nanosun are visible. Minor deviations from the intended design cannot be resolved. (c) The time-integrated photoemission background pattern of the probe pulse has two major regions of high photoemission located below the circular disk and at the upper left arm. In the latter case the maximum yield is obtained in the middle of the silver rod and not in the gap region where the highest yield is expected. (d) The pump pulse creates a local excitation similar to the probe pulse, but has in comparison smaller yield in the lower gap region. Adapted from [2].

approximately 200 fs. Furthermore, the subpulses are detuned in their center frequencies. Still, a good accordance in the time-integrated photoemission distributions was observed.

3.3. Ultrafast Nanoscale Excitation Switching

To resolve the evolution of the local excitation generated by the polarization-shaped pump pulse as depicted in Fig. 3.1 the cross-correlation measurements were performed with delay step sizes of 10 fs. This is well below the temporal resolution of the method which is mainly determined by the temporal width of the probe pulse (40 fs) according to Eq. (3.9).

Figure 3.5 presents the results of the cross-correlation measurement after subtraction of the delay-invariant photoemission background. Contour plots of the emission patterns for delays $\tau = 13$ fs (a) and $\tau = 213$ fs (b) are shown. The photoemission distributions display striking differences. The local excitation generated by the s-polarized subpulse ($\tau = 13$ fs) has a clear maximum in the dashed green ROI1 located below, i.e. shifted in negative y-direction, the circular central disk. Obviously, the s polarization couples effectively to the lower part of the nanostructure. The interplay of the vertically oriented arm and the disk enables a strong field in the gap region. The excitation by the first subpulse of ROI2 (red) is comparatively low. Within 200 fs the situation has changed drastically. In the second subpulse p polarization is dominant causing a strong localization of electric fields in ROI2, which lies on the upper left arm of the structure. In ROI1 (green) only low photoemission is observed. The yield within the gap region between lower arm and disk is smaller than in the vicinity. The specific shape of the emission pattern cannot be explained only by the momentary polarization state, because the orientations of three additional arms equally match the projection of the polarized field component onto the sample surface. However, local structural properties in ROI2 might cause the excitation dipole moment to be considerably increased.

Still, besides the momentary polarization of the incident radiation, other control mechanisms, such

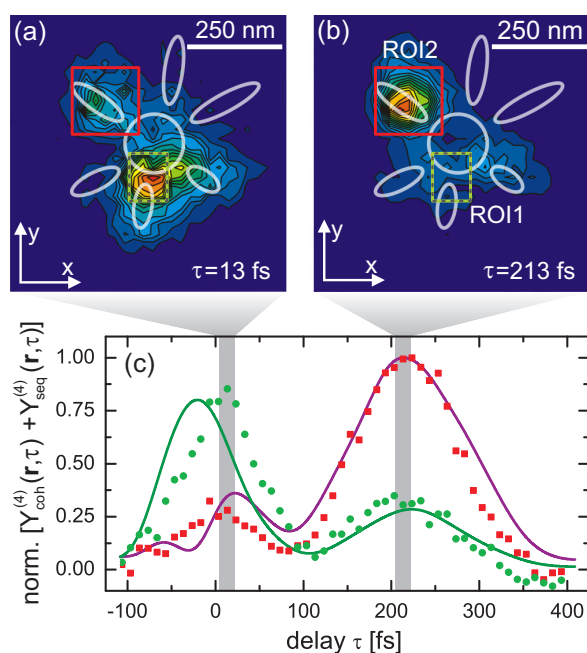


Figure 3.5: Ultrafast excitation switching at silver nanostructure. (a,b) Normalized photoemission patterns after subtraction of the delay-independent background signal at delays $\tau = 13$ fs (a) and $\tau = 213$ fs (b). The regions of interest for the delay-dependent signals are indicated as dashed green (ROI1) and solid red (ROI2) rectangles in relation to the nanostructure (gray outlines). (c) Delay-dependent cross-correlation from ROI1 (green) and ROI 2 (red) as defined in (a) and (b). The photoemission strength is normalized to the maximum value of the average number of counts per CCD pixel in the ROI. Simulations of the local cross-correlation are indicated as olive and purple line for ROI1 and ROI2, respectively. The simulations are based on the measured temporal field intensities inserted into Eq. (3.9).

as spectral sensitivity of the local excitation and local field compression (see Chapter 1.3.5), might influence the spatiotemporal evolution of the excited-electron distribution. However, selective excitation of the ROIs by the different spectral positions of the two pump subpulses is excluded because each spectral component of the pump pulse shows the same spatial switching behavior if the polarization is changed from TM to TE. Furthermore, the spatial switching is achieved for flat spectral phases ruling out local field compression mechanisms for spatial selectivity. Hence, the polarization degree of freedom is responsible for the distribution of the local excitation.

The averaged yield in the ROIs during the cross-correlation measurement is depicted in Figure 3.5c normalized to its maximum value. ROI1 is represented by green dots and ROI2 by red dots. The temporal position of the snapshots shown in 3.5a and b are indicated by gray bars. The width of these bars was chosen for a good visibility and should not be confused with the spatial resolution of the method. The olive and purple lines are simulated cross-correlations based on the temporal field intensities of both polarization components determined with dual-channel spectral interferometry. In the overlap of the probe pulse with the s-polarized pump subpulse at zero delay an enhancement of the signal in ROI1 is observed with respect to ROI2. The signal strength changes with the intensity in the subpulse and has its maximum around $\tau = 0$ fs, but the ratio between the regions of interest remains stationary. Similarly, during the p-polarized excitation pulse a stationary emission pattern was observed which is localized in ROI2.

Under the assumption that the local near-field response in the ROIs is dominated by a dipolar coupling to the far-field modes the local excitation is calculated from the temporal electric fields of the pulses. The intensities of both polarization components are inserted independently into Eq. (3.9). Then for each polarization component the weights of the contribution to the simulated yield in ROI1 and ROI2 are adjusted to get a combined signal which reflects the measured cross-correlation. Interestingly, this is only achieved if the s component has a reducing impact on the photoemission in ROI2 during the first subpulse, because the yield expected from the p polarization direction already exceeds the measured values, when the weight of this component is

gauged at the yield during the second pulse. This emphasizes the dependence of the excitation pattern on the complete polarization state.

3.4. Conclusion

In this chapter spatiotemporal control of optical near-field distributions excited with polarization-shaped light pulses has been demonstrated. The evolution of the local optical near-field generated by a polarization-shaped pump pulse has been detected in an incoherent two-photon photoemission cross-correlation experiment using a bandwidth-limited circular probe pulse. In a theoretical treatment under the assumption of fast dephasing and short excited-electron lifetime it has been shown that the delay-dependent signals $Y_{seq}^{(4)}(\mathbf{r}, \tau)$ and $Y_{coh}^{(4)}(\mathbf{r}, \tau)$ are proportional to the local electric field intensity of the pump pulse. As it was further demonstrated in [2] this technique enables the investigation of more complex pulse shapes e.g. for pulse shapes found in adaptive optimizations. Furthermore, those coherent control experiments were performed for optimizations goals including the spatial and temporal properties of the local excitation of the nanostructure. In principle, also a two-photon two-color experiment as presented in the previous chapter might provide similar information without the necessity to cancel coherences with fast mechanical oscillations in the probe arm and to reduce the work function E_W by deposition of Cs. However, since the investigated structure has very small feature sized also for a frequency-doubled probe pulse localized resonances of the nanostructure are expected. Thus, they would create an inhomogeneous excitation pattern which might even be stronger localized compared to fundamental excitation due to the smaller wavelength.

The feasibility of spatiotemporal excitation control as demonstrated experimentally enables the development of new techniques for studying electronic relaxation and transport within nanostructures. Instead of probing quantum systems with a far-field focus, nanostructures can be employed as tailored antennas to couple light energy into systems located in their vicinity. By separating pump and probe interactions on time and length scales relevant for a nanosystem the excitation scheme of the proposed nanoscopic ultrafast space-time-resolved spectroscopy [85] is realized. In a future experiment this technique will enable to investigate transport processes in novel plasmonic devices such as plasmonic waveguides or in thin layers molecular layers, e.g. J-aggregates [272–276], directly in time and space.

4. Principles of Coherent 2D Nanoscopy

Coherent 2D nanoscopy combines time-resolved photoemission microscopy with two-dimensional optical spectroscopy. The basic concepts of TR-PEEM have been discussed in Section 1.4. In Section 3 the ultrafast switching of electronic excitation at a nanostructure was demonstrated in an incoherent TR-PEEM experiment which resolved lateral changes with sub-diffraction resolution and simultaneously on femtosecond time scale. Coherent 2D nanoscopy gives access to spectroscopic information by analyzing the local photoemission yield excited by laser pulse sequences with controlled relative delays and relative phases between the subpulses. The excitation scheme of coherent two-dimensional nanoscopy is based on coherent optical two-dimensional spectroscopy (Appendix D) though comprising some modifications that are explained in Section 4.2. The newly developed coherent 2D nanoscopy technique will be demonstrated in experiments in Chapter 5 and 6.

Basic ideas of 2D nanoscopy were introduced by Tobias Brixner and further developed in a joint effort [4]. A description of 2D nanoscopy in Liouville space has been published by Philip Tuchscherer [126]. The extension of the 2D nanoscopy to investigate the local electric field in fast dephasing systems, the Fourier-transform simulations of 2D nanoscopy spectra and the fit routine for fast data evaluation which are discussed in this chapter are based on my work.

4.1. Bringing Nonlinear Spectroscopy to the Nanoscale

Optical coherent two-dimensional (2D) spectroscopy is a nonlinear spectroscopy technique [15, 47, 50]. Thus, it probes higher order contributions to the polarization $\mathbf{P}(t)$. There are various other optical nonlinear spectroscopy methods e.g. pump-probe transient absorption spectroscopy [277], coherent Anti-Raman spectroscopy (CARS) [278–280] and nonlinear fluorescence spectroscopy [15]. They all have in common that optical waves are used as input inducing oscillations of the polarization. The output signal is again optical and contains information on the nonlinear optical response of the sample. An expanded version of Eq. (1.20) relates the total polarization, i.e. linear and nonlinear, contributions as

$$\mathbf{P}(t) = \sum_n \mathbf{P}^{(n)}(t) = \varepsilon_0 \left\{ \sum_n \chi^{(n)} \mathbf{E}^n(t) \right\}. \quad (4.1)$$

The coefficients $\chi^{(n)}$ are the n -th order susceptibilities of the medium. In general these susceptibilities are tensorial quantities. In the limit of weak electric fields $\mathbf{E}(t)$ only the linear term has a relevant influence on the total polarization and higher-order terms are not accessible by spectroscopic means. Thus, nonlinear optical spectroscopy benefits from the ongoing improvement of laser systems providing ultrashort laser pulses. The increase of spectral bandwidth and peak intensity while reducing the pulse duration enables the investigation of higher-order contributions to the polarization [10, 15].

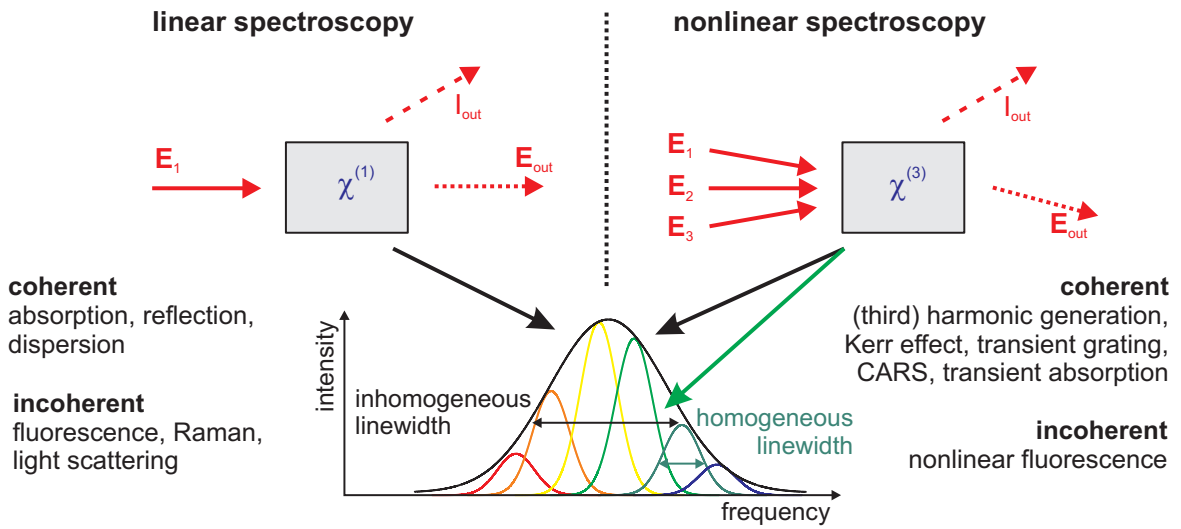


Figure 4.1.: Comparison of linear optical spectroscopy and nonlinear optical spectroscopy. Linear optical spectroscopy probes the linear polarization of a sample. The polarization is connected with the incoming field \mathbf{E}_1 via the linear susceptibility $\chi^{(1)}$. Coherent output is given by reflected and transmitted electric field \mathbf{E}_{out} at the input frequency. Detection of incoherent signal intensities I_{out} e.g. fluorescence and phosphorescence yield also provide information on the linear polarization. Nonlinear optical spectroscopy probes higher order terms of the polarization. Here, the example of the third-order susceptibility $\chi^{(3)}$ is used. The coherent nonlinear spectroscopy techniques like CARS, optical 2D spectroscopy and transient absorption use three input electric fields \mathbf{E}_1 , \mathbf{E}_2 , \mathbf{E}_3 and detect an outgoing signal \mathbf{E}_{out} . The wavevector and frequency of the output signal is determined by the type of four-wave mixing process that is investigated. Incoherent detection is used in case of nonlinear fluorescence [15]. Coherently detected signals are given by third harmonic generation, Kerr effect, saturable absorption and various other nonlinear effects [15, 281]. Whereas with linear spectroscopy only the inhomogeneous linewidth (black solid line in lower graph) is accessible, nonlinear spectroscopy techniques, e.g. optical 2D spectroscopy, are able to resolve the homogeneous linewidth characterizing the dephasing of the individual quantum systems (colored solid lines) within the investigated volume.

Figure 4.1 presents a schematic comparison of linear optical spectroscopy and nonlinear optical spectroscopy with an emphasis on the observable spectral lineshape of a resonance peak. In coherent linear spectroscopy the examined signal is either a transmitted or a reflected optical wave from the investigated sample. The signal has the identical frequency as the input electric field, but acquired a change of phase and amplitude through the interaction with the medium. These changes are directly connected to the linear susceptibility $\chi^{(1)}$ of the material which determines the linear dielectric tensor $\varepsilon_r(\omega)$. Linear spectroscopy can also be performed incoherently e.g. by measuring the intensity of spontaneous fluorescence process after the absorption of a photon. Linear spectroscopy measures the inhomogeneous linewidth of spectral resonances, which can be considerably broadened compared to the homogeneous linewidth characterizing the dephasing time of a single quantum system in the investigated volume. Inhomogeneous broadening takes place in the investigation of many particle systems or quantum systems in fluctuating environmental conditions [281]. Then, the center frequencies of the individual quantum systems are not identical but distributed along the spectral axis.

Nonlinear optical spectroscopy involves the multiple interaction of coherent radiation with the material. The second-order polarization leads to sum frequency generation, with the special

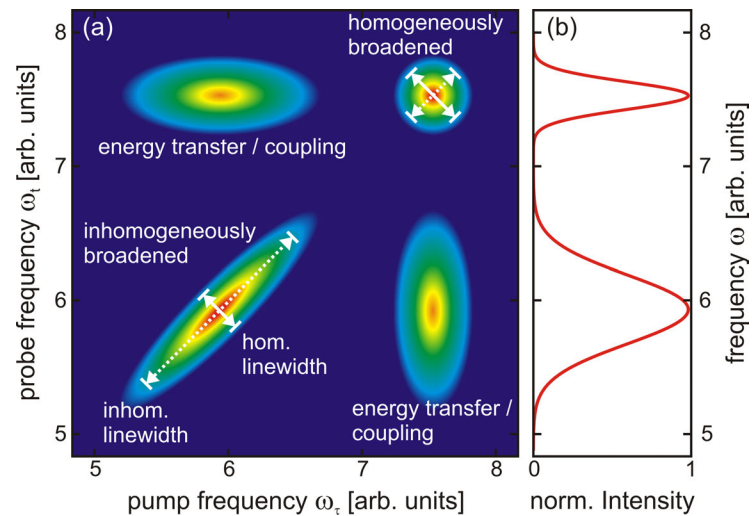
case of second harmonic generation (SHG), and difference frequency generation (DFG), which is employed for example in optical parametric amplification [108]. In most materials $\chi^{(2)}$ is negligible as it requires a broken inversion symmetry of the electronic potential. However, in nanostructured systems the interfaces of the structures break the inversion symmetry and $\chi^{(2)}$ is rather strong. Thus, SHG from nanoparticles has been of interest for investigating plasmonic lifetimes for the last 15 years [282–287]. The third-order polarization is connected to an even wider range of phenomena [15, 108, 280]. The coherent third-order interactions can all be described in terms of four-wave mixing (FWM). The fourth wave in the $\chi^{(3)}$ -process is the optical signal that is emitted by the induced polarization $\mathbf{P}^{(3)}$. The wavevector and frequency of the emitted signal \mathbf{E}_{out} depend on the type of FWM process and follow the phase matching and energy conservation condition. Several nonlinear optical spectroscopy experiments are particularly designed to resolve or at least approach the homogeneous linewidth e.g. saturation and spectral hole burning spectroscopy [281, 288–290]. With optical coherent 2D spectroscopy a more general spectroscopic scheme is used that even enables the full retrieval of the susceptibilities $\chi^{(n)}$ up to the third order [15, 45, 47, 50].

Optical coherent 2D Spectroscopy is based on concepts originating from nuclear magnetic resonance spectroscopy (NMR) [51, 291–294]. The spectroscopic signal is generated by driving a quantum system with a series of electric field pulses into a coherent state associated with an oscillating polarization which decays via the coherent emission of a photon. The radiation is detected by means that allow the reconstruction of the electric field. In NMR this is achieved in time domain as the excitation and detection frequencies are in the MHz regime and well accessible by electronic devices. NMR probes the precession of spins via the emitted magnetic field. The angular frequency of the precession is determined by the local magnetic field at the position of the quantum system. Thus, the chemical environment of the individual spin system is investigated. Besides spectroscopic applications also NMR tomography, a three dimensional image generating technique, has been demonstrated and is widely used in medical and technological applications [295].

Optical coherent spectroscopy uses light pulses ranging from the infrared to UV to access those electronic states of molecules in which electronic coupling and transfer can play an important role. In the most general optical 2D spectroscopy scheme three ultrashort laser pulse are sent to the sample from three distinct directions represented by the wavevectors \mathbf{k}_1 , \mathbf{k}_2 and \mathbf{k}_3 . They create a third-order polarization via four-wave mixing leading to the emission of an optical signal after a delay t with respect to the last of the excitation pulses. The signal is measured as function of the delays τ and T between the first and the second as well as the second and the third excitation pulse, respectively. By Fourier transformation of the delays τ and t the obtained signal is represented in two-dimensional frequency space with axes labeled ω_τ and ω_t . By selection of the wavevector \mathbf{k}_{out} the particular phase matching condition of the investigated four-wave mixing process is employed to separate the outgoing signal from other contributions that correspond to different $\chi^{(3)}$ -processes. The detection of the signal is performed in spectral domain and the electric field reconstruction is achieved via spectral interferometry with a reference pulse (Appendix A). A further discussion of the experimental realization of two-dimensional optical spectroscopy is presented in Appendix D.4.

Two-dimensional spectroscopy is advantageous compared to linear spectroscopy techniques as spectral information that overlaps in a linear spectrum is separated in a two-dimensional repre-

Figure 4.2: Comparison between optical 2D spectroscopy and linear spectroscopy signals. (a) Schematic of two-dimensional spectrum showing different phenomena visible in coherent optical 2D spectroscopy. Homogeneous and inhomogeneous linewidth differ in ensembles with quantum systems emitting at different frequencies. Energy and coherence transfer is visible as off-diagonal peaks. Adapted from [50]. (b) A linear spectrum of the identical system does not resolve coupling and shows inhomogeneously broadened spectral widths.



resentation. A schematic illustration of such a two-dimensional spectrum is shown in Figure 4.2. A basic interpretation of 2D spectra considers ω_τ as the pump frequency and ω_t as the probe frequency. In an ensemble of quantum systems with inhomogeneously broadened distribution of resonance frequencies each individual quantum system absorbs and reemits radiation according to its homogeneous linewidth and its individual resonance frequency. In a linear spectrum, which is accessible with a conventional optical spectrometer, the individual signals add up to an inhomogeneously broadened lineshape, whereas in two-dimensional spectroscopy the broadening is only visible on one of the diagonals, i.e. for equal pump and probe frequency. The emission of a signal with a probe frequency ω_t detuned from the pump frequency ω_τ is an indication for coupling and population transfer within the quantum system. Using femtosecond lasers pulses molecular coupling and transport phenomena are examined with sufficient bandwidth and temporal resolution. Transport phenomena of fundamental relevance in nature are for example the exciton-transport in light harvesting complexes of plants and bacteria, responsible for the high efficiency of the photosynthesis process of these organic molecule complexes [48]. Thus, with coherent optical 2D spectroscopy it is possible to investigate simultaneously the homogeneous and inhomogeneous linewidth of spectral resonances as well as a vast range of correlation phenomena in an ensemble of molecular systems.

The main differences in the excitation and detection scheme of coherent optical 2D spectroscopy and 2D nanoscopy are depicted in Figure 4.3 [4]. The input for optical 2D spectroscopy consists of three optical waves. In a four-wave mixing process via interactions with a multilevel system a coherent optical signal is generated which is fully characterized by means of optical spectroscopy, e.g. spectral interferometry with a reference pulse. Since the input and output signals are optical, the achievable spatial resolution is limited by diffraction. As the numerical aperture that is employed for focusing into the sample has to be small to distinguish excitation pathways via phase-matching, conventional optical 2D spectroscopy usually is performed with weakly focused beams. In contrast, 2D nanoscopy (see Fig. 4.3b) also uses optical waves as input but detects the local photoemission yield as the output signal using a PEEM. The photoemission yield is associated with the electronic population in the quantum system created via the interaction with the incident electric fields. The electric field $E_{2D}(t)$ consists of a sequence of four femtosecond

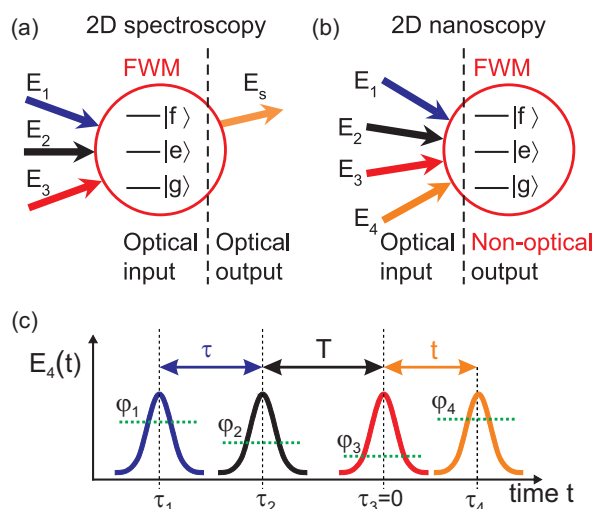


Figure 4.3: Comparison between coherent optical 2D spectroscopy and 2D nanoscopy. (a) Coherent 2D spectroscopy detects the outgoing optical signal E_S generated by four-wave mixing of three ingoing optical waves E_1 , E_2 and E_3 via interaction with an ensemble of quantum system. The subscripted numbers indicate time ordering. (b) In 2D nanoscopy four ingoing optical waves E_i ($i = 1, \dots, 4$) are used as input and the non-optical output is the resulting electronic population. (c) Excitation pulse sequence $E_{2D}(t)$ employed in 2D nanoscopy consisting of four femtosecond laser pulses at temporal positions τ_i . By varying the relative delays τ , T , and t and the phase offsets with respect to a common carrier oscillation φ_i spectroscopic information is retrieved from the generated local photoemission yield. Adapted from [4]

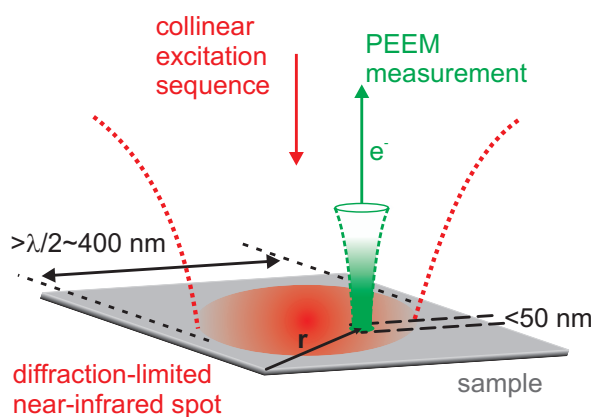
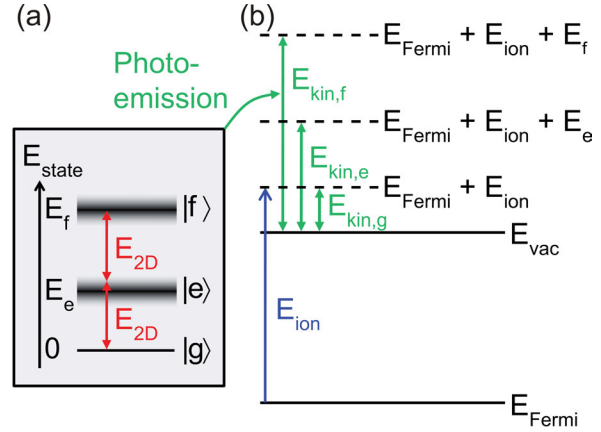


Figure 4.4: Schematic illustration of spatial resolution in 2D nanoscopy obtained with excitation pulse sequence and detected local photoemission yield. The diffraction-limited spot achievable by spatial focusing of far-field excitation pulses is indicated with red coloring. PEEM resolves local photoemission signal (green) at position \mathbf{r} with sub-50 nm lateral resolution. Adapted from [4]

subpulses ($i=1, \dots, 4$) at temporal positions τ_1 , τ_2 , τ_3 and τ_4 . The temporal separations between the pulses are labeled τ , T , and t and are varied independently (see Fig. 4.3c). Hence, the quantity t , which is in coherent optical 2D spectroscopy the time interval between the last pulse in the excitation sequence and the emitted optical signal, now denotes the temporal separation of the third and fourth excitation pulse. By convention, the absolute time is set to zero at the third pulse, i.e. $\tau_3 = 0$. Numerical Fourier transformation with respect to τ and t produces 2D spectroscopic information for a particular population time T . In contrast to conventional optical 2D spectroscopy the light pulses are collinear, i.e. they have identical wavevectors \mathbf{k}_i . Furthermore, the detected signal is incoherent. Therefore, phase matching cannot be used to select specific excitation pathways of the quantum system. This is compensated for in 2D nanoscopy by employing phase cycling [46, 49], which involves the systematic variation of the phases of the four subpulses denoted as φ_i . As it will be further explained in Section 4.2.4, the different signal contributions have, in analogy to the phase matching condition, individual dependences on the relative phases between the subpulses. These relative phases are labeled $\varphi_\tau = \varphi_2 - \varphi_1$, $\varphi_T = \varphi_3 - \varphi_2$, and $\varphi_t = \varphi_4 - \varphi_3$. A linear combination of the data obtained for different combinations of the relative phases enables to retrieve unambiguous spectral information [46, 49, 296].

Figure 4.5: 2D Nanoscopy excitation scheme for a quantum three-level system. (a) Excitation of a quantum three-level system by a laser pulse sequence $E_{2D}(t)$ generates populations of electrons or collective excitations, e.g. plasmons. (b) The photoelectrons which are emitted as a result of the excitation or by an additional ionizing pulse with photon energy E_{ion} exhibit the energy signature of the three level system. Adapted from [4].



In Figure 4.4 the spatial resolution of 2D nanoscopy is schematically presented. The collinear excitation pulse sequence (Fig. 4.4c) homogeneously excites the sample in the field of view of the photoemission electron microscope. The minimal focus spot size of a common optical microscope is indicated by a red area on the sample. The actual excitation spot size is considerably larger ($\approx 70 \mu\text{m}$). The resolution of PEEM is approximately 50 nm - clearly below the optical diffraction limit of the excitation pulses. The detected photoemitted electrons have a higher momentum as photons of the same kinetic energy E_{kin} . The wavelengths corresponding to a kinetic energy of $E_{kin} = 1 \text{ eV}$ are

$$\lambda_{ph} = \frac{hc}{E} \approx 1 \mu\text{m} \quad \text{and} \quad \lambda_e = \frac{h}{\sqrt{2m_e E}} \approx 1 \text{ nm} . \quad (4.2)$$

Thus, the photon wavelength λ_{ph} is three orders of magnitude larger than the electron wavelength λ_e . Accordingly, the resolution limit for photoelectrons given by diffraction is in the single nanometer regime, depending on the numerical aperture of the electron optic.

Figure 4.5 illustrates the excitation scheme of coherent 2D nanoscopy [4]. For a general representation Figure 4.5 is split into two parts. The left diagram describes the interaction of a quantum system with the excitation field E_{2D} . The quantum system corresponds either to phenomena of collective nature, such as surface plasmon polaritons in metallic systems or excitons in molecular aggregates, or to single-particle states, such as distinct transitions in the electronic band structure. The probe process (Fig. 4.5b) occurs via a single-particle state, i.e. the photoemission state. Because collective states cannot be represented on a single-particle energy scale, the quantum state preparation via the interaction with E_{2D} and the probe process are separated.

The investigated quantum system is treated in this schematic as a three-level system with a ground state $|g\rangle$, a first electronically excited state $|e\rangle$, and a second excited state $|f\rangle$. By interaction with the electric field E_{2D} of a four pulse sequence as depicted in Figure 4.3c transitions between the different levels are induced. As a result of the four-wave interaction, the system is driven into one of the population states $|g\rangle$, $|e\rangle$, or $|f\rangle$ which are probed via photoelectron emission and measured by photoemission electron microscopy (PEEM). If the energy of the quantum system $E_{state} = \{0, E_e, E_f\}$ is insufficient to create photoemission from states below the vacuum energy E_{vac} , an ionization laser can provide additional energy E_{ion} . Thereby, the photoelectrons emitted from an initial state at the Fermi level, E_{Fermi} , have a kinetic energy

above the vacuum level E_{vac} which are given as

$$E_{kin} = E_{Fermi} + E_{ion} + E_{state} - E_{vac} \quad (4.3)$$

In the diagram in Figure 4.5b the maximum photoelectron energies for given values of E_{ion} and E_{state} are presented as dashed lines. The photoemission yield is determined as a function of the delays τ , T , and t , and of the relative phases φ_τ , φ_T , and φ_t for a selected kinetic energy. The phase information is used for extracting signals of distinct excitation pathways utilizing a phase cycling routine (see Section 4.2.4).

The above discussion of 2D nanoscopy emphasizes that this spectroscopic technique monitors the influence of a multidimensional set of parameters on the electron emission yield. The more degrees of freedom have to be accessed, the more tedious are the involved data acquisition and evaluation processes. A helpful simplification is achieved by setting the delay T and relative phase φ_T between the second and third pulses to fixed values. A variation of these parameters enables to study for example the temporal dynamics of the population state in the quantum system, but it is not necessary for obtaining 2D spectral information. In the following simulations and experiments both parameters are set to zero effectively creating a pulse sequence consisting of three excitation pulses with delays τ and t and relative phases φ_τ and φ_t .

There are highly attractive quantum systems for the investigation by coherent two-dimensional nanoscopy for example quantum dots [297–301] and excitons in organic molecule systems, particularly J-aggregates [272–276] and Alq3 [302–306].

In quantum dots the confinement of electronic wave functions leads to a splitting of electronic energy levels. Quantum dots offer long coherence lifetimes and can be driven into Rabi-oscillations [73, 307, 308]. Quantum dots couple to other nanoscopic devices such as other quantum dots or nanowire and nanoantennas [309, 310]. 2D nanoscopy offers the possibility to investigate the energy and coherence transfer on the length scale of the interacting systems.

J-aggregates are formed by organic dye molecules by self-organization. These supramolecular systems show a strong absorption to optical radiation with narrow bandwidth compared to the monomer. The sharp resonance is connected to a delocalization of excitonic states in the J-aggregates. The exciton delocalization in thin J-aggregate films depends on several internal and environmental conditions that affect the homogeneous and inhomogeneous lineshape measured by optical 2D spectroscopy [276]. 2D nanoscopy provides the possibility to observe spectroscopic signatures of excitonic transfer and delocalization effects in molecular films directly in space. Also photosynthetic molecular aggregates exhibit ultrafast excitonic transfer processes on the nanoscale and a nonlinear spectroscopy method with high spatial resolution would be beneficial [311].

The abbreviation Alq3 (short for Tris(8-hydroxyquinolino)aluminum) denotes a chemical compound which is employed in organic light emitting diodes [302–305]. Recently, it has been demonstrated that thin Alq3 layers on cobalt form an unoccupied hybrid interface state (uHIS) which is accessible in multiphoton photoemission experiments [306]. These experiments showed a spin-dependent lifetime of the interface state of 0.5–1 ps. An investigation of the identical system with 2D nanoscopy gives access to coherent processes in the uHIS and higher excited electronic states of Alq3.

The above description of coherent 2D nanoscopy assumes that the excited quantum system consists of distinct energy levels. Inelastic decay processes are considered to be on timescales,

which are accessible by the excitation pulse sequence. Electronic coherences in strongly dephasing systems like a bulk metal are short-lived and typically vanish within an optical cycle. For nanoscaled systems with quasi-instantaneous decoherence an approximative treatment of the electron emission was discussed in Section 1.4.3. There, the photoemission yield is not determined by coherent effects, but by transition rates that describe the excitation of electrons into the continuum of unoccupied states above the Fermi energy and finally beyond the vacuum energy. The emission probability of the electrons is given by the n -th power of the local field intensity. The application of 2D nanoscopy, therefore, allows for measuring properties of the local response function instead of probing coherent transitions between electronic states. Since in a nanoscopic system the local electric field is determined by collective electronic response to the incident electric field (see Section 1.3.3), 2D nanoscopy at fast electronic dephasing probes the spectral properties of collective phenomena like localized surface plasmons and surface plasmon polaritons via the detection of single electron states (see Figure 4.5). In Figure 4.6 this idea is schematically illustrated. The local response to the laser pulse sequence generates a local field electric field. The temporal evolution of the local electric field intensity depends on the interplay of the excitation pulse sequence and the local response function. Hence, a variation of the relative delays and phases in the laser pulse sequence determines the interference of the subpulses in the local electric field. This is exemplarily depicted for two laser pulse sequences which only differ in their particular phase combinations (red solid and blue dotted lines). In case of the pulse sequence represented by the red lines the relative phase between the first and second pulse is $\varphi_\tau = \pi$ and between the last two pulse the phase is $\varphi_t = 0$. For the other sequence the phases are $\varphi_\tau = 0$ and $\varphi_t = \pi$. The intensity during the first pulse in the local electric field is identical in both sequences. In the overlap with the second pulse the intensity is decreased (red solid line) or enhanced (blue dotted line) because of the interference of the local electric fields according to the relative phase φ_τ . The similar observation holds in the overlap of the second and the third pulse of each sequence, but with constructive interference for the red line. This schematic example emphasizes that the relative phases do influence the evolution of the temporal intensity. Consequently, the electron yield also is a function of the delays and relative phases.

In contrast to ultrafast nano-optical experiments performed with an excitation sequence consisting of two pulses, 2D nanoscopy is able to generate unambiguous spectral information. In two-pulse experiments as described in [282–287] the influence of the inhomogeneous line broadening on the signal has to be taken into account. The homogeneous linewidth of single oscillators is retrieved only approximatively under assumption of a particular inhomogeneous resonance frequency distribution [285, 287]. Additionally, 2D nanoscopy goes beyond the four-wave mixing experiment on hybrid nanostructures demonstrated by Utikal *et al.* [312, 313]. There, the coherent control of plasmonic modes in a grating structure has been investigated using the optical third-harmonic signal excited by a degenerated optical 2D spectroscopy pulse sequence. However, in this example the spatial resolution was considerably above the diffraction limit. Furthermore, no full variation of the parameters of the three-pulse sequence was performed and evaluated, but spectral information were retrieved by comparing the signal to a model function at sparsely distributed delay positions.

The 2D nanoscopy experiments that are presented in this thesis are evaluated and explained completely using the incoherent model for electron emission from strongly dephasing materials. In contrast to the case of conventional optical 2D spectroscopy, a full description of the electronic

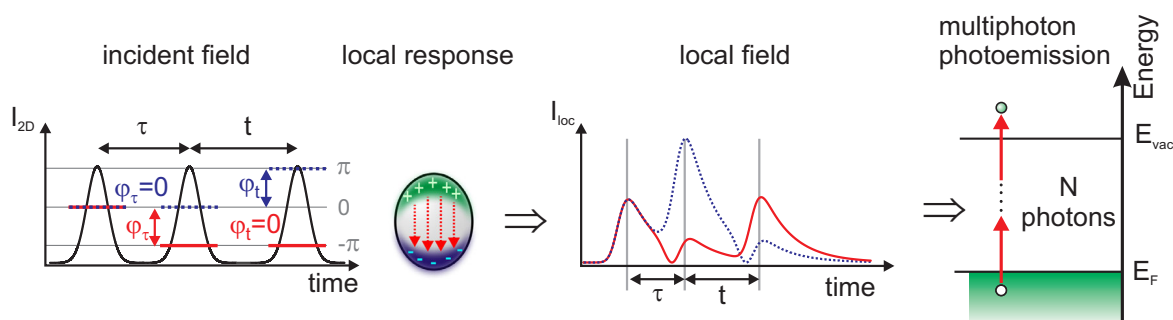


Figure 4.6.: 2D Nanoscopy excitation scheme in fast dephasing systems. From left to right: Schematic illustrations of excitation laser pulse sequences with differing relative phase combinations, nanoscopic system generating local field enhancement according to response function, resulting local electric field intensities and nonlinear electron emission process which is driven by local field intensity. For comparison two excitation pulse sequences with differing relative phase combinations (red solid lines and dotted blue lines) are presented. The relative phases φ_τ and φ_t denote the phase difference between the first and the second pulse and the third and the fourth pulse of the sequence, respectively. The third delay T and the relative phase φ_T between the second and third pulse were set to zero. The local fields that are excited by the two sequences are clearly distinct in their temporal evolution.

structure by means of the density matrix is not necessary, as the electron yield are directly related to local field intensities. Nevertheless, a brief introduction to the basic theoretical concepts of 2D spectroscopy is given in Appendix D. It is explained, how coherent light-matter interaction and propagation of electronic states in time are calculated using a Liouville space formalism. In Section 4.2 it is demonstrated that a modified description employing four interactions with the incoming electric field yields excitation pathways into population states, which are probed by coherent 2D nanoscopy. The considerations of Section 4.2.1 emphasize the strong similarity between both nonlinear spectroscopy techniques. However, this description of 2D nanoscopy has to be replaced for fast dephasing systems. A transformation from the Liouville representation of excited electronic states towards a description of 2D nanoscopy in consistence with the local response model of multiphoton photoemission introduced by Merschdorf *et al.* [227] is presented in Section 4.2.2. It is demonstrated that also in this case a multidimensional correlation function can be reconstructed from the linear local response function, which connects the electric fields of the input sequence.

The last section of this chapter introduces a simulation routine which enables the computation of two-dimensional spectra for arbitrary linear response functions and realistic excitation conditions in systems with strong dephasing of electronic coherences. Section 4.3 also deals with a fast converging fit routine that retrieves spectral information from measured 2D nanoscopy spectra. To compensate for the influences of limited spectral bandwidth and the local order of nonlinearity, a rescaling method is introduced in Section 4.3.3 which will be applied in Chapter 6.

4.2. Principles of Coherent 2D Nanoscopy

This section presents the theoretical description of 2D nanoscopy. The main difference with respect to the description of optical 2D spectroscopy (see Appendix D) lies in the detected signal, which is the local photoemission yield instead of coherent optical radiation. The implications

that follow from this changed excitation scheme were discussed in Section 4.1. Here, these modifications are implemented in the Liouville space description of the spectroscopy technique (Section 4.2.1). In strongly dephasing systems 2D nanoscopy probes the properties of the local electric field. In Section 4.2.2 it is demonstrated that upon excitation with a pulse sequence with variable parameters the photoemission yield is given by several contributions which differ in their dependence from the relative phases between the laser pulses. In Section 4.2.3 different contributions to the photoemission yield are introduced at the example of a Lorentz oscillator response function. Afterwards, the phase cycling technique is discussed which enables to retrieve isolated signals with unambiguous spectral features (Section 4.2.4).

4.2.1. Liouville Space Description of 2D Nanoscopy

In conventional 2D spectroscopy the measured signal is the coherent radiation emitted from the excited polarization in the investigated sample [15]. As it is briefly summarized in Appendix D, the evolution of the density matrix operator $\rho(t)$ describing the electronic system is treated in case of small time-dependent perturbations via the expansion into a series (see Eq. (D.20)) in which the elements $\rho^{(n)}(t)$ describe the contributions to the density matrix after n interactions with the electric field. A Liouville space notation is employed (see Appendix D.2), since it allows to represent the n -th order density matrix $\rho^{(n)}(t)$, which is an operator in Hilbert space (see Eqs. (D.2) and (D.6)), as a vector $|\rho^{(n)}(t)\rangle\rangle$ which is addressed by superoperators [15]. In this perturbative treatment $|\rho^{(n)}(t)\rangle\rangle$ is determined by the correlation function $S^{(n)}(t_n, t_{n-1}, \dots, t_1)$ (see Eq. (D.27)), which is given by a sequence of n interactions, each denoted by the dipole coupling operator \mathcal{V} , and the temporal propagation of the system between the interactions according to the Greens function $\mathcal{G}(t)$.

In 2D nanoscopy the time-averaged local photoemission yield $Y_m(\mathbf{r})$ from population state $|mm\rangle\rangle$ is detected by PEEM. As it is presented in Figure 4.5, the final excitation step can be driven by an ionization pulse, if the electron energy in $|mm\rangle\rangle$ lies below the vacuum energy. If signals from several populations are recorded, they are distinguishable by their specific final kinetic energy $E_{kin,m}$. As simplest approximation, the time-averaged photoemission yield $Y_m^{(n)}(\mathbf{r})$ is given by the integral over the momentary probability $\mathcal{P}_m^{(n)}(\mathbf{r}, t)$ for multiphoton photoemission originating from the m -th population state after n interactions with the excitation pulse sequence

$$Y_m^{(n)}(\mathbf{r}) = \int_{-\infty}^{\infty} \mathcal{P}_m^{(n)}(\mathbf{r}, t) dt . \quad (4.4)$$

The local photoemission probability $\mathcal{P}_m^{(n)}(\mathbf{r}, t)$ is considered to be proportional to the population in $|mm\rangle\rangle$. Hence, a direct transfer from the population state into the free electron states takes place, which is not affected by saturation or other nonlinear effects. For the sake of simplicity the local photoemission probability will be set identical to the population in $|mm\rangle\rangle$, which is calculated via the scalar product with the n -th order density matrix.

$$\mathcal{P}_m^{(n)}(\mathbf{r}, t) = \langle\langle mm | \rho^{(n)}(\mathbf{r}, t) \rangle\rangle \quad (4.5)$$

Because of the high spatial resolution of the PEEM the density matrix $\rho(\mathbf{r}, t)$ has to be treated as a local quantity in 2D nanoscopy. By substituting the density matrix analog to Eq. (D.25) the momentary photoemission yield denotes

$$\mathcal{P}_m^{(n)}(\mathbf{r}, t) = \int_0^\infty \dots \int_0^\infty dt_1 \dots dt_n \mathcal{R}_m^{(n)}(\mathbf{r}, t_n, t_{n-1}, \dots, t_1) E(\mathbf{r}, t - t_n) E(\mathbf{r}, t - t_n - t_{n-1}) \dots E(\mathbf{r}, t - t_n - t_{n-1} - \dots - t_1). \quad (4.6)$$

Here, the correlation function $\mathcal{R}_m^{(n)}(\mathbf{r}, t_n, t_{n-1}, \dots, t_1)$ describes the n -th order nonlinear response of the electronic system to the incident electric field $E(\mathbf{r}, t)$. The t_i denote relative delays between the interactions (see Eq. (D.24)). To emphasize that $\mathcal{R}_m^{(n)}$ leads to an electronic population in the m -th population state, whereas $S^{(n)}$ describes the polarization of the medium as a response to the incident electric fields (see Appendix D.2), different notation of the correlation functions are used. In analogy to Eq. (D.27), the correlation function $\mathcal{R}_m^{(n)}$ is given by

$$\mathcal{R}_m^{(n)}(\mathbf{r}, t_n, t_{n-1}, \dots, t_1) = \left(\frac{i}{\hbar}\right)^n \langle\langle mm | \mathcal{G}(\mathbf{r}, t_n) \mathcal{V}(\mathbf{r}) \mathcal{G}(\mathbf{r}, t_{n-1}) \mathcal{V}(\mathbf{r}) \dots \mathcal{G}(\mathbf{r}, t_1) \mathcal{V}(\mathbf{r}) | \rho(-\infty) \rangle\rangle. \quad (4.7)$$

This equation is transformed into the interaction picture by using a time-dependent dipole coupling operator

$$\mathcal{V}(\mathbf{r}, t) = \exp\left(\frac{i}{\hbar} \mathcal{L}(\mathbf{r}) t\right) \mathcal{V}(\mathbf{r}) \exp\left(-\frac{i}{\hbar} \mathcal{L}(\mathbf{r}) t\right), \quad (4.8)$$

where the exponential terms denote the temporal propagation of the electronic states determined by the unperturbed Liouville operator $\mathcal{L}(\mathbf{r})$. The dipole operator for an immediate interaction at $t = 0$ contracts to $\mathcal{V}(\mathbf{r}, 0) = \mathcal{V}(\mathbf{r})$.

By inserting the Liouville space Greens function $\mathcal{G}(\mathbf{r}, t)$ according to Eq. (D.21)

$$\mathcal{G}(\mathbf{r}, t) = \Theta(t) \exp\left(-\frac{i\mathcal{L}(\mathbf{r})t}{\hbar}\right) \quad (4.9)$$

and using Eq. (4.8) the correlation function is written as

$$\mathcal{R}_m^{(n)}(\mathbf{r}, t_n, t_{n-1}, \dots, t_1) = \left(\frac{i}{\hbar}\right)^n \Theta(t_1) \dots \Theta(t_{n-1}) \delta(t_n) \langle\langle mm | \mathcal{V}(\mathbf{r}, t_{n-1} + \dots + t_1) \mathcal{V}(\mathbf{r}, t_{n-2} + \dots + t_1) \dots \mathcal{V}(\mathbf{r}, t_1) \mathcal{V}(\mathbf{r}, 0) | \rho(-\infty) \rangle\rangle. \quad (4.10)$$

Eq. (4.10) also includes the assumption that the final population state $|mm\rangle$ decays by a simple exponential function. Therefore, the temporal propagation after the last interaction denotes

$$\langle\langle mm | \mathcal{G}(\mathbf{r}, t_n) = \langle\langle mm | \Theta(t_n) \exp\left(-\frac{i}{\hbar} \mathcal{L}(\mathbf{r}) t_n\right) = \Theta(t_n) \exp\left(-\frac{t_n}{\gamma}\right) \langle\langle mm |, \quad (4.11)$$

where γ is a constant decay parameter. The integration over t_n yields a photoemission rate that is proportional to the population directly after the last interaction at t_{n-1} . Hence, the single sided exponential decay is omitted in Eq. (4.10) for the sake of simplicity and replaced by a δ -function.

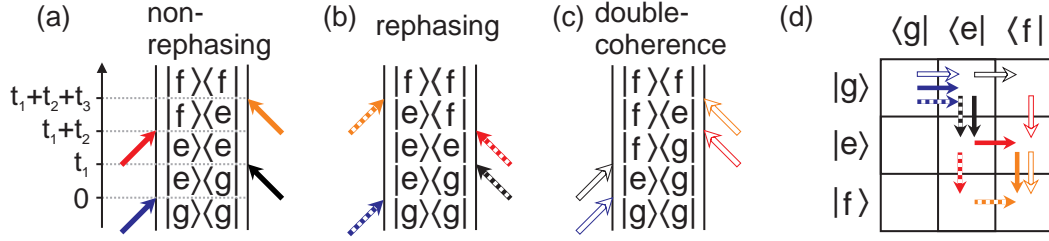


Figure 4.7.: Double-sided Feynman diagrams (DSFD) of Liouville pathways leading into double excited state $|f\rangle\langle f|$ of three level quantum system, according to $\mathcal{R}_f^{(4)}$. (a) DSFD of non-rephasing excitation. (b) DSFD of rephasing excitation. (c) DSFD of double-coherence excitation. (d) Reduced density matrix representation of non-rephasing (solid arrows), rephasing (dashed arrows) and double-coherence (open arrows) excitation pathways.

The basic concept of 2D nanoscopy involves a four wave mixing process leading to a population state (see Figure 4.3). Accordingly, the 4-th order momentary photoemission yield $\mathcal{R}_m^{(4)}$ has to be calculated:

$$\mathcal{R}_m^{(4)}(\mathbf{r}, t_4, t_3, t_2, t_1) = \left(\frac{i}{\hbar}\right)^4 \Theta(t_1)\Theta(t_2)\Theta(t_3)\delta(t_4) \langle\langle mm | \mathcal{V}(\mathbf{r}, t_3 + t_2 + t_1) \mathcal{V}(\mathbf{r}, t_2 + t_1) \mathcal{V}(\mathbf{r}, t_1) \mathcal{V}(\mathbf{r}, 0) | \rho(-\infty) \rangle\rangle. \quad (4.12)$$

Comparing this equation with Eq. (D.29) it is obvious that optical 2D spectroscopy and 2D nanoscopy are closely related. As a consequence of the similarity between the correlation functions $\mathcal{R}_m^{(4)}$ and $S^{(3)}$, also the possible excitation pathways are similar. Thus, with 2D nanoscopy it is possible to obtain coherent spectroscopic information comparable to optical 2D spectroscopy by detecting the incoherent photoemission signal.

In both techniques four dipole interactions with the electric field are involved. Their relative delays to the first interactions are 0 (first interaction itself), t_1 , $t_1 + t_2$ and $t_1 + t_2 + t_3$. A difference is given by the selection of a particular population state denoted as $|m\rangle$ in Hilbert notation via the kinetic energy of the photoelectron. Such a filtering of the signal is not feasible in optical 2D spectroscopy. The final state of the quantum systems in optical 2D spectroscopy is always below the highest accessible eigenstate, because the last interaction with the electric field necessarily leads to the emission of the detected photon. For this reason the excitation pathways in Figure D.1 all end in the ground state. In 2D nanoscopy the photon energy can be absorbed completely. Thus, in a three-level system with a ground state $|g\rangle$, a first electronically excited state $|e\rangle$, and a second excited state $|f\rangle$ the correlation function $\mathcal{R}_f^{(4)}$ determines the excitation of the highest population state $|f\rangle$ via absorption of two photons.

In Figure 4.7 the excitation pathways leading to the double excited state of the three level system are represented by double-sided Feynman diagrams and by a combined density matrix pictogram. By inversion of the diagrams the complex conjugate pathways are retrieved. In contrast to excitation pathways of optical 2D spectroscopy (see Fig. D.1) the orange arrow, indicating the last interaction, points towards the Feynman diagrams transferring the coherent state into the population state $|f\rangle\langle f|$. Nevertheless, similarly to the findings of optical 2D spectroscopy the different excitation pathways lead to *non-rephasing*, *rephasing* and *double-coherence* signals, presented in Figure 4.7a, b and c, respectively. In all three cases the excitation pathways exhibit a

coherent state after the first and third interaction. Rephasing and non-rephasing signals differ in the phase evolution after the third interaction. Whereas, the non-rephasing signal is connected to coherent states oscillating with frequencies of identical sign, the rephasing pathways contains the states $|e\rangle\langle g|$ and $|e\rangle\langle f|$. They are associated with frequencies $(E_e - E_g)/\hbar$ and $(E_e - E_f)/\hbar$, which have opposite signs. The double-coherence excitation pathway does not include the population state $|e\rangle\langle e|$ after the second interaction, but the double-coherent state $|f\rangle\langle g|$.

Additionally, 2D nanoscopy also includes the excitation pathways identical to optical 2D spectroscopy. However, these do not lead to population in the highest state $|f\rangle$, but in the single excited state $|e\rangle$ or ground state $|g\rangle$ and are described by the correlation functions $\mathcal{R}_e^{(4)}$ and $\mathcal{R}_g^{(4)}$, respectively. A systematic description of these pathways is given in [4].

4.2.2. 2D Nanoscopy in Strongly Dephasing Systems

In this section the general description of 2D nanoscopy is further adapted to meet the conditions in metallic systems with short electron dephasing times. Instead of providing insight into the electronic excitation processes, the assumptions that will be made lead to a simplified model that describe the photoemission process in dependence from the local field intensity. These derivations demonstrate that the obtained photoemission yield exhibits the spectral signature of the local electric fields at the surface of the sample. Hence, 2D nanoscopy is, in addition to the investigation of quantum systems, applicable to examine collective coherent effects like plasmonic resonances in an environment that exhibits a strong dephasing of electronic excitations.

The short dephasing times in metals are caused by the broad bandwidth of unoccupied electronic states above the Fermi energy [227]. Furthermore, the lifetimes of the corresponding states is typically in the few-femtosecond regime (see Eq. (1.60)) [175, 223–225]. The following derivations are performed in the limit of instantaneous dephasing and relaxation processes approximating the Liouville Greens function of the electronic system $\mathcal{G}(\mathbf{r}, t)$ by a Dirac delta function. By substituting $\mathcal{G}(\mathbf{r}, t) = \delta(t)$ the general expression for the correlation function of 2D nanoscopy Eq. (4.7) is rewritten as

$$\mathcal{R}_m^{(n)}(\mathbf{r}, t_n, t_{n-1}, \dots, t_1) = \left(\frac{i}{\hbar}\right)^n \langle\langle mm | (\mathcal{V}(\mathbf{r}))^n | \rho(-\infty) \rangle\rangle \prod_{l=1}^n \delta(t_l). \quad (4.13)$$

Accordingly, $\mathcal{R}_m^{(n)}(\mathbf{r}, t_n, t_{n-1}, \dots, t_1)$ consists of a time-independent interaction part which projects the equilibrium state $\rho(-\infty)$ onto the m -th population state after a series of n dipolar interactions and a product of temporal delta functions. The photoemission, therefore, is forced to also take place instantaneously, because all relative delays between the interactions are set to zero by the delta functions. Substituting Eq. (4.13) into Eq. (4.6) and carrying out the integration over all time variables t_l yields for the momentary photoemission rate

$$\mathcal{P}_m^{(n)}(\mathbf{r}, t) \propto (E(\mathbf{r}, t))^n = (E^+(\mathbf{r}, t) + E^-(\mathbf{r}, t))^n. \quad (4.14)$$

Thus, the photoemission rate is proportional to the momentary electric field at the spatial position \mathbf{r} . Calculating the n -th power of $(E^+(\mathbf{r}, t) + E^-(\mathbf{r}, t))$ creates a sum of $2n + 1$ different products $(E^+(\mathbf{r}, t))^p (E^-(\mathbf{r}, t))^q$ with $p + q = n$. Except for the case $p = q = n/2$, all these terms have an unbalanced number of positive and negative frequency contributions. Consequently, they

are rapidly oscillating in t and do not survive the integration over t that provides the measured photoemission yield, which denotes

$$Y_m^{(n)}(\mathbf{r}) \propto \int_{-\infty}^{\infty} dt (E^+(\mathbf{r}, t)E^-(\mathbf{r}, t))^{n/2} \propto \int_{-\infty}^{\infty} dt (I(\mathbf{r}, t))^{n/2}. \quad (4.15)$$

The introduction of an instantaneous decay process, therefore, leads to strong simplification of the excitation process by neglecting the electronic properties of the system which are denoted by the density matrix. The total photoemission yield $Y_m^{(n)}(\mathbf{r})$ is proportional to the $n/2$ -th power of the temporal electric field intensity at position \mathbf{r} , which is always a real and positive quantity. From this simple relation it is not obvious that a non-trivial local correlation function analog to $S^{(n)}$ and $\mathcal{R}_m^{(n)}$ exists which determines the local photoemission yield created by the incident electric field. In the following part of this section it is demonstrated that such a correlation function, nevertheless, can be reconstructed from the linear local response function.

Implicitly, Eq. (4.15) contains the local response properties of the system, because the local electric field $E(\mathbf{r}, t)$, which drives the photoemission process, is the convolution of the temporal response function $A(\mathbf{r}, t)$ and the incident electric field of the laser pulse sequence $E_p(t)$, which is considered to be homogeneous over the complete sample. Therefore, the momentary photoemission yield is extended in explicit notation to

$$\begin{aligned} \mathcal{P}_m^{(n)}(\mathbf{r}, t) &= (E^+(\mathbf{r}, t)E^-(\mathbf{r}, t))^{n/2} = \prod_{h=1}^{n/2} E^+(\mathbf{r}, t)E^-(\mathbf{r}, t) \\ &= \prod_{i=1}^{n/2} \left\{ \int_{-\infty}^{\infty} dt_i^* A(\mathbf{r}, t_i^*) E_p^+(t - t_i^*) \right\} \prod_{j=n/2+1}^n \left\{ \int_{-\infty}^{\infty} dt_j^* A(\mathbf{r}, t_j^*) E_p^-(t - t_j^*) \right\}. \end{aligned} \quad (4.16)$$

Now all contributing electric fields are written independently as n convolutions. The commutativity of the multiplication allows the employed ordering of the indices using $i = \{1, \dots, n/2\}$ for positive frequency contributions and $j = \{n/2 + 1, \dots, n\}$ for negative frequency contributions. Since the time variables $(t_1^*, t_2^*, \dots, t_n^*)$ are independent, it is possible to rearrange the equation towards one single multidimensional integral containing all products.

$$\begin{aligned} \mathcal{P}_m^{(n)}(\mathbf{r}, t) &= \int_{-\infty}^{\infty} \dots \int_{-\infty}^{\infty} dt_1^* dt_2^* \dots dt_n^* \prod_{i=1}^{n/2} A(\mathbf{r}, t_i^*) E_p^+(t - t_i^*) \prod_{j=n/2+1}^n A(\mathbf{r}, t_j^*) E_p^-(t - t_j^*) \\ &= \int_{-\infty}^{\infty} \dots \int_{-\infty}^{\infty} dt_1^* dt_2^* \dots dt_n^* \mathcal{Q}(\mathbf{r}, t_1^*, t_2^*, \dots, t_n^*) \prod_{i=1}^{n/2} E_p^+(t - t_i^*) \prod_{j=n/2+1}^n E_p^-(t - t_j^*) \end{aligned} \quad (4.17)$$

In the last line the commutativity of the multiplication was used to combine all local fields and construct a new correlation function $\mathcal{Q}(\mathbf{r}, t_1^*, t_2^*, \dots, t_n^*)$. This relation already resembles Eqs. (D.26) and (4.6) describing the signal in optical 2D spectroscopy and 2D nanoscopy for systems

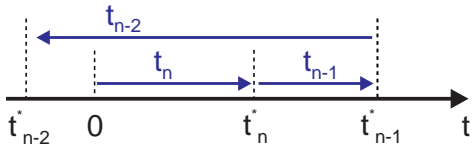


Figure 4.8: Absolute and relative time variables. The diagram illustrates the relation of absolute time variables $t_1^*, t_2^*, \dots, t_n^*$ and relative time differences t_1, t_2, \dots, t_n according to Eq. (4.18).

with longer coherence lifetimes. In the next step the absolute time variables times $t_1^*, t_2^*, \dots, t_n^*$ are substituted by relative time differences t_1, t_2, \dots, t_n :

$$t_1^* = \sum_{j=1}^n t_j \quad t_2^* = \sum_{j=2}^n t_j \quad \dots \quad t_n^* = t_n \quad (4.18)$$

Figure 4.8 illustrates the relation between absolute and relative time variables schematically. The absolute time variables times $t_1^*, t_2^*, \dots, t_n^*$ do not have to be ordered in their value. Accordingly, each relative delay step $t_j = t_j^* - t_{j+1}^*$ can have an arbitrary sign. Since the derivatives $\frac{dt_j^*}{dt_j} = 1$ and the integration boundaries are infinite, the substitutions are simple replacements:

$$\mathcal{P}_m^{(n)}(\mathbf{r}, t) = \int_{-\infty}^{\infty} \int_{-\infty}^{\infty} \dots \int_{-\infty}^{\infty} dt_1 dt_2 \dots dt_{2n} \mathcal{Q}(\mathbf{r}, t_1, t_2, \dots, t_n) \prod_{k=1}^n E_p^{\pm}(t - \sum_{j=k}^n t_j) \quad (4.19)$$

This equation is analog to the equations (D.26) and (4.6) as well as to a formula used in [296] to describe the signal of collinear multi-dimensional optical spectroscopy. The notation $E_p^{\pm}(t - \sum_{j=k}^n t_j)$ indicates that the k -th electric field contribution consists either of positive or negative frequency components. In total Eq. (4.16) enforces that equal numbers of positive and negative frequency components exist. Explicitly, the new correlation function \mathcal{Q} is given by the product of the temporal response functions in dependence of the relative delays.

$$\mathcal{Q}(\mathbf{r}, t_1, t_2, \dots, t_{2n}) = \prod_{k=1}^n A(\mathbf{r}, \sum_{j=k}^n t_j) \quad (4.20)$$

The derivations performed up to this point show that even for the case of instantaneous dephasing and relaxation of the electronic system the local photoemission signal in a 2D nanoscopy measurements contains spectroscopic informations. However, not the material properties are investigated but the local response function, which determines the local electric fields on the surface. It was demonstrated that the construction of a correlation function $\mathcal{Q}(t_1, t_2, \dots, t_n)$ using the local response functions leads to a similar mathematical relation as in case of the density matrix based correlation functions $\mathcal{S}^{(n)}$ and $\mathcal{R}_m^{(n)}$ (see Eqs. (D.26) and (4.6)).

In the remaining part of this section it is demonstrated how spectroscopic information is retrieved by applying an excitation sequence $E_3^+(t, \tau_1, \tau_3, \varphi_1, \varphi_2, \varphi_3)$ consisting of three laser pulses. Three-pulse sequences are also employed in the experimental demonstrations of 2D nanoscopy presented in Chapter 5.3 and Chapter 6.3. The second pulse in the sequence is positioned at $t = 0$, whereas τ_1 and τ_3 denote the temporal separations of the first and third pulse with respect to the second pulse. The positive frequency components of the sequence create a temporal field:

$$E_3^+(t, \tau_1, \tau_3, \varphi_1, \varphi_2, \varphi_3) = \tilde{E}_L^+(t + \tau_1)e^{i[\omega_L t + \varphi_1]} + \tilde{E}_L^+(t)e^{i[\omega_L t + \varphi_2]} + \tilde{E}_L^+(t - \tau_3)e^{i[\omega_L t + \varphi_3]} . \quad (4.21)$$

The temporal field $E_3^-(t, \tau_1, \tau_3, \varphi_1, \varphi_2, \varphi_3)$ is obtained by complex conjugation and is associated with the negative spectral components. The positive sign before τ_1 in the first term accounts for the fact that the first pulse is shifted by a negative delay. Thus, τ_1 remains a positive defined quantity. Since the exponential terms do not include the delays τ_1 and τ_3 , the field envelopes \tilde{E}_L^+ of the first and third pulse move independently from the electric field oscillations, which remain fixed to the rotating frame defined by the carrier oscillations of the laser. The phases φ_1 , φ_2 and φ_3 denote the relative phase difference to the rotating frame [314].

In the following derivations the laser pulses in the excitation sequence will be treated as arbitrarily short. The temporal pulse envelopes become $\delta(t)$ -functions. The momentary photoemission rate $\mathcal{P}_m^{(n)}(\mathbf{r}, t, \tau_1, \tau_3, \varphi_1, \varphi_2, \varphi_3)$ is calculated by substituting $E_3(t)$ in Eq. (4.17). This is explicitly presented in Appendix E.1 for the case $n = 4$. The convolutions are simplified by the $\delta(t)$ -functions and the photoemission rate is rewritten as a sum over contributions with specific dependence on the relative phases φ_1 , φ_2 and φ_3 :

$$\mathcal{P}_m^{(n)}(\mathbf{r}, t, \tau_1, \tau_3, \varphi_1, \varphi_2, \varphi_3) = \sum_{\alpha, \beta, \gamma} \tilde{\mathcal{P}}(\mathbf{r}, t, \tau_1, \tau_3, \alpha, \beta, \gamma) e^{i(\alpha\varphi_1 + \beta\varphi_2 + \gamma\varphi_3)} \quad (4.22)$$

The term $\tilde{\mathcal{P}}(\mathbf{r}, t, \tau_1, \tau_3, \alpha, \beta, \gamma)$ describes the temporal evolution of the local photoemission rate in dependence of the excitation pulse delays τ_1 and τ_3 and three additional parameters α , β and γ , which indicate the effective number of interactions with the first, second and third pulse of the excitation sequence, respectively (see also Eqs. (4.25)–(4.27)). This partial photoemission signal itself is determined by a sum of contributions

$$\tilde{\mathcal{P}}(\mathbf{r}, t, \tau_1, \tau_3, \alpha, \beta, \gamma) = \sum_{\substack{\text{Eqs. (4.25)} \\ \text{-(4.27)}}} c_{\alpha_-, \beta_-, \gamma_-}^{\alpha_+, \beta_+, \gamma_+} B_{\alpha_-}^{\alpha_+}(\mathbf{r}, t, -\tau_1) B_{\beta_-}^{\beta_+}(\mathbf{r}, t, 0) B_{\gamma_-}^{\gamma_+}(\mathbf{r}, t, \tau_3) . \quad (4.23)$$

The terms denoted as $B_{d_-}^{d_+}(t, \tau)$ represent the contributions of the first, second and third pulse of the sequence. Each of these terms is given by a product of the local response functions shifted to the position τ of one of the excitation pulses

$$B_{d_-}^{d_+}(\mathbf{r}, t, \tau) = [A^+(\mathbf{r}, t - \tau)e^{i\omega_L \tau}]^{d_+} [A^-(\mathbf{r}, t - \tau)e^{-i\omega_L \tau}]^{d_-} , \quad (4.24)$$

where d_{\pm} is substituted by α_{\pm} , β_{\pm} or γ_{\pm} and the delay τ by $-\tau_1$, 0 and τ_3 in case of the first, second and third excitation pulse, respectively. Each factor in $B_{d_-}^{d_+}(\mathbf{r}, t, \tau)$ consist of the local response function shifted by a delay as well as an exponential term, which acts on the phase. The phase factor originates from the rotating frame definition of the excitation pulse sequence. It has an important impact on the resulting 2D nanoscopy spectra, because it centers the oscillator frequency ω_L at the zero position of the frequency axes (see Fig. 4.9). The sum in Eq. (4.23) is weighted by $c_{\alpha_-, \beta_-, \gamma_-}^{\alpha_+, \beta_+, \gamma_+}$ indicating the number of permutations of the local response functions that yield identical parameters α_{\pm} , β_{\pm} and γ_{\pm} . These interaction parameters are positive integer values and obey the following conditions:

$$\alpha_+ - \alpha_- = \alpha \quad \text{and} \quad \beta_+ - \beta_- = \beta \quad \text{and} \quad \gamma_+ - \gamma_- = \gamma \quad (4.25)$$

$$\alpha_+ + \beta_+ + \gamma_+ = n/2 \quad \text{and} \quad \alpha_- + \beta_- + \gamma_- = n/2 \quad (4.26)$$

$$\alpha + \beta + \gamma = 0. \quad (4.27)$$

These conditions are associated with the identical number of positive and negative frequency components that contribute to the signal according to Eq. (4.15). If the parameters additionally fulfill

$$|\alpha| + |\beta| + |\gamma| = n, \quad (4.28)$$

each excitation pulse contributes purely with positive or negative frequencies. Then, partial photoemission signal $\tilde{\mathcal{P}}(\mathbf{r}, t, \tau_1, \tau_3, \alpha, \beta, \gamma)$ consists of a unique combination of local response functions and the summation in Eq. (4.23) becomes unnecessary. If $|\alpha| + |\beta| + |\gamma| < n$, several summands exist that share the identical dependence on the relative phases and contribute to the specific $\tilde{\mathcal{P}}(\mathbf{r}, t, \tau_1, \tau_3, \alpha, \beta, \gamma)$. Using Eqs. (4.25)–(4.27) the weight factor in Eq. (4.23) is determined by:

$$c_{\alpha_+, \beta_+, \gamma_+}^{\alpha_+, \beta_+, \gamma_+} = \frac{2(n/2!)}{\alpha_+! \beta_+! \gamma_+! \alpha_-! \beta_-! \gamma_-!}. \quad (4.29)$$

For the phase factor it can be deduced from the conditions of the indices (see Eq. 4.27) that

$$\Phi(\beta, \gamma, \varphi_{21}, \varphi_{31}) = e^{i(\beta\varphi_{21} + \gamma\varphi_{31})} = e^{i(\alpha\varphi_1 + \beta\varphi_2 + \gamma\varphi_3)} \quad (4.30)$$

is valid. Hence, the phase factor for fixed parameters β and γ is expressed as a two-dimensional function $\Phi(\beta, \gamma, \varphi_{21}, \varphi_{31})$ dependent of the relative phase differences $\varphi_{21} = \varphi_2 - \varphi_1$ between the first and second pulse and $\varphi_{31} = \varphi_3 - \varphi_1$ between the first and the third pulse. The phase factor plays an important role in the phase cycling technique that is introduced in Section 4.2.4.

The derivations in this section showed that the correlation function $\mathcal{Q}(t_1, t_2, \dots, t_n)$ leads to the generation of partial photoemission signals $\tilde{\mathcal{P}}(\mathbf{r}, t, \tau_1, \tau_3, \alpha, \beta, \gamma)$, which are classified by the numbers of interaction with the individual pulses in the excitation sequence.

To obtain the spectral information from the delay-dependent data, Fourier transformations along the τ_1 and τ_3 axes are performed. Then, Equation (4.23) transforms into

$$\tilde{\mathcal{P}}(\mathbf{r}, t, \omega_{\tau_1}, \omega_{\tau_3}, \alpha, \beta, \gamma) \propto \sum_{\substack{\alpha_+, \alpha_-, \\ \beta_+, \beta_-, \\ \gamma_+, \gamma_-}} B_{\alpha_-}^{\alpha_+}(t, \omega_{\tau_1}) \cdot B_{\beta_-}^{\beta_+}(t, 0) \cdot B_{\gamma_-}^{\gamma_+}(t, \omega_{\tau_3}). \quad (4.31)$$

In frequency space the contributions of the different excitation pulses can still be multiplied, as only the response to the first pulse depends on τ_1 and only the response to the third pulse depends on τ_3 . Accordingly, the two-dimensional spectrum is determined by two one-dimensional functions along the two orthogonal frequency directions ω_{τ_1} and ω_{τ_3} . However, in general $B_{\alpha_-}^{\alpha_+}(t, \omega_{\tau_1})$ and $B_{\gamma_-}^{\gamma_+}(t, \omega_{\tau_3})$ are given by the convolution of the Fourier transformed factors which the temporal contributions $B_{\alpha_-}^{\alpha_+}(t, \tau_1)$ and $B_{\gamma_-}^{\gamma_+}(t, \tau_3)$ consist of (see Eq. (4.24)). Thus, $\tilde{\mathcal{P}}(\mathbf{r}, t, \omega_{\tau_1}, \omega_{\tau_3}, \alpha, \beta, \gamma)$ is determined by the specific response function $A(\mathbf{r}, \omega)$ and Eq. (4.31) cannot be further simplified without knowledge of $A(\mathbf{r}, \omega)$. In the following section the response function of a single Lorentz oscillator is employed for the analytic calculation of the corresponding 2D nanoscopy spectra.

4.2.3. 2D Nanoscopy for Single Harmonic Oscillators in Strongly Dephasing Systems

In this section, the 2D nanoscopy signals generated by a single oscillator response function in a strongly dephasing system are discussed. An exponentially decaying oscillation is used as local response function

$$A^+(t) = \Theta(t)e^{i\omega_{Lo}t - \gamma_{Lo}t}, \quad (4.32)$$

which approximates the temporal behavior of a Lorentz oscillator at center frequency ω_{Lo} and spectral width γ_{Lo} (see Appendix F). The temporal evolution of the partial photoemission rate $\tilde{P}(t, \tau_1, \tau_3, \alpha, \beta, \gamma)$ is calculated by explicitly inserting Eq. (4.32) into Eq. (4.23). In Appendix E.2 it is shown that in case of $n = 4$ and interaction parameters α , β and γ following Eqs. (4.25)–(4.27) as well as Eq. (4.28) the partial photoemission yield is given by:

$$\tilde{Y}^{(4)}(\tau_1, \tau_3, \beta, \gamma) \propto \Theta(\tau_1)e^{-i(\beta+\gamma)(\omega_{Lo}-\omega_L)-(4-|\beta|-|\gamma|)\gamma_{Lo}\tau_1}\Theta(\tau_3)e^{-i\gamma(\omega_{Lo}-\omega_L)-(4-|\gamma|)\gamma_{Lo}\tau_3}. \quad (4.33)$$

The identical interaction parameters β and γ , which determine the phase factor $\Phi(\beta, \gamma, \varphi_{21}, \varphi_{31})$, which has to be multiplied to $\tilde{P}(t, \tau_1, \tau_3, \alpha, \beta, \gamma)$ in Eq. (4.22), also determine the oscillation periods of the partial signal in dependence of the delays and the detuning frequency $\omega_{Lo} - \omega_L$. For each possible combination of β and γ , therefore, a specific phase-dependence $e^{i(\beta\varphi_{21} + \gamma\varphi_{31})}$ and a specific delay-dependence $\tilde{Y}^{(4)}(\tau_1, \tau_3, \beta, \gamma)$ exist. In the Section 4.2.4 it is demonstrated that the identification of a signal with a particular phase factor $\Phi(\beta, \gamma, \varphi_{21}, \varphi_{31})$ by phase cycling enables the unambiguous retrieval of the corresponding partial signal $\tilde{Y}^{(4)}(\tau_1, \tau_3, \beta, \gamma)$. Fourier transformation of Eq. (4.33) along both delay axes yields the two-dimensional spectral signal

$$\tilde{Y}^{(4)}(\omega_{\tau_1}, \omega_{\tau_3}, \beta, \gamma) \propto \frac{1}{-(\beta + \gamma)(\omega_{Lo} - \omega_L) - \omega_{\tau_1} + i(4 - |\beta| - |\gamma|)\gamma_{Lo}} \times \frac{1}{\gamma(\omega_{Lo} - \omega_L) + \omega_{\tau_3} - i(4 - |\gamma|)\gamma_{Lo}}. \quad (4.34)$$

The ω_{τ_1} -term is the approximative solution for the positive frequency part of a Lorentz oscillator response function and the ω_{τ_3} -term is the approximative solution for the negative frequency part (see Appendix F). The oscillator function along the ω_{τ_1} -axis is located at a central frequency $\omega_{\tau_1} = -(\beta + \gamma)(\omega_{Lo} - \omega_L) = \alpha(\omega_{Lo} - \omega_L)$ and has a spectral width $\gamma_{\tau_1} = (4 - |\beta| - |\gamma|)\gamma_{Lo} = |\alpha|\gamma_{Lo}$. The oscillator function along the ω_{τ_3} -axis has its resonance position at $\omega_{\tau_3} = -\gamma(\omega_{Lo} - \omega_L)$ and exhibits a spectral width of $\gamma_{\tau_3} = (4 - |\gamma|)\gamma_{Lo} = (|\alpha| + |\beta|)\gamma_{Lo}$. As it is presented in later parts of this thesis, a phenomenological fit function based on Eq. (4.34) is employed to evaluate 2D nanoscopy spectra obtained by Fourier transform time domain simulations (see Section 4.3.3) and by experiments (see Chapter 6.3.3).

From the general formula in Eq. (4.33) the partial yield for specific combinations of α , β , γ which follow the above conditions can be deduced. In optical 2D spectroscopy the different contributions to the signal are associated with specific electronic phenomena. The description

of 2D nanoscopy in strongly dephasing systems discussed in this section does not distinguish between the electronic excitation pathways (see Eq. (4.15)), but allows the distinction of partial photoemission signals $\tilde{Y}(\mathbf{r}, t, \tau_1, \tau_3, \alpha, \beta, \gamma)$ created by particular combinations of interfering local electric fields. Despite these fundamental differences, the nomenclature of the 2D nanoscopy signals is associated to specific conventional 2D spectroscopy signals to indicate the identical numbers of interactions. The contribution with $\alpha = -1$, $\beta = 2$ and $\gamma = -1$ is connected to a rephasing signal called photon echo [15, 296]. The partial photoemission yield is given by

$$\tilde{Y}^{(4)}(\tau_1, \tau_3, 2, -1) \propto \Theta(\tau_1)\Theta(\tau_3)e^{(-i(\omega_{Lo}-\omega_L)-\gamma_{Lo})\tau_1}e^{i(\omega_{Lo}-\omega_L)-3\gamma_{Lo})\tau_3} \quad (4.35)$$

The photon echo signal oscillates in τ_1 with the negative detuning $-(\omega_{Lo} - \omega_L)$ of the oscillator frequency ω_{Lo} with respect to the rotating frame frequency ω_L and in τ_3 with the positive detuning $(\omega_{Lo} - \omega_L)$. Hence, the oscillations occur in antidiagonal delay direction, i.e. an equal increase of the delays τ_1 and τ_3 does not affect the phase of signal. The decay of the signal differs for both delay axes. The decay is faster in τ_3 direction by a factor of three.

Another valid combination of parameters is $\alpha = 2$, $\beta = -1$ and $\gamma = -1$ leading to a contribution that is associated with the third-order double quantum coherence signal (third-order 2Q-2D) in conventional 2D spectroscopy [296, 315] and exhibits the excitation pathway presented in Figure 4.7c.

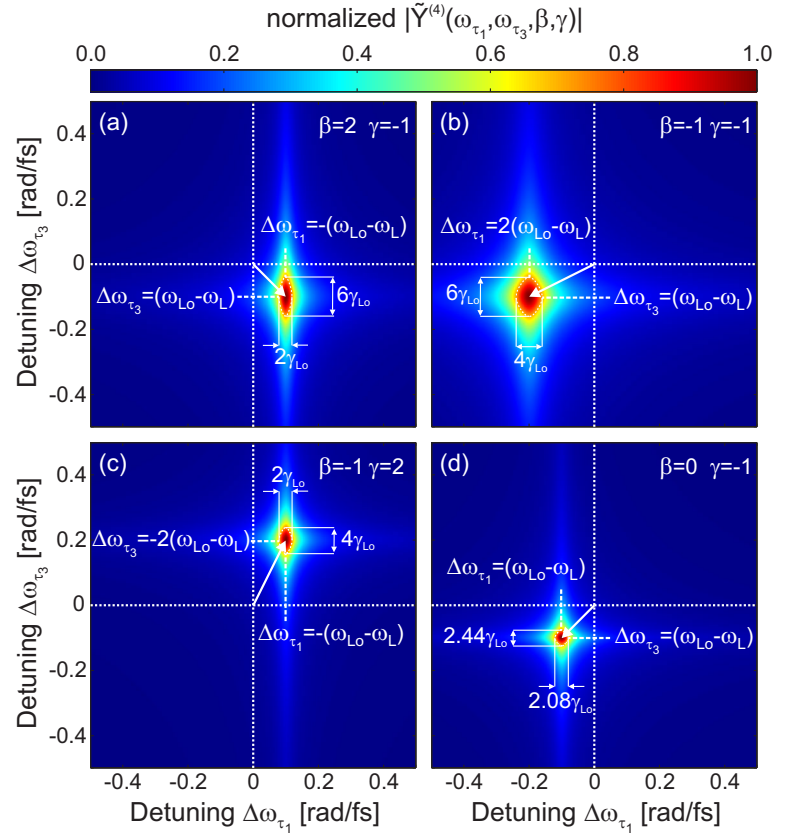
$$\tilde{Y}^{(4)}(\tau_1, \tau_3, -1, -1) \propto \Theta(\tau_1)\Theta(\tau_3)e^{i2(\omega_{Lo}-\omega_L)-2\gamma_{Lo})\tau_1}e^{i(\omega_{Lo}-\omega_L)-3\gamma_{Lo})\tau_3} \quad (4.36)$$

This signal is oscillating with the doubled positive frequency detuning along the τ_1 -axis and decays in this direction twice as fast as the photon echo signal. Yet, in τ_3 -direction it shows the identical evolution as $\tilde{Y}^{(4)}(\tau_1, \tau_3, 2, -1)$. Hence, the spectral resonances are shifting in off-diagonal direction for this kind of signal.

By inserting the interaction parameters of the specific signals into Eq. (4.34) the spectral signals corresponding to Eqs. (4.35) and (4.36) are calculated. The oscillator parameters in the examples presented in Fig. 4.9 are set to $\omega_{Lo} - \omega_L = -0.1$ rad/fs and $\gamma_{Lo} = 0.02$ rad/fs. The two-dimensional plots show the spectral amplitude $|\tilde{Y}^{(4)}(\omega_{\tau_1}, \omega_{\tau_3}, \beta, \gamma)|$. The horizontal and vertical white dotted lines indicate the position of zero detuning on each axis, i.e. where ω_{τ_1} and ω_{τ_3} equal the rotating frame frequency ω_L . The white arrows pointing from the center position (ω_L, ω_L) of the plots to the resonance peaks emphasize the direction and length of the frequency shift of the respective partial 2D nanoscopy signal $\tilde{Y}^{(4)}(\omega_{\tau_1}, \omega_{\tau_3}, \beta, \gamma)$. In each plot the spectral width at the $(\sqrt{2})^{-1}$ -level of the resonance peak is marked in ω_{τ_1} - and ω_{τ_3} -direction by white lines and arrows. The spectra corresponding to the photon echo signal ($\beta = 2$, $\gamma = -1$) and the third-order double quantum coherence signal ($\beta = -1$, $\gamma = -1$) are shown in Fig. 4.9a and b, respectively. It is obvious that the resonance peaks are shifted to different positions and exhibit different widths. In accordance with the observation for the delay-dependent signals (see Eqs. (4.35) and (4.36)), the photon echo signal is shifted along the diagonal direction, whereas the signal in Fig. 4.9b is located at off-diagonal position. The spectral widths in ω_{τ_3} -directions are identical for both signals, but along ω_{τ_1} the photon echo signal exhibits a width of only $2\gamma_{Lo}$ compared to $4\gamma_{Lo}$ for the third-order double quantum coherence signal.

The 2D nanoscopy signal $\tilde{Y}^{(4)}(\omega_{\tau_1}, \omega_{\tau_3}, -1, 2)$ shown in Figure 4.9c is the analog to the reverse double quantum coherence signal (2Q-2D) of optical 2D spectroscopy [296]. The spectral

Figure 4.9: Analytical 2D nanoscopy amplitude spectra for a single Lorentz oscillator detuned by $\omega_{L_0} - \omega_L = -0.1$ rad/fs for various combination of interaction parameters β and γ . White arrows indicate the shift of the resonance position with respect to (ω_L, ω_L) as well as the width of the resonance peaks at $1/\sqrt{2}$ of the normalized amplitude signals. (a) 2D nanoscopy signal analog to photon echo signal of conventional 2D spectroscopy ($\beta = 2, \gamma = -1$). (b) 2D nanoscopy signal analog to third-order double quantum coherence signal ($\beta = -1, \gamma = -1$). (c) 2D nanoscopy signal analog to the reverse double quantum coherence signal ($\beta = -1, \gamma = 2$). (d) 2D nanoscopy signal analog to reverse transient grating signal ($\beta = 0, \gamma = -1$).



resonance peak appears at $\Delta\omega_{\tau_1} = -(\omega_{L_0} - \omega_L)$ and $\Delta\omega_{\tau_3} = -2(\omega_{L_0} - \omega_L)$ and has a width of $2\gamma_{L_0}$ in ω_{τ_1} -direction and a width of $4\gamma_{L_0}$ in ω_{τ_3} -direction.

The spectroscopic signals $\tilde{Y}^{(4)}(\tau_1, \tau_3, 2, -1)$, $\tilde{Y}^{(4)}(\tau_1, \tau_3, -1, -1)$ and $\tilde{Y}^{(4)}(\tau_1, \tau_3, -1, 2)$ cannot be obtained within an experiment using a two-pulse sequence, because they comprise the interaction with three independent pulses. Thus, there is no connection between these 2D nanoscopy signals and interferometric autocorrelation (IAC) measurements. However, the contributions corresponding to an IAC signal are also contained in the total photoemission signal $Y^{(4)}(\tau_1, \tau_3, \varphi_{21}, \varphi_{31})$, but they exhibit different relative phase factors $\Phi(\beta, \gamma, \varphi_{21}, \varphi_{31})$ and appear at different spectral positions, since at least one of the parameters α , β or γ has to be zero.

The 2D nanoscopy signal which is associated by its interaction parameters $\alpha = 1, \beta = 0$ and $\gamma = -1$ to the reverse transient grating signal of optical 2D spectroscopy [316] is not covered by the above consideration. Since the absolute values of the parameters add up to $|\alpha| + |\beta| + |\gamma| = 2$, the total number of interactions $n = 4$ is not reached. However, the two missing interactions have to occur without a change of the parameters. This is only possible if the interactions take place within one of the excitation pulses and are counteracting on the oscillation frequency, i.e. have opposite frequency components. This is expressed by temporal contributions $B_{d_{\pm}}^{d_{\pm}}(t, \tau)$ with non-zero d_+ and d_- . These contain a non-oscillating term $A^+(t + \tau)A^-(t + \tau)$ which is identical to the local field intensity generated by the local response after excitation by the respective laser pulse. Effectively, the oscillatory part as well as the phase factor remain unaffected by

the additional interactions and are directly connected to Eqs. (E.20) and (4.30). However, the delay-dependence of the signal changes according to the involved pulse. Since the additional interactions can take place during either of the excitation pulses, three contributions add up to $\tilde{\mathcal{P}}(t, \tau_1, \tau_3, 1, 0, -1)$ and lead to the partial photoemission yield

$$\tilde{Y}^{(4)}(\tau_1, \tau_3, 0, -1) \propto \Theta(\tau_1)\Theta(\tau_3)e^{i(\omega_{L_0}-\omega_L)-\gamma_{L_0}\tau_1}e^{i(\omega_{L_0}-\omega_L)-3\gamma_{L_0}\tau_3} \times \{e^{-2\gamma\tau_1} + 2 + e^{+2\gamma\tau_3}\}. \quad (4.37)$$

The factor of two for the second summand is caused by the twice higher number of permutations $c_{0,1,1}^{1,1,0} = 4$ that are achieved for the contribution with the additional interactions during the second excitation pulse. In case of the first and third pulse the weights are $c_{1,0,1}^{2,0,0} = c_{0,0,2}^{1,0,1} = 2$.

The spectral 2D nanoscopy signal $\tilde{Y}^{(4)}(\omega_{\tau_1}, \omega_{\tau_3}, 0, -1)$ is presented in Figure 4.9d. The spectral detuning of the resonance peak is in both frequency directions identical to the difference between oscillator frequency and rotating frame frequency, i.e. $\Delta\omega_{\tau_1} = \Delta\omega_{\tau_3} = (\omega_{L_0} - \omega_L)$. In contrast to the others signals presented in Figure 4.9, the spectral width at $(\sqrt{2})^{-1}$ -level is not an integer multiple of γ_{L_0} , because of the interplay of the three contributions to the reverse transient grating signal.

Similar results as for the reverse transient grating signal $\tilde{Y}^{(4)}(\tau_1, \tau_3, 0, -1)$, i.e. a reshaping of the spectral feature due to several interactions that effectively do not change the values of α , β and γ , are observed for the photon echo signal at higher orders of nonlinearity ($n \geq 6$). This aspect is dealt with in simulations presented in 4.3.2 and 4.3.3.

4.2.4. Phase Cycling

In contrast to conventional optical two-dimensional spectroscopy, phase matching is not applicable in 2D nanoscopy to select specific contributions to the detected signal for two reasons. First, the pulse shaper based setup of 2D nanoscopy requires a collinear geometry of the excitation pulse sequence. Accordingly, all excitation pulses have the same wave vector \mathbf{k} . Second, the detected photoemission signal is incoherent and does not contain any momentum information irrespective from the excitation geometry.

In 2D nanoscopy phase cycling [46, 49, 296] is employed utilizing the different phase-dependences of the contributing signals (see Eqs. (4.22) and (4.30)). Already for the coherently emitted four-wave mixing signals of optical nonlinear spectroscopy it has been shown that particular signal contributions are distinguishable by their individual dependence on the relative phases between the pulses of the excitation sequence [317, 318]. Warren *et al.* demonstrated that by phase cycling even for incoherently emitted signals, e.g. fluorescence of excited chromophore states, the full coherent information is retrieved [46, 49]. Phase cycling reconstructs a specific signal by linear combination of signals which have been obtained under identical conditions except for the relative phases of the pulse sequence. In analogy to the phase matching condition in optical two-dimensional spectroscopy the set of phase cycling coefficients, which state the contribution of a particular phase setting to this linear combination, are unique for an excitation pathway as long as sufficient phase combinations are recorded. An instructive explanation of phase cycling is given by [296]. The influence of phase cycling on simulated 2D nanoscopy data is presented in the next section in Figure 4.15.

As discussed in the previous section, the partial contributions $\tilde{Y}^{(n)}(\mathbf{r}, \tau_1, \tau_3, \beta, \gamma)$ contain different spectral information. In the 2D nanoscopy experiment only the total photoemission yield after n interactions

$$Y^{(n)}(\mathbf{r}, \tau_1, \tau_3, \varphi_{21}, \varphi_{31}) = \sum_{\beta, \gamma} \tilde{Y}^{(n)}(\mathbf{r}, \tau_1, \tau_3, \beta, \gamma) \Phi(\beta, \gamma, \varphi_{21}, \varphi_{31}) \quad (4.38)$$

is accessible. The phase factor $\Phi(\beta, \gamma, \varphi_{21}, \varphi_{31})$ uniquely determines the dependence of the partial contributions $\tilde{Y}^{(n)}(\mathbf{r}, \tau_1, \tau_3, \beta, \gamma)$ of the relative phase differences between the excitation pulses. A variation of φ_{21} and φ_{31} generates oscillations of the signal with periodicities given by β and γ . To obtain a partial contribution with specific values of β and γ , the obtained signal $Y^{(n)}(\mathbf{r}, \tau_1, \tau_3, \varphi_{21}, \varphi_{31})$ has to be projected onto the corresponding basis vectors of the phase-dependence space:

$$\tilde{Y}^{(n)}(\mathbf{r}, \tau_1, \tau_3, \beta, \gamma) = \frac{1}{4\pi^2} \int_0^{2\pi} \int_0^{2\pi} Y^{(n)}(\mathbf{r}, \tau_1, \tau_3, \varphi_{21}, \varphi_{31}) e^{-i(\beta\varphi_{21} + \gamma\varphi_{31})} d\varphi_{21} d\varphi_{31} . \quad (4.39)$$

In an experiment the integration can only be achieved by sampling the phase differences within the pulse sequence in finite steps $\Delta\varphi_{21} = 2\pi/L$ and $\Delta\varphi_{31} = 2\pi/M$. The integral is therefore replaced by a discrete sum with $L \times M$ sampling points

$$\tilde{Y}^{(n)}(\mathbf{r}, \tau_1, \tau_3, \beta, \gamma) = \frac{1}{LM} \sum_{m=0}^{M-1} \sum_{l=0}^{L-1} Y^{(n)}(\mathbf{r}, \tau_1, \tau_3, l \cdot \Delta\varphi_{21}, m \cdot \Delta\varphi_{31}) c_{L,M}^{\beta, \gamma}(l \cdot \Delta\varphi_{21}, m \cdot \Delta\varphi_{31}) , \quad (4.40)$$

where the weight of each sampling points is determined by the respective phase cycling coefficient

$$c_{L,M}^{\beta, \gamma}(l \cdot \Delta\varphi_{21}, m \cdot \Delta\varphi_{31}) = e^{-i[l\beta\Delta\varphi_{21} + m\gamma\Delta\varphi_{31}]} . \quad (4.41)$$

In addition to the wanted signal $\tilde{Y}^{(n)}(\mathbf{r}, \tau_1, \tau_3, \beta, \gamma)$ also aliased signals can remain after phase cycling. This is caused by the discrete Fourier transformation which has a periodicity given by the number of sampling points in the corresponding dimension. Thus, the signal $\tilde{Y}^{(n)}(\mathbf{r}, \tau_1, \tau_3, \beta, \gamma)$ cannot be separated from those signals with $\tilde{Y}^{(n)}(\mathbf{r}, \tau_1, \tau_3, \beta + pL, \gamma + qM)$ for integers p and q . In this thesis a phase cycling scheme was used that is given by setting $L = 4$ and $M = 4$. The resulting 4×4 phase cycling scheme is very flexible, since the identical set of delay- and phase-dependent data provides unambiguous spectroscopic signals $\tilde{Y}^{(4)}(\mathbf{r}, \tau_1, \tau_3, \beta, \gamma)$ for all possible combinations of β and γ involving interactions with all three pulses of the excitation sequence. Thus, if higher order contributions to the measured signal $Y^{(n)}(\mathbf{r}, \tau_1, \tau_3, \varphi_{21}, \varphi_{31})$ with $n > 4$ are weak or even completely excluded for experimental reasons, only the desired signal is selected by this phase cycling scheme. To specifically filter the photon echo signal $\tilde{Y}^{(4)}(\mathbf{r}, \tau_1, \tau_3, 2, -1)$, a phase cycling scheme involving only 10 steps is sufficient [296]. However, it cannot be employed for the selection of different contributions.

4.3. Simulation of Coherent 2D Nanoscopy

This section discusses a Fourier transform time domain simulation technique that numerically calculates 2D nanoscopy spectra in strongly dephasing systems for arbitrary spectral response

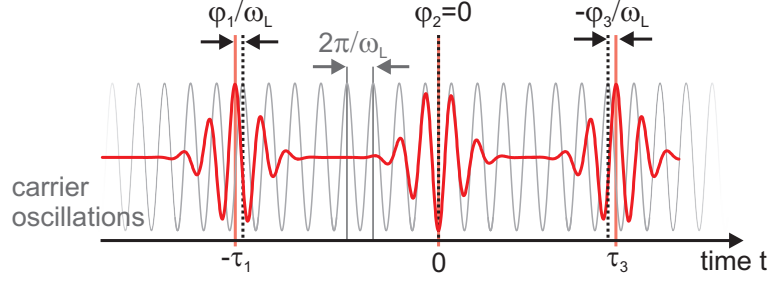


Figure 4.10.: Laser pulse sequence $E_3(t, -\tau_1, 0, \tau_3, \varphi_1, 0, \varphi_3)$ containing three subpulses with identical intensity (red line) and carrier oscillations (gray line) of the reference system oscillating with the laser frequency ω_L , i.e. with a period time $2\pi/\omega_L$. The delays τ_1 , τ_2 and τ_3 shift the pulse envelopes of the subpulses. The relative phases φ_1 , φ_2 and φ_3 are visible as offset of the field oscillation with respect to the carrier oscillations. The second subpulse was set to zero delay and zero relative phase.

functions $A(\omega)$ by explicitly calculating the temporal local electric field corresponding to the theoretical derivations in Section 4.2.2. By analogy with the 2D nanoscopy experiments (see Chapters 5.3 and 6.3) the simulated delay- and phase-dependent photoemission signal $Y^{(4)}(\tau, t, \varphi_\tau, \varphi_t)$ is phase cycled and Fourier transformed to retrieve the two-dimensional signal contributions $\tilde{Y}^{(4)}(\omega_\tau, \omega_t, \beta, \gamma)$ (see Section 4.3.1). To facilitate the understanding of the basic principles of the simulation technique and of the different representations of the simulated signals, Section 4.3.1 mainly deals with Lorentz oscillators excited by delta-shaped excitation pulses. However, in the Fourier transform time domain simulations it is possible to employ excitation sequence with realistic electric field pulses, i.e. exhibiting a limited spectral bandwidth, as well as to change the nonlinear order N of the multiphoton photoemission processes. Thus, it predicts two-dimensional spectra in strongly dephasing systems even for conditions that cannot be easily treated analytically (see Section 4.3.2). In Section 4.3.3 a fast and reliable method for retrieving spatial resolved spectral information from measured 2D nanoscopy spectra is introduced which is utilized in the evaluation of the experimental data in Chapter 6.3.

4.3.1. Fourier Transform Time Domain Simulations

In time domain the electric field E_p^+ of the excitation pulse sequence with p pulses of identical intensity is described by a sum over the individual electric field pulses:

$$E_p^+(t, \tau_1, \dots, \tau_p, \varphi_1, \dots, \varphi_p) = \sum_{n=1}^p E_n^+(t, \tau_n, \varphi_n) = \frac{1}{p} \sum_{n=1}^p E_L^+(t - \tau_n) e^{i[\omega_L \tau_n + \varphi_n]}. \quad (4.42)$$

$E_n^+(t)$ is the complex electric field of the n -th laser pulses in the sequence. The pulses are shifted in time by their respective delay τ_n and in phase by φ_n . In the overlap of the individual pulses constructive and destructive interference takes place according to the relative delays and phases. Similar to Eq. (4.21) a rotating frame definition of the electric field is used. The phase term $\omega_L \tau_n$ shifts the oscillations within the pulse so that the temporal displacement by τ_n does only effect a shift of the pulse envelope but not of the phase relation with respect to the carrier oscillations of the original laser pulse $E_L^+(t)$. Hence, two pulses separated by for example $\tau_n - \tau_{n+1} = \pi/\omega_L$ still interfere constructively, if they have the identical values $\varphi_n = \varphi_{n+1}$ which denotes the phase difference to the carrier oscillations. An example for a three pulse sequence

$E_3(t, -\tau_1, 0, \tau_3, \varphi_1, 0, \varphi_3)$ is given in Figure 4.10. The three subpulses have identical envelopes but differ in their temporal positions determined by their respective delays τ_1 , τ_2 and τ_3 , where τ_2 is set to 0 fs, as well as their relative phases φ_1 , φ_2 and φ_3 with respect to the rotating frame, i.e. the carrier oscillations at the laser frequency ω_L .

In the simulations the temporal local electric field is calculated by inverse Fourier transformation of the product of the linear spectral response function and the spectral representation of the electric field of the excitation pulse sequence.

$$E_{loc}(t, \tau_1, \dots, \tau_p, \varphi_1, \dots, \varphi_p) = \mathcal{F}^{-1} \{A(\omega)E_p(\omega, \tau_1, \dots, \tau_p, \varphi_1, \dots, \varphi_p)\} \quad (4.43)$$

Hence, the convolution in time domain can be circumvented, which would require a high computational effort for the simulations. The electric field of the excitation pulse sequence in spectral domain is obtained via Fourier transformation of Eq. (4.42):

$$E_p^+(\omega, \tau_1, \dots, \tau_p, \varphi_1, \dots, \varphi_p) = \sum_{n=1}^p E_n^+(\omega, \tau_n, \varphi_n) . \quad (4.44)$$

Substituting the single pulse spectral field by

$$\begin{aligned} E_n^+(\omega, \tau_n, \varphi_n) &= \frac{1}{p} \mathcal{F} \{E_L^+(t - \tau_n) e^{i[\omega_L \tau_n + \varphi_n]}\} \\ &= \frac{1}{p} \mathcal{F} \{E_L^+(t) \circ \delta(t - \tau_n)\} e^{i[\omega_L \tau_n + \varphi_n]} \\ &= \frac{E_L^+(\omega)}{p} e^{-i[(\omega - \omega_L)\tau_n - \varphi_n]} \end{aligned} \quad (4.45)$$

yields the spectral electric field of the pulse sequence

$$\begin{aligned} E_p^+(\omega, \tau_1, \dots, \tau_p, \varphi_1, \dots, \varphi_p) &= \frac{E_L^+(\omega)}{p} \sum_{n=1}^p e^{-i[(\omega - \omega_L)\tau_n - \varphi_n]} \\ &= E_L^+(\omega) M_p(\omega, \tau_1, \dots, \tau_p, \varphi_1, \dots, \varphi_p) . \end{aligned} \quad (4.46)$$

Now, the local field in time domain $E_{loc}(t)$ is obtained by inserting $E_p(\omega)$ into Eq. (4.43). The multiplication of the local response function $A(\omega)$ with the laser spectrum $E_L(\omega)$ determines the identical envelopes and phase modulations of the p pulses of the local electric field after Fourier transformation. All delay and phase parameters are combined to a single function $M_p(\omega, \tau_1 \dots \tau_N, \varphi_1 \dots \varphi_N)$ that defines the modulations of the spectral amplitude and spectral phase that have to be applied to the original spectrum $E_L(\omega)$ to generate the pulse sequence. Thus, $M_p(\omega, \tau_1 \dots \tau_p, \varphi_1 \dots \varphi_p)$ represents the transmission and dispersion settings that a pulse shaper in amplitude and phase shaping configuration has to achieve in the 2D nanoscopy experiments.

The simulation of 2D nanoscopy spectra requires the calculation of the local electric field in time domain while varying the delay and phase parameters of the excitation sequence consisting of three independent pulses. The second pulse of the sequence contains the two central pulses in a

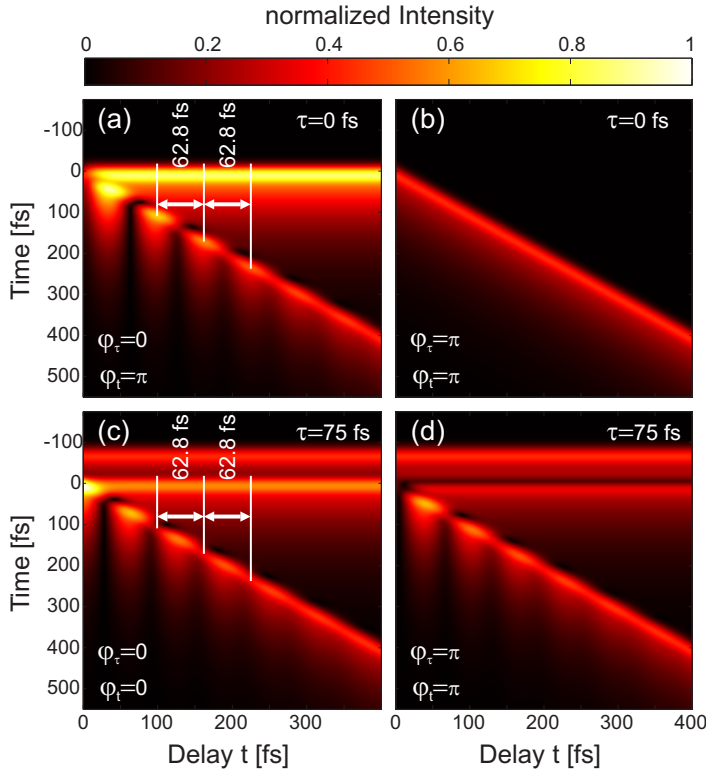


Figure 4.11: Simulated temporal local field intensities of a Lorentz oscillator ($\omega_{Lo} = 2.46$ rad/fs, $\gamma_{Lo} = 0.01$ rad/fs) excited by a laser pulse sequence in dependence of delay t . The excitation sequence consisted of 17.2 fs Gaussian shaped laser pulses at center frequency 2.36 rad/fs. The delay τ and the relative phases φ_τ and φ_t are indicated in the plots. (a) The arrows and vertical lines mark the delay differences between the beating maxima of the third pulse in the sequence. (b) The first two pulses are not visible, because they appear at identical temporal positions and interfere destructively ($\tau = 0$ fs and $\varphi_\tau = \pi$). Accordingly, no beating is observed in (b). (c) Intensity minima are observed at the same positions as in (a) due to the change of φ_t from 0 to π . (d) Identical phases as in (b), but $\tau = 75$ fs. Incomplete interference of first pulses leads to beating of third pulse intensity.

four-pulse sequence of the general excitation scheme depicted in Figure 4.3c shifted to identical temporal positions. In analogy to the parameter definition in 2D spectroscopy (Figure D.2) in the following the relative delays $\tau_2 - \tau_1$ and $\tau_3 - \tau_2$ are denoted as τ and t , respectively. The notations of the phase differences change to

$$\varphi_\tau = \varphi_{21} = \varphi_2 - \varphi_1 \quad (4.47)$$

$$\text{and } \varphi_t = \varphi_{31} - \varphi_{21} = \varphi_3 - \varphi_2. \quad (4.48)$$

Using a three-pulse sequence, the parameters T and φ_T , which would define the relative delay and relative phase between the central pulses in a four-pulse sequence (see Figure 4.3), are set to zero. A further adjustment is given by using a three-pulse sequence with identical pulse envelopes, instead of employing a center pulse with enhanced intensity caused by the constructively interfering central pulses in a four-pulse sequence. This operation has a minor effect on the obtained signal contributions, as it changes only a constant factor in the phase cycled signals with $|\alpha| + |\beta| + |\gamma| = n$. In the other cases, the spectral positions of the signals remain unchanged, but the shape of the features is altered as the relative weight of the contributions involving the center pulse are reduced. For each phase and delay step the total photoemission yield is determined by

$$Y^{(n)}(\tau, t, \varphi_\tau, \varphi_t) = \int_{-\infty}^{\infty} (I_{loc}(t, \tau, t, \varphi_\tau, \varphi_t))^{n/2} dt. \quad (4.49)$$

The number of interactions was set to $n = 4$ for the simulations presented in this section. Hence, the photoemission rate depends on the square of the momentary field intensity.

A representation of the local electric field intensity as a function of the delay t between the two last pulses of the excitation sequence is given in Figure 4.11. The employed excitation sequence contained three Gaussian shaped laser pulses with temporal width of 17.2 fs at a center frequency of $\omega_L = 2.36$ rad/fs as depicted schematically in Figure 4.6. The delay τ between the first and the center pulse is fixed in each of the plots. The same holds for the relative phases φ_τ and φ_t between the first and the second as well as between the second and the third pulse, respectively. The delay t is varied in steps of 2 fs from 0 fs to 400 fs. At each delay step the temporal intensity of the local field is plotted. The simulated local response function belongs to a Lorentz oscillator at $\omega_{Lo} = 2.46$ rad/fs and a width determined by $\gamma_{Lo} = 0.01$ rad/fs.

The data that is presented in Figure 4.11 is only a small fraction of the full scan that is necessary for simulating 2D spectra. The phase combinations have to be varied according to the phase cycling scheme that will be applied. The delays τ and t both have to be varied in sufficiently small steps and covering a sufficiently large delay range to have access to all relevant spectral information with satisfying spectral resolution.

The position of the pulses is visible in the plots as three linear lines. Two of the lines are horizontal, because they represent the local electric field intensity excited by the first two laser pulses which have fixed temporal positions. In Figure 4.11a and b the first two local field pulses overlap. Hence, they are not distinguishable. The third line, i.e. the local electric field generated by the third laser pulse, shifts towards positive time positions by the value of the delay t . Differences in the plots are caused by the parameters τ , φ_τ and φ_t . A spectral phase $\varphi_t = \pi$ is used in Figure 4.11a, b and d leading to a destructive interference of the last pulses at the zero delay position. For later delays a beating of the third pulse intensity is observed in Figure 4.11a, because the oscillations of the local field pulses are detuned from the rotating frame frequency by 0.1 rad/fs. As a consequence, the beating period is 62.8 fs. For $\varphi_t = 0$ the interference between center excitation pulse and last excitation pulse is constructive causing a shift of the beat pattern presented in Figure 4.11c. In Figure 4.11b no beating occurs, as the first two pulses cancel each other completely and only the third pulse remains. After separating the first two pulses by 75 fs (Fig. 4.11d) the beating is observed also for this phase combination.

The identical Lorentz oscillator response function as in Figure 4.11 is used to simulate a 2D nanoscopy spectrum. The results of this simulation are depicted in Figures 4.12, 4.13 and 4.14. For excitation a constant spectrum was applied leading to a sequence of δ -shaped laser pulses. The definition of a center frequency cannot be applied to these infinitesimally short excitation events. However, the evolution of the excitation pulse phases is determined by the rotating frame frequency which is set to $\omega_L = 2.36$ rad/fs. The delays τ and t were varied independently from 0 fs to 1000 fs in steps of 5 fs. In Figures 4.12 and 4.13 only a detail of this two-dimensional delay range is plotted, but the complete data is used in the Fourier transformation for generating the spectral signal (see Fig. 4.14). The rotating frame definition of the electric field pulses (see Eq. (4.42)) allows for a flexible choice of the sampling point distance. The step size determines the maximal frequency detuning that is detectable. The employed step size of 5 fs is larger than the average oscillation period of the laser pulses (2.66 fs). Nevertheless, for detecting signals with small detuning from the laser frequency the spacing is sufficient. Thus, much larger step sizes are possible than without using the rotating frame, enabling to cover the two-dimensional

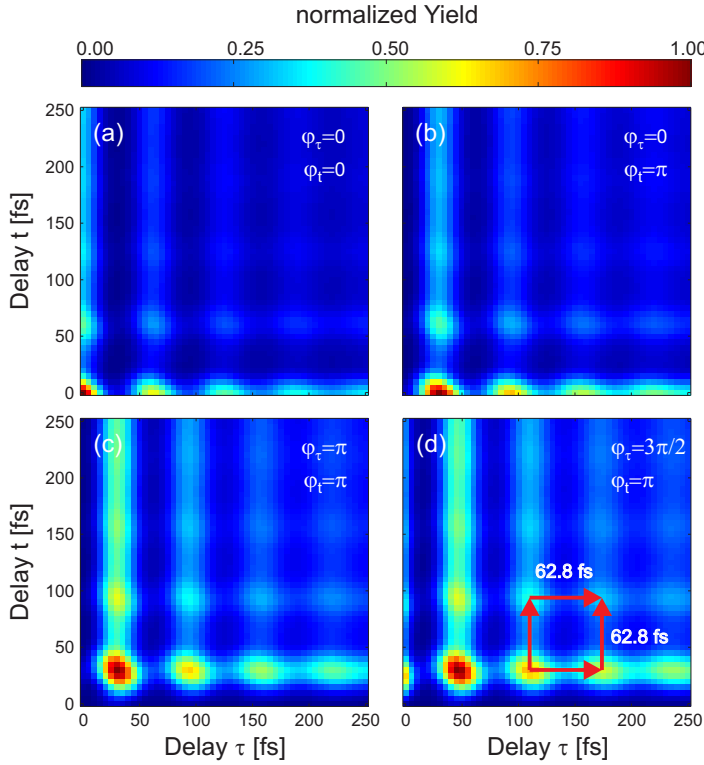


Figure 4.12: Simulated 2D nanoscopy signals for a single Lorentz oscillator ($\omega_{Lo} = 2.46$ rad/fs and $\gamma_{Lo} = 0.01$ rad/fs) driven by a constant excitation spectrum before phase cycling. Delay-dependent signals $Y^{(4)}(\tau, t, \varphi_\tau, \varphi_t)$ differ in the relative phases φ_τ and φ_t of the excitation pulse sequence and are normalized to their respective maxima. Delay-dependent signal for (a) $\varphi_\tau = 0$ and $\varphi_t = 0$, (b) $\varphi_\tau = \pi$ and $\varphi_t = 0$, (c) $\varphi_\tau = \pi$ and $\varphi_t = \pi$ and (d) $\varphi_\tau = 3\pi/2$ and $\varphi_t = \pi$. In all photoemission signals a beating of the yield is observed. The positions of the maxima depend on the phase combinations. The red arrows in (d) mark the beating period of 62.8 fs for both delay directions. The beating period corresponds to a detuning by 0.1 rad/fs.

delay range with fewer sampling points [314]. This is most advantageous in the experimental realization of 2D nanoscopy, but also leads to a reduced computational effort for the simulations. For sixteen phase combinations the delay-dependent photoemission yield $Y^{(4)}(\tau, t, \varphi_\tau, \varphi_t)$ was simulated. The phases φ_τ and φ_t were varied independently in steps of $\pi/2$ from 0 to $3\pi/2$. Due to Eqs. (4.47) and (4.48) this also corresponds to an independent scan of φ_{21} and φ_{31} . Accordingly, a 4×4 phase cycling scheme, providing 4 sampling points for each relative phase dimension is possible with the obtained data (see Section 4.2.4). The simulated delay-dependent signals of four of these phase combinations are presented in Figure 4.12. The photoemission yield is a real and positive quantity. Therefore, the normalized yield ranges from zero to the maximum value of the respective plot. To generate the photoemission signal in Figure 4.12a, a pulse sequence without phase offset between the carrier oscillations and the electric fields of the pulses was employed, as $\varphi_\tau = 0$ and $\varphi_t = 0$. The third phase $\varphi_\tau = 0$ is fixed to zero for the complete simulation. Consequently, the local electric field pulses interfere constructively at zero delay, i.e. the complete overlap of all pulses, and a distinct maximum of the photoemission is visible there. If either of the delays is increased, the yield strongly decreases. Along both axes as well as for the diagonal a minimal signal is achieved for delays of approximately 30 fs. The signal recuperates with a further increase of the delays and reaches a local maximum at $\tau = t \approx 63$ fs. This beating behavior is directly connected to the interference of the local electric field pulses as depicted in Figure 4.11. It is caused by the detuned oscillator frequency. Consequently, a beating period of 62.8 fs is expected. However, the exact positioning of the local minima and maxima is also affected by the decay of the signal according to the oscillator lifetime. In case of $\varphi_\tau = \pi$ and $\varphi_t = 0$ (Figure 4.12b) the highest photoemission is observed shifted towards positive τ values. The reason for this lies in the destructive interference of the first pulse with the other pulses of

(a)		φ_{21}			
		0	$\pi/2$	π	$3\pi/2$
φ_{31}	0	1	-1	1	-1
	$\pi/2$	i	$-i$	i	$-i$
	π	-1	1	-1	1
	$3\pi/2$	$-i$	i	$-i$	i

(b)		φ_τ			
		0	$\pi/2$	π	$3\pi/2$
φ_t	0	1	$-i$	-1	i
	$\pi/2$	i	1	$-i$	-1
	π	-1	i	1	$-i$
	$3\pi/2$	$-i$	-1	i	1

Table 4.1.: Phase cycling coefficients for filtering out the photon echo signal $\tilde{Y}^{(4)}(\tau, t, 2, -1)$ by 4×4 phase cycling, i.e. $L = M = 4$. Colors are employed to facilitate the identification of the values. (a) Phase cycling coefficients $c_{4,4}^{2,-1}(\varphi_{21}, \varphi_{31})$ according to Eq. (4.41). (b) Phase cycling coefficients $\bar{c}_{4,4}^{2,-1}(\varphi_\tau, \varphi_t)$ according to Eq. (4.50).

the sequence in the overlap. Thus, the beating pattern has changed along the τ direction. The minima and maxima positions are shifted by half the beating period with respect to Figure 4.12a. A similar observation is made in Figure 4.12c corresponding to an excitation sequence with $\varphi_\tau = \pi$ and $\varphi_t = \pi$. Here, the beating pattern is shifted in both delay direction with respect to 4.12a. The lowest yield is obtained in the overlap of all pulses and the highest yield is achieved when the pulses are separated by approximately 60 fs. In Figure 4.12d the relative phases are set to $\varphi_\tau = 3\pi/2$ and $\varphi_t = \pi$. Four red arrows are plotted to guide the eye. They emphasize that the beating period observed in the data is in a good correspondence to the expected value based on the detuning of the oscillator.

A separate Fourier transformation of the delay data for each phase combination creates two-dimensional signals in frequency domain that contain the contributions of all excitation pathways. This will be further discussed at the example of Figure 4.15. To selectively obtain a particular signal, phase cycling has to be applied. In principle, this is possible prior or after the Fourier transformation, as this is a linear mathematical operation. To save computational effort, phase cycling of the delay data is favorable, since only a single Fourier transformation is necessary and allocated memory is reduced.

The phase cycling coefficients of the photon echo signals $c_{4,4}^{2,-1}(\varphi_{21}, \varphi_{31})$, i.e. the weights of the delay-dependent signals in the linear combination, are calculated using Equation (4.41). The results are displayed in Table 4.1a. By substituting $\varphi_{21} = \varphi_\tau$ with $\varphi_{31} = \varphi_t + \varphi_\tau$ the phase cycling coefficients can also be expressed as a function of φ_τ and φ_t :

$$c_{4,4}^{2,-1}(\varphi_{21}, \varphi_{31}) = e^{-i[2\varphi_{21} - \varphi_{31}]} = e^{-i[2\varphi_\tau - (\varphi_t + \varphi_\tau)]} = e^{-i[\varphi_\tau - \varphi_t]} = \bar{c}_{4,4}^{2,-1}(\varphi_\tau, \varphi_t). \quad (4.50)$$

The coefficients in $(\varphi_\tau, \varphi_t)$ -notation are presented in Table 4.1b. The choice of notation does not change the value of the coefficient for a particular signal. Furthermore, for each specific phase combination $(\varphi_{21}, \varphi_{31})$ or $(\varphi_\tau, \varphi_t)$ the phase cycling coefficient remains independent from the number of sampling points of the phase cycling scheme. For example, $c_{4,4}^{2,-1}(\pi, \pi) = \bar{c}_{4,4}^{2,-1}(\pi, 0) = -1$ is valid for 2×2 , 4×4 or even 8×6 and all other cases of phase cycling that include this sampling point.

After application of the phase cycling scheme for reconstruction of the photon echo signal the delay-dependent data $\tilde{Y}^{(4)}(\tau, t, 2, -1)$ is complex valued. Instead of a beating pattern the

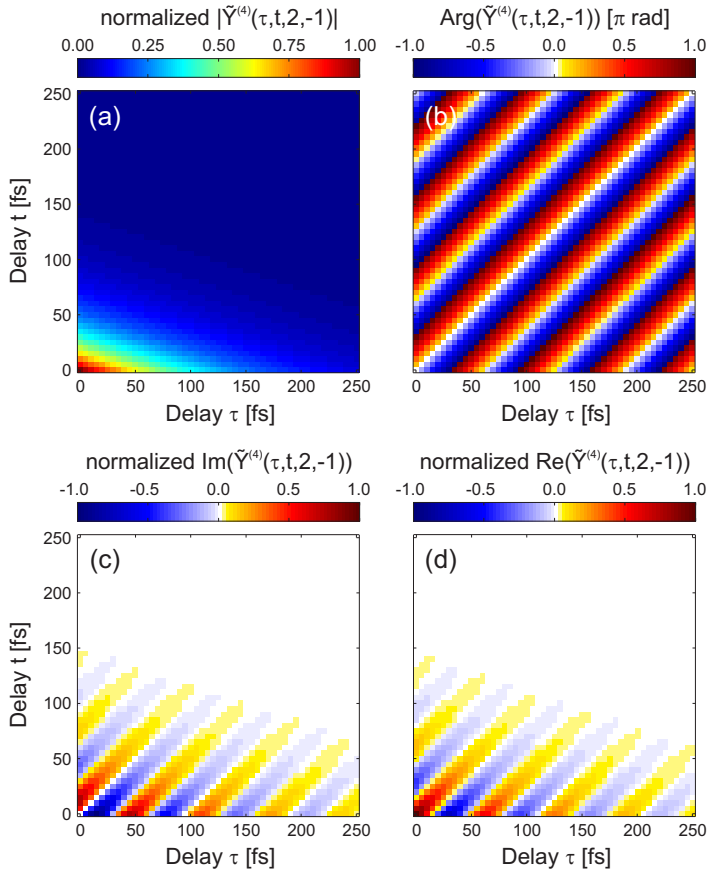
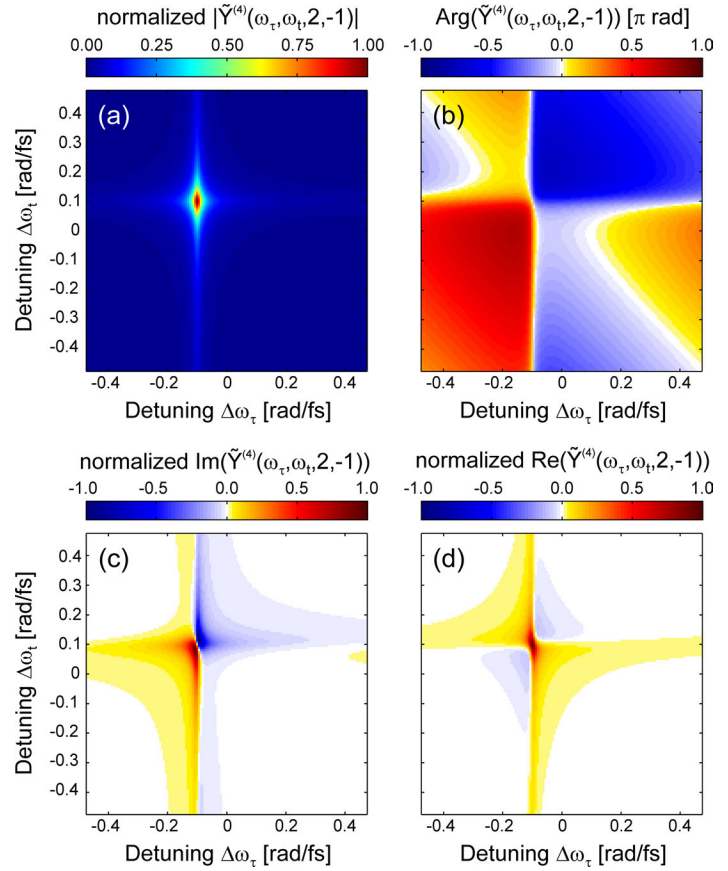


Figure 4.13: Simulated phase cycled 2D nanoscopy time domain signals for a single Lorentz oscillator driven by a constant excitation spectrum. (a-d) Delay-dependent photoemission signal $\tilde{Y}^{(4)}(\tau, t, 2, -1)$ of a single Lorentz oscillator at a center frequency $\omega_{Lo} = 2.46$ rad/fs and with a spectral width $\gamma_{Lo} = 0.01$ rad/fs after application of phase cycling scheme for reconstruction of the photon echo signal. (a) The amplitude of the simulated signal decays exponentially in τ and in t direction. (b) The phase of the signal is increasing linearly in antidiagonal direction. (c) Imaginary part of the delay-dependent signal. (d) Real part of the delay-dependent signal.

amplitude (Figure 4.13a) now exhibits a smooth exponential decay for both pulse delay directions. The decay constants for both delay directions differ noticeably. Along t the decay takes place three times faster. This behavior is related to the faster blurring of the beating pattern along the t direction in the not phase cycled data, whereas the decay of the yield appears symmetric in Figure 4.12. The asymmetric decay ratio is in a good accordance to the prediction of Eq. (4.35). The phase of the signal (Figure 4.13b) is increasing linearly in antidiagonal direction, i.e. for decreasing τ and increasing t , and is constant for the diagonal direction, i.e. for increasing τ and t . Due to wrapping the phase at π and $-\pi$ the periodic pattern emerges. Corresponding to the evolution of the phase in the imaginary and real part (Figure 4.13c and d, respectively) oscillations appear. The oscillation period is 62.8 fs for both directions delay directions. The different color scale used in these plots emphasizes the small oscillations in the imaginary and real part. Nevertheless, the decay of these signals is directly linked to the decay of the amplitude.

Fourier transformation of the phase cycled delay data generates a complex valued two-dimensional spectrum $\tilde{Y}^{(4)}(\omega_\tau, \omega_t, 2, -1)$. The amplitude and phase as well as the real and imaginary parts of the 2D spectrum corresponding to the simulated delay data are presented in Figure 4.14. The plot is centered around the rotating frame frequency $\omega_L = 2.36$ rad/fs. The displacement of a spectral feature from this central position indicates the frequency detuning $\Delta\omega_\tau$ and $\Delta\omega_t$ relative to the rotating frame. The Lorentz oscillator with center frequency $\omega_{Lo} = 2.46$ rad/fs, therefore, is shifted by $\Delta\omega_\tau = -0.1$ rad/fs and $\Delta\omega_t = 0.1$ rad/fs along the diagonal direction. The negative displacement along ω_τ is connected to the evolution of the delay-dependent phase

Figure 4.14: Simulated 2D nanoscopy spectrum $\tilde{Y}^{(4)}(\omega_\tau, \omega_t, 2, -1)$ obtained by two-dimensional Fourier transformation of delay axes in Figure 4.13. (a) The amplitude spectrum shows a resonance shifted by 0.1 rad/fs along the diagonal with respect to the excitation center frequency of $\omega_L = 2.36$ rad/fs. The spectral phase (b) is antisymmetric with respect to inversion around the resonance position. (c) The imaginary part of $\tilde{Y}^{(4)}(\omega_\tau, \omega_t, 2, -1)$ changes the sign at the resonance peak position. (d) In the real spectrum the simulated features show inversion symmetry with respect to the resonance position. At the resonance peak positive values are reached. In positive and negative diagonal direction a change of sign takes place.



given by Eq. (4.35) and shown in Figure 4.13b. As the delay-dependent amplitude is following an exponential function for both directions, the amplitude lineshape after Fourier transformation has a Lorentzian profile. However, the peak is elongated along the ω_t -axis by a factor of three. The linear increase of the phase along the antidiagonal delay direction corresponds to a spectral shift of the resonance peak towards negative ω_τ and positive ω_t frequency direction. The size of this spectral shift is given by the inverse oscillation period in Figure 4.13c and d. The spectral phase is zero at the resonance position and, consequently, the spectrum is completely real at the maximum of the peak. The real part of the 2D spectrum is symmetrically shaped, whereas the imaginary part and the phase are antisymmetric with respect to inversion around the resonance position.

An example for the influence of different degrees of phase cycling on 2D nanospectra is presented in Figure 4.15. The photoemission yield generated by a Lorentz oscillator with center frequency $\omega_{Lo} = 2.06$ rad/fs spectral width of $\gamma = 0.01$ rad/fs was simulated for the identical 4×4 phase combinations as used before and identical laser frequency $\omega_L = 2.36$ rad/fs. The linear combination of the two-dimensional delay data is performed partially (1, 2, 4 and 8 sampling points) and for all 16 steps. In the 1×1 phase cycling scheme the signal $Y^{(4)}(\tau, t, 0, 0)$ is directly Fourier transformed. Consequently, it includes all possible contributions to the signal. Spectral peaks that are shifted according to the detuning frequency $\omega_{Lo} - \omega_L$ are visible along the diagonals in all four quadrants of the spectrum and along the frequency axes. At the edges of the depicted frequency range spectral features appear that correspond to contributions oscillating with the

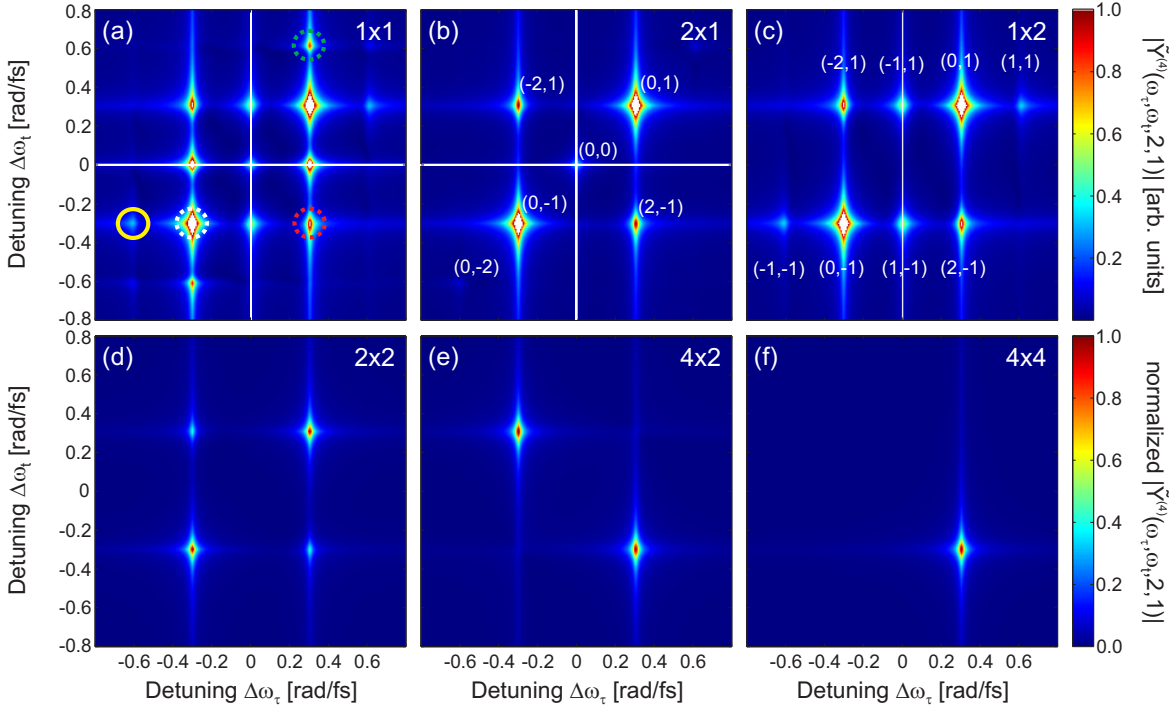


Figure 4.15.: Influence of phase cycling on amplitude spectra of photon echo contribution $\tilde{Y}^{(4)}(\omega_\tau, \omega_t, 2, -1)$ of a Lorentz oscillator with frequency detuning $\omega_{Lo} - \omega_L = -0.3$ rad/fs spectral width of $\gamma = 0.01$ rad/fs. The color scale in (a–c) was adjusted to show all features. The amplitude spectra in (d–f) are normalized to their respective maximum. (a) Direct Fourier transformation of the signals for $\varphi_{21} = 0$ and $\varphi_{31} = 0$. The circles mark the position of the contributions discussed in Figure 4.9. (b) 2×1 phase cycling eliminates spectral peaks with $\beta = \pm 1$ by employing two sampling points in φ_{21} -direction. The white parentheses indicate the values (β, γ) of the interaction parameters of the surviving features. (c) 1×2 phase cycling eliminates spectral peaks with $\gamma = \{-2, 0, 2\}$. (d) After 2×2 phase cycling those features remain which appear both in (b) as well as (c). (e) 4×2 phase cycling eliminates all spectral peaks except for $(2, -1)$ and $(-2, -1)$. (f) 4×4 phase cycling unambiguously retrieves the photon echo signal $\tilde{Y}^{(4)}(\omega_\tau, \omega_t, 2, -1)$.

doubled detuning frequency in one (off-diagonal positions) or even both (diagonal positions) frequency directions. Here, only those frequency combinations (ω_τ, ω_t) are allowed that satisfy Eqs. (4.25)–(4.27). The exemplary signals discussed in Section 4.2.3 are indicated by circles. The resonance peaks of the photon echo signal $\tilde{Y}^{(4)}(\omega_\tau, \omega_t, 2, -1)$ (dashed red) are located on the antidiagonal direction and those of the reverse transient grating signal $\tilde{Y}^{(4)}(\omega_\tau, \omega_t, 0, -1)$ (dashed white) on the diagonal. The spectral features corresponding to the third-order double quantum coherence signal $\tilde{Y}^{(4)}(\omega_\tau, \omega_t, -1, -1)$ (solid yellow) and the contribution analog to the reverse double quantum coherence signal $\tilde{Y}^{(4)}(\omega_\tau, \omega_t, -1, 2)$ (dashed green) are shifted in off-diagonal direction. The vertical line at $\Delta\omega_\tau = 0$ and the horizontal line at $\Delta\omega_t = 0$ are caused by the completely positive two-dimensional delay signal creating a non-oscillating offset. The 2×1 phase cycling involves the two phase combinations $(\varphi_\tau, \varphi_t) = \{(0, 0), (\pi, \pi)\}$ which corresponds to $(\varphi_{21}, \varphi_{31}) = \{(0, 0), (\pi, 0)\}$. The delay-dependent data for these two phase settings is subtracted. After phase cycling with these two sampling points the spectral peaks with $\beta = \pm 1$ have vanished. The others remain, as in these cases the difference to the β value

of the photon echo signal ($\beta = 2$) is given by $L = 2$ multiplied with an integer, where L is the order of the phase cycling in φ_{21} direction. Analog, the 1×2 phase cycling suppresses signals with $\gamma = \{-2, 0, 2\}$ including the complete offset at $\Delta\omega_t = 0$. The spectral positions of the remaining features are given by $(\Delta\omega_\tau, \Delta\omega_t) = (-(\beta+\gamma)[\omega_{Lo} - \omega_L], -\gamma[\omega_{Lo} - \omega_L])$.

In case of 2×2 phase cycling the offset is suppressed in both directions. Still, the 2×2 phase cycling includes redundant signals (see Figure 4.15c), but those peaks that are detuned by the doubled frequency, e.g. the third-order double quantum coherence signal, are not visible anymore. The 2D spectrum shows a symmetry with respect to inversion at the origin, since for all peaks positioned at $(\Delta\omega_\tau, \Delta\omega_t)$ also the peaks at $(-\Delta\omega_\tau, -\Delta\omega_t)$ are allowed due to aliasing effects. The dominant spectral features are located on the diagonal, i.e. on the line with $\Delta\omega_\tau = \Delta\omega_t$. These diagonal features vanish completely in the 4×2 phase cycling scheme, since also $\beta = 0$ is excluded. The observed spectral features belong to the photon echo signal and its complex conjugated process which has inverted frequency axes. Only the full 4×4 phase cycling scheme (see Figure 4.15f) is able to create totally asymmetric 2D spectra and to completely remove the redundant spectral features for the given 4×4 combinations of φ_{21} and φ_{31} . Finally, the isolated peak at $-\Delta\omega_\tau = \Delta\omega_t = -0.3$ rad/fs remains.

Figure 4.15a presents all contributions $\tilde{Y}^{(4)}(\omega_\tau, \omega_t, \beta, \gamma)$, since effectively no phase cycling is applied. It is obvious that the different spectral contributions differ in their respective amplitudes. The peaks of the photon echo signal appear to be weak compared to other contributions, e.g. the reverse transient grating signal $\tilde{Y}^{(4)}(\omega_\tau, \omega_t, 0, -1)$. Consequently, by filtering the photon echo specific phase combination most of the obtained electron yield is rejected. Thus, in the evaluation of measurements with low signal-to-noise ratio it is advantageous to additionally evaluate other signal contributions, such as the reverse transient grating signal, because these contain complementary information on the same local linear response function.

2D nanoscopy has a very high spatial resolution, thus the ultimate goal is to probe isolated oscillators, e.g. single molecules. For those systems an inhomogeneous broadening cannot occur by definition. However, even in the case of a contribution of several oscillators at a particular spatial position 2D nanoscopy allows for distinguishing between homogeneous and inhomogeneous linewidths. Figure 4.16 presents simulated 2D spectra for an ensemble of oscillators with varying center frequency. Each of the oscillators has a spectral width $\gamma_{Lo} = 0.02$ rad/fs. The oscillators are distributed around a center frequency of $\omega_c = 2.36$ rad/fs according to a Gaussian distribution with standard deviation $\sigma = 0.09$ rad/fs. The spectral signal is obtained by calculating the phase cycled delay signals of the Lorentz oscillator on equidistant spectral positions and adding all contributions weighted by the distribution function. The phase combination corresponding to the photon echo signal in conventional 2D spectroscopy is used. Afterwards, the combined data is Fourier transformed to generate the spectrum shown in Figure 4.16a. The inhomogeneous broadening of the simulated spectra appears along the white dotted diagonal line in negative ω_τ and positive ω_t direction. This is the direction a spectral peak in the photon echo signal shifts, if the resonance frequency increases. In the simulated 2D spectrum it is obvious that the spectral feature is elongated and its major principal axis is oriented along this diagonal direction. The width along the orthogonal direction (dashed) is considerably smaller.

The spectral amplitudes along the diagonal and antidiagonal cuts through the resonance peak are depicted in Figure 4.16b as circles and triangles. The peak of the spectral amplitude along the diagonal direction exhibits attributes of a Gaussian distribution and is clearly broader than the lineshape in antidiagonal direction. The homogeneous lineshape belonging to a single oscillator

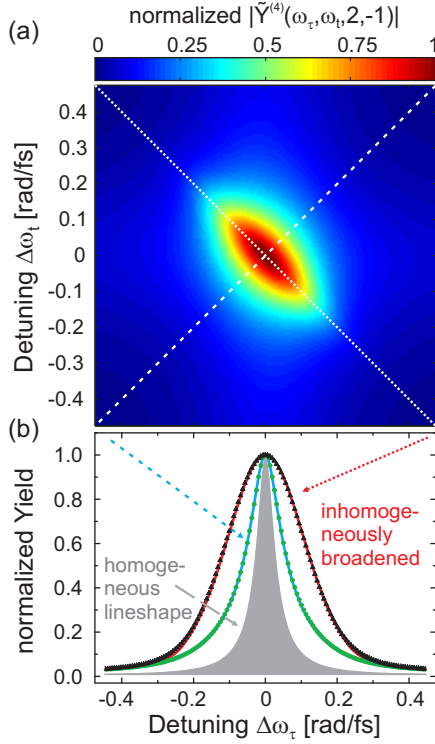


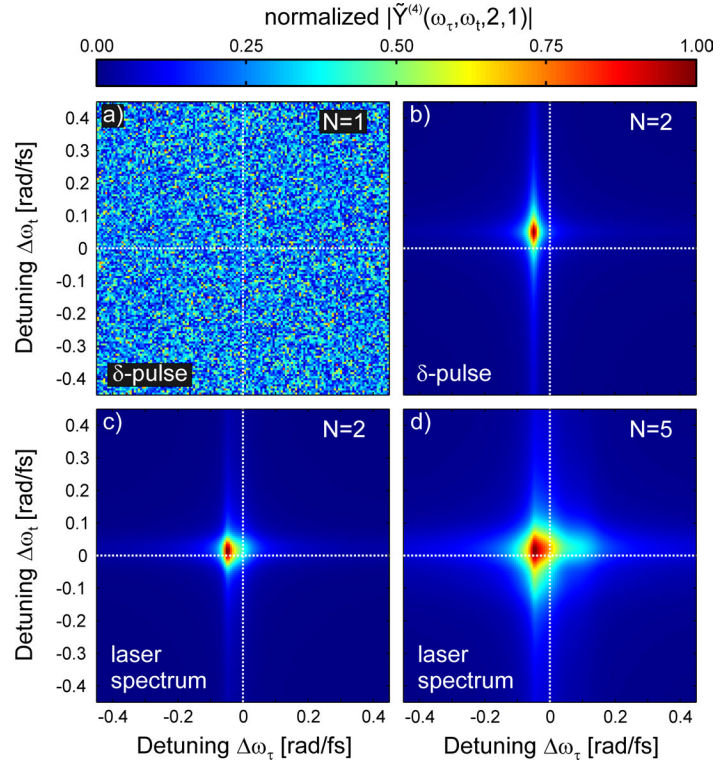
Figure 4.16: Simulation of inhomogeneously broadened two-dimensional spectrum. (a) The two-dimensional spectrum for Lorentz oscillators with a homogeneous linewidth of $\gamma_{Lo} = 0.02$ rad/fs and a Gaussian distribution of center frequencies ω_{Lo} is calculated by Fourier transformation of the weighted sum of the individual delay signals. The center frequency of the distribution is set to $\omega_c = 2.36$ rad/fs and the width is $\sigma = 0.09$ rad/fs. The white dotted and white dashed lines indicate the diagonal and antidiagonal cuts that are presented in (b), respectively. (b) Symbols mark the simulated data along the dashed diagonal line (green circles) and the dotted antidiagonal line (black triangles) projected onto the $\Delta\omega_\tau$ -axis. The inhomogeneously broadened signal was also calculated for identical parameters γ_{Lo} , σ and ω_c according to Eq. (4.51). The results are presented as solid red (diagonal) and solid blue (antidiagonal) lines. The homogeneous lineshape obtained for a single oscillator at $\omega_{Lo} = 2.36$ rad/fs is indicated by the gray shaded area.

at $\omega_{Lo} = 2.36$ rad/fs is shown for comparison as gray shaded area. In the homogeneous case the diagonal and antidiagonal direction are identical. It is obvious that the simulated spectral amplitude of the inhomogeneous signal is broadened along both directions. Hence, the spectral width along the antidiagonal cut does not directly yield γ_{Lo} . Nevertheless, In analogy to optical 2D spectroscopy [319], the spectral information included in the diagonal and antidiagonal cuts through a resonance peak in a 2D nanoscopy spectrum is sufficient to unambiguously retrieve the homogeneous and inhomogeneous linewidths parameters γ_{Lo} and σ . The solid lines in Figure 4.16b are calculated by employing a direct time domain notation of the partial photoemission yield:

$$\tilde{Y}^{(4)}(\tau, t, 2, -1) = \tilde{Y}^{(4)}(0, 0, 2, -1)\Theta(\tau)\Theta(t)e^{-\gamma_{Lo}(3t+\tau)-\sigma^2(t-\tau)^2/2+i\omega_c(t-\tau)}. \quad (4.51)$$

This formula is derived from Eq. (4.35). It is valid under the assumptions of infinitesimal short excitation pulses and exponential decay of the field amplitudes. With Eq. (4.51) the two-dimensional delay signal for identical parameters as in the simulations is retrieved which generates the inhomogeneously broadened 2D spectrum after Fourier transformation. The simulated and calculated lineshapes are almost identical except for small deviations in the tails of the spectral signals, which occur because of the limited range of sampling points for the simulated data. Thus, Eq. (4.51) perfectly describes the 2D nanoscopy spectra of a Gaussian distribution of Lorentz oscillators and can be employed to exactly reconstruct the linewidths parameters γ_{Lo} and σ as well as the center frequency ω_c from inhomogeneously broadened resonance peaks.

Figure 4.17: Comparison between 2D nanoscopy spectra calculated for different excitation conditions and 4×4 photon echo phase cycling scheme. For each of the normalized amplitude spectra the response of a Lorentz oscillator with center frequency $\omega_{Lo} = 2.41$ rad/fs and spectral width $\gamma_{Lo} = 0.01$ rad/fs was simulated. The rotating frame frequency was set to $\omega_L = 2.365$ rad/fs. (a,b) Excitation with δ -shaped pulses corresponding to a flat spectral amplitude and spectral phase. The nonlinear order of the photoemission process was set to $N = 1$ (a) and $N = 2$ (b). Horizontal and vertical lines indicate the zero detuning positions for both frequency axes. (c,d) Excitation with bandwidth-limited pulses with Gaussian excitation spectrum at center frequency $\omega_L^{exp} = 2.365$ rad/fs and spectral FWHM set to 0.061 rad/fs. The nonlinear order of the photoemission process was set to $N = 2$ (c) and $N = 5$ (d).



4.3.2. Influence of Limited Excitation Bandwidth and Above Threshold Nonlinearities on 2D Nanoscopy Spectra

The simulations described in the previous section were performed for four interactions with the local electric field causing a quadratic dependence of the photoemission yield on the temporal intensity. A sequence of infinitesimally short excitation pulses was assumed corresponding to a constant excitation spectrum. However, the available spectral bandwidth of the excitation pulse sequence in the 2D nanoscopy experiments is limited. Since the local electric field is the product of the linear spectral response of the nanosystem $A(\omega)$ and the laser spectrum (see Eq. (4.43)), a laser spectrum which is modulated in the overlap with $A(\omega)$ has a considerable influence on the spectral position and shape of the local electric field of the nanosystem. This is the case, for example, if the bandwidth-limited duration of the laser pulse is in the range of the coherence lifetime of the system and the corresponding laser spectrum is about as broad as $A(\omega)$. Additional to this effect, the nonlinear order of the emission process depends on the material properties of the investigated sample. If the work function exceeds twice the photon energy, i.e. $E_W \geq 2\hbar\omega$, 2PPE is not possible and higher-order photoemission processes contributing to $Y^{(n)}(\tau, t, \varphi_\tau, \varphi_t)$ have to be considered in the Fourier transform time domain simulations. The following study demonstrates the influence of the limited excitation bandwidth and the nonlinear order N of the excitation process on simulated 2D nanoscopy spectra.

In Figure 4.17 the simulated 2D nanoscopy spectra for a Lorentz oscillator are plotted for several excitation conditions. The oscillator frequency is $\omega_{Lo} = 2.41$ rad/fs and the spectral width is

$\gamma_{Lo} = 0.01$ rad/fs. In the impulsive limit the excitation pulses are δ -shaped corresponding to an infinite spectral bandwidth of the excitation. Two 2D nanoscopy spectra for this case are shown in Figure 4.17a and b. The spectrum for $N = 1$ contains no spectral features except for numerical noise which is strongly enhanced by the normalization of the data. The absence of any spectral information agrees with the condition that at least four interactions with the electric field are necessary to generate a photon echo signal. This is fulfilled in Figure 4.17b. Here, the simulated data match the analytic formula Eq. (4.37). The spectral resonance appears shifted by $\omega_{Lo} - \omega_L$ and the shape of the spectral feature is slightly elongated in ω_t -direction.

Using realistic pulse lengths and spectral widths of the excitation pulses the spectrum for the same oscillator changes considerably as visible in Figure 4.17c. The simulated center frequency of $\omega_L^{exp} = 2.365$ rad/fs and the spectral FWHM of 0.061 rad/fs of the laser spectrum were adapted to the experimental conditions of the 2D nanoscopy measurement described in Chapter 6.3. These parameters were obtained by fitting the spectrum of the experimental laser system (*Newport Spectra-Physics Tsunami*) measured right before the UHV chamber of the PEEM. Without introducing additional phase modulations these values were used to define the pulse sequence according to Eq. (4.46). Also the rotating frame frequency was set to $\omega_L = 2.365$ rad/fs. It is obvious that the 2D spectrum for these excitation conditions deviates in the spectral position and size, because now it also contains spectral information of the excitation pulses. As a consequence, the obtained spectral features is shifted towards the center frequency of the laser and the detuning is reduced. This effect is more pronounced along the ω_{τ_3} -direction.

Also the nonlinear order of the excitation process influences the resulting 2D spectrum. Figure 4.17d presents the amplitude spectrum of the identical oscillator and excitation spectrum as previously, but with a higher nonlinearity of the photoemission process. Compared to the results in Figure 4.17b and c again a reduction of the detuning is observed. Furthermore, the resonance peak is clearly broadened and has an increasingly asymmetrical shape.

The reason for the broadening is analog to the consideration concerning the reverse transient grating signal $\tilde{Y}^{(4)}(\tau, t, 0, -1)$ in Section 4.2.2, which is the sum of three delay-dependent terms (see Eq. (4.37)). An increase of the nonlinear order is connected to a higher total number of interfering electric field components. To meet the condition of the phase cycling scheme, additional counteracting interactions have to occur within the pulses. Therefore, the photon echo signal $\tilde{Y}^{(n)}(\tau, t, 2, -1)$ is given by several possible combinations of interactions with the individual pulses of the excitation sequence. Finally, this leads to a faster decay of the delay-dependent signal $\tilde{Y}^{(n)}(\tau, t, 2, -1)$ with increasing n , corresponding to a broader resonance peak after Fourier transformation. The spectral position of the signal is not directly affected by the higher number of interactions, because it is still determined by the interaction parameters β and γ , which are given by the phase cycling scheme. However, in the combination with a limited excitation bandwidth this broadening effectively leads to a further shift of the spectral position towards the center of the excitation spectrum.

The results of this section have a direct impact on the evaluation of experimental data. It has been demonstrated that experimental restrictions, as the limited excitation bandwidth, influence the detected 2D nanoscopy spectra as well as the local nonlinear order of the electron emission process. A retrieval of spectral information on experimental 2D nanoscopy data has to compensate for these effects and rescale the obtained spectral parameters accordingly.

4.3.3. Fast Data Evaluation Routine for 2D Nanoscopy Measurements

The simulation of 2D nanoscopy data by calculating the photoemission yield in the temporal domain allows for including the effects of the laser spectrum and the nonlinear order of the photoemission process. Nevertheless, in the evaluation of obtained 2D nanoscopy data the full time domain simulation of the signals is too slow for fitting the local nanospectra at each spatial pixel. With currently implemented routines and the available state-of-the-art personal computer system the fit of a 2D nanoscopy spectrum convergences typically within 30 minutes. As the field of view of the PEEM is mapped onto about one million detector pixels and for each of the pixels an individual 2D spectrum is generated, a full analysis of a single 2D nanoscopy measurement would require several years of computation. Thus, a different approach to extract spectral information from 2D nanoscopy data has to be employed. The fast data evaluation method presented in this section is crucial for retrieving the spatial distributions of the local oscillator frequency and coherence lifetime which are presented in Figure 6.15 in Chapter 6.

The fast data evaluation routine generates two-dimensional spectra from an analytic fit function $\tilde{Y}_{fit}(\omega_\tau, \omega_t)$ in spectral domain without the need to simulate the electric fields in time domain. In analogy to Eq. (4.34) the phenomenological lineshape function is written as the product of two Lorentzian response functions (see Appendix F):

$$\begin{aligned} \tilde{Y}_{fit}(\omega_\tau, \omega_t) &= a \cdot A_{Lo}(\omega_\tau, b\omega'_{Lo}, c\gamma'_{Lo}) \cdot A_{Lo}(\omega_t, d\omega'_{Lo}, e\gamma'_{Lo}) \\ &= a \cdot \frac{1}{b^2\omega'^2_{Lo} - \omega_\tau^2 + c \cdot 2i\gamma'_{Lo}\omega_\tau} \cdot \frac{1}{d^2\omega'^2_{Lo} - \omega_t^2 + e \cdot 2i\gamma'_{Lo}\omega_t} \end{aligned} \quad (4.52)$$

where a , ω'_{Lo} and γ'_{Lo} are used as free parameters for fitting and b , c , d and e are given by the type of investigated signal. For example, by setting these parameters to $b = -1$, $c = 1$, $d = 1$ and $e = 3$ the photon echo signal $\tilde{Y}^{(4)}(\omega_{\tau_1}, \omega_{\tau_3}, 2, -1)$ at $N = 2$ is reproduced. The computational effort is much lower for this analytic approach. Therefore, fitting a 2D nanoscopy spectrum is more than a thousand times faster. However, this parametrization does not include the excitation spectrum and does not deal explicitly with the nonlinearity of the process. Accordingly, the fitted lineshape parameters ω'_{Lo} and γ'_{Lo} deviate from the actual parameters of the local linear response function ω_{Lo} and γ_{Lo} .

In the following it is shown that a biunique transformation between the fitted data points in ω'_{Lo} - γ'_{Lo} parameter space and the spectral response parameters ω_{Lo} and γ_{Lo} exist. Thus, each point $(\omega_{Lo}, \gamma_{Lo})$ in the linear response parameter space is related to a particular point $(\omega'_{Lo}, \gamma'_{Lo})$ in the fit parameter space and vice versa. This relation is retrieved by calculating 2D nanoscopy spectra via Fourier transform time domain simulations for a realistic excitation bandwidth and different values of N . For these spectra the input parameter ω_{Lo} and γ_{Lo} of the simulation are known. By fitting the simulated spectra using the simplified phenomenological lineshape the corresponding points in ω'_{Lo} - γ'_{Lo} parameter space are determined.

Figure 4.18 depicts schematically, how the experimental results evaluated with the simplified lineshape model are processed to yield the linear response parameters of the investigated system. The results of the lineshape fit of simulated data, which are depicted in Fig. 4.19 and 4.20, define the transformation (red dotted arrow) of the simulation input parameter (red dots) into the fit parameter space. Interpolation of the obtained results decreases the spacing between the data points to further increase the point density. The regular grid in ω_{Lo} - γ_{Lo} space becomes distorted in ω'_{Lo} - γ'_{Lo} space (see Fig. 4.19). However, as long as the lines of the distorted grid

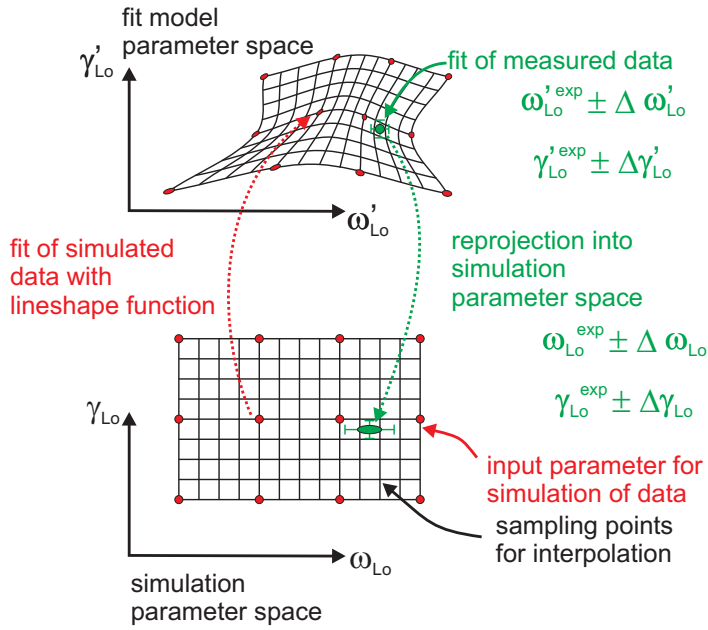


Figure 4.18: Rescaling of fitted experimental parameters to compensate for limited excitation bandwidth and nonlinear electron emission processes. Simulated data with well known spectral parameters are fitted by the phenomenological lineshape function $\tilde{Y}_{\text{fit}}(\omega_{\tau}, \omega_t)$ according to Eq. (4.52) at sampling points in linear response parameter space $(\omega_{L0}, \gamma_{L0})$. The positioning of the corresponding fit parameters $(\omega'_{L0}, \gamma'_{L0})$ in the lineshape function space is distorted, but allows the unique reprojection of fitted parameters of experimentally obtained spectra.

do not cross, each measured data point $(\omega'_{L0, \text{exp}}, \gamma'_{L0, \text{exp}})$ always identifies a unique position on the distorted grid. Thus, a reprojection (green dotted arrow) into the linear response parameter space is possible. The method applied in this thesis involves for each fitted data point to generate the corresponding probability distribution in ω_{L0} - γ_{L0} space according to the fitted parameters and their respective fit uncertainties $\Delta \omega'_{L0}$ and $\Delta \gamma'_{L0}$. The probability distribution for linear response parameters is then analyzed and yields the rescaled center frequency $\omega_{L0, \text{exp}}$ and spectral width $\gamma_{L0, \text{exp}}$ as well as the rescaled fit uncertainties $\Delta \omega_{L0}$ and $\Delta \gamma_{L0}$.

2D nanoscopy spectra are calculated by Fourier transform time domain simulations and afterwards fitted by the analytic data evaluation routine to determine the relation between the position $(\omega'_{L0}, \gamma'_{L0})$ in the fitted parameter space and the actual response parameters ω_{L0} and γ_{L0} . The simulations are based on the linear response function of a single Lorentz oscillator and utilize varying input parameters. In total the three-dimensional input parameter space $(\omega_{L0}, \gamma_{L0}, N)$ is covered by 36788 points with unequal spacing. The nonlinear order of the photoemission process is varied between 2 and 10. The photon echo signal $\tilde{Y}^{(n)}(\omega_{\tau}, \omega_t, 2, -1)$ is retrieved by 4×4 phase cycling. In Figure 4.19a the black squares show the simulated positions in ω_{L0} - γ_{L0} space. The center frequency ω_{L0} ranges between 2.25 rad/fs to 2.48 rad/fs and the spectral width γ_{L0} exhibits values in the interval from 0.002 rad/fs to 0.6 rad/fs. There are three regions with different density of simulated points. The highest point density was used for $\gamma_{L0} \leq 0.04$ rad/fs. In the interval $0.04 \text{ rad/fs} \leq \gamma_{L0} \leq 0.16 \text{ rad/fs}$ the steps in γ_{L0} -direction are increased by a factor of 5 to 0.01 rad/fs and above $\gamma_{L0} = 0.16 \text{ rad/fs}$ the separation between the simulated points is further enlarged. The Gaussian excitation spectrum is centered at $\omega_L = 2.365 \text{ rad/fs}$ with a FWHM of 0.061 rad/fs matching the excitation spectrum employed in Chapter 6.3. Accordingly, the simulated frequency range is about 4 times as wide than the FWHM. The Fourier transform simulations employed the same steps of the delays τ and t as the 2D nanoscopy measurements in Chapter 6.3. Therefore, also the spectral sampling points are identical to the measured 2D nanoscopy spectra. In addition, the same parameters were substituted into Eq. (4.52) to define

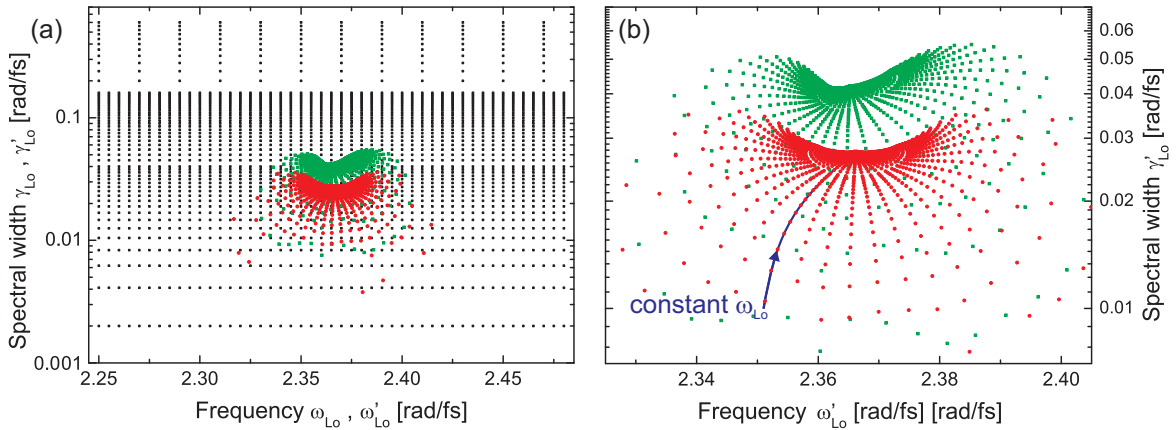


Figure 4.19.: Simulation data point positions in frequency and spectral width domain (black) and fitted parameters by the phenomenological lineshape function (red, green) for parameters $-b = d = 1$ and $c = e = 1$. (a) Full simulated range of simulated data. The red dots indicate parameters fitted to simulation data for nonlinear order $N = 2$ and green dots were fitted to simulation data for $N = 5$. Fitted parameter converge for increasing input spectral width towards the center frequency of excitation spectrum. The fitted spectral width is lower in case of $N = 2$. (b) Detail of (a) without simulation data. In the distribution for $N = 2$ (red dots) a blue arrow indicates a line of points simulated for constant ω_{L0} and increasing γ_{L0} .

$\tilde{Y}_{fit}(\omega_\tau, \omega_t)$ identically to the analysis of the experiment. Consequently, the fit results which are obtained for the simulations are directly applicable to evaluate the experimental 2D nanoscopy data.

In Figure 4.19 the relation between simulation input and fit output parameters is presented for the example of two different orders of nonlinearity N . Whereas the black squares indicate the input parameter, the red and green dots mark the positions of the respective fit parameters in ω'_{L0} - γ'_{L0} space for nonlinear orders of 2 and 5. The simulated data points are on a regular grid with additional points for small γ_{L0} . In contrast, the fit parameters distributions are bent and contracted. The fitted data points cover a smaller region in their parameter space. Especially the spectral width γ'_{L0} ranges within only one order of magnitude, whereas the simulation data covers a broader γ_{L0} -interval. All lines of constant ω_{L0} converge with increasing γ_{L0} towards the center frequency of the excitation spectrum, which becomes the dominant spectral feature in the local electric field, when the spectral width of the Lorentz oscillator is broader than the excitation spectrum. The lines of constant ω_{L0} do not cross for the investigated region in parameter space. Accordingly, a biunique transformation between simulation parameter space and simplified lineshape space exists. Thus, for each point in simulated parameter space $(\omega_{L0}, \gamma_{L0})$ a direct mapping into simplified lineshape space $(\omega'_{L0}, \gamma'_{L0})$ is feasible.

An alternative representation of the data presented in Figure 4.19 is given by the two-dimensional maps in Figure 4.20. Here, the obtained fit parameters ω'_{L0} and γ'_{L0} are plotted separately in dependence of ω_{L0} and γ_{L0} . The upper plots (a–c) depict the fitted spectral width γ'_{L0} and the lower plots (d–f) show the fitted center frequency ω'_{L0} for different orders of nonlinearity. In the ideal case of unlimited spectral bandwidth of the excitation spectrum the isovalue lines in the parameter maps would be horizontal or vertical, but for the realistic excitation spectrum they are bent. Furthermore, there is a maximum and minimum center frequency ω'_{L0} that is reached with

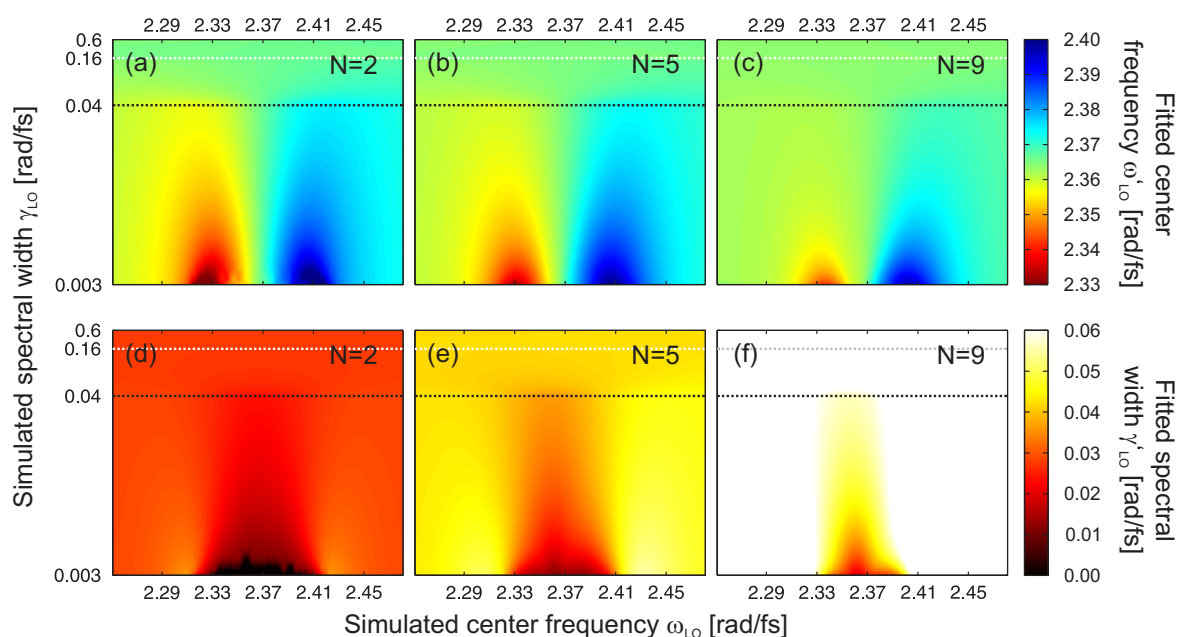


Figure 4.20.: Simulation and fit parameters for the nonlinear orders $N = n/2 = 2$ (a,d), $N = 5$ (b,e) and $N = 9$ (c,f). In all plots the simulated spectral width axes increase linearly between the ticks. The boundaries of these regions are highlighted with horizontal dotted lines. (a,c,e) Fitted center frequency ω'_{Lo} . The range of obtained ω'_{Lo} values narrows with γ_{Lo} as well as the nonlinear order N . For ω_{Lo} leaving the overlap with the excitation spectrum the fitted frequency ω'_{Lo} shifts back towards the laser frequency ω_L . (b,d,f) Fitted spectral width γ'_{Lo} increase, with N for fixed simulation parameters ω_{Lo} , γ_{Lo} .

the lineshape fit. For smaller and larger simulated frequencies the fitted values shift back towards the center of the laser spectrum. The best distinction between the input frequencies is achieved for small γ_{Lo} . The fitted spectral width γ'_{Lo} increases with the input width γ_{Lo} . However, γ'_{Lo} also varies with ω_{Lo} and typically is smaller in the overlap with the excitation spectrum.

In this section the fast fit routine based on the analytical formula for 2D nanoscopy spectra of a Lorentz oscillator was implemented and tested with simulated data. Since the fit routine does not include the nonlinear order of the photoemission process and the excitation spectrum, the fit parameters deviations of the fitted parameters ω'_{Lo} and γ'_{Lo} from the input parameters of the simulation ω_{Lo} and γ_{Lo} occurred. However, it was demonstrated that a rescaling of the fit parameters is possible which enables retrieving the spectral information of simulated and experimentally measured 2D nanospectra from the fit. Results of the fast data evaluation routine including the rescaling of the fitted spectral parameters according to the excitation spectrum and local order of nonlinearity will be presented in Chapter 6.3. There, the electron emission from localized photonic modes in amorphous thin-film silicon layers is investigated by 2D nanoscopy employing a 4×4 phase cycling scheme.

5. Hybridization of Dark and Bright Plasmonic Modes

Surface-enhanced spectroscopy techniques e.g. surface-enhanced Raman spectroscopy (SERS) benefit from the high local electric field at structured metal surfaces and metal nanoparticles [29–34]. The field enhancement at the surface provides localized electric fields that are strong enough to enable the detection of single molecular Raman signals [34]. Understanding the nature of the strong field enhancement on corrugated metal surfaces and finding methods to tailor the excitation might improve SERS technologies.

The following chapter deals with the investigation of a corrugated silver surface by polarization-shaped laser pulses in coherent control experiments [3]. Multiphoton photoemission hot spots are individually addressed and manipulated using adaptive pulse shaping. In a reproducible manner complex shaped pulses are used for tailoring the local photoemission yield leading to a better nanofocusing of the excitation, to control of the hot spot shape and to a photoemission yield exceptionally higher than observed for bandwidth limited pulses. Polarization parameter scans of spectral phase properties give first evidence for long-living coherences which might be caused by the corrugated topography of the silver surface.

In a first demonstration of two-dimensional nanoscopy (Section 5.3) the spectral properties of the hot spot photoemission is investigated [4]. Local lifetimes in the range of 100 fs are detected with a sub-wavelength resolution. The results of a two-pulse nanoscopy experiment are explained by the hybridization of dark and bright plasmonic modes leading to Fano-like resonances (Section 5.4).

This chapter combines data from several experiments at the same sample. All presented experiments were conducted in Kaiserslautern with cooperative effort from all participating groups. My contribution to the coherent control experiments had its emphasis on the adaptive optimization process, the multidimensional pulse parameter scan and the pulse characterization. I contributed in the implementation of the 2D nanoscopy routine as well as in planning and conducting the 2D nanoscopy measurements. I developed and improved the data evaluation routines to automatically analyze the 2D nanoscopy as well as the two-pulse nanoscopy experiments. Furthermore, I performed the investigation of the two-pulse nanoscopy concerning a hybridization of dark and bright plasmonic modes.

5.1. Experimental Setup and Sample Characterization

The experimental setup used for coherent control measurements and for 2D nanoscopy is almost identical. Both employ photoemission electron microscopy (PEEM) and the illumination of the sample with femtosecond laser pulses tailored by a polarization pulse shaper. As it is obvious in Figure 5.1, the setup is equal to the setup of the experiments discussed in Chapter 2 and Chapter 3, but it does not include the optical components for overlapping a second pulse at the sample. In the coherent control experiments (Section 5.2) the femtosecond polarization pulse

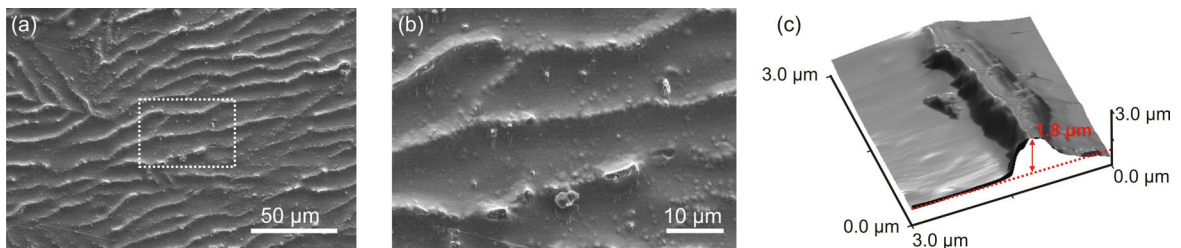
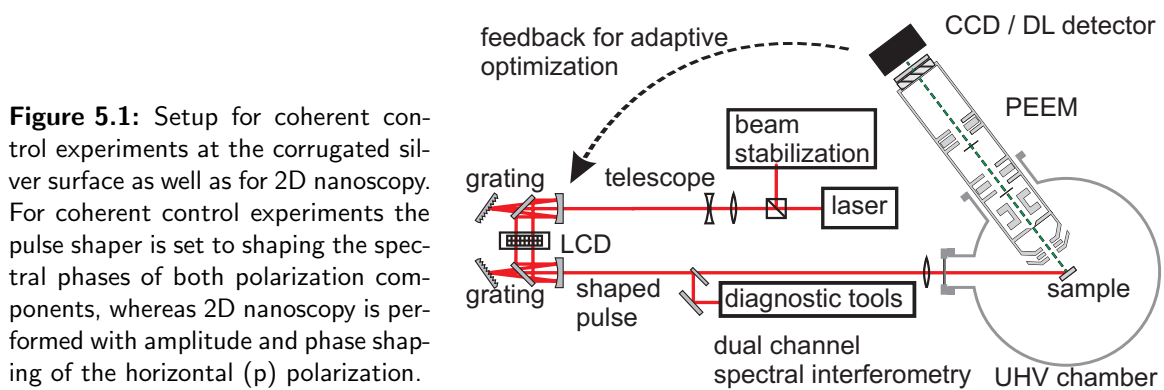


Figure 5.2.: Characterization of the corrugated silver surface. (a) Scanning electron microscopy (SEM) image of the investigated sample. (b) Enlarged detail of the SEM image in the area indicated by the dashed rectangle in (a). The topography of the surface is dominated by ridge and valley structure with typical distances of $10 \mu\text{m}$. (c) AFM topographical image of one of the ridge structures. The observed height indicated by the red arrow is $1.8 \mu\text{m}$.

shaper is configured to independently shape the spectral phases of both polarization components (see Chapter 1.2.2). For 2D nanoscopy measurements (Sections 5.3 and 5.4) simultaneous amplitude and phase shaping of the horizontal (p) polarization component is achieved and the vertical (s) component is blocked. The feedback for the adaptive optimizations is provided by a computer based evaluation routine that corrects the spatial drift of the sample position between the photoemission images (see Appendix B) and calculates the fitness function according to the ROI definition. An evolutionary algorithm creates the pulse shapes to be tested by cloning and mixing the pulse parameters of the best individuals. In 2D nanoscopy the pulse shapes are predefined by the parameters of the two-dimensional delay scan and the phase cycling method. The sample consists of polycrystalline silver. The surface of the sample was prepared by repeated sputtering with argon ions and annealing. The surface topography was investigated by scanning electron microscopy (SEM) and atomic force microscopy (AFM). In the SEM images (see Figure 5.2a and 5.2b) it is apparent that the silver film exhibits surface corrugations with ridges and valleys. There is no clear periodicity observed in the distribution of ridges and valleys. Typically, the width of the valleys perpendicular to the ridges is in the range of $10 \mu\text{m}$. However, this value varies significantly depending on the position of the sample. The ridge structures were additionally investigated by AFM (Figure 5.2c). Here, it is noticeable that the width and height of these structures partially exceed $1 \mu\text{m}$.

Upon illumination with ultrashort laser pulses the photoemission from the corrugated silver surface is localized at photoemission hot spots, i.e. confined regions with drastically enhanced

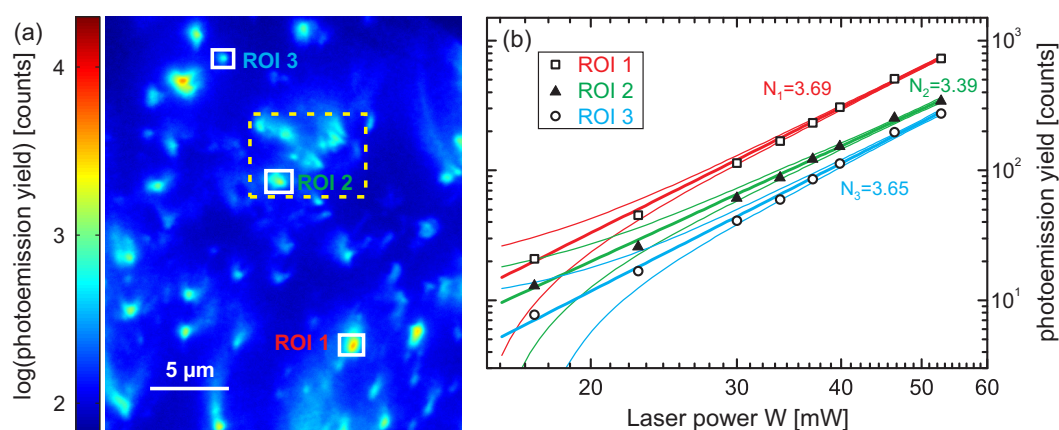


Figure 5.3.: PEEM image of silver surface for illumination with bandwidth limited near infrared femtosecond laser pulses and intensity-dependence of photoemission yield evaluated at three spatial regions. (a) PEEM image obtained with ultrashort near-infrared laser pulses show photoemission hot spot, whereas surface topography is not visible. Three regions of interest (ROI 1, ROI 2 and ROI 3) are marked by white solid rectangles. The yellow dashed rectangle indicates the detail of the field of view which is presented in Figure 5.4. (b) Photoemission yield as a function of laser power for regions of interest indicated in Figure 5.4. Values from ROI 1, ROI 2 and ROI 3 are represented by white squares, black triangles and white circles, respectively. Fits of the photoemission yield are colored according to (a). Fat solid lines are indicating the best fits by a power law $Y(W) = a + b \cdot W^N$ and thin solid lines show the confidence interval for a 2σ significance level. The exponents retrieved by the fit are $N_1 = 3.69 \pm 0.23$, $N_2 = 3.39 \pm 0.25$ and $N_3 = 3.65 \pm 0.24$ for ROI 1, ROI 2 and ROI 3, respectively.

photoemission yield. This is visible in Figure 5.3a, which presents the photoemission distribution obtained with bandwidth-limited near-infrared laser pulses. The emission from these hot spots is too strong for a further enhancement of the total yield without damaging the detector. Thus, the surface topography is not visible for these illumination conditions. The position of three regions of interest (ROI 1, ROI 2 and ROI 3) are indicated by white rectangles. Each of them includes a photoemission hot spot. These hot spots differ by their individual photoemission strength. The highest yield is obtained in ROI 1 and the lowest in ROI 3. By attenuating the laser beam with an adjustable neutral density filter and tracing the local photoemission yield the nonlinear order N of the photoemission process is estimated. The dependence of the averaged local photoemission yield on W at the three regions of interest is presented in Figure 5.3b. The points for the regions were fitted independently by a power law with constant offset given by $Y(W) = a + b \cdot W^N$. The fit parameters a and b denote the offset and a multiplicative factor to the laser power, respectively. Figure 5.3b presents the experimental and the fitted data in logarithmic plots. The fitted offset a has been subtracted beforehand to facilitate an easier cognition of the nonlinear order N . The ROIs differ in their absolute photoemission yield, but they show similar behavior for variation of W . They all exhibit an almost linear linear trend with slopes given by their respective fit coefficients $N_1 = 3.69 \pm 0.23$, $N_2 = 3.39 \pm 0.25$ and $N_3 = 3.65 \pm 0.24$. The multiplicative factor b scales with the vertical position of the data in Fig. 5.3b without affecting the slope. The obtained values of the nonlinear exponent N indicate that at least 3 photons per electrons had to be absorbed to overcome the work function and generate photoemission. The local field enhancement at certain positions of the sample in combination with the nonlinear photoemission process leads to the observed strong photoemission hot spots exceeding the yield of other parts

of the surface by orders of magnitude. In the following it will be investigated whether the field enhancement at those hot spots can be coherently controlled, i.e. whether a manipulation via tailoring the spectral phase and the polarization state of the incident electric field is feasible.

5.2. Optical Near-Field Control of Hot Spot Photoemission on Silver

In this section four examples for coherent control on the corrugated silver surface are presented. Most of the experimental results have been published in [3]. In the first part (Section 5.2.1) it is demonstrated that a complex pulse shape achieves a strong enhancement of the local electric field compared to bandwidth limited pulses. Secondly, near-fields are controlled on subwavelength length scales offering possibilities to manipulate the electron emission yield distribution at single hot spots (Section 5.2.2). An important issue for coherent control experiment is the reproducibility of the optimal pulse shape in consecutive optimizations. In Section 5.2.3 the results of two independent adaptive optimizations are analyzed verifying that the obtained pulse shapes are to a large extent identical. The last example (Section 5.2.4) involves scanning simultaneously different pulse parameter that define the polarization state and the temporal structure of the laser pulses. This method gives a systematic access to the local response of each individual hot spot.

5.2.1. Near-field Superenhancement

Figure 5.4a presents the detail of the field of view which is highlighted in Figure 5.3 by the yellow dashed rectangle. For this image an unshaped bandwidth-limited laser pulse was used for excitation. A distribution of hot spots is observable indicating the localization of optical near-field at the surface. Two new regions of interest at which the local photoemission yield is controlled are indicated by a red rectangle (ROI-1) and a yellow dashed rectangle (ROI-2), respectively. The ROIs have a spatial distance of about 500 nm and are clearly distinct in their local photoemission signals.

In order to selectively excite one of the hot spots while the multiphoton photoemission at the other spot is suppressed, this optimization goal has to be expressed in a fitness function $f_{1,2}$ that depends on the time-integrated and spatially averaged photoemission signals $Y_{\text{ROI-1}}$ and $Y_{\text{ROI-2}}$ of the respective ROIs.

$$f_{1,2}(\varphi_1(\omega), \varphi_2(\omega)) = \frac{Y_{\text{ROI-1}}}{Y_{\text{ROI-2}}} \quad (5.1)$$

This fitness function is evaluated for each individual of the evolutionary algorithm and used as a feedback for the selection process and for the generation of the individuals of the next iteration step. Two opposing adaptive optimizations were performed maximizing and minimizing the fitness function $f_{1,2}(\varphi_1(\omega), \varphi_2(\omega))$. The resulting multiphoton photoemission images are presented in Figure 5.4b and 5.4c. Quasi-3D representations of the corresponding polarization-shaped laser pulses are shown in Figure 5.4e and 5.4f. The temporal evolution of the polarization state is illustrated as a sequence of elliptical cylinders for different time steps (separated by 8.7 fs) in a slowly varying envelope approximation. The coloring represents the momentary center frequencies of the elliptical cylinders by rainbow colors. The horizontal and vertical polarization components of the electric field vector in the laboratory frame are illustrated as projection shadows. The time

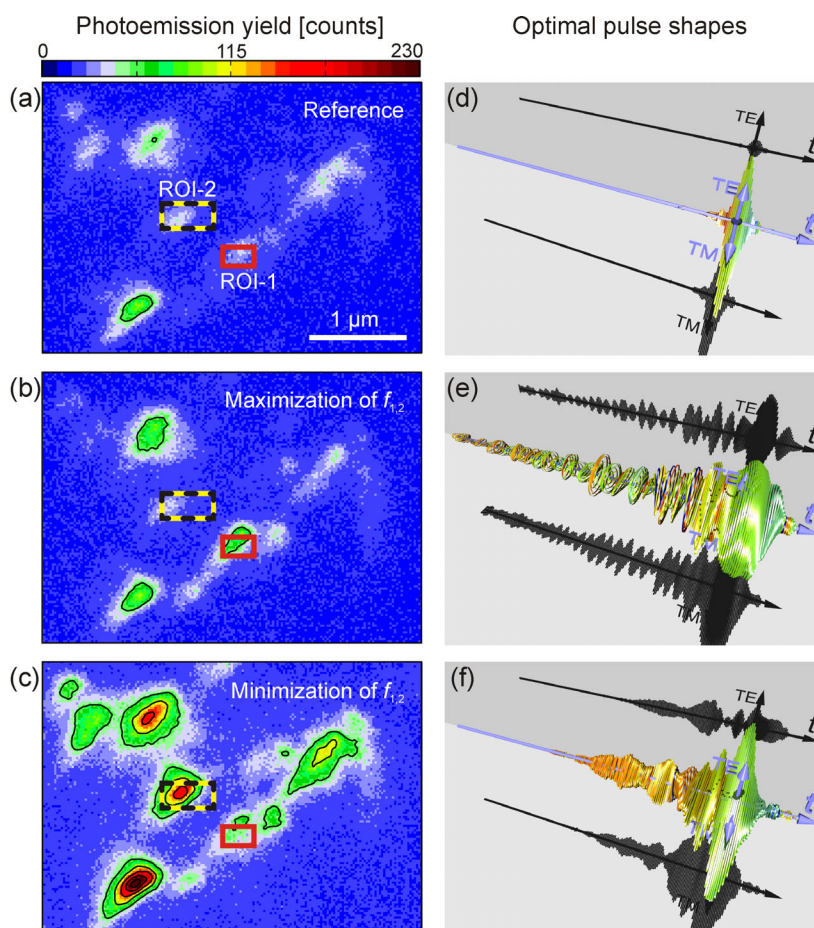


Figure 5.4.: Near-field control on a corrugated silver film. (a,c,e) Photoelectron emission distributions obtained with a transform-limited reference pulse (a) and polarization-shaped laser pulses selected by evolutionary algorithm to maximize (c) and minimize (e) the fitness function $f_{1,2}(\varphi_1(\omega), \varphi_2(\omega))$ defined as the ratio between the regions of interest (Eq. (5.1)). The regions of interest are indicated by a red solid rectangle (ROI-1) and a yellow dashed rectangle (ROI-2). The PEEM images show the same region with identical color scale. (b,d,f) Quasi-3D representation of the temporal evolution of the laser pulse shapes used for excitation in (a),(c) and (e), respectively. The presented time interval starts at -1.8 ps and ends at 300 fs. The time steps between two of the elliptical cylinders are 8.7 fs. The pulses are normalized to their individual maximum electric field. The horizontal arrow marked with TM (transverse magnetic) indicates the horizontal p-polarized field orientation and the vertical arrow (TE, i.e. transverse electric) points towards s-polarization. (b) Unshaped laser pulse for reference image. Due to being transform limited the linear polarization has to remain constant through the complete pulse. (d) Optimal pulse shape retrieved for maximization of the fitness function $f_{1,2}$. (f) Optimal pulse shape for minimization of $f_{1,2}$. Adapted from [3].

axis from -1.8 ps to 0.3 ps is identical in all images, but the size of the ellipses are normalized to the peak intensities of the individual pulses. The temporal duration of the unshaped laser pulse is 50 fs (see Fig. 5.4d). This reference pulse is linearly polarized in horizontal (p) orientation. Both optimized pulses are strongly elongated and feature pulse durations significantly longer than the ultrashort coherence lifetimes of localized surface plasmons reported in literature [172, 320–323]. Furthermore, they comprise complex variations of the polarization state. For both optimized pulses a negative third-order dispersion (TOD) is responsible for the train of prepulses. Despite these similarities, the optimized pulse shapes differ in the details of the temporal structure and the evolution of the polarization state.

In comparison with the photoemission for the transform-limited laser pulse (Figure 5.4a) the maximization of $f_{1,2}$ indeed yields a strong signal in ROI-1, whereas the photoemission in ROI-2 is suppressed. Despite the local changes in the ROIs the total photoemission yield of the complete depicted area is not affected significantly compared to the bandwidth-limited reference pulse. In case of the minimization of the fitness function $f_{1,2}$ (Figure 5.4c) a distinct enhancement of ROI-2 relative to ROI-1 is achieved. Additionally, there is a surprising increase of the photoemission yield which drastically exceeds the yield generated by the reference pulse in the region of interest. Note that the acquisition conditions for all three PEEM images were identical and they share the same color scale. Even though the goal of the coherent control experiments was to optimize the ratio of the local photoemission in the ROIs, the total yield in the complete depicted area is increased by a factor of up to three. This is remarkable, since often in coherent control experiments the relative control of two channels, e.g. two regions of interest, leads to reduction of the total output, e.g. the total photoemission. In this case the opposite behavior is observed. An analogue finding was reported in the coherent control of multiphoton excitation of Rb atoms where shaped laser pulses lead to an increased signal because of the interplay of the involved atomic energy levels [324]. Here, the neighboring areas and hot spots of an individual hot spot seem to be crucial for the observed *near-field superenhancement*. The term *superenhancement* is used in accordance with the term *superradiance* [325–327], which is related to radiative emission enhanced by collective effects in the surrounding medium. Thus, the superenhanced multiphoton photoemission from a hot spot is the observation of a photoemission yield of unexpected strength which appears to be influenced by the environment of the hot spot [3].

The results of the adaptive optimizations do not allow for an independent evaluation of the influence of the TOD and the complex evolution of polarization state of the pulses on the local photoemission because of the limitations of a closed-loop experiment. The contributions of the TOD and the polarization state to the control of the local photoemission are investigated in Section 5.2.4 in two-parameter scans of these pulse parameters. Further contributions to the complex pulse structure may originate from the random topography of the silver surface and by interactions and interference of localized near-field modes.

5.2.2. Sub-Diffraction Control of Photoemission Hot spots

In the previous example the controlled regions of interest could have been accessed also by optical far-field methods, since they were separated by a distance of more than half the wavelength. Here, subwavelength control of the photoemission distribution of a single hot spot is investigated. The two ROIs at this hot spots, i.e. ROI-3 (red solid rectangle) and ROI-4 (black dashed rectangle) are separated by about 150 nm (see Figure 5.5a) and, therefore, well below the diffraction limit. The fitness function is again chosen as the ratio of the time-integrated averaged photoemission

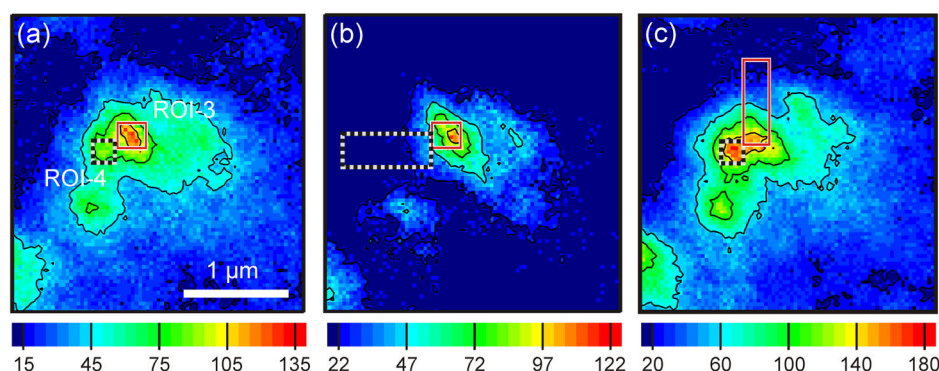


Figure 5.5.: Adaptive control of hot spot photoemission distributions below diffraction limit. The presented details of PEEM images are showing the identical spatial region. (a) Photoemission distribution of unshaped reference pulse. The center positions of ROI-3 (white and red rectangle) and ROI-4 (dashed black rectangle) are separated by approximately 150 nm. In both regions significant photoemission is observed. The color bar presents the photoemission counts per pixel. (b) Photoemission distribution after adaptive localization of the yield in ROI-3, achieved by maximization of $f_{3,4}(\varphi_1(\omega), \varphi_2(\omega))$ (Eq. (5.2)). To support a fast convergence of the evolutionary algorithm, ROI-4 was extended to the left. (c) ROIs and photoemission pattern for the optimized localization in ROI-4 corresponding to a minimization of $f_{3,4}(\varphi_1(\omega), \varphi_2(\omega))$. ROI-3 was enlarged to the top.

yield in the respective ROIs:

$$f_{3,4}(\varphi_1(\omega), \varphi_2(\omega)) = \frac{Y_{\text{ROI-3}}}{Y_{\text{ROI-4}}}. \quad (5.2)$$

Thus, by maximizing $f_{3,4}$ the photoemission localized in ROI-3 is enhanced relative to ROI-4. Adaptive optimizations for maximization and minimization of $f_{3,4}$ were performed. The resulting photoemission distributions are depicted in Figure 5.5b and 5.5c, respectively. To improve the performance of the adaptive optimization scheme, the ROIs were adjusted by enlarging ROI-4 to the left in case of the enhancement of ROI-3 and by enlarging ROI-3 to the top in case of the enhancement of ROI-4. These adaptations in the definition of the regions did not change those parts of the ROIs that define the boundary between the regions. Instead, areas with relatively low photoemission yield for bandwidth-limited pulses were added to the ROI which was not favored by the optimization goal. The ROIs are defined in a way that the value of the fitness function for unshaped laser pulses is clearly above 1. Effectively, this definition ensures a fast convergence, while maintaining the identical optimization goal as for the original ROIs. Especially, it suppresses solutions that diminish the total photoemission yield, since those cases only achieve fitness function values close to 1.

The maximization of $f_{3,4}$ resulted in suppression of the photoemission in ROI-4 and other parts of the hot spot and a high photoemission yield localized in ROI-3. The minimization of $f_{3,4}$ created a photoemission distribution with its maximum in ROI-4, but the contrast between both regions is not as high as in Figure 5.5b. Moreover, the photoemission is not confined to ROI-4, but it is spread over the complete hot spot reaching over a distance of more than one micrometer. Apparently, the adaptive optimizations addressed at least two different local resonators selectively by different pulses. For this reason, the local response function has to change considerably on a subwavelength length scale. Interestingly, these two modes seem to be confined unequally. Whereas the resonator in ROI-3 creates strongly localized photoemission, the mode created by

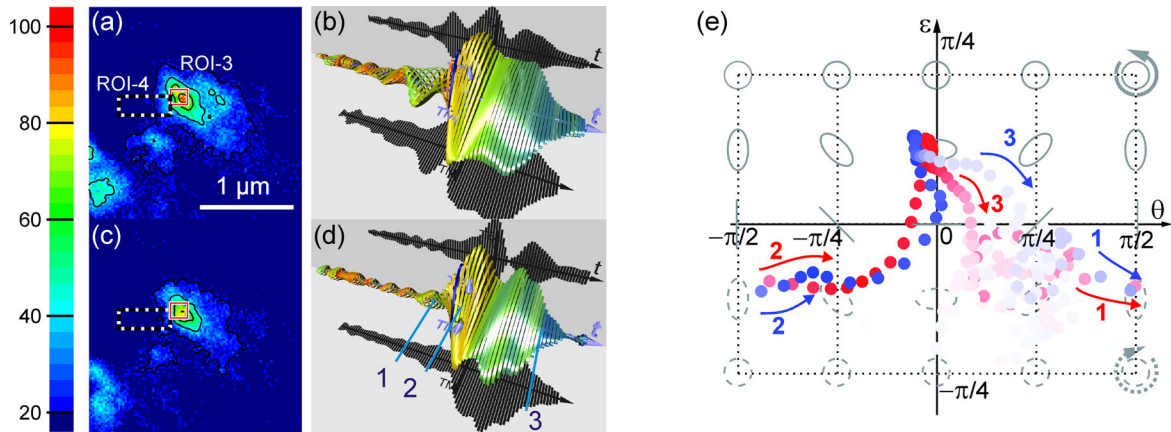


Figure 5.6.: Reproducible coherent control of subwavelength near-field distributions at a single hot spot. (a,c) Multiphoton photoemission distribution at a hot spot excited by the optimal pulse shapes found for two independent adaptive optimizations with identical fitness function and regions of interest. (b,d) Quasi-3D representations of the optimal pulse shapes used for illumination in (a) and (c). The presented time interval in both representations ranges from -500 fs to 300 fs. The temporal separation between the ellipses indicating the momentary polarization state is 8.7 fs. The amplitudes of each pulse are normalized to their respective maximum. The temporal positions 1, 2 and 3, which are also highlighted in (e), are indicated by blue lines in (d). (e) Poincaré representation of the optimal pulses for the same time interval and temporal separation between the data points. The colored arrows define the temporal directions in the plotted data. The respective numbers denote their temporal position as presented in (d). The red dots indicate the evolution of the polarization state in the pulses belonging to (a) and (b). The blue dots mark the pulse for (c) and (d). The color saturation corresponds to the normalized total intensity at the temporal step. Adapted from [3].

minimizing $f_{3,4}$ is bigger than the wavelength. The total photoemission yield of the optimized pulses enhancing ROI-3 is lower as for the reference pulse. The overall photoemission after optimization of ROI-4 exceeds that of the reference, but the enhancement is not as strong as in Section 5.2.1.

5.2.3. Reproducibility of Adaptive Optimizations

In this example for coherent control experiments on a corrugated silver film the optimization described in Section 5.2.2 that enhanced the photoemission in ROI-3 was verified in a consecutive optimization with identical optimization goal and fitness function. Differences in the optimizations occur in the deviating choice of the starting gene pool. Hence, the individuals of the subsequent optimizations were initially located in other positions of the parameter space. Still, both optimizations successfully converged and localized the photoemission distribution in ROI-3 and suppressing excitation in ROI-4 (see Figure 5.6a and c). The total yield obtained for the second optimization is slightly reduced, but the excitation pattern is very similar. By evaluating the optimal pulse shapes it is tested, whether the achievement of the same optimization goal has lead to convergence towards identical optimal individuals. The quasi-3D representations of the initial and the subsequent optimizations are presented for comparison in Figure 5.6b and d. As already observed in Section 5.2.1, the pulse shapes are elongated considerably and show a complex structure. A high consistency of the pulse shapes is observed, especially in the high



Figure 5.7: Detail of PEEM image for unshaped laser pulse. Three ROIs are defined for evaluation of the two-parameter scans. The results of the two-parameter scans are presented in Figure 5.8. Taken from [3].

intense parts of the pulses, where the polarization is turning from linear horizontal to vertical orientation. Also smaller features exhibit a good accordance suggesting that they also influence the control efficiency.

To evaluate and compare the evolution of the polarization states, the Poincaré representation of the optimized pulse shapes are plotted in Figure 5.6e. The position on the Poincaré surface defines the orientation θ and ellipticity ϵ that were introduced in Chapter 1.1. For each ellipse depicted in the quasi-3D representations a point on the Poincaré surface is plotted. The color saturation of the marker indicates the total intensity at the temporal position. The red circles belong to the first optimization (Fig. 5.6a) and the blue circles to second (Fig. 5.6c). The optimal pulse shapes of both adaptive optimizations follow almost identical trajectories in the Poincaré plot. They start with a series of low intense prepulses in which the polarization states varies around $\theta = \pi/4$ and $\epsilon = -\pi/10$. The first arrows mark a transition towards slightly elliptically polarization states with principal axes pointing in vertical direction (TE). The intensity further increases in the region marked by the second arrow and the orientation of the polarization state begins to rotate while maintaining the ellipticity. Hence the polarization state follows a horizontal line on the Poincaré surface. In both pulses this rotation further progresses until almost horizontal polarization is reached. Here, also ϵ is affected. An increase of the ellipticity value first leads to completely linear polarization at $\epsilon = 0$ and finally to a change of the sense of rotation of the electric field vector. The point in time at which ϵ is zero can be identified easily in Figure 5.6d via a distinct dip in the projection of the vertical component. The polarization state remains in both pulses at almost identical positions on the Poincaré surface for over 100 fs as it is observable by the high point density around $\theta = -\pi/20$ and $\epsilon = -\pi/8$. Then the intensity decays and the polarization state varies within the same region as during the prepulses.

Altogether, the results of the consecutive adaptive optimizations and the pulse characterizations demonstrated that the coherent control experiments on the corrugated silver surface are highly reproducible. The obtained optimal photoemission distributions and the optimal pulse shapes are identical in the most important features. Thus, even for changed starting conditions e.g. different pool of individuals a convergence to the same global optimum of the control landscape was observed.

5.2.4. Multidimensional Pulse Parameter Scans

As it was demonstrated in Sections 5.2.1–5.2.3, adaptive optimizations at photoemission hot spots found optimal pulse shapes and, thereby, enabled the coherent control of localized near-fields on corrugated silver surface. A common feature of these pulse shapes is are prepulses that are related to a nonvanishing third-order dispersion (TOD). Furthermore, a polarization dependence

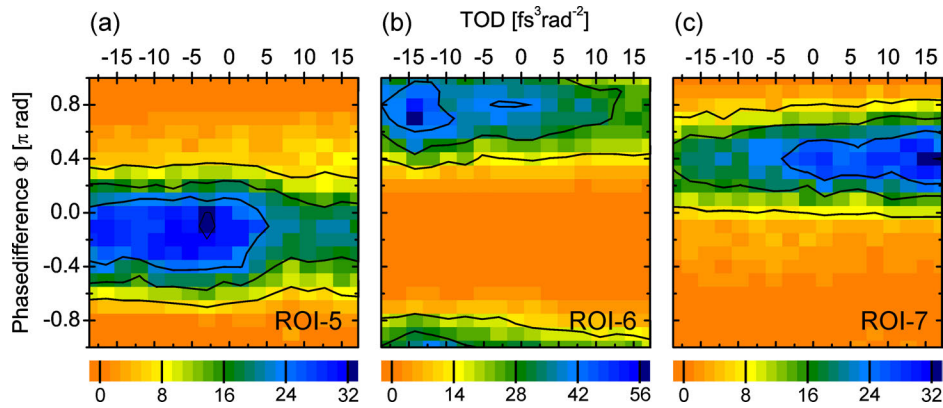


Figure 5.8.: Average photoemission yield for ROIs indicated in Figure 5.7 in two-parameter scan of third-order dispersion (TOD) and relative phase difference Φ applied with the two-layer LCD. The TOD is scanned in the interval from $-18.7 \cdot 10^3 \text{ fs}^3\text{rad}^{-2}$ to $17.2 \cdot 10^3 \text{ fs}^3\text{rad}^{-2}$ and the relative phase is scanned from $-\pi$ to π . (a) The maximum in ROI-5 was observed at $\text{TOD}_5 = 3.0 \cdot 10^3 \text{ fs}^3\text{rad}^{-2}$ and $\Phi_5 = 0.31 \text{ rad}$. (b) The maximum of ROI-6 is located at $\text{TOD}_6 = -14.2 \cdot 10^3 \text{ fs}^3\text{rad}^{-2}$ and $\Phi_6 = 2.1 \text{ rad}$. (c) The maximum at ROI-7 is at $\text{TOD}_7 = 17.2 \cdot 10^3 \text{ fs}^3\text{rad}^{-2}$ and $\Phi_7 = 1.2 \text{ rad}$. Adapted from [3].

could be suspected in all the control experiments. Two-parameter scans are performed to investigate, whether these two pulse properties are indeed sufficient for controlling selectively localized excitations of the corrugated silver surface. The first scanned parameter is the TOD which is added equally to both polarization components. The second parameter is the phase difference between the polarization components $\Phi = \varphi_1 - \varphi_2$. Here, Φ is frequency-independent. As discussed in Section 2, the local response of nanostructured systems strongly varies by changing Φ . An advantage of the two-parameter scan compared to the adaptive optimizations is that simultaneously all pixels in the complete field of view are probed independently, whereas the closed loop method is always connected to the evaluation of localized ROIs and optimal pulse shapes are only associated to the local excitation in these ROIs and their vicinity.

After the data acquisition process three regions of interest are selected in the PEEM image excited by the unshaped reference laser pulse (see Fig. 5.9a). The regions ROI-5, ROI-6 and ROI-7 are located at separated photoemission hot spots. ROI-5 (red) and ROI-7 (yellow) are located close together, but do not overlap, and ROI-6 (white) is separated by approximately $5.5 \mu\text{m}$.

The TOD is scanned from $-18.7 \cdot 10^3 \text{ fs}^3\text{rad}^{-2}$ to $17.2 \cdot 10^3 \text{ fs}^3\text{rad}^{-2}$ and for each TOD value the phase difference Φ of the polarization components is scanned from $-\pi$ to π . During the two-parameter scan the photoemission in the complete field of view is recorded. For the regions ROI-5, ROI-6 and ROI-7 the time-integrated average photoemission yield as a function of TOD and Φ is depicted in Figure 5.8a, 5.8b and 5.8c, respectively. The position of each pixel in these graphs indicates the TOD and the phase difference and the color of the pixel states the corresponding photoemission in the ROI. Above the pixels the contour lines are drawn for a better visibility of the maximum photoemission positions in the spectral phase parameter space. The three ROIs differ in the optimal values for Φ and the TOD. The maximum in ROI-5 was observed at $\text{TOD}_5 = 3.0 \cdot 10^3 \text{ fs}^3\text{rad}^{-2}$ and $\Phi_5 = 0.31 \text{ rad}$. Thus, the maximum is located close to the unshaped laser pulse in the origin of the parameter space. The maxima of ROI-6 and ROI-7 are at large positive and negative TOD values ($\text{TOD}_6 = -14.2 \cdot 10^3 \text{ fs}^3\text{rad}^{-2}$ and $\text{TOD}_7 = 17.2 \cdot 10^3 \text{ fs}^3\text{rad}^{-2}$). The optimal phase differences were $\Phi_6 = 2.1 \text{ rad}$ and $\Phi_7 = 1.2 \text{ rad}$.

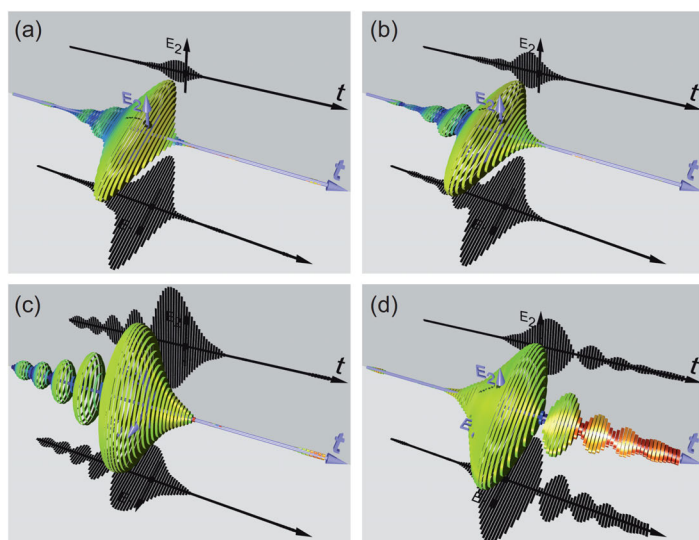


Figure 5.9: Optimal pulses of two-dimensional pulse parameter scans in quasi-3D representation. (a) Unshaped p-polarized reference pulse with duration of 50 fs. (b) Pulse shape obtained from Jones-matrix calculations for the optimal parameters for ROI-5 identified in Fig. 5.8a (c) Pulse shape obtained from Jones-matrix calculations for the optimal parameters for ROI-6 identified in Fig. 5.8b (d) Pulse shape obtained from Jones-matrix calculations for the optimal parameters for ROI-7 identified in Fig. 5.8c

However, there are also some similarities between the plots. In all cases there is no significant correlation between the relative phase Φ and the TOD visible. These pulse parameters appear to be independent. For optimizations it is important to identify independent control parameters to achieve a fast convergence. With two-parameter scans it is possible to prove such an independence for the investigated region of the parameter space.

The optimal pulse parameters identified for each ROI are employed to calculate the optimal pulse shapes based on the previously determined Jones-matrix of the experimental setup (see Section A.3). The optimal pulse shapes are shown in quasi-3D representation together with the unshaped laser pulse for comparison in Figure 5.9. The representations show the same time interval from -300 fs to 300 fs. The temporal separation of adjacent ellipses is 5.8 fs. For ROI-5 (Fig. 5.9b) the introduced cubic spectral phase leads to only a minor elongation of the pulse compared the reference. The phase difference of $\Phi = -0.31$ rad causes a slight ellipticity of the pulse. The optimal TOD was significantly higher in case of ROI-6 generating a series of prepulses. The polarization state is clearly elliptic with the major axis pointing almost in p-direction, i.e. vertically. The temporal intensity evolution of the optimal pulse for ROI-7 in contrast shows a series of subsequent pulses as a result of the highly positive TOD.

By the pulse parameter scan optimal control parameter for several individual hot spots were determined simultaneously. Apparently, the phase difference Φ has a strong impact on the selective excitation of individual hot spots. The further adjustment of the TOD leads to an optimal local photoemission. From these findings it seems likely that also in this case the polarization state is a parameter for achieving spatial control, whereas the TOD is responsible for local pulse compression.

Since the phase difference between the polarization components and the third order dispersion do not fully describe the spectral phases $\varphi_1(\omega)$ and $\varphi_2(\omega)$, only a two-dimensional section of the control parameter space was investigated. However, the experimental scheme can easily be extended to higher dimensions and include for example also a linear or quadratic contribution to the spectral phase. Otherwise, this is connected with a higher number of necessary sampling points, i.e. PEEM images. A high-dimensional parameter scan soon will be less effective to achieve a certain goal for coherent control as an adaptive optimization. Nevertheless, the results

obtained in the pulse parameter scans contain information for all spatial positions in the field of view. Hence, the pulse parameter scan has to be performed only once, whereas an adaptive optimization is limited to the investigated regions of interest and has to be repeated to analyze another spatial position.

5.2.5. Conclusion

In this section the localization of the multiphoton photoemission yield attributed to optical near-fields on a corrugated silver surface was manipulated by means of ultrafast nanoscale coherent control. In adaptive optimizations of the spectral phases of both input polarization components the localized resonances at photoemission hot spots were addressed. The ratio between the local photoemission yield in regions of interest separated on the order of the diffraction limit (see Section 5.2.1) and below the the diffraction limit (see Section 5.2.2) was controlled. In both experiments a switching between two opposite excitation patterns was achieved. The optimal laser pulses showed a surprising complexity and duration. Furthermore, a strong enhancement of the photoemission yield compared to the transform-limited reference pulse was observed. Therefore, the results of the adaptive optimizations indicate that the dynamics of the optical near-fields at the photoemission hot spots and in their surrounding are more complex than expected for individual localized surface plasmon resonances.

The two-dimensional pulse parameter scan (see Section 5.2.4) again showed that elongated pulse shapes with strong negative and strong positive TOD locally achieve the highest photoemission yield. This emphasizes the possible existence of long-living coherent modes on the corrugated silver surface. As the typical coherence lifetimes of LSP modes are in the few femtosecond regime (see Chapter 1.3.3), localized surface plasmons can be excluded as candidates. The complex local response could be connected to delocalized near-field modes in the vicinity of the individual photoemission hot spots. Since for smooth metal-vacuum interfaces such stationary delocalized modes have not been reported, they appear to be associated to the random surface structure of the sample.

In this section the time-integrated photoemission signal generated by the polarization-shaped laser pulses was used as feedback of the adaptive optimizations and the pulse parameter scans. As no time-resolved excitation scheme was employed, the evaluation of the optimal pulse shapes provides only indirect information on the temporal evolution of the localized optical near-fields. In the following sections of this chapter the local excitation dynamics at the photoemission hot spot on the corrugated silver surface are examined by 2D nanoscopy (see Section 5.3) and in a modified two-pulse nanoscopy experiment (see Section 5.4).

5.3. Coherent 2D Nanoscopy on a Corrugated Silver Surface

In the experiments presented in this section 2D nanoscopy probes local spectral properties of the photoemission from hot spots on the corrugated silver surface. The principles of this spatial-resolved ultrafast nonlinear spectroscopy technique have been explained in Chapter 4. Since the decoherence of excited electrons in the metal is fast, the photoemission data contains information on the local electric field on the surface as it is discussed in Chapter 4.2.2. Hence, the 2D nanoscopy measurement determines the local response function $A(\mathbf{r}, \omega)$ describing the collective electronic response to the incident electric field. The investigated sample is the same used in

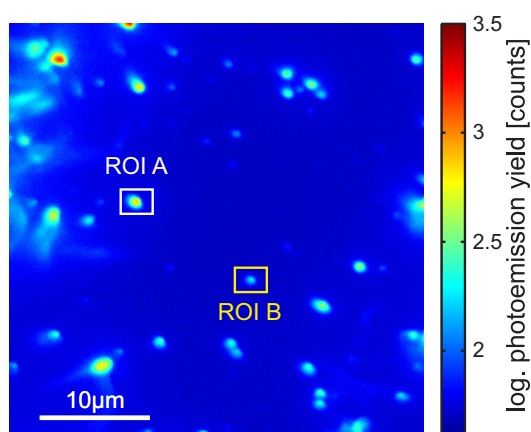


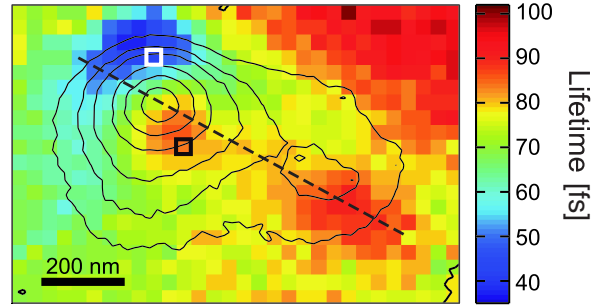
Figure 5.10: PEEM reference image of corrugated silver surface for 2D nanoscopy with wide field of view. The photoemission yield is plotted on a logarithmic scale. Two regions of interest are highlighted. In ROI A (white rectangle) a hot spot with fast decaying delay-dependent 2D nanoscopy signal. At the hot spot in ROI B (yellow rectangle) 2D nanoscopy with high spatial resolution was performed.

the previous sections of this chapter, but the position of the field of view on the sample has been changed. The experimental setup has already been presented in Section 5.1. In contrast to the control experiments the polarization pulse shaper is set to amplitude and phase-shaping mode enabling the generation of purely horizontally polarized pulse sequences. The optical setup does not include a second beam of higher carrier frequency as it is suggested in Section 4.2. However, in principle an implementation of an ionization pulse in the setup is feasible, as it has been demonstrated successfully in Section 2.

The overview PEEM image of the sample shown in Figure 5.10 strongly resembles those obtained in the control experiments (see Fig. 5.3a). A random distribution of photoemission hot spots is observed. There is a distinct variation in the photoemission yield of the individual spots. Two regions of interest were defined. ROI A contains a photoemission hot spot that shows a fast decay of the delay-dependent 2D nanoscopy signal. Results from ROI A are only presented as a part of Figure 5.12d. The 2D nanoscopy measurement evaluated in the following is performed with smaller field of view ($18 \mu\text{m}$) and improved spatial resolution at ROI B. The size of each pixel was estimated to be $(18 \text{ nm})^2$.

The 2D nanoscopy measurement determines the local photoemission yield $Y(\mathbf{r}, \tau, t, \varphi_\tau, \varphi_t)$ for every spatial position \mathbf{r} while varying four independent parameters of the collinear excitation pulse sequence (see Fig. 4.3). At each delay step PEEM images for four phase combinations $((\varphi_\tau, \varphi_t) \in \{(0, 0)(0, \pi)(\pi, 0)(\pi, \pi)\})$ are recorded. These allow for a 2×2 phase cycling of the obtained signals as it is described in Chapter 4.2.4. The delays τ and t are scanned independently from 0 fs to 280 fs in step of 4fs. The population time is set to $T = 0$ fs and the phase between second and third pulse of the sequence was set to $\varphi_T = 0$ during the complete experiment. At each delay step a reference PEEM image of ROI B is obtained additionally to the photoemission data for the four phase combinations. To generate an isolated reference pulse, all pulses of the sequence are shifted to zero delay with no relative phase, i.e. $\tau = t = T = 0$ fs and $\varphi_\tau = \varphi_t = \varphi_T = 0$. The reference images are employed for the drift correction of the PEEM images discussed in Appendix B and for monitoring eventual changes of the photoemission yield in the field of view under standardized conditions. These fluctuations occur during the measurement time of about twelve hours for the complete 2D nanoscopy experiment, which is necessary for scanning the delays and relative phases of the pulse sequence and taking in total 25205 PEEM images.

Figure 5.11: Spatial map of local oscillator lifetime (color) at hot spot in ROI B and contour plot (black lines) of photoemission distribution. Local 2D nanospectra obtained by binning of 2×2 adjacent pixels were fitted by an oscillator model function. The binned pixel size was $(36 \text{ nm})^2$. The 2D nanospectra obtained for the highlighted pixel 1 (white) and pixel 2 (black) are presented in Figure 5.12. Taken from [4].



Having completed the experimental data acquisition process the drift correction scheme (see Appendix B) is applied to ensure stationary positioning of the sample in the PEEM images. Afterwards, for each spatial position the delay-dependent results of all phase combinations $Y(\mathbf{r}, \tau, t, \varphi_\tau, \varphi_t)$ are combined according to Eq. (4.40), where the phase cycling coefficients are determined by Eq. (4.50):

$$\begin{aligned} \tilde{Y}(\mathbf{r}, \tau, t, 2, -1) &= \sum_{l=0}^1 \sum_{m=0}^1 e^{-i(l-m)\pi} \frac{Y(\mathbf{r}, \tau, t, l \cdot \pi, m \cdot \pi)}{4Y_{ref}} \\ &= \sum_{l=0}^1 \sum_{m=0}^1 (-1)^{l-m} \frac{Y(\mathbf{r}, \tau, t, l \cdot \pi, m \cdot \pi)}{4Y_{ref}}. \end{aligned} \quad (5.3)$$

Here, the division through the reference signal $Y_{ref} = Y(\mathbf{r}, 0, 0, 0, 0)$, obtained with an unshaped laser pulse for each delay step, accounts for temporal changes in the signal. As it emphasized by Eq. (5.3), the coefficients are all real-valued. Accordingly, the phase cycled time domain signal $\tilde{Y}(\mathbf{r}, \tau, t, 2, -1)$ is also real-valued. After Fourier transformation the 2D spectra are point symmetric as already discussed for Figure 4.15. The order of phase cycling does not suffice to exclude the redundant signal for $(\beta, \gamma) = (-2, 1)$ which contains spectral peaks inverted at the center frequency. Additionally, also the signals belonging to $(\beta, \gamma) = (0, -1)$ and $(\beta, \gamma) = (0, 1)$ survive the phase cycling and still contribute to $\tilde{Y}(\mathbf{r}, \tau, t, 2, -1)$. Nevertheless, the evaluation of the 4 step phase cycling data already gives an insight in the possibilities of 2D nanoscopy.

The spatial map depicted in Figure 5.11 is a combination of several types of data. The contour plot (black lines) indicates the photoemission distribution in ROI B for unmodulated laser pulses. An asymmetrically shaped hot spot is visible which exhibits a small local maximum in the photoemission yield which is displaced by about 420 nm along the black dashed line with respect to the main peak. The order of nonlinearity of the photoemission process was estimated analog to Figure 5.3 to be $N \approx 4$ during the 2D nanoscopy measurements. An explanation for this increased value compared to Figure 5.3 is the partial loss of the deposited Cs on the silver surface causing an increase of the work function. The colored pixel in Figure 5.11 present the local coherence lifetime T_2 obtained by fitting the local two-dimensional nanoscopy spectrum by an oscillator model function. The individual pixels are obtained by binning 2×2 adjacent pixels of the PEEM detector. The binned pixel size was $(36 \text{ nm})^2$. Details of the local nanospectra and the corresponding fits will be discussed below for two of the pixels. Pixel 1 is marked by a white square and pixel 2 by a black square. Additionally, the coherence lifetime along the black dashed line will be presented in 5.12c. The color scale of the lifetime map ranges from 35 fs to

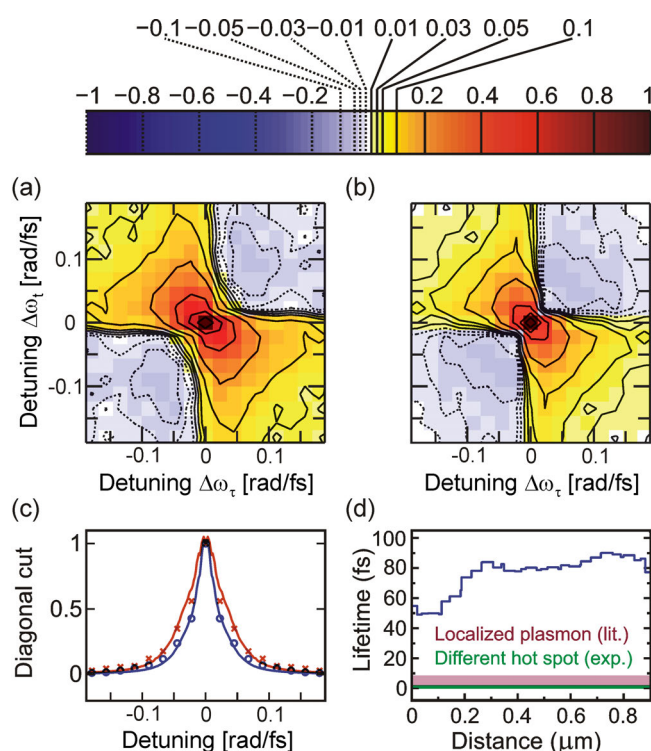


Figure 5.12: Local evaluation of 2D nanoscopy spectra. (a) Real part of 2D spectrum at pixel 1. (b) Real part of 2D spectrum at pixel 2. (c) Antidiagonal cut, i.e. along $\Delta\omega_\tau = -\Delta\omega_t$, through real part of 2D spectrum at pixel 1 (red crosses) and 2 (blue circles) and fits (solid lines in respective colors) along this cut. (d) Spatial cut along line indicated in lifetime map in Figure 5.12. For comparison, the range of lifetime values of localized plasmon resonances found in literature (red) and the lifetime determined from hot spot in ROI A in Figure 5.10 (green) are indicated. Adapted from [4].

100 fs. Whereas, pixel 1 is located in a region with a fitted dephasing time T_2 of about 40 fs, T_2 at the environment of pixel 2 is significantly higher. Slowest dephasing was observed in the photoemission signals originating from the region around the weaker photoemission maximum. In Figure 5.12 details of the 2D nanoscopy measurement in ROI B are presented. The local nanospectra at pixel 1 and 2 were normalized and their real parts are plotted in Figure 5.12a and b, respectively. The size of the frequency pixels (0.022 rad/fs in both directions) derives from the maximal delay of the scan. Accordingly, the maximum frequency detuning from the laser frequency $\omega_L = 2.36$ rad/fs depends on the delay step sizes and amounts to ± 0.774 rad/fs for both axes. In Figure 5.12a and b the center details of the nanospectra are depicted with frequency axes ranging from -0.187 rad/fs to 0.187 rad/fs. The general shape of the nanospectra is very similar for both spatial positions. Since the time domain signals are completely real-valued (see Eq. (5.3)), the two-dimensional spectra are symmetric with respect to the inversion at the center frequency position. The real part is positive on the antidiagonal ($\Delta\omega_\tau = -\Delta\omega_t$) and on the diagonal ($\Delta\omega_\tau = \Delta\omega_t$) it changes from positive values at the center to negative values for larger frequencies. In both 2D nanoscopy spectra the maximum signal is located at the zero-detuning position. Differences between the two-dimensional spectra are visible in the spectral width. In case of pixel 1 the obtained spectrum is broader. Apparently, the local response at this photoemission hot spot is in resonance with the excitation laser. This was expected because of the high local photoemission yield. However, the lack of observed spectral shift is not unambiguously associated with an unshifted local response spectrum. The overlap between the photon echo signal and its redundant mirror signal might cause an amplitude maximum for zero detuning as long as the signals are not separated sufficiently with respect to their spectral widths.

The local lifetime $T_2(\mathbf{r})$ shown in Figure 5.11 is based on an evaluation of the measured 2D nanoscopy spectra by means of a least-square fits minimizing the deviations of simulated 2D

spectra. A single Lorentz oscillator response function was employed for calculating the delay-dependent local photoemission signal (see Eqs. (4.43) and (4.49)). After phase cycling and Fourier transformation, the normalized 2D spectra are compared with the experimental results. During the fit the oscillator frequency $\omega_{Lo}(\mathbf{r})$ remains fixed to the center frequency of the laser spectrum. Thus, the spectral feature always appears at zero detuning in the 2D nanoscopy spectra and the spectral width $\gamma_{Lo}(\mathbf{r}) = 1/T_2(\mathbf{r})$ is the only varied parameter [4]. In the diagram in Figure 5.12c the red crosses and blue circles indicate the real part of the 2D spectra at pixel 1 and 2, respectively, along the antidiagonal cut ($\Delta\omega_\tau = -\Delta\omega_t$). Evidently, also in this representation the spectral feature at pixel 1 is broader than the lineshape observed at pixel 2. The solid lines show the reconstruction of the data by the fit.

In Figure 5.12d the local lifetime evolution along the dashed line in Figure 5.11 is shown as a blue line. For comparison two additional values are indicated. The red area marks the range of lifetimes expected from literature. The green line is obtained from fitting the local nanospectrum from ROI A. Here, a very short lifetime of $T_2 < 1$ fs was retrieved. This is within the margins of error in a good accordance to the literature. It also gives evidence that with 2D nanoscopy short lived excitations can be detected and analyzed. The resulting lifetimes along the cut in ROI B are distinctly exceeding these values. Furthermore, the spatial dynamics of the lifetime parameter demonstrate that with 2D nanoscopy it is feasible to resolve changes in the local spectral properties on sub-diffraction length scale.

In this first demonstration of coherent 2D nanoscopy the applicability of this newly developed two-dimensional spectroscopy technique for the investigation of nanostructured samples was tested. The combination of photoemission electron microscopy and pulse shaping provides stable collinear laser pulse sequences and achieves a spatial resolution below the diffraction limit. Phase cycling is employed to retrieve local spectral information based on photoemission signals originating from areas as small as $(36 \text{ nm})^2$. To obtain unambiguous spectral information, a higher degree of phase cycling is necessary. In Chapter 6 2D nanoscopy experiments performed with 4×4 phase cycling are used to determine the frequency detuning and linewidth of strongly localized photonic modes in thin-film solar cells.

In the remaining section of this chapter a two-pulse experiment is discussed. Since only one delay parameter is scanned and only one relative phase parameter is involved, this relative phase is scanned with much smaller steps sizes than possible for 2D nanoscopy. In contrast to the 2D nanoscopy experiments the obtained data are analyzed in time domain. By Fourier transform simulations the local spectral response at defined regions of interest is retrieved using physical model functions.

5.4. Hybridization of Plasmonic Modes on a Corrugated Ag Surface

To further investigate the dynamics of the local excitations at the corrugated silver surface a second time-resolved experiment is performed. Starting from the generalized four pulse sequence of 2D nanoscopy (see Figure 4.3c), the delays τ and t are set to 0 fs and the relative phases between the first and the second pulse (φ_τ) as well as between the third and the fourth pulse (φ_t) are set to zero. This adaptations generate a sequence $E_2(t, -T, 0, -\varphi_T, 0)$ containing only two pulses with relative delay T and relative phase φ_T . The electric field of the excitation two-pulse

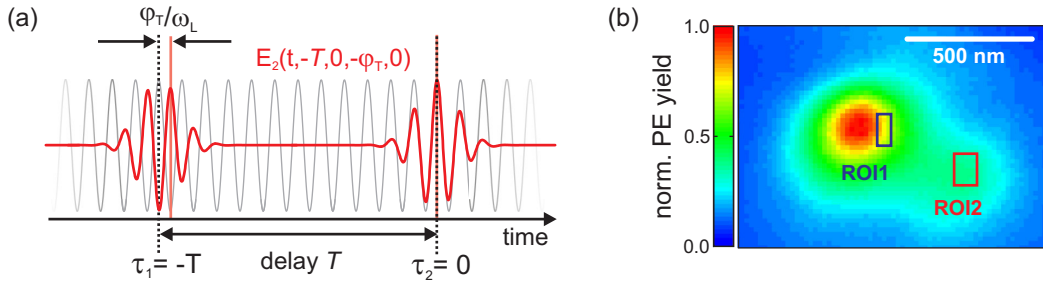


Figure 5.13.: Two-pulse nanoscopy experiment. (a) Schematic representation of the electric field $E_2(t, -T, 0, -\varphi_T, 0)$ (red solid line) in the two-pulse nanoscopy experiment. The graph exhibits fewer field oscillations than in the actual experiment to emphasize the influence of the relative phase between the subpulses. The delay T denotes the temporal separation of the pulse envelope maxima. The relative phase φ_T is defined with respect to the carrier oscillations (gray solid line) at the central laser frequency ω_L . To guide the eye, the temporal positions of the electric envelope maxima and the highest positive electric fields within the subpulse are marked by dotted black and red solid lines, respectively. (b) Detail of PEEM image of investigated hot spot with ROI1 (blue) and ROI2 (red) indicated as rectangles. Adapted from [4].

sequence is written according to Eq. (4.46) as

$$E_2(\omega, -T, 0, -\varphi_T, 0) = \frac{E_L(\omega)}{2} \left(e^{i[(\omega - \omega_L)T - \varphi_T]} + 1 \right), \quad (5.4)$$

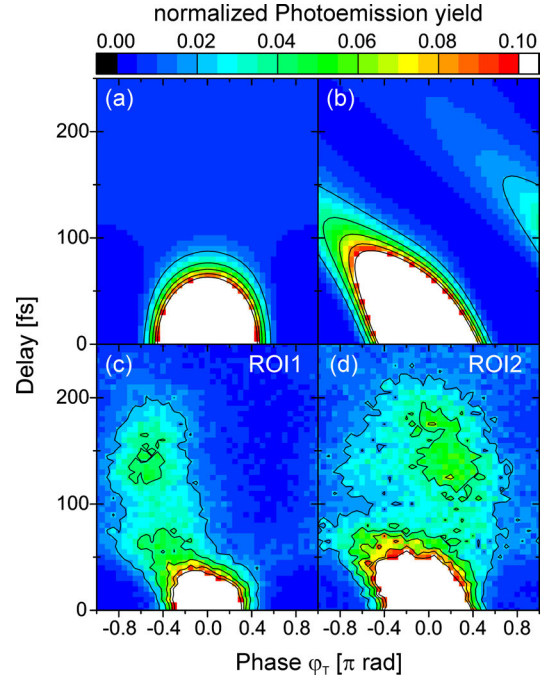
where $E_L(\omega)$ is the spectrum of the unshaped laser pulse. Figure 5.13a depicts this excitation sequence schematically. The first excitation pulse is shifted to the temporal position $\tau_1 = -T$ and exhibits the phase $\varphi_1 = -\varphi_T$ with respect to the carrier frequency oscillation, whereas the second pulse remains fixed at $\tau_2 = 0$ and $\varphi_2 = 0$. The first subpulse excites a local electric field according to the local response function. A variation of φ_T at each delay step T probes the remaining coherence for the particular temporal position, since the local electric field is further enhanced or suppressed by the second pulse as a function of T and φ_T .

In Section 5.4.1 results of the two-pulse nanoscopy experiment are presented. They are obtained from confined spatial regions at the same hot spots as investigated in Section 5.3. The data is shown in two-dimensional plots as function of the delay T and the relative phase φ_T . The results of the measurement significantly differ in their characteristics from simulated data obtained for single Lorentz response functions. A physical model based on the hybridization of dark and bright plasmonic modes is introduced in Section 5.4.2. It explains the detected long-lived coherences and the coherent beating behavior by coherent energy transfer between a localized and a delocalized plasmonic mode. In Section 5.4.3 the experimental results are evaluated employing the hybridization model to fit the local spectral response function. Additionally, two alternative fit functions are used to determine whether also other physical models are able to fit the measured photoemission data and obtain local spectral response function similar to the hybridization model.

5.4.1. Experimental Results and Representation by Delay-Phase-Plots

The two-pulse nanoscopy experiment is conducted at the identical sample position as the previously presented 2D nanoscopy measurements and the same photoemission hot spot is selected for further

Figure 5.14: T - φ_T -plots of two-pulse nanoscopy simulations and measurements. (a) Simulated photoemission yield for broad Lorentz oscillator ($\gamma_{Lo} = 0.8$ rad/fs) with spectral response located at the center frequency of the excitation spectrum ($\omega_L = 2.36$ rad/fs, FWHM = 0.061 rad/fs). (b) Simulated photoemission yield for small bandwidth Lorentz oscillator ($\gamma_{Lo} = 0.01$ rad/fs) with center frequency $\omega_{Lo} = 2.39$ rad/fs detuned from the excitation spectrum. (c,d) Photoemission yield in ROI1 (c) and ROI2 (d) in two-pulse nanoscopy scan. Adapted from [4].



evaluation. The hot spot photoemission distribution for excitation by reference pulses is presented in Figure 5.13b. Two regions of interest (ROI1 and ROI2) are indicated by colored rectangles. They are separated by approximately 400 nm, i.e. half of the excitation wavelength. During the two-pulse measurement the time-integrated local photoemission yield is determined while scanning the delay T in steps of 5 fs from 0 fs to 250 fs and independently scanning φ_T from $-\pi$ to π in steps of $\pi/20$.

The results of measured and simulated two-pulse nanoscopy experiments are presented as contour lines and colored pixels in T - φ_T -plots (see Figures 5.14, 5.15 and 5.17). These show the applied relative phase φ_T on the horizontal axis and the delay T on the vertical axis. The T - φ_T -plots are periodic in φ_T . Accordingly, the pixels at $\varphi_T = -\pi$ and $\varphi_T = \pi$ show identical information. The false color plot and the contour line depict the local photoemission yield at the investigated sample position. For a better visibility the color scale is adjusted to show the dynamic between zero and ten percent of the maximum yield.

Simulations of the photoemission yield are performed for the same values of delay T and phase φ_T as in the experiment. The photoemission yield $Y^{(2N)}(T, \varphi_T)$ generated by the pulse sequence is calculated in analogy with the Fourier transform time domain simulation of 2D nanoscopy (see Chapter 4.3.1) via substituting Eq. (5.4) into Eqs. (4.43) and (4.49):

$$Y^{(2N)}(T, \varphi_T) \propto \int_{-\infty}^{\infty} [\mathcal{F}^{-1} \{A(\mathbf{r}, \omega) E_2(\omega, -T, 0, -\varphi_T, 0)\}]^{2N} dt. \quad (5.5)$$

The nonlinear order of the photoemission process during the two-pulse nanoscopy experiments has been determined to be $N = 4$ in a laser power scan similar to Fig. 5.3b. For each combination of delay and phase the photoemission yield is calculated by inserting a response function $A(\mathbf{r}, \omega)$ into Eq. (5.5) and solving the integral numerically. Figure 5.14a and b present T - φ_T -plots of single

Lorentz oscillators excited by a Gaussian excitation spectrum with center frequency identical to the rotating frame frequency $\omega_L = 2.36$ rad/fs used for the pulse sequence definition and spectral FWHM of 0.061 rad/fs.

For a large-bandwidth oscillator (Fig. 5.14a) the spectral response function is flat in the overlap with the excitation spectrum. The temporal evolution of the local electric field closely follows the excitation pulses and the photoemission yield rapidly decays with T . For each delay step the highest photoemission is observed at $\varphi_T = 0$. This behavior is caused by the rotating frame definition of the electric field pulse sequence. As the local electric field oscillation frequency is identical to ω_L , which is simultaneously the center frequency of the excitation spectrum, the first and second local electric field pulses always interfere constructively at $\varphi_T = 0$.

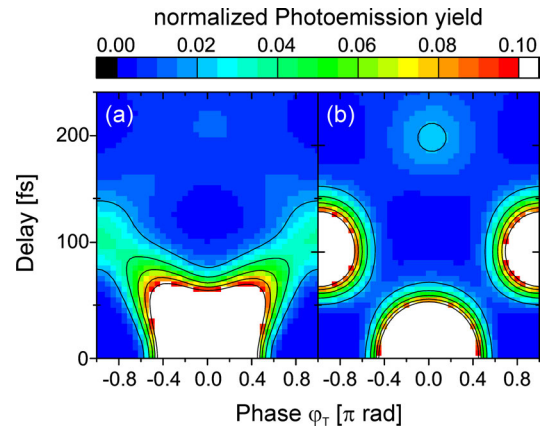
Figure 5.14b shows the T - φ_T -plot for a Lorentz oscillator with smaller bandwidth ($\gamma_{Lo} = 0.01$ rad/fs) and a center frequency $\omega_{Lo} = 2.39$ rad/fs, which is detuned with respect to the excitation frequency. The smaller bandwidth leads to an elongation of the observed trace in the T - φ_T -plot because the local electric field excited by the first pulse decays slower. The contour line indicating the 2%-level reaches out to a delay of $T = 155$ fs instead of $T = 85$ fs for the broadband response (see Fig. 5.14a). Furthermore, the φ_T position of maximal photoemission yield shifts to negative values with the delay T because the oscillations of the local electric field are faster than the rotating frame frequency $\omega_L = 2.36$ rad/fs. Accordingly, the local field acquires an additional phase during T that has to be compensated for by φ_T to achieve constructive interference with the local electric field excited by the second pulse. Here, an advantage of the two-pulse nanoscopy experiment compared to the 2D nanoscopy scheme with 2×2 phase cycling is visible. Whereas in the 2D nanoscopy measurements on the silver surface (see Section 5.3) no detuning from the center frequency could be detected for symmetry reasons, the T - φ_T -plots contain such spectral information. However, the spectral response function is not directly visible, but has to be retrieved by further evaluation procedures e.g. fitting a model function to the T - φ_T -plots.

A difference to 2D nanoscopy is that the T - φ_T -plots show the photoemission yield as a function of the phase φ_T , whereas the results of 2D nanoscopy are presented for fixed phase combinations prior to phase cycling (see Fig. 4.12) or as a complex-valued partial signal after phase cycling as a function of two delays (see Fig. 4.14). Therefore, the observation of a beating in the photoemission signal $Y^{(4)}(\tau, t, \varphi_\tau, \varphi_t)$ (see Fig. 4.12) indicates a detuning from the center frequency ω_L . In the T - φ_T -plots the corresponding information is visible in vertical direction, i.e. for constant φ_T . For example, in Figure 5.14b the photoemission signal at $\varphi_T = 0$ exhibits its maximum at zero delay but it also recurs after a delay $T = 2\pi/(\omega_{Lo} - \omega_L) \approx 210$ fs. However, it is obvious in the complete T - φ_T -plot that the signal decays gradually and monotonously while it accumulates an increasing phase difference to the rotating frame oscillating at the laser frequency ω_L .

The spatially integrated results in ROI1 and ROI2 are shown in Figure 5.14c and d normalized to their individual maximum. In both ROIs phase-dependent photoemission signals are observed which extend to delays T greater than 200 fs indicating long coherence lifetimes at the investigated sample positions. However, the details of the T - φ_T -plots differ.

For delays between 0 fs and 100 fs in ROI1 (Fig. 5.14c) the phase position of the photoemission maximum shifts towards negative relative phases φ_T . This indicates, similar to Figure 5.14b, a detuning of the local response function towards higher frequencies. For delays larger than 75 fs the highest emission is observed for relative phases $\varphi_T \approx -\pi/2$ and remains stationary at this

Figure 5.15: T - φ_T -plots of two-pulse nanoscopy simulations with two oscillators at center frequencies $\omega_{L01} = 2.33$ rad/fs, $\omega_{L02} = 2.39$ rad/fs and spectral widths $\gamma_{L01} = \gamma_{L02} = 0.01$ rad/fs. (a) Incoherent sum of photoemission yield of single oscillators. (b) The coherent superposition of the oscillator response function generates the local electric field which is used to calculate the photoemission yield.



position. A coherent beating of the photoemission signal occurs which is not observed in the single oscillator T - φ_T -plots. After a fast initial drop to a minimum value at $T = 90$ fs, the local photoemission yield recurs around $T = 135$ fs and $\varphi_T = -0.55\pi$. In case of the single oscillator response functions only a monotonous decay of the yield with the delay T is possible.

In case of ROI2 (Fig. 5.14d) an even more pronounced detuning for smaller delays is observed. Similar to ROI1 the photoemission yields drops to a minimum at approximately $T = 90$ fs and a beating of the photoemission signal occurs in the delay interval between 100 fs and 210 fs. However, the observed beat is located at slightly positive φ_T values and is tilted in the sense that for larger delays the phase position of the highest emission approaches $\varphi_T = 0$.

The T - φ_T -plots of both ROIs exhibit characteristics that cannot be achieved by a single Lorentz oscillator. A beating behavior is not feasible by excitation of a single oscillator because it involves the superposition of at least two different frequencies. Furthermore, in case of a single localized plasmonic resonance the strong internal and radiative damping leads to a fast loss of the excitation – typically within 10 femtoseconds or shorter [172]. Consequently, for a single LSP resonance the obtained T - φ_T -plot is expected to resemble the broadband response case discussed in Figure 5.14a. Nevertheless, the photoemission is confined to the hot spot. Thus, a strong field enhancement, typical for localized surface plasmons, is observed.

Since the beating as well as the particular shapes of the T - φ_T -plots in Figure 5.14c and d cannot be explained by a single oscillator, more complex physical models have to be tested that involve at least two resonances. As it is emphasized by Figure 5.15, already two Lorentz oscillators are able to generate more complex traces in the T - φ_T -plots. Here, two cases are distinguished.

In case of non-overlapping local electric fields the oscillators independently drive local photoemission processes and the T - φ_T -plot is the incoherent sum of the single traces. An example for the incoherent sum of the oscillator signals is shown in Figure 5.15a. The same excitation spectrum as in Figure 5.14 is used. The oscillators are detuned by -0.03 rad/fs and 0.03 rad/fs from the center frequency $\omega_L = 2.36$ rad/fs and both have a spectral width of 0.01 rad/fs and identical maximum amplitudes. The individual T - φ_T -plots are identical to Figure 5.14b or are given by inversion at the vertical line through $\varphi_T = 0$. Since the photoemission yield is a real and positive quantity, the single oscillator T - φ_T -plots always add constructively and when both traces meet, the total yield is enhanced.

If the local electric fields overlap, they interfere and the local response function is given by the

coherent superposition of the single oscillator response functions

$$A_{2Lo}(\omega) = \frac{A_{1/2}}{\omega_{Lo1}^2 - \omega^2 + i2\gamma_{Lo1}\omega} + \frac{1}{\omega_{Lo2}^2 - \omega^2 + i2\gamma_{Lo2}\omega} . \quad (5.6)$$

The parameter $A_{1/2}$ determines the ratio of the Lorentz oscillator amplitudes. Figure 5.15b presents the T - φ_T -plot calculated for of the coherent superposition of the identical Lorentz oscillators as before. The amplitude ratio is set to $A_{1/2} = 1$. Here, the T - φ_T -plot is stronger modulated. The observed pattern shows a distinct beating. The photoemission is suppressed at the positions where the single oscillators exhibit considerable yield but the superposed electric fields interfere destructively, e.g. at $T = 60$ fs and $\varphi_T = -\pi/2$ as well as $\varphi_T = \pi/2$. For constructive interference a strong enhancement of the photoemission yield is visible leading to strong signals at $T = 105$ fs and $\varphi_T = \pm\pi$ as well as $T = 210$ fs and $\varphi_T = 0$. The length of the delay interval between the beats is inversely related to the frequency difference (0.06 rad/fs $\approx 2\pi/(105$ fs)).

Also with two oscillators individual lifetimes of more than 100 fs are needed to achieve elongated traces in the T - φ_T -plot as measured in ROI1 and ROI2. These cannot be provided only by localized plasmon resonances due to their strong damping. Even though surface plasmon polaritons exhibit sufficiently long lifetimes (see Chapter 1.3.2), SPPs are not stationary but propagate along the surface almost with the speed of light. Thus, the SPP leaves the position of its excitation as long as it is not confined by the surface topography e.g. by reflection at steep walls or nanostructures arrays forming a Bragg mirror [328, 329]. Furthermore, the excitation of SPPs by ultrashort laser pulses in general leads to the generation of a broadband wave packet containing the superposition of small-bandwidth SPP modes. Consequently, the excitation of an isolated sharp SPP mode requires a surface structure that acts as a plasmonic resonator for standing SPP modes and selects a specific SPP wavelength. Such a standing SPP mode is still delocalized along the micro-resonator but might contribute to the localized photoemission of a hot spot via the interaction with a LSP. This is the basic idea of the hybridization model which is discussed in Section 5.4.2. It will be used in Section 5.4.3 to simulate and fit the experimental data. There, it is investigated, whether the long coherence lifetime of the complex beating is caused by the hybridization of a localized plasmon mode, which interacts strongly with the incident radiation, and surface plasmon polariton modes, which provide long coherence lifetimes.

Additional to the evaluation with the hybridization model, two alternative approaches for generating a response function are employed in Section 5.4.3. In the first one the response function of two coherently superposed Lorentz oscillators $A_{2Lo}(\omega)$ is employed. With this model function it is tested whether the results which are obtained by the hybridization model are reproducible by another physical model. In the second alternative approach the spectral response is fitted by unconstrained fit parameters instead of using a physical model. Containing more degrees of freedom and using independent sampling points to represent the spectral amplitude and phase the unconstrained fit is expected to optimally reconstruct the spectral information. A comparison between the lineshape of the hybridization model and the unconstrained fit parameters demonstrates the accuracy of the hybridization model fit in the description of the optimal spectral response function.

5.4.2. Hybridization Model for Coupled Plasmon Modes

Hybridization of localized plasmonic mode is a phenomena observed in core-shell particles and other types of artificial nanostructures [195–199]. The coupling of localized dipolar plasmonic modes

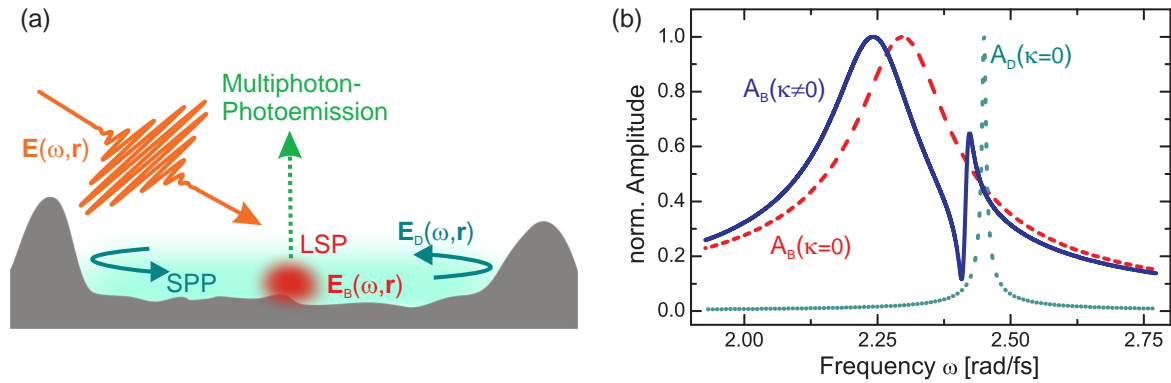


Figure 5.16.: Hybridization of dark and bright plasmonic modes. (a) Schematic illustration of hybridization model. A localized plasmonic resonance (red) is excited by an ultrashort laser pulse. It couples to a standing surface plasmon polariton mode (green). Due to the surface topography the SPP mode is confined to the vicinity of the localized surface resonance. Thereby, the coherence of the local excitation is transferred into the SPP mode which reexcites the bright mode after the initial excitation has decayed. (b) Response functions of plasmonic bright (red dashed) and dark (green dotted) mode without coupling, i.e. $\kappa = 0$, and hybridized bright mode (solid blue, $\kappa = 0.2 \text{ rad}^2/\text{fs}^2$). The uncoupled bright and the dark plasmonic modes have Lorentz oscillator response functions with parameters $\omega_B = 2.3 \text{ rad/fs}$, $\gamma_B = 0.08 \text{ rad/fs}$ and $\omega_B = 2.45 \text{ rad/fs}$, $\gamma_B = 0.003 \text{ rad/fs}$. The hybridized bright mode is shifted towards lower frequencies and contains a sharp Fano-like modulation, which originates from the interaction with the dark mode. Adapted from [4]

that interact strongly with the far-field and localized modes with quadrupolar geometry, which are less effected by radiative damping, leads to Fano-shaped resonances [197–199]. Hybridization between localized surface plasmon modes and standing SPP modes is a possible mechanism for long-lived coherent excitations at photoemission hot spots. In this section a mathematically treatment of the response function of the hybridized plasmonic modes is given.

Figure 5.16a depicts schematically the components of the hybridization model. At particular positions the structural defects and corrugations of the silver surface acts as nanoantenna for concentration of light energy into localized plasmonic modes (red). A laser pulse excites the bright mode creating strong field oscillations due to the field enhancement effects of localized plasmon modes. Even though the dark SPP mode is delocalized, the interaction with the surface topography confines it to the micro-environment of the localized mode and selects a specific SPP wavelength. Whereas a LSP couples strongly to the far-field, energy transfer between a standing SPP (green) and the optical far-field is inhibited by the momentum mismatch between SPPs and photons of the same frequency. Due to this behavior the localized plasmon mode is called *bright* and the SPP mode is called *dark*. The response spectrum of the bright mode is broad (Fig. 5.16b) due to the strong damping of LSPs (see Chapter 1.3.3). Nevertheless, the bright mode couples to the standing SPP mode because of overlapping fields in presence of the surface material which induces the possibility of interaction. This hybridization enables a transfer of energy and coherence from the localized mode into the standing surface plasmon polariton mode. The decay of the dark modes is considerably slower and the coherence is preserved longer. Typical coherence lifetimes of freely propagating SPP modes on silver are 200 fs [143, 330]. In principle the standing SPP mode achieves identical lifetimes as long as it is confined by an efficient process that limits leakage of the plasmon mode, e.g. reflection at steep walls which are the most obvious

topographical features of the investigated corrugated silver surface (see Figure 5.2). After the localized excitation has declined, the SPP mode reexcites the hot spot via the same interaction. Mathematically, the local response function at the position of the bright mode is deduced by solving the differential equations of two coupled oscillators similar to [197, 198]

$$\frac{\partial^2 E_B(t)}{\partial t^2} + 2\gamma_B \frac{\partial E_B(t)}{\partial t} + \omega_B^2 E_B(t) - \kappa [E_B(t) - E_D(t)] = gE_0(t) \quad (5.7)$$

$$\frac{\partial^2 E_D(t)}{\partial t^2} + 2\gamma_D \frac{\partial E_D(t)}{\partial t} + \omega_D^2 E_D(t) - \kappa [E_D(t) - E_B(t)] = 0, \quad (5.8)$$

where γ_k describes the damping parameter, connected to the dephasing time via $T_2^k = 1/\gamma_k$, for the bright mode ($k = B$) or the dark mode ($k = D$), respectively [4]. The local restoring force is given by ω_k . The effective coupling strength of the two modes is represented by the coupling constant κ and g determines the strength of the coupling to the incoming light field $E_0(t)$ that acts as driving force only on the bright mode. The mode overlap of bright and dark mode determines the interaction strength κ and thereby the influence of the linear coupling term on the oscillators. Solving Eqs. (5.7) and (5.8) is simplified by Fourier transformation into the frequency space. Then, all derivatives are replaced resulting in

$$-\omega^2 E_B(\omega) + 2i\omega\gamma_B E_B(\omega) + \omega_B^2 E_B(\omega) - \kappa [E_B(\omega) - E_D(\omega)] = gE_0(\omega) \quad (5.9)$$

$$-\omega^2 E_D(\omega) + 2i\omega\gamma_D E_D(\omega) + \omega_D^2 E_D(\omega) - \kappa [E_D(\omega) - E_B(\omega)] = 0. \quad (5.10)$$

The system of equations can be written as

$$\underbrace{\begin{pmatrix} \mathcal{J}_B & \kappa \\ \kappa & \mathcal{J}_D \end{pmatrix}}_{\hat{A}^{-1}} \begin{pmatrix} E_B(\omega) \\ E_D(\omega) \end{pmatrix} = \begin{pmatrix} gE_0(\omega) \\ 0 \end{pmatrix}, \quad (5.11)$$

with $\mathcal{J}_k = \omega_k^2 - \omega^2 + i2\gamma_k\omega - \kappa$. The solutions are determined by calculating the inverse matrix \hat{A} via the determinant and the adjugate of \hat{A}^{-1} .

$$\hat{A} = \frac{1}{\det(\hat{A}^{-1})} \text{adj}(\hat{A}^{-1}) = \frac{1}{\mathcal{J}_B \mathcal{J}_D - \kappa^2} \begin{pmatrix} \mathcal{J}_D & -\kappa \\ -\kappa & \mathcal{J}_B \end{pmatrix}. \quad (5.12)$$

After multiplication of Eq. (5.11) with \hat{A} from the left the electric fields are given by:

$$\begin{pmatrix} E_B(\omega) \\ E_D(\omega) \end{pmatrix} = \hat{A} \begin{pmatrix} gE_0(\omega) \\ 0 \end{pmatrix} = \begin{pmatrix} A_B(\omega) \\ A_D(\omega) \end{pmatrix} gE_0(\omega). \quad (5.13)$$

Where, $A_B(\omega)$ and $A_D(\omega)$ are the local response functions of the bright and dark mode. In full notation they are written as

$$A_B(\omega) = \frac{\omega_D^2 - \omega^2 + i2\gamma_D\omega - \kappa}{(\omega_B^2 - \omega^2 + i2\gamma_B\omega - \kappa)(\omega_D^2 - \omega^2 + i2\gamma_D\omega - \kappa) - \kappa^2} \quad (5.14)$$

$$A_D(\omega) = \frac{-\kappa}{(\omega_B^2 - \omega^2 + i2\gamma_B\omega - \kappa)(\omega_D^2 - \omega^2 + i2\gamma_D\omega - \kappa) - \kappa^2}. \quad (5.15)$$

An example for the hybridized bright mode response function $A_B(\omega)$ is presented in Figure 5.16b. The bright mode response function $A_B(\omega)$ now contains spectral features originating from the coupling with the long-living standing SPP mode. The coupling constant κ determines the strength of the contribution of the dark mode to the bright mode and vice versa. Furthermore, κ leads to a detuning of the single oscillator responses towards negative frequencies because in \mathcal{J}_B and \mathcal{J}_D the coupling effectively reduces the resonance frequency ω_k . The coupling strength g between the localized plasmonic resonance of the bright mode and the light field influences the resulting oscillator strength, but it has no further effect on the spectral amplitude and phase.

5.4.3. Evaluation of Two-Pulse Nanoscopy Experiment

The hybridization model introduced in Section 5.4.2 is used to calculate the photoemission yield generated in the two-pulse nanoscopy experiments. Having calculated $Y^{(2N)}(T, \varphi_T)$ by inserting the response function $A_B(\omega)$ of the bright mode into Eq. (5.5) for every delay and phase step the resulting T - φ_T -plot is compared to the measured data (see Figure 5.14c and d) to fit the free parameter ω_B , ω_D , γ_B , γ_D and κ . As the first delay steps of the T - φ_T -plots are dominated by a fast decline of the signal, the least-square evaluation of the simulated data is performed for delays $T \geq 60$ fs. Hence, the fit aims to reproduce the observed long-living coherences and quantum beats of the photoemission signals.

The experimental results of both ROIs are fitted simultaneously in an iterative scheme. Thereby, it is possible to couple two individual localized oscillators to the same SPP mode. The assumption that in both cases the identical dark mode is involved, is motivated by the spatial proximity of both ROIs. At the start of the iterative fitting the local response function for ROI1 $A_B(\text{ROI1}, \omega)$ is determined for freely chosen dark mode parameters. Then, the local response parameters of ROI2 are adapted in two steps. First, with fixed ω_D and γ_D the coupling and the bright mode response in ROI2 are fitted. Afterwards, these bright mode parameters and the coupling remain fixed and the dark mode is adjusted. The same two steps are repeated with alternating ROIs until convergence is reached [4].

The response function $A_{2Lo}(\omega)$ of the two coherently superposed oscillator model described by Eq. (5.6) is used as alternative physical model for the evaluation. Figure 5.15b emphasizes that such a response function is able to generate coherent beats in the T - φ_T -plots. If the response function was built by adding the single oscillator intensities instead of the electric fields, i.e. if the incoherent sum was evaluated, no coherent beating would be observable as it is presented by Figure 5.15a. Thus the incoherent sum of two oscillators is no suitable model for the evaluation.

The third method to fit the spectral response function employs unconstrained fit parameters instead of a parametrization according to a physical model. $A(\omega)$ is represented by independent amplitude and phase values at 21 sampling points, which are distributed evenly in the frequency range from 2.25 rad/fs to 2.45 rad/fs. No higher sampling point density is applied to restrict the number of fit parameters to a value which is still appropriate to the complexity of the problem. Between the sampling points no interpolation is applied, i.e. the amplitude and phase of the response function is set to the value of the nearest sampling point. This avoids unambiguous spectral phase evolution between the sampling points.

All three methods for fitting the two-pulse nanoscopy data obtained in ROI1 successfully converged. However, there are differences in the details of the reconstruction. Figure 5.17 presents the

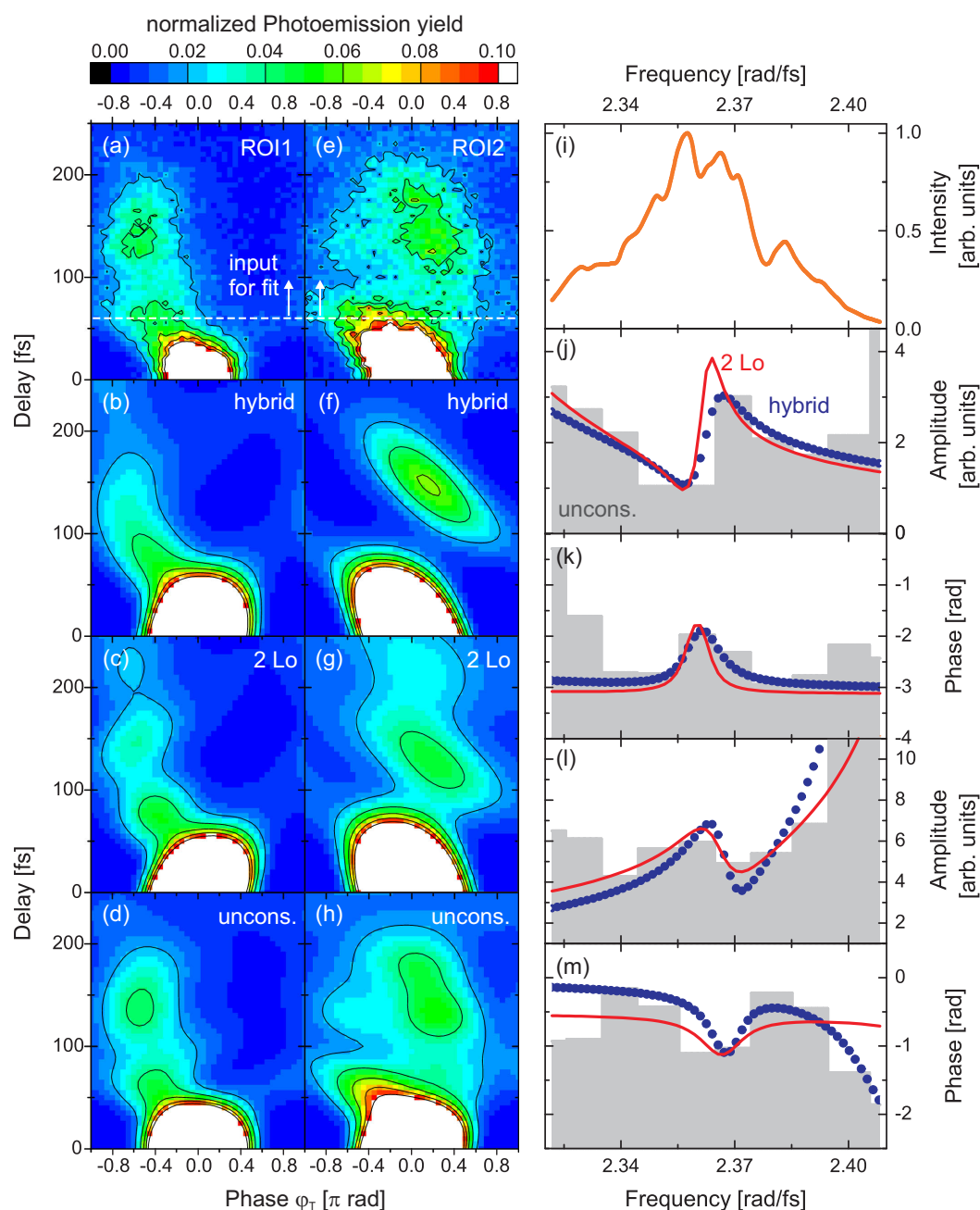


Figure 5.17.: Evaluation results for two-pulse nanoscopy scan in ROI1 (a–d) and ROI2 (e–h). (a,e) Measured photoemission data. White dashed lines and white arrows indicate regions of the T - ϕ_T -plots that are used as input for the fit routine. (b,f) Fit by hybridization model response function $A_B(\omega)$. (c,g) Fit by the coherent superposition of two Lorentzian oscillators $A_{2Lo}(\omega)$. (d,h) Fit by unconstrained parameters. (i) Excitation spectrum. (j) Fitted linear response amplitude of hybridization model $A_B(\omega)$ (blue dots), unconstrained parameters (gray bars) and two Lorentzian oscillators $A_{2Lo}(\omega)$ (red line) for ROI1. Sampling point positions of $A_B(\omega)$ and $A_{2Lo}(\omega)$ are identical to the simulated frequency steps. The gray bars indicate the intervals of constant amplitude and phase values of the local response function retrieved by the unconstrained parameter fit. The height of each bar represents the respective value. (k) Fitted linear response phase for ROI1. (l) Fitted linear response amplitude for ROI2. (m) Fitted linear response phase for ROI2.

	Hybridization model, $A_B(\omega)$					Two superposed oscillators, $A_{2Lo}(\omega)$				
	ω_B	γ_B	ω_D	γ_D	κ	ω_{Lo1}	γ_{Lo1}	ω_{Lo2}	γ_{Lo2}	$A_{1/2}$
ROI1	2.285	0.020	2.382	0.0043	0.114	2.273	0.005	2.362	0.006	17.66
ROI2	2.414	0.011	2.382	0.0043	0.059	2.431	0.009	2.365	0.013	17.22

Table 5.1.: Fit parameters for hybridization model and two superposed Lorentz oscillators. All values are denoted in units of [rad/fs] except for the coupling parameter κ ([rad²/fs²]) and $A_{1/2}$ defining the amplitude ratio.

measured and simulated T - φ_T -plots (a–d) as well as the corresponding linear response functions (j,k). The most important features of the measured data were the detuning towards negative phases φ_T , a distinct photoemission in the few percent regime up to a delay of 200 fs and a beating of the signal that leads to a recurrence of the yield at $T \approx 135$ fs. All three models reconstruct the detuning as well as the long lifetime of the coherence. Differences occur in the beating behavior. The reconstructed photoemission signal of the hybridization model exhibits rather a gradual decay of the maximum yield. The unconstrained parameter fit (Fig. 5.17c) follows closely the measured signal. The beating as well as other minor details of the photoemission trace are reconstructed. Even for low yield at positive φ_T values the accordance with the experimental data is high. The two superposed oscillators show distinctive beating in the signal (Fig. 5.17d). However an extra beat at $T = 220$ fs is observed. Additionally, the photoemission persists longer than in the original data.

The amplitudes and phases of the fitted linear response functions for ROI1 are presented in Figure 5.17j and k, respectively. The measured laser spectrum is depicted above (Fig. 5.17i) to indicate the spectral overlap with the response features. The response function fitted by the hybridization model is depicted as blue dots, which are located at the frequency positions employed in the numerical simulation of the T - φ_T -plot. The response function of the unconstrained parameter fit is indicated by gray bars. The height of each bar represents the amplitude or phase value in the interval that is given by the width of the bar. The red line shows the response function of the two coherently superposed Lorentz oscillators.

A comparison of the amplitudes shows that in all three cases a Fano-like lineshape was retrieved. In the hybridization model (blue dots) this feature is caused by the coupling of the sharp dark mode response with the broad response of the localized mode. The unconstrained parameter fit (gray bars) has more degrees of freedom compared to the physical models and has the smallest deviations in the reconstructed photoemission signal. Nevertheless, it converges to an almost identical solution for the local response function as the hybridization model. Also the coherent superposition of two Lorentz oscillators (red line) achieves a similar amplitude spectrum generating an even sharper spectral feature than the hybridization model. Presumably, this is responsible for the elongated beating behavior of the reconstructed two-pulse scans. There is also a good accordance between the retrieved spectral phases of all signals. At the spectral position of the Fano-like feature a bending towards positive phases values and back is observed. Otherwise the phase is flat in the investigated spectral interval.

The measured photoemission signal for ROI2 (see Fig. 5.17e) exhibits a strong beating around $T \approx 135$ fs for positive phase values. The shift in phase of the maximum is smaller compared to ROI1. The observed trace is not as sharp as for ROI1. This is caused by the smaller total yield from this spatial position as well as a small contribution of the signal from ROI1, which

is also measured as a background signal in ROI2. The diagrams in Figure 5.17f–h present the reconstructed two-pulse data. Similarly to the previous evaluation, all fits converged still showing deviations. The best fit performance was observed for the unconstrained parameters. Here, the measured photoemission signal was closely reproduced. The fit result of the hybridization model exhibits the main features of the experimental data. As it is shown in Table 5.1, the iterative fitting of ROI1 and ROI2 ensured that the identical dark mode parameters were obtained for both regions. The fit results, therefore, differ only in the bright mode parameters ω_B , γ_B and the coupling constant κ . The coherent superposition of two Lorentzian oscillators again generates a two-pulse nanoscopy trace that shows a longer coherence lifetime and a higher number of beats than the original signal.

The retrieved response function of the unconstrained response parameter fit shows only small modulations of the spectral amplitude in the central part of the excitation spectrum and an increase towards higher frequencies (Fig. 5.17l and m). For the physical model functions the increase of the spectral amplitude is reproduced. Also there is a good accordance in the spectral phases of hybridization model and the unconstrained parameter fit. However, the Fano-like modulation of the amplitude generated in the hybridization model is not observed as clearly for the unconstrained parameter fit. These amplitude modulations are visible in the two superposed Lorentz oscillator response, but they are less distinct. In the spectral phase, though, the deviations for the two oscillators with respect to the other fit functions are significant, as the characteristic bending of the phase is not reproduced.

5.4.4. Conclusion and Outlook

The two-pulse nanoscopy experiment gives further evidence of long-living coherences on the corrugated silver film and of changes of the coherence behavior on sub-diffraction length scale. Thus, it supports the observation of the coherent control experiments (see Section 5.2) and the 2D nanoscopy measurement at the identical photoemission hot spot (see Section 5.3). The T - φ_T -plots contain spectral information which are extracted by fitting physical model functions to the measured photoemission data. Also a fit by an unconstrained parameterization is possible which reconstructs the spectral response function at discrete frequency positions.

Qualitatively, the fitted T - φ_T -plots all agree with the experimental results of the two-pulse nanoscopy experiment. Because of the higher number of free parameters, the unconstrained parameter model has advantages in finding a good accordance of the results even for the smaller details of the photoemission data. The coherent superposition of two oscillators reconstructed the main features of the measured data but also generated extra beats which are not visible in the input signals. With the hybridization model it is possible to fit the response functions in ROI1 and ROI2 using the identical dark mode. Thus, both T - φ_T -plots have been fitted simultaneously using in total only eight free parameters.

Whereas the spectral response functions of the physical models $A_B(\omega)$ and $A_{2Lo}(\omega)$ are restricted to lineshapes that are basically determined by five parameters, the unconstrained parameter fit is able to achieve arbitrary response functions. Nevertheless, the retrieved spectral response functions of all three parameterizations are very similar. For both ROIs Fano-like modulations of the amplitude spectra are observed. Also in the spectral phases good agreement between all parameterizations is achieved. Thus, it is concluded that the spectral information encoded in the T - φ_T -plots is to a large extent unambiguously reconstructed. Fano-like resonances as a

result of coupling between two plasmonic modes have been previously reported only for artificial nanostructures [199].

The qualitative and quantitative agreement of the fit results does not allow the decision whether either a superposition of localized plasmonic modes or the hybridization of dark and bright plasmonic modes is responsible for the extended coherent beating. In principle a coherent superposition of localized plasmonic modes is a possible mechanism. However, the fitted lifetimes of these independent oscillators (see Table 5.1) are much longer than for localized plasmonic resonances reported in literature. Furthermore, the superposition model requires the spatial overlap of the electric fields. For localized modes at different frequencies only a partial overlap can be expected. Otherwise, if the overlap is significant, a coupling between the oscillators would presumably be introduced and the response would be even more complex. In the hybridization model the long lifetimes are provided by the interaction with standing SPP modes in between the ridge structures of the corrugated surface. The observed dark mode bandwidth of $\gamma_B = 0.043$ rad/fs is in a good accordance to typical lifetimes for SPPs on silver. The retrieved bandwidths of the bright mode in both ROIs are still considerably above the expected values. Nevertheless, the fitted spectral positions of the bright mode are in the low-intense part of the laser spectrum (ROI2) or even outside of the laser spectrum (ROI1). Since only those parts of the local response function contribute to the T - φ_T -plots that overlap with the excitation spectrum, only a fraction of the oscillator lineshape is evaluated. Accordingly, there are uncertainties in the parameters of the bright mode which might explain the small fitted linewidth.

FDTD simulations, which will be presented elsewhere, emphasize that the observed surface topography of the silver film is indeed suitable to trap standing plasmon modes in microresonators formed by the μm -sized walls. Additional FDTD simulations have been made to design and characterize nanoantennas and silver microresonators that can be employed in a further experiment demonstrating the interaction of localized surface plasmons and SPP modes. The results of these calculations are used as a guideline for the fabrication of experimental samples with defined surface topography in the facilities of the Nano-Bio Center at the University of Kaiserslautern which will be used in a future experiment concerning the hybridization of LSP and SPP modes.

6. Localization of Photonic Modes in Thin-Film Solar Cells

Besides the atomic composition of a material also the structural properties have a strong impact on the interaction with light, e.g. localized plasmonic resonances drastically change the scattering and absorption behavior of matter on sub-diffraction length scale. But also for larger structure dimensions and extended systems unusual optical properties are observed. Photonic crystals are regular lattices of nanoscopic light scattering objects [331, 332]. In photonic crystals the propagation of light with energies in the photonic band gap is prohibited [331, 333]. Hence, they can be used for resonators and waveguides that drastically effect the properties of incorporated materials [75, 332, 334]. Photonic structures in nature can be found in minerals, animals and plants [335–337]. The interplay between short range order with long range disorder in biological structures can lead to brilliant noniridescent coloration and whiteness [338, 339]. The influence of disorder on the interaction with light has become a growing field of scientific research [340]. Recently, experiments to understand and employ multiple scattering in disordered media have been performed in which focusing and imaging through opaque media was investigated [340–350]. There have been speculations, whether in disordered media a strong localization of photonic modes takes place analog to Anderson localization of electrons [351, 352]. Transverse localization of photonic modes propagating through disordered waveguides has already been demonstrated [353]. In a nonlinear far-field microscopy experiment precursors of strong light localization were observed [354] in a disordered ZnO nanoneedle array.

Scattering of light at disordered media also plays an important role in the photon management in thin-film photovoltaics. Optimized light trapping, i.e. the enhancement of the effective optical path length within an absorber medium, is essential for thin-film solar cells to achieve high photon absorption cross sections. Light trapping concepts involve ordered or disordered structural modification of the absorptive layer in the solar cells or embedding of nanostructured objects. The solar cell efficiency is enhanced by scattering and guiding of light and charge carrier injection processes. In this chapter nanotextured amorphous silicon (a-Si) thin-film solar cells are investigated by optical spectroscopy techniques and 2D nanoscopy. The aim of the experiments is to identify the absorption enhancement mechanism that is involved with the structural disorder of the absorber layer. Even though implemented into commercial devices, the impact of the nanotexturing is still debated on. Light trapping might be achieved by single scattering events at the nanotextured interfaces, which extend the propagation length and effectively the absorption within the silicon layer, or by localization of light. The experimental observations presented here indicate the existence of localized photonic modes which enhance the absorption in the long-wavelength cut-off region of the amorphous silicon layer.

In the first part of this chapter the basic concepts of thin-film solar cells are discussed (Section 6.1) focusing on the necessity to implement means of light trapping to enhance the device efficiency. In Section 6.2 differently designed thin-film solar cells are examined by various methods to characterize the microscopic structure of the deposited layer stacks as well as their ability

to efficiently absorb radiation. Optical spectroscopy experiments demonstrate a more efficient absorption by nanotextured thin-film solar cells. In Section 6.3 2D nanoscopy experiments on a specially designed sample are presented. The retrieved spatial resolved distribution of the local coherence lifetime and center frequency show localized electron emission from confined locations with individual spectral properties. A nonlinear order of the electron emission process significantly above the multiphoton photoemission threshold is explained by a model for ultrafast thermionic emission. The results emphasize the generation of photonic modes in the nanotextured silicon layers as a dominant absorption channel in nanotextured amorphous silicon thin-film solar cells.

The experimental investigation of light trapping in thin-film solar cells discussed in this chapter is also presented in a recently submitted paper [92]. Several experimental techniques are combined for characterization of the sample and the underlying light trapping mechanism. The design and fabrication of the thin-film solar cells as well as the investigation of the structural and spectral properties upon incoherent illumination were performed by Florian Lükermann. The ultrafast backscattering spectroscopy experiments were executed and evaluated by Dominik Differt. The emphasis of my work were the 2D nanoscopy experiments of the amorphous silicon thin-film solar cells and the data evaluation process. I developed simulation routines to generate 2D nanoscopy spectra as presented in Chapter 4.3 and established a fast fit routine that enabled the automatized retrieval of spatial-resolved spectral information and the correction of effects introduced by the local order of nonlinearity and the excitation spectrum.

6.1. Hydrogenated Amorphous Silicon Thin-Film Solar Cells

Photovoltaic devices are an important contribution to a renewable generation of electric power. The photovoltaic effect is the conversion of light energy into electricity. Photons are absorbed leading to electronic excitations which are, depending on the absorbing material, described as electron-hole pairs (semiconductors) [90, 355, 356] or excitons (molecules) [91, 357–362]. The excited charge carriers of opposite types are separated spatially and transported to electrodes. Between these electrodes a voltage builds up, when the photovoltaic device is illuminated by light. For this reason, the solar cell can be employed as a supply for electric power providing a constant direct current under stable illumination conditions.

Amorphous thin-film solar cells are a cost effective variant of semiconductor photovoltaics [90, 356]. They consist of layers of amorphous semiconductors and transparent conductive oxides. A well established absorber material employed in thin-film solar cells is hydrogenated amorphous silicon (a-Si:H) [91]. In the following, concepts of thin-film solar cell design are briefly presented. In Section 6.1.1 the basic components and material properties of a-Si:H thin-film solar cells are discussed. Section 6.1.2 deals with various photon management strategies and their connection to the localization of light.

6.1.1. Thin-Film Solar Cells

The most important components of a hydrogenated amorphous silicon thin-film solar cell are depicted schematically in Figure 6.1a. Basically, a solar cell of this type is a p-i-n diode embedded in a transparent conductive oxide (TCO) [356]. The p-i-n diode consists of a p-doped, an intrinsic and a n-doped zone within the a-Si:H layer. This layer stack is deposited on a glass substrate and

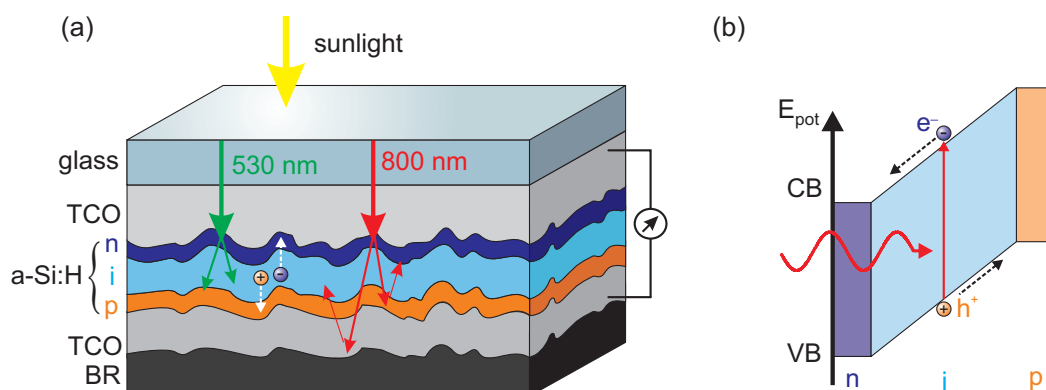


Figure 6.1.: Light energy conversion in thin-film solar cells. (a) Schematic cross section of a hydrogenated amorphous silicon (a-Si:H) thin-film solar cell. The scale of the thicknesses does not reflect the real conditions. Incoming sunlight is transmitted by the glass substrate and the structured transparent conductive oxide (TCO) into the a-Si:H layer. On the adjacent TCO layer a metal coating acts as a backreflector (BR) that redirects transmitted light components back into the active layer of the solar cell. The absorption of visible light (green) in a-Si:H is higher compared to near-infrared light (red). (b) Schematic electron potential across the p-i-n diode consisting of n-doped (n), intrinsic (i) and p-doped (p) a-Si:H. Colored regions indicate the gap between valence band (VB) and conduction band (CB). The absorption of a photon (red oscillating line) within the intrinsic zone leads to electron-hole pair generation. The separation of electrons (e^-) and holes (h^+) is driven by the potential energy gradient.

covered on the backside by a metallic back contact. The sunlight is transmitted through the glass substrate into the absorbing semiconductor layer. There, electron-hole pairs are generated by photoexcitation. The separation process is caused by the internal electric field of the p-i-n diode (Fig. 6.1b) [356]. The electrons (e^-) and holes (h^+) follow the potential gradient towards the n-doped and p-doped zone of the a-Si:H layer, respectively. In the conduction band of the n-doped zone the electrons still have a higher potential energy than in the valence band of the p-doped zone of the diode. Accordingly, the solar cell is a source for direct current, when connected to a circuit. The electric current flows through the TCO layers and the metal backreflector which act as the top- and back-electrode of the solar cell.

In the schematic representation of the thin-film solar cell presented in Figure 6.1 two aspects are implied which will be discussed further in this and the following section: First, the material properties, which cause a wavelength-dependent absorption within the active layer, and, second, strategies to enhance the total absorption such as the texturing of the solar cell interfaces and the implementation of a backreflector.

Hydrogenated amorphous silicon as a material for photovoltaic devices has several advantages compared to crystalline silicon (c-Si) [91, 356]. Especially the fabrication process is much more cost-efficient, since it has been successfully scaled to large module areas using plasma enhanced chemical vapor deposition (PECVD). Nevertheless, a-Si:H exhibits a reduced absorption in the near-infrared regime and an enhanced carrier recombination. Thus, the thickness of the absorbing a-Si:H layer has to be adapted to simultaneously achieve an efficient generation of electron-hole pairs as well as a low-loss carrier separation and transport to the electrodes of the solar cell. Optimal thicknesses of the a-Si:H layer are typically about 300 nm. Therefore, the total amount of absorbing material of a-Si:H thin-film solar cells is three orders of magnitude smaller than for

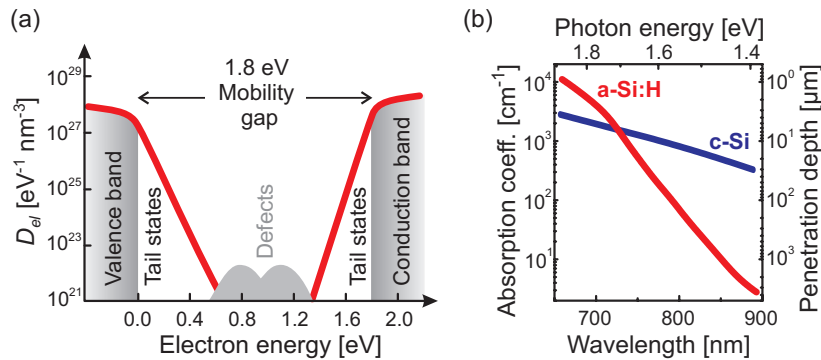


Figure 6.2.: Electronic density of states and absorption of hydrogenated amorphous silicon (a-Si:H). (a) The electronic density of states D_{el} (red graph) of hydrogenated amorphous silicon (a-Si:H) is characterized by a mobility gap of approximately 1.8 eV. The shaded areas emphasize the energetic position of the valence band, the conduction band and the defects states. With lower photon energies absorption into tail states and defects states is still possible. In these excited states the electron mobility is strongly reduced compared to the conduction band. (b) Absorption coefficients for photons in crystalline silicon (c-Si, blue) and amorphous silicon (a-Si:H, red) as a function of wavelength. Adapted from [92].

conventional crystalline devices [356].

The electronic density of states of a-Si:H differs from c-Si [91, 214]. Amorphous silicon is affected by the missing long range order. The energy gap of 1.8 eV between valence and conduction band is larger than the indirect band gap in crystalline silicon (1.1 – 1.2 eV) and is referred to as mobility gap. This denotation expresses that within this gap electronic states exist which are localized and do not contribute significantly to electronic transport processes. A schematic representation of the electronic density of states D_{el} of a-Si:H is depicted in Figure 6.2a. At the band edges D_{el} does not drop sharply but decays exponentially with the electron energy difference. The electronic states reaching into the mobility gap are called tail states [91, 363]. The tail states originate from the disorder in amorphous silicon and have a strongly reduced mobility, as they contribute to charge transport only via a hopping process. Furthermore, defect states are found in the middle of the gap.

The absorption coefficients of a-Si:H and c-Si are depicted in Figure 6.2b as a function of the photon wavelength close to the mobility gap energy of amorphous silicon [364]. The absorption is inversely related to the penetration depth of light into the material, which is also indicated in the diagram. At visible frequencies the absorption coefficient of a-Si:H clearly exceeds the absorption coefficient of c-Si. Below the mobility gap energy the absorption coefficient drops drastically, since the tail states, which have a reduced density of states, are involved in the absorption.

6.1.2. Photon Management in Thin-Film Solar Cells

In the near-infrared regime the penetration depth exceeds the typical absorber thickness of an a-Si:H thin-film solar cell (≈ 300 nm) by more than two orders of magnitude. Thus, without further measures only a small fraction of the incident light at 800 nm wavelength is absorbed. Losses occur by reflection and transmission as it is shown schematically in Figure 6.3a. For this reason, photon management strategies which enhance the absorption cross section are necessary to improve the performance of the thin-film photovoltaic devices towards their theoretical limits [365]. Some

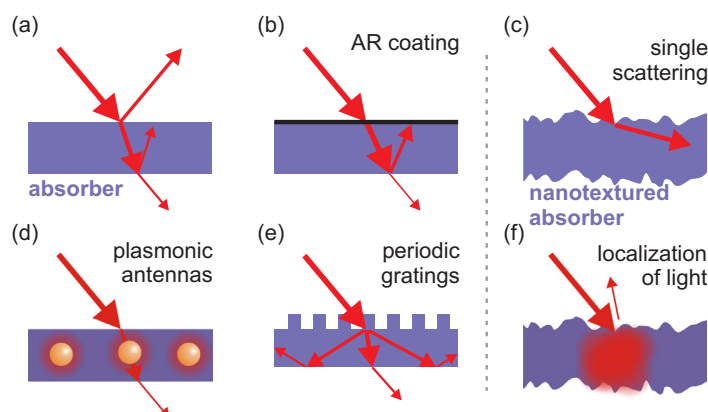


Figure 6.3: Photon management strategies in thin-film solar cells. (a) Bare absorber layer with reflection and transmission losses. (b) Antireflection coating (AR). (c) Corrugated interfaces enhancing propagation length by scattering of light into the absorber layer. (d) Embedded nanoparticles as plasmonic resonators scattering and concentrating electric fields in the absorber layer. (e) Periodic grating structures. (f) Localization of light via multiple scattering at disordered structures. Adapted from [92].

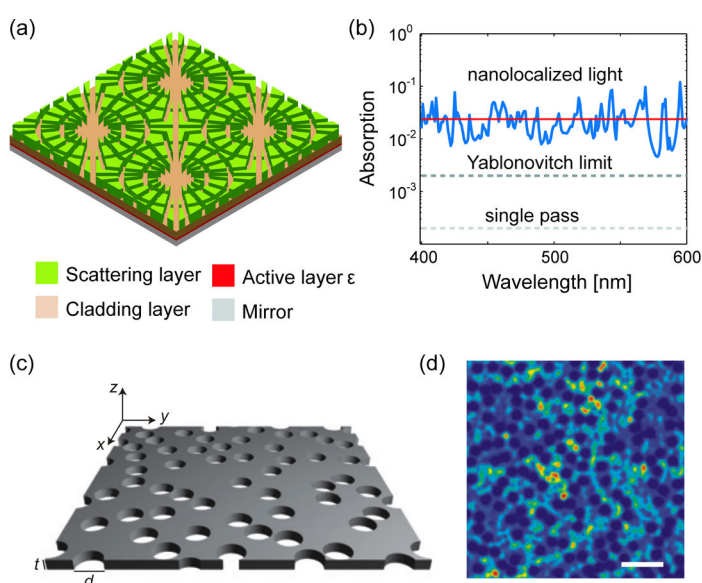


Figure 6.4: Light trapping and localization in nanostructured systems [371, 378]. (a) Solar cell model system with nanostructured scattering layer on top of the absorber layer. The period of the quadratic pattern is $1.2 \mu\text{m}$. (b) Absorption cross section (blue line) of structure in (a) is significantly above the Yablonovitch limit (dark gray dashed line) due to localization of light within the thin absorber layer. (c) Thin (100 nm) silicon layer perforated by randomly placed circular holes with 270 nm diameter. (d) Electric field energy density within perforated silicon layer at 667 nm wavelength ($\omega = 2.83 \text{ rad/fs}$). The length of the white bar is $1 \mu\text{m}$.

of the recently investigated methods involve optimized anti-reflection coating [366], plasmonic enhanced absorption [25, 170, 367], embedding of photonic crystals [368–370], gratings [371, 372] and randomly nanotextured interfaces [373–376] and random two-dimensional nanostructures for light localization [377, 378].

Two competing mechanisms for the absorption enhancement via nanotextured interfaces are presented in Figure 6.3c and f. The first one involves the scattering of the incident light at the disordered interface into multiple directions. This effectively elongates the propagation distance within the active layer and increases the absorption. In the other case multiple interactions with the disordered interfaces lead to light localization, trapping the photons in a confined area until the localized photonic mode decays. The localization of propagating waves in disordered systems was demonstrated by Philip Anderson at the example of electrons [351]. However, it is a universal wave phenomenon which has also been observed in acoustics and microwave optics [379]. First theoretical investigations of the absorption enhancement caused by corrugated absorber interfaces were performed by Yablonovitch *et al.* using statistical ray optics [380, 381]. The

predicted maximal enhancement factor was $4n^2$, where n denotes the refractive index quotient between a thick absorbing layer and the surrounding medium. In thin-film solar cells the spatial dimensions require a treatment of the optical wave properties of the electromagnetic field, e.g. by finite-difference time domain method simulations. In those theoretical investigations absorber structures were identified [371, 382, 383] that enable absorption enhancement beyond the limit determined by Yablonovitch [380]. In Figure 6.4a and b a compound scattering and absorber structure is shown that exhibits an absorption cross section an order of magnitude above this limit. In another example (see Fig. 6.4c and d) disorder was introduced into a thin absorbing layer by randomly cutting circular holes through it [378]. Despite the loss of material, the absorption was enhanced by a factor of ten because of light localization effects that trapped incident radiation inside the layer. As it is visible in Figure 6.4d, at confined regions within the layer the field is strongly enhanced.

In the following experiments it is examined, whether a nanotexturing of the layer stack of a thin-film solar cell similarly causes a disordered scattering environment in the vicinity of the absorber layer that leads to the localization of light to confined photonic modes. Furthermore, it is investigated, whether the localization of photonic modes is an important mechanism for the enhancement of the absorption cross section.

6.2. Sample Characterization

Thin-film solar cells with smooth and with nanotextured interfaces were prepared. For reasons of applicability in PEEM experiments modifications of the nanotextured solar cell design had to be made leading to a third type of sample with exposed nanotextured a-Si:H layer. Section 6.2.1 discusses the structural properties of the investigated samples based on atomic force microscopy (AFM) and scanning electron microscopy (SEM) characterizations. The influence of the different absorber stack designs on the absorption is investigated and evaluated in Section 6.2.2. Ultrafast backscattering spectroscopy (Section 6.2.3) is used to examine the lifetimes of photonic modes in solar cells.

6.2.1. Sample Designs and Structural Properties

Three different thin-film solar cell designs have been produced and tested. They are depicted schematically as cross sections in Figure 6.5a–c. The first two types contain a full silicon diode consisting of a p-i-n layer sequence which is sandwiched between two TCO layers. The major part of the a-Si:H layer is an undoped (intrinsic) layer (≈ 250 nm) in between thin ($\approx 10 - 20$ nm) p- and n-doped layers. The third type of sample is a prototype which does not offer the full functionality as a solar cell, since the fabrication process was terminated after finishing the intrinsic zone of the hydrogenated amorphous silicon (a-Si:H) layer. Hence, the exposed nanotextured a-Si:H layer has no electric contact, as the second TCO layer is missing. For all three samples no backreflector was deposited. Thus, also an illumination from the backside is feasible, i.e. the light enters through the exposed TCO layer or, respectively, the a-Si:H layer instead of the normal operation through the glass substrate. The thickness of the exposed absorber layer (100 nm) in the latter type of sample is considerably smaller than in standard thin-film solar cell devices. Due to the low penetration depths of low-energy electrons in solids it is, nevertheless, certain that in

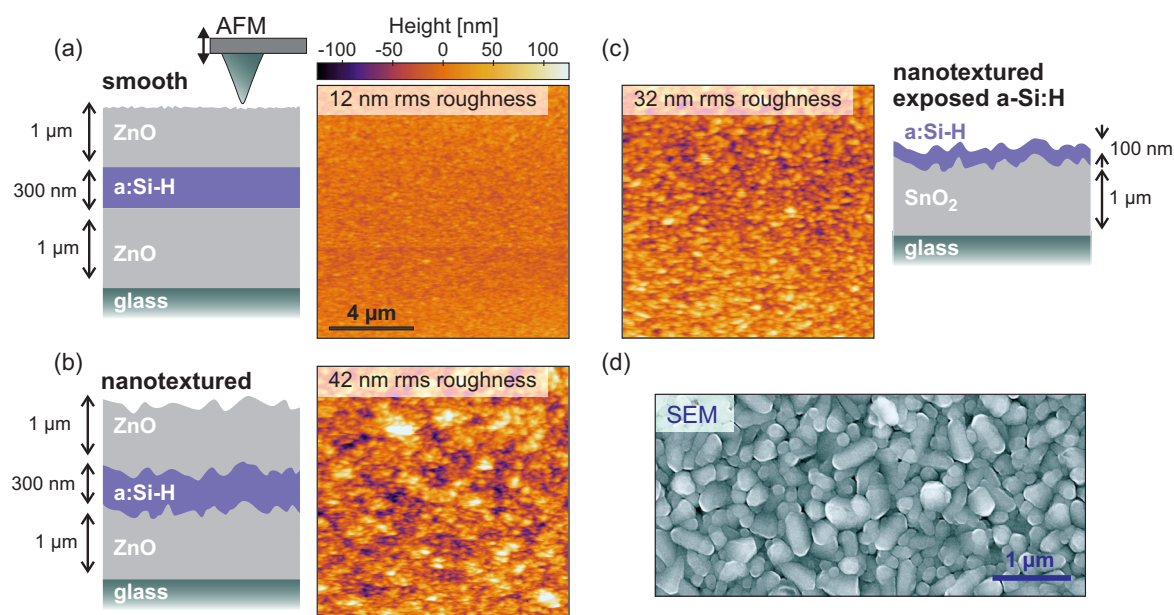


Figure 6.5.: Structural properties of investigated thin-film solar cells. (a–c) Schematic cross sections through the different investigated types of a-Si:H thin-film solar cell absorber stacks with layer thicknesses and material properties indicated. The AFM images show large scale surface morphologies ($12 \times 12 \mu\text{m}^2$) and the rms roughness of the respective sample. (a) Sample with smooth interfaces (b) Sample with nanotextured interfaces (c) Sample with nanotextured exposed a-Si:H layer (d) SEM image of thin-film solar cell produced under the same conditions as the nanotextured exposed a-Si:H layer investigated with 2D nanoscopy. Adapted from [92].

PEEM experiments the emitted electrons originate from the amorphous silicon and not from the TCO beneath. Moreover, the absorption of near infrared light from TCO is marginal and leads to no substantial photoexcitation of electrons.

The amorphous silicon layers are generated by plasma enhanced chemical vapor deposition (PECVD). A radio frequency driven plasma decomposes the precursor gas silane (SiH_4) and deposits the a-Si:H film at a substrate temperature between 500 K and 550 K. By adding of doping gases during the deposition, p- and n-doped a-Si:H layers are fabricated which contain boron or phosphor, respectively. The surface morphology of the layer stack is predominantly given by the nanotexture of the TCO layer on the glass substrate. Due to the conformal growth of the adjacent layers the interface texture is mainly reproduced through the complete device. The properties of the random TCO nanotexture is determined by the deposition process and the employed material [376]. For the samples with embedded silicon layer ZnO was deposited by DC magnetron sputtering (smooth) and low pressure chemical vapor deposition (nanotextured). In case of the sample with exposed nanotextured a-Si:H layer the TCO layer consists of SnO_2 .

The exposed surfaces of the thin-film solar cell are investigated with atomic force microscopy (AFM) and scanning electron microscopy (SEM). The employed AFM setup is homebuilt and operates under ambient conditions. The lateral and vertical displacement scales have been calibrated using a commercial calibration sample. The maximum field of view of the device is approximately $25 \times 25 \mu\text{m}^2$. The areas shown in Figure 6.5 have a lateral size of about $12 \times 12 \mu\text{m}^2$. To remove the influence of a surface tilt, the raw data has been fitted by a plane

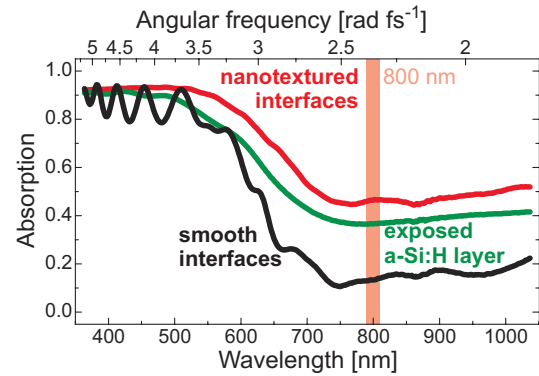


Figure 6.6: Linear UV-VIS absorption spectra for different thin-film solar cell designs. The samples were illuminated through the glass side. The center wavelength of the femtosecond laser pulses used in the ultrafast experiments is highlighted by a red rectangle. Taken from [92].

and only the residual vertical displacement is presented. On large lateral distances the surface is flat. On a microscopic scale surface roughness with correlation lengths of typical several hundred nanometer are visible. Even for the sample with smooth interfaces the height varies by ± 50 nm. However, the root mean square (rms) roughness, as a measure for the vertical displacement, as well as the typical structure sizes are still significantly lower than for the nanotextured samples. The interface corrugations of the nanotextured solar cell with TCO layer (Fig. 6.5b) are larger than of the exposed a-Si:H layer (Fig. 6.5c) with respect to the structure dimensions as well as to the rms roughness. Details of the exposed nanotextured surface of the a-Si:H layer are presented in the scanning electron microscopy image in Figure 6.5d. The field of view is smaller than in the AFM images. Structure sizes appear magnified by about a factor of five. Due to the different contrast mechanism the edges of the structures are emphasized. The observed structures are round and only few sharp edges and corners are visible. These grains are typically a few hundred nanometers in diameter and appear to be distributed randomly, there is no indication of a short-range or long-range order.

6.2.2. Linear Absorption Spectroscopy

To investigate the influence of the nanotexturing on the light trapping efficiency the absorption cross section of the three solar cell samples was determined. A conventional optical spectrometer setup (*Perkin Elmer Lambda 950*) was employed for obtaining UV-VIS absorption spectra which are depicted in Figure 6.6. The absorption $Abs(\omega)$ was estimated via

$$Abs(\omega) = \frac{1 - T(\omega) - R(\omega)}{I_0(\omega)}, \quad (6.1)$$

where $T(\omega)$ denotes the transmitted intensity, $R(\omega)$ is the reflected intensity and $I_0(\omega)$ denotes the incident intensity. The UV-VIS measurements are performed with illumination from the glass side, in contrast to the backscattering experiments presented in Section 6.2.3 and the 2D nanoscopy measurements (Section 6.3), in which the light enters from the layer side. The graph presented in Figure 6.6 covers the wavelength range from 350 nm to 1050 nm. The red rectangle at 800 nm indicates the spectral position of the femtosecond laser pulses used in Sections 6.2.3 and 6.3.

All three samples absorb 80%–95% of the incident light for wavelength smaller than 550 nm, but already a stronger absorption in the nanostructured samples is distinguishable. The sample with

smooth interfaces exhibits an oscillating behavior of the absorption in this spectral regime caused by Fabry-Pérot resonances within the TCO layer. Thus, standing waves between the parallel TCO interfaces are formed which interfere with the incident radiation and, thereby, enhance or reduce the reflection at the first TCO interface. These Fabry-Pérot resonances do not appear in case of the nanotextured samples, since the scattering of the light at the interfaces destroys the global Fabry-Pérot resonance. Approaching the range of the interband cut-off between 600 nm and 700 nm a distinct drop is visible in each of the spectra. At near-infrared wavelength Fabry-Pérot resonances are negligible also for the smooth sample. Here, the difference in the total absorption is most distinct. Whereas for smooth interfaces the absorption within the solar cell is below 20%, the nanostructured samples exhibit absorptions of about 40% (exposed a-Si:H) and 50% (nanotextured with TCO). Thus, even though the thickness of the exposed a-Si:H layer is only 100 nm, it significantly absorbs a higher fraction of the incident light. The enhanced absorption in the nanotextured sample does improve the efficiency of the photovoltaic device. The solar cells fabricated with nanotextured interfaces show under standardized illumination conditions an increased short circuit current density ($I_{SC} = 15 \text{ mA cm}^{-2}$) compared to the smooth solar cells ($I_{SC} = 11 \text{ mA cm}^{-2}$).

From the results of the linear absorption spectroscopy it is obvious that the nanotextured interfaces strongly increase the absorption efficiency of thin-film solar cells. Furthermore, it is demonstrated that the absorption enhancement also takes place in the exposed 100 nm a-Si:H layer, which can be investigated by means of photoemission microscopy. Apparently, the identical mechanism increases the absorption in the nanotextured solar cells with and without exposed a-Si:H layer. Using incoherent radiation the absorption spectra cannot be related to the temporal evolution of the light within the silicon layer. A distinction between scattering into the active layer at the surface corrugations and localization of light in the silicon is not feasible.

6.2.3. Ultrafast Backscattering Spectroscopy Experiments

A first insight into the interaction of coherent laser pulses with thin-film solar cells is provided by investigating the laser pulse components that are scattered in the absorptive silicon layer and leave the sample in an angle deviating from the specular reflection. A schematic illustration of the corresponding experiment is presented in Figure 6.7a. The laser beam is focused to a spot with a diameter of approximately $15 \mu\text{m}$ under a small incidence angle with respect to the surface normal. In this focal region the electric field is absorbed, transmitted through the solar cell or reflected in specular direction at the interfaces. However, a minor fraction is scattered by the randomly structured interfaces and is collected by the focusing mirror. The backreflected signal is detected in a spectral interferometry (SI) experiment (Appendix A.1.2) to retrieve the spectral amplitude and phase. Since it involves a linear detection method, it is suited to characterize the low intense signals. The reference pulse superposes with the scattered light components at a beam splitter, which separates the backreflected from the incident beam. The reference pulse has been fully characterized by a previous SPIDER measurement [384–387]. SPIDER (spectral phase interferometry for direct electric-field reconstruction) is a nonlinear self-referencing spectral interferometry technique, which can only be employed for pulses with sufficient intensity. Light is coupled into the spectrometer via a single mode fiber with the entrance aperture placed in the focus of a microscope objective. Thus, the setup is similar to confocal optical microscopy in the sense that radiation not originating from the position of the excitation focal spot is rejected [388]. The detection method itself is only frequency-resolved, but by variation of the sample position

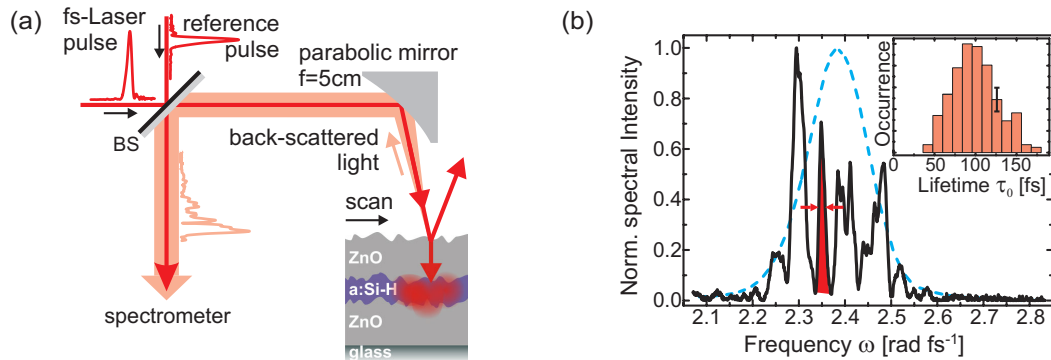


Figure 6.7.: Spectral interferometry of backscattered radiation from a-Si:H thin-film solar cells. (a) Schematic representation of the spectral interferometry setup. Bandwidth-limited femtosecond laser pulses (25 fs pulse duration, 790 nm center wavelength, 80 MHz repetition rate) are focused with an incidence angle of 2° onto the movable sample. The achieved spot diameter at e^{-2} of the full intensity was $15 \mu\text{m}$. The spectral composition and the temporal evolution of the scattered light in backward direction are determined by spectrometry without reference pulse and spectral interferometry using a fiber-coupled polychromator equipped with CCD detector. (b) Normalized backscattered spectral intensity at one position on the sample with nanotextured interfaces (black solid line) and normalized laser spectrum (blue dashed line). An individual spectral line is shaded red. The red arrows mark the spectral width (FWHM = 0.0013 rad/fs). The corresponding resonance coherence lifetime is $\tau_0 = 159$ fs. The inset presents the lifetime distribution histogram determined from peaks in 25 different spectra recorded along a $100 \mu\text{m}$ lateral scan of the sample. The black bar in the inset represents the estimated statistical uncertainty. Adapted from [92].

lateral scans of the excitation spot are feasible.

The obtained backscattering spectra of identical samples differ considerably in their exact shape in dependence of the focus position and the incidence angle. A typical spectrum from the solar cell with nanotextured interfaces and covering TCO layer is presented in Figure 6.7b. In contrast to the broadband excitation spectrum of the femtosecond laser pulses, the backscattered spectrum contains several distinct peaks. The spectral linewidth of those peaks considerably exceeds the spectrometer resolution of approximately 1 mrad/fs at the center frequency. Consequently, the peak widths are attributed to the lifetime of resonant modes from which light leaks out of the sample. A statistical evaluation of the peak widths in 25 individual spectra, which have been measured along a lateral scan with $100 \mu\text{m}$ length, a lifetime distribution of the underlying spectral resonances was determined. The distribution is presented as histogram in the inset of Figure 6.7b. It is centered at approximately 100 fs and has a FWHM of about 50 fs. During this time interval near-infrared light propagates a distance of $7.5 \mu\text{m}$ in bulk amorphous silicon and even $15 \mu\text{m}$ in the TCO. Within the thin-film solar cell this is only achieved by modes that propagate laterally along the a-Si:H layer or in closed or involuted pathes.

The spatial dependence of the backscattered spectral amplitude is presented in Figure 6.8. Along the horizontal axis the lateral displacement of the sample with respect to the focal spot is shown. The lateral scan range was $100 \mu\text{m}$. The vertical direction contains the spectral information. Again, a clear distinction between nanotextured and smooth interfaces is obvious. Whereas the spectrum of the backscattered light from the sample with smooth interfaces strongly resembles the incident laser spectrum and remains almost unchanged during the lateral scan (Fig. 6.8a),

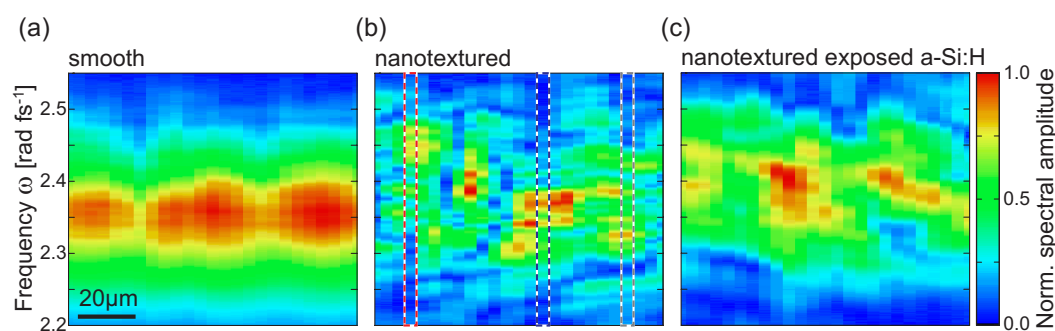


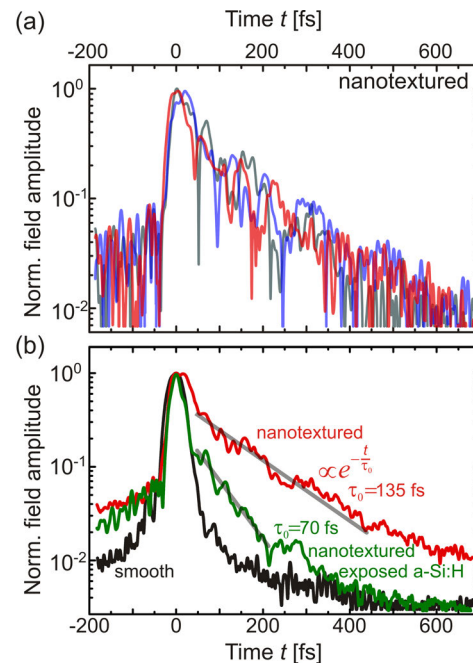
Figure 6.8.: Spatial resolved backscattering spectra obtained from (a) sample with smooth interfaces, (b) sample with nanotextured interfaces and (c) sample with nanotextured exposed a-Si:H layer. Spatial variation of the backscattered field amplitude is presented as a function of the lateral sample displacement (black bar indicates the displacement scale). The colored dashed rectangles in (b) indicate the positions used for spectral interference measurements shown in Fig 6.9a. Adapted from [92].

the spectra of the nanotextured samples exhibit strong modulations that clearly change with the lateral position. In case of the nanotextured solar cells with both TCO layers (Fig. 6.8b) the spectral features are most distinct and exceed the variations observed for the nanotextured exposed a-Si:H layer (Fig. 6.8c). In this last case, the modulations are broader and the laser spectrum is still visible as a background signal. The background contribution is caused by an enhanced diffuse reflection at the exposed air–a-Si:H interface, which involves a more abrupt change of the refractive index ($n_{Si}/n_{air} \approx 4$) than for the air–TCO interface ($n_{TCO}/n_{air} \approx 2$) of the samples with covered absorber layer. Nevertheless, the spectral structure indicates resonant behavior in both nanotextured samples, which is responsible for the backscattering of the coherent radiation. The average spectral peak width of the modulated spectra was obtained by a statistical analysis of the lateral scan data. The results of the sample with nanotextured interfaces are presented in the inset of Figure 6.7b. The TCO covered sample exhibits an average resonance lifetime of about $\tau_0 = 100$ fs. The exposed nanotextured a-Si:H layer yields lifetimes in the range of 60 fs. In both cases this values is significantly longer than the 1–2 fs necessary for light to propagate through the thin absorber in vertical direction.

Having retrieved the spectral phase, the temporal evolution of the backscattered light components is calculated via Fourier transformation of the electric field. Figure 6.9 shows the reconstructed electric field pulses at three different positions on the nanotextured solar cell with TCO layer. In all of these cases an asymmetric shape is observed. The leading edges of the pulses exhibit a fast and unmodulated rise of the field amplitude. After the peak position an elongated decay of the signal is observed, which is strongly modulated by a complex beating. The general similarity of the obtained temporal amplitudes at the investigated spatial positions is caused by the qualitative agreement of the spectra containing several peaks with small spectral bandwidth. The contributions of the spectral peaks to the temporal field beat according to their distinct oscillation frequency. The exact spectral position and width of these peaks, however, determines the details of the beating behavior, which differ with the spatial position.

For a further comparison of the three solar cell samples, the temporal electric fields retrieved at the lateral scan positions presented in Figure 6.8 were incoherently averaged. The averaging is conducted by summing the temporal amplitudes of all lateral scan positions while neglecting the phase. The results are normalized to their respective maximum. This operation suppresses the

Figure 6.9: Backscattered electric field from a-Si:H thin-film samples in time domain representation. (a) Temporal evolution of the backscattered field amplitude reconstructed at different positions from the lateral spectral interferometry on the nanotextured solar cell. The position is indicated by color according to the rectangles shown in Fig. 6.8b. (b) Incoherent average of the time-dependent backscattered field amplitudes recorded along the lateral scans presented in Figure 6.8. Fitted single exponentials (gray lines) are shown for the initial field amplitude decay for the samples with nanotextured interfaces (red line) and nanotextured exposed a-Si:H layer (green line). Taken from [92].



coherent beating of the individual contributions and emphasizes the evolution of the electric field envelope. The averaged temporal field of the sample with smooth interfaces is depicted as a black line in Figure 6.9. Basically, the obtained profile corresponds to the incident laser pulse shape. A small increase of the temporal width is caused by the inhomogeneous spectral absorption in the a-Si:H layer. In contrast, the averaged temporal fields of the nanotextured samples exhibit an exponentially decaying tail with suppressed beating behavior. With an exponential fit the average lifetime of the backscattered electric fields is estimated. The lifetimes of about $\tau_0 = 135$ fs for the samples with nanotextured interfaces (red line) and $\tau_0 = 70$ fs for the nanotextured exposed a-Si:H layer (green line), are in agreement with the statistical linewidth analysis of the obtained backscattered spectra.

In the spectral interferometry experiments on the nanotextured thin-film solar cells long-lived coherent contributions to the backscattered radiation are identified on various spatial positions. The propagation length of near-infrared light in amorphous silicon during the estimated lifetime of 130 fs is about $10 \mu\text{m}$. This exceeds the a-Si:H layer thickness by a factor of 30. The enhancement of the effective propagation length through the absorbing layer causes an enhanced total absorption of the incident light compared to solar cells with smooth interfaces (Section 6.2.2). Thus, the nanotexturing does improve the photon management in the solar cell. Furthermore, the enhanced absorption is associated to a light trapping mechanism which elongates the effective residence duration of the light in the absorbing layer. The spatial resolution of the employed method does not permit to unambiguously estimate, how the light trapping takes place in the thin-film solar cells. From the spatial variations of the backscattered spectra on length scales of $10 \mu\text{m}$ to $20 \mu\text{m}$ it is deduced that the long-lived coherent states occur on distances smaller or equal to the size of the laser focus. The backscattered radiation has to originate from the focal spot position, as the confocal detection method rejects contributions from displaced locations.

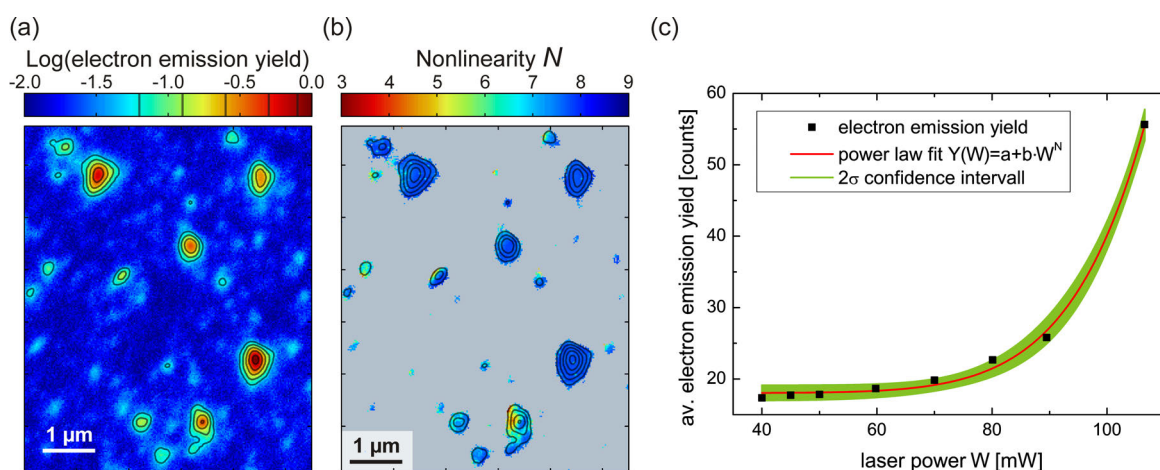


Figure 6.10.: Nonlinear order of electron emission process from the sample with exposed nanotextured a-Si:H layer. (a) Local electron emission distribution with yield on normalized logarithmic scale. (b) Nonlinearity distribution map based on power function fit of the emission yield at spatial pixels above 5% of the maximum yield in (a). (c) Averaged emission yield of complete field of view above 2.5% threshold. Fit by power function $Y(W) = a + b \cdot W^N$ estimated the nonlinear exponent $N = 8.37 \pm 0.57$. Adapted from [92].

6.3. 2D Nanoscopy on Nanotextured Thin-Film a-Si:H

In this section 2D nanoscopy on the nanotextured thin-film solar cell with exposed a-Si:H layer are presented. The general electron emission from the sample exhibits strong lateral variations. The electron yield scales with a nonlinear order which strongly exceed the value given by a direct multiphoton excitation (Section 6.3.1). These results are attributed to a thermionic emission model describing the highly nonlinear emission of electrons as a consequence of fast electron gas thermalization processes after ultrafast absorption of light energy by localized photonic modes (Section 6.3.2). The 2D nanoscopy measurements (Section 6.3) are analyzed by the evaluation routine presented in Chapter 4.3.3 revealing the spatial resolved distribution of the local coherence lifetime and center frequency.

6.3.1. Nonlinear Hot Spot Electron Emission from Nanotextured a-Si:H

The PEEM measurements shown in this chapter are performed with the *Focus NI-PEEM* setup (see Chapter 1.4.2), which allows an illumination in near normal-incidence geometry. The optical setup used to generate the collinear excitation pulse sequence for 2D nanoscopy is almost identical to the one presented in the previous chapters. However, it was adapted to couple optimally into the new PEEM.

In Figure 6.10 a detail of the PEEM image for illumination with bandwidth limited laser pulses used as reference in the 2D nanoscopy measurement are presented. The electron emission distribution from the nanotextured a-Si:H layer is inhomogeneous, exhibiting several localized hot spots with varying strength. The typical distances of the spots are in good accordance to the topographic properties of the surface shown in Figure 6.5c and d. A quantity that has to be determined prior to the 2D nanoscopy measurements is the nonlinear order N of the emission process. It is estimated from the dependence of the local emission yield of the laser intensity. PEEM images

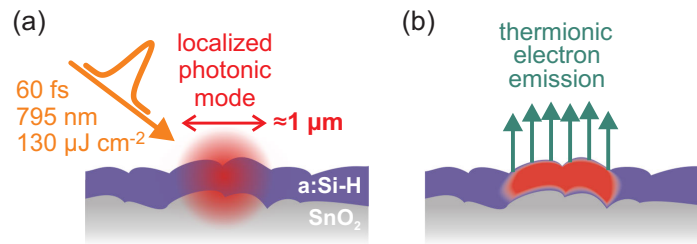


Figure 6.11.: Thermionic emission from a-Si:H excited by enhanced absorption in localized photonic modes. (a) Ultrashort laser pulse couples to localized photonic mode. (b) Absorbed energy locally heats the electron gas. Thermalization leads to a small population of high-energy electrons which leave the sample in a thermionic emission process. Adapted from [92].

of several laser power steps were obtained and drift corrected (see Appendix B). The laser power dependence of each spatial pixel above a threshold of 5% of the maximal yield is fitted individually by a power function $Y(W) = a + b \cdot W^N$. The parameter N , which describes the exponent, is the nonlinear order of the electron emission process. Figure 6.10b shows the spatial distribution of N which exceeds a value of 7 at most positions. Visible are the strong and medium strong hot spots in the investigated region. Data from positions with low photoemission is left out and replaced by a gray shaded area.

In Figure 6.10c the laser-power-dependent emission yield of the complete field of view is presented for a lowered threshold of 2.5% of the maximum yield. The black squares indicate the obtained averaged electron emission yield per pixel. The results of the power law fit are presented as red line and the corresponding 2σ confidence interval is indicated by the green area. At an incident laser power below 50 mW the averaged emitted yield barely increases above the background level of the detector. Even the strongest emitting spots give very weak signals. The electron emission is strongly increasing with the laser power resulting in a fitted nonlinearity of $N = 8.37 \pm 0.57$.

The nonlinear order of the electron emission process from the exposed a-Si:H surfaces has been determined to be $N \approx 8$ at positions of high electron yield. In a multiphoton absorption process involving eight photons ($\hbar\omega \approx 1.55$ eV at 800 nm wavelength) per electron the accumulated energy would strongly exceed the work function E_W of the material. For overcoming the work function already four photons would suffice leading to an electron yield proportional to the fourth power of the local intensity (see Chapter 1.4.3). Also above-threshold photoemission and strong-field emission processes would not provide such an enhanced nonlinearity of the signal [105, 389, 390]. Accordingly, an additional electron emission mechanism has to be responsible for this observation. In the following section it is discussed how the thermalization of the electron gas excited by ultrashort laser pulses leads to the occupation of electronic states above the vacuum energy and, consequently, to the thermionic emission of electrons. The total emission yield of such a process is strongly affected by the absorbed energy and scales with high nonlinear order with respect to the fluence of the incident laser pulses.

6.3.2. Thermionic Emission from Photonic Mode Heated Hot Spots

Thermionic emission of electrons is a well known process which has many applications, e.g. hot cathodes in vacuum tubes [93, 94, 391–393]. By illumination with picosecond or femtosecond

laser pulses photo-induced ultrafast thermionic emission is achieved without a further external heating [95, 394]. The basic idea behind the ultrafast thermionic emission model explained in this section is depicted in Figure 6.11. The incident light couples to localized photonic modes and is efficiently absorbed in the a-Si:H layer. The absorption of photons within about 100 fs generates an athermal electronic energy distribution. The absorbed energy leads to a strong local heating of the electron gas in the overlap with the photonic mode. After establishing a thermalized electron gas via electron-electron interactions, the electron distribution exhibits a high-energy tail containing electrons with sufficient energy to leave the sample in a thermionic electron emission process. The emission yield varies highly nonlinear with the electron gas temperature and, consequently, with the absorbed energy density. Thus, thermionic emission explains the observed nonlinear order N .

On the time scales of the excitation by the femtosecond laser pulse the energy transfer between the electronic system and the phonons of the absorber material are negligible. Consequently, the complete absorbed energy density ϵ_{abs} is deposited into the electron gas. In the temporal overlap with the excitation pulse, the sequential absorption into states above the vacuum energy causes the transiently dominant multiphoton photoemission from the sample. Afterwards, the electron gas is still significantly excited and the electron energy distribution is athermal. The electron gas thermalizes via electron-electron scattering into a thermal distribution, i.e. the population of the electrons ρ_{el} follows

$$\rho_{el}(E, T, E_F) = D_{el}(E)f(E, T, E_F) = \frac{D_{el}(E)}{1 + \exp\left[\frac{E-E_F}{k_B T}\right]}, \quad (6.2)$$

where $D_{el}(E)$ denotes the electronic density of states, $f(E, T, E_F)$ is the Fermi distribution, E_F is the Fermi energy and k_B denotes the Boltzmann constant. The new equilibrium state is reached, when the occupation of the electronic states is given by a Fermi distribution with the new electron gas temperature T_{el}^{max} . In the absence of cooling mechanisms which acts on the same time scale as the electron gas thermalization process, the absorbed energy density ϵ_{abs} remains in the electronic system. Consequently, T_{el}^{max} is the temperature at which the energy density difference $\Delta\epsilon$ between the initial and excited electron system, which is calculated by

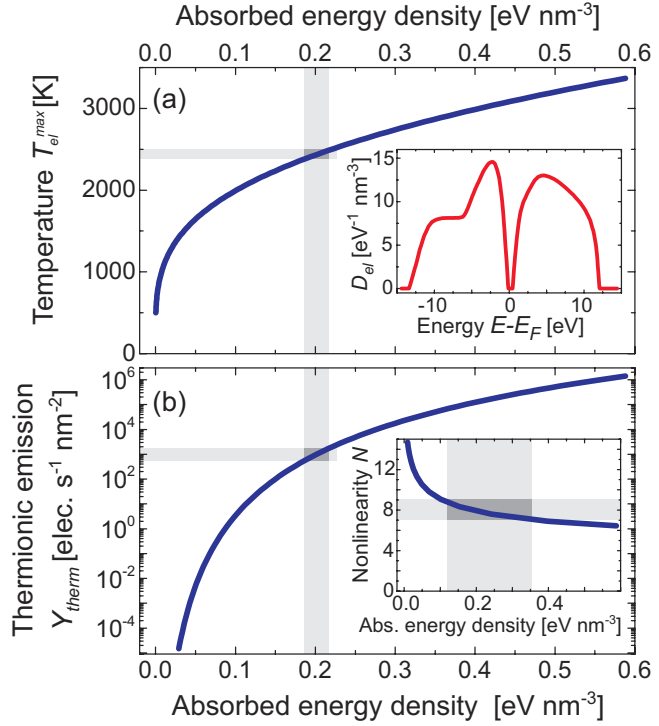
$$\Delta\epsilon(T_{el}^{in}, T_{el}^{max}) = \int_{-\infty}^{\infty} E \cdot (\rho_{el}(E, T_{el}^{max}, E_F) - \rho_{el}(E, T_{el}^{in}, E_F)) dE \quad (6.3)$$

$$= \int_{-\infty}^{\infty} E \cdot D_{el}(E) \left\{ \frac{1}{1 + \exp\left[\frac{E-E_F}{k_B T_{el}^{max}}\right]} - \frac{1}{1 + \exp\left[\frac{E-E_F}{k_B T_{el}^{in}}\right]} \right\} dE, \quad (6.4)$$

equals the absorbed energy density ϵ_{abs} . Here, T_{el}^{in} is the initial electron gas temperature, which is identical to the phonon gas temperature prior to the excitation.

According to Eq. (6.4), the final temperature T_{el}^{max} is determined by $D_{el}(E)$ and ϵ_{abs} . In the following the density of states is given by a recent theoretical model of a-Si:H [395] with density scale calibrated using a theoretical model for amorphous silicon [396]. In the inset of Figure 6.12a the employed D_{el} is presented. Variations of the hydrogen content alter the density of states,

Figure 6.12: Thermionic emission model for a-Si:H. (a) Maximum electron gas temperature T_{el}^{max} as a function of absorbed energy density ϵ_{abs} . The initial temperature of the electron gas was set to 300 K. The gray rectangles mark the most likely temperature and energy density intervals observed from the nanotextured a-Si:H layer. The inset shows the electronic density of states D_{el} of a-Si:H. (b) Thermionic emission yield Y_{therm} as a function of ϵ_{abs} . The inset shows the nonlinear order of the emission process N in dependence of ϵ_{abs} . Gray rectangles mark the intervals in which the nonlinearity N lies between 7 and 9. Adapted from [92].



thus a relative uncertainty in $D_{el}(E)$ of approximately 10% is expected. The Fermi energy is set to mid gap energy position corresponding to a neutrally charged undoped semiconductor. Figure 6.12a shows the final electron temperature T_{el}^{max} of a-Si:H in dependence of the absorbed energy density per pulse. The temperature rises very fast for small ϵ_{abs} values, since the electronic band gap prohibits the excitation of electrons close to the Fermi energy. Thus, only a small fraction of the electronic population has to be transferred to generate an equilibrium occupation $f(E, T_{el}^{max}, E_F)$ with strongly increased T_{el}^{max} . At increased ϵ_{abs} the temperature rises slower as the influence of the band gap is reduced.

The thermalized electron density $\rho_{el}(E, T, E_F)$ has a high energy tail reaching above the vacuum energy of the material enabling the thermionic emission of electrons. The Richardson-Dushman equation

$$Y_{therm}(T) = AT^2 \exp \left[-\frac{E_W^{ef}}{k_B T} \right] \quad (6.5)$$

describes the thermionic emission yield $Y_{therm}(T)$ as a function of temperature [93, 94]. The remaining parameters $A = 60 \text{ AK}^{-2}\text{cm}^{-2} = 3.7 \cdot 10^6 \text{ electrons s}^{-1}\text{K}^{-2}\text{nm}^{-2}$ and $E_W^{ef} = 4.9 \text{ eV}$ denote the Richardson constant and the effective work function, respectively. Equation (6.5) is used to calculate the thermionic emission yield for the identical absorbed energy density range as in Figure 6.12a. The Richardson constant A is material-dependent. However, the necessary corrections, which are in the order of unity, influence the emission yield $Y_{therm}(T)$ only as a constant factor, but do not change the nonlinearity with respect to ϵ_{abs} . For low absorbed energy densities the emission yield rises strongly. Since the yield-axis is plotted logarithmically, the slope of the graph indicates the nonlinearity N of the emission process. This parameter is also depicted

in the inset in Fig. 6.12b. The steepness of the curve decreases for higher ϵ_{abs} . A nonlinearity value in the interval $7 < N < 9$ is achieved for energy densities between 0.12 and 0.35 eVnm⁻³. This region is highlighted by the gray rectangles in Figure 6.12b. A slope of $N = 8$ is found most likely at $E_{abs} = 0.2$ eVnm⁻³. As it is indicated in Figure 6.12a, this corresponds to a final electron gas temperature $T_{el}^{max} \approx 2500$ K.

The thermionic emission model presented above does not include effects of electron gas cooling. Energy relaxation occurs via several mechanisms. Locally the electronic energy density is reduced via the transport of hot electrons into adjacent regions of an inhomogeneously excited system, the thermionic electron emission and electron-phonon scattering. Nevertheless, the equilibrium model for thermionic emission is still applicable to estimate the absorbed energy density in the a-Si:H layer because these phenomena are weak in their influence on the electron density ρ_{el} or occur on longer time scales than the electron thermalization. An example for the latter case is the cooling of the electron gas by heat transfer into the phonon gas. In amorphous silicon the electron gas cooling time is reduced compared to crystalline silicon, since the restriction to the phonon energy and wavevector distributions given by the dispersion relation in c-Si are removed [397]. Still, at a maximum electron gas temperature of 2000 K the electron relaxes within about 400 fs. Thus, the thermalized state characterized by T_{el}^{max} is reached and maintained, before the temperature decays to the electron-phonon equilibrium value.

In principle the thermionic electron emission is an analog to the evaporative cooling used to prepare ultracold diluted gases and Bose-Einstein condensates [398–401]. The high energy electrons leave the material and reduce the average electron energy. However, at an electron gas temperature of 2500 K the cooling by thermionic emission occurs at a rate of 5 neV ps⁻¹ nm⁻². Accordingly, the influence of the electron emission on the temperature is marginal compared to the cooling by electron-phonon scattering.

A spatially inhomogeneous absorption of the ultrashort laser pulses leads to lateral variations of the electron density $\rho_{el}(\mathbf{r}, E, T, E_F)$ causing internal electron transport within the sample. Diffusive transport involves the multiple scattering of electrons pursuing a biased random walk. Ballistic transport is faster with electrons traveling at the Fermi velocity of approximately 10⁶ m/s. Considering the electron-phonon equilibration time in a-Si this leads to 0.4 μ m as an upper limit for the electron propagation length. Hence, even the fastest electrons are merely leaving the photonic mode in the relevant time interval.

After the thermalization process the local electron temperature $T_{el}(\mathbf{r}, t)$ decays from its maximum value $T_{el}^{max}(\mathbf{r})$ due to the discussed relaxation channels. Thus, also the thermionic yield $Y_{therm}(T_{el})$ decreases according to the Richardson-Dushman equation (Eq. (6.5)). Because of the strong nonlinear relation between yield and temperature, the emission rapidly vanishes and the time-integrated photoemission signal is dominated by the peak emission at $T_{el}^{max}(\mathbf{r})$.

Based on the thermionic emission model described above, the yield of the hot spot emission pattern visible in PEEM is connected to the local thermalized electron temperature $T_{el}^{max}(\mathbf{r})$. The PEEM image, therefore, reflects the local heating of the absorber layer due to the interaction with localized photonic modes. Equation (6.4) relates $T_{el}^{max}(\mathbf{r})$ with ϵ_{abs} (see Figure 6.12b). Accordingly, via the electron emission yield the absorbed energy density is monitored.

Figure 6.13 shows the identical detail of the PEEM image used for determining the nonlinearity N in the previous section. The logarithmic yield scale was adapted to indicate all pixels with yield values below 2.5% of the maximal yield by gray color. The gray areas are omitted because the

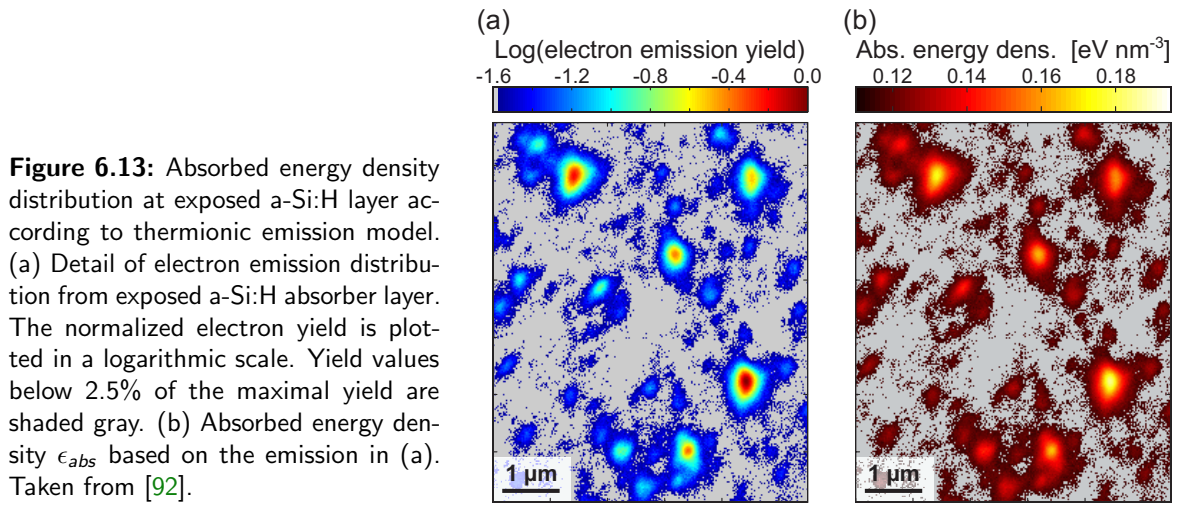


Figure 6.13: Absorbed energy density distribution at exposed a-Si:H layer according to thermionic emission model. (a) Detail of electron emission distribution from exposed a-Si:H absorber layer. The normalized electron yield is plotted in a logarithmic scale. Yield values below 2.5% of the maximal yield are shaded gray. (b) Absorbed energy density ϵ_{abs} based on the emission in (a). Taken from [92].

obtained yield approaches the background noise level. For all pixels above this threshold ϵ_{abs} was calculated according to the relation presented in Figure 6.12b. The electron yield measured with PEEM does not indicate the absolute electron emission rate, which could be directly compared to Y_{therm} predicted by the thermionic emission model. Instead, the experimental yield is a relative quantity, which is affected by several experimental conditions with uncertain influence. Thus, the measured nonlinearity N is used for estimating the absorbed energy density ϵ_{abs} at the spatial position of maximum electron yield. The simulated nonlinearity reaches the experimentally obtained value of $N = 8$ at the energy density $\epsilon_{abs} = 0.2 \text{ eV nm}^{-3}$. Using this ϵ_{abs} -value as maximal absorbed energy density all other pixels of the ϵ_{abs} -distribution were evaluated accordingly via the $\epsilon_{abs}-Y_{therm}$ relation displayed in Figure 6.12b. Areas below the yield threshold were omitted and indicated in Figure 6.13b by a gray shading.

The absorbed energy density distribution allows for estimating the average absorbed fluence per pulse. The laterally averaged absorbed energy density is $\epsilon_{abs}^{av} = 0.06 \text{ eV nm}^{-3}$, calculated under the assumption that the gray shaded areas below the emission threshold do not contribute significantly to the absorption. Considering the absorption process to take place homogeneously across the silicon layer, integration over the film thickness of 100 nm yields an averaged absorbed fluence of $100 \mu\text{J cm}^{-2}$. Thus, the thermionic electron emission pattern from localized photonic modes is associated to a total absorption cross section of 75% of the incident fluence of 130 mJ cm^{-2} . This estimation is, within the uncertainties of the measurement and the modelling, in a quantitative agreement to the 40% absorption of the nanotextured exposed amorphous silicon layer at 800 nm determined by linear spectroscopy (Fig. 6.6). For this reason, the demonstrated absorption enhancement in the nanotextured solar cells is explained by a dominant absorption from localized photonic modes.

In the electron-phonon equilibrium, which occurs after the emission has vanished, the local lattice temperature at the peak position of the ϵ_{abs} -distribution is enhanced by each laser pulse by 20 K, considering a heat capacity of a-Si of $0.01 \text{ eV K}^{-1} \text{ nm}^{-3}$ [402]. The efficient heat transfer into the substrate is responsible for maintaining a temperature below 500 K, at which a degradation of the film properties sets in, even though the sample is illuminated enduringly with a pulse repetition rate of 80 MHz.

The ultrashort laser pulses provide the necessary field intensity to considerably change the electron

density of states D_{el} during the optical excitation. Also multiphoton absorption is possible and occurs with a certain rate, but it does not contribute significantly to the electron emission yield. However, most of the energy is deposited into the electron gas via single-photon absorption and the electron-electron interaction during the thermalization process generates the high-energy tail of the electron distribution. The simple model for the electron emission in fast dephasing systems (see Chapter 1.4.3) does not include electron thermalization but only considers multiphoton photoemission pathways in which individual electrons gain sufficient energy to overcome the work function. Nevertheless, finally the emitted electron yield depends directly from the local electric field intensity. In the thermionic emission process the local absorbed energy density is also determined by the localized electric field, i.e. the linear response of the localized photonic mode driving the emission hot spot. Even though the electrons gain their energy in the thermalization of the heated electron gas, the final electron yield is again proportional to I^N . Thus, the identical mathematical description of 2D nanoscopy is valid as in the case of multiphoton photoemission.

6.3.3. 2D Nanoscopy on Nanotextured Thin-Film a-Si:H

To evaluate, whether the hot spot electron emission is associated with localized photonic modes, it is necessary to obtain a spectroscopic evidence that the disjunct spots exhibit characteristic local response functions. A clear distinction between local 2D nanoscopy spectra from the hot spots would indicate that the local resonance behavior is determined by the scattering environment of the individual location instead of a common extended mode. Furthermore, it is investigated, if the localized modes show the elongated decay times which have been observed with spectral interferometry of the backscattered radiation (Section 6.2.3). An agreement with the SI results would emphasize that the absorption enhancement in nanotextured solar cells, which is observed by linear absorption spectroscopy (Section 6.2.2), the enhanced nonlinearity of the emission process and the findings of the backscattering SI and 2D nanoscopy experiments are all aspects of the identical phenomenon, which is localization of light in long-living photonic modes.

The 2D nanoscopy measurements were performed with a collinear pulse sequence consisting of three independent pulses generated by the femtosecond laser pulse shaper. Thus, the delay T and the relative phase φ_T in the four-pulse notation of conventional 2D spectroscopy (see Fig. 4.3c) were set to zero. During the 2D nanoscopy experiment the delays τ and t were scanned in steps of 10 fs from 0 fs to 280 fs. The relative phases were varied according to a 4×4 phase cycling scheme in steps of $\pi/2$ from 0 to $3\pi/2$ (see Chapter 4.2.4 and 4.3.1). The acquisition time of 1100 ms of the CCD camera was adapted to provide the optimal dynamic range of the measured electron yield. Since the CCD camera achieves 12 bit numerical bandwidth and the typical background signal is approximately $2^4 = 16$, the optimal signal to background ratio is $2^8 = 256$. The background is mostly given by a constant offset signal of the CCD, whereas the noise is considerably smaller. For each step of those four parameters an individual PEEM image was recorded for bandwidth limited reference pulses and cross-correlated with the initial reference image to detect the relative spatial drift between sample and electrostatic lens system and numerically reposition the obtained data (see Appendix B). Then, the delay-dependent signal is phase cycled as presented in Chapter 4.2.4 and Fourier transformed. The complete field of view includes the spectral information of more than 10^6 independent spatial pixels. Hence, an evaluation of the spectroscopic signal has to be performed with a fast and reliable routine which adapts to the local nonlinear order of the emission process.

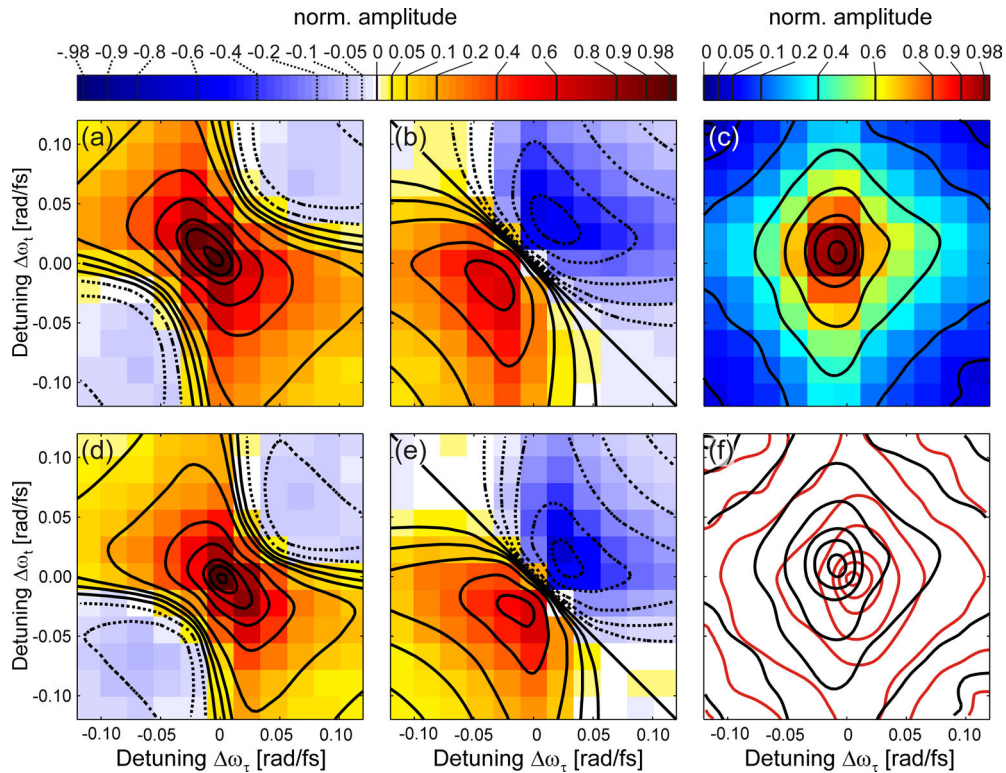


Figure 6.14.: Experimental local 2D nanoscopy and fit results. The phase cycling scheme filtering the photon echo signal was applied. (a–c) Real part, imaginary part and spectral amplitude of 2D nanoscopy spectrum in ROI1. (d) and (e) Real part and imaginary part of 2D nanoscopy spectrum in ROI2. ROI1 and ROI2 are defined according to Figure 6.15. The contour lines in (a–e) indicate the results of the fit routine. The color scale and spacing of the contour lines is normalized to the maximum values of the respective real spectra. (f) Contour plot of experimental spectral amplitudes obtained in ROI1 (black) and ROI2 (red).

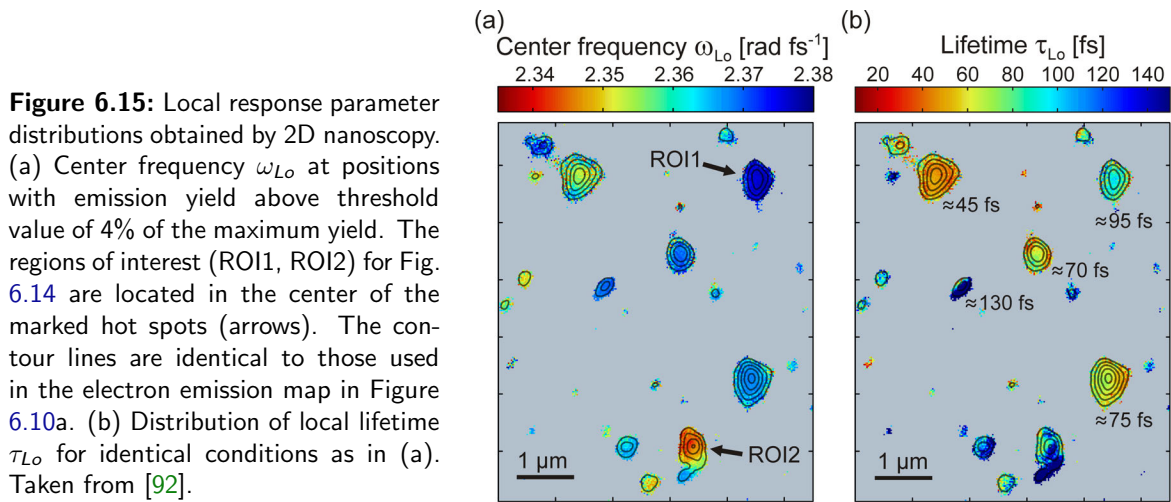
Figure 6.14 presents the experimental 2D nanoscopy spectra at two distinct spatial positions (ROI1, ROI2) which are marked in Figure 6.15. These regions of interest are both 5×5 pixel in size, i.e. the covered area is $(125 \text{ nm})^2$. Effectively, the choice of extended regions of interest containing several pixels improves the achievable dynamic range of the electron yield, but for the cost of a reduced spatial confinement of the data. In all plots the frequency detuning axes cover the interval between -0.12 rad/fs and 0.12 rad/fs . The phase cycling coefficients were chosen to yield the photon echo signal $\check{Y}(\mathbf{r}, \omega_t, \omega_\tau, 2, -1)$. The diagrams in Figure 6.14a and b show the real part and the imaginary part of the 2D nanoscopy spectrum in ROI1, respectively. The colored pixel indicate the experimental data, whereas the contour lines are given by the results of the fit routine. The spectral resonance is detuned towards positive ω_t direction corresponding to a local response function shifted to higher frequencies with respect to the excitation carrier frequency ω_L . The observed shift is smaller than the spectral width and is on the scale of a single spectral pixel. Nevertheless, the detuning is visible both in the real as well as in the imaginary part and is clearly supported by the complete shape of the resonance peak. The fit algorithm optimizes the parameter of the complex fit function $\check{Y}_{fit}(\omega_\tau, \omega_t)$ (Eq. (4.52)) by simultaneously minimizing the deviation to the real and imaginary part of the measured spectrum. The obtained fit parameters

are $\omega'_{Lo}(\text{ROI1}) = 2.371$ rad/fs and $\gamma'_{Lo}(\text{ROI1}) = 0.041$ rad/fs. There is a very good agreement in position and shape of the experimental and fitted spectral features in Figure 6.14a and b. The real and imaginary part of the fit function follow symmetry conditions with respect to the antidiagonal of the 2D spectrum. This is on account of fixing the remaining parameters of the lineshape function $\tilde{Y}_{fit}(\omega_\tau, \omega_t)$ to $-b = d = 1$, leading to the shift of the resonance peak in accordance to the photon echo signal, and to $c = e = 1$, causing the spectral feature to be equally broad in both frequency directions. For this reason, the fit algorithm is not capable to reconstruct the slight deviations from the symmetric shape visible in the experimental data.

The amplitude spectrum of ROI1 is presented in Figure 6.14c. Here, the contour lines are calculated by interpolating the experimental data. Also in this diagram the frequency detuning is visible. The spectral feature is elongated in ω_t -direction, but because of the high nonlinear order and the influence of the excitation spectrum, the 3 : 1 ratio predicted by Eq. (4.35) is not achieved.

The spectral resonance position in ROI2 is detuned towards lower frequencies. The spectral width is smaller, i.e. the resonance peak is less broad. The evaluation with the fit routine yields the fit parameters $\omega'_{Lo}(\text{ROI2}) = 2.355$ rad/fs and $\gamma'_{Lo}(\text{ROI2}) = 0.032$ rad/fs. The diagram in Figure 6.14f combines the contour lines indicating the amplitude spectra in ROI1 (black) and ROI2 (red). Despite the partial overlap of both spectral features, the difference in the center positions is obvious. As it is discussed in Chapter 4.3.3, the nonlinearity N and the limited bandwidth excitation spectrum influence the obtained 2D spectrum by broadening and shifting it towards the center frequency of the laser spectrum. The actual center frequencies of the local response functions at ROI1 and ROI2, therefore, are more distinct. Similarly, the spectral width has to be corrected. After rescaling the fit parameters according to the local nonlinearity N and the simulated results of Chapter 4.3.3, the linear response parameters are $\omega_{Lo}(\text{ROI1}) = 2.376$ rad/fs and $\gamma_{Lo}(\text{ROI1}) = 0.010$ rad/fs and $\omega_{Lo}(\text{ROI2}) = 2.347$ rad/fs and $\gamma_{Lo}(\text{ROI2}) = 0.008$ rad/fs. Thus, the frequency difference between both resonance positions is larger than the spectral widths of the response functions. The 2D nanospectra at ROI1 and ROI2 are additionally fitted using the Fourier transform time domain technique to simulate the photoemission yield, which enables to directly include the effects of the laser spectrum and the local nonlinear order of the emission process (see Chapter 4.3.2). Here, very similar fit results are obtained. The retrieved response parameters are $\omega_{Lo}(\text{ROI1}) = 2.374$ rad/fs and $\gamma_{Lo}(\text{ROI1}) = 0.012$ rad/fs and $\omega_{Lo}(\text{ROI2}) = 2.349$ rad/fs and $\gamma_{Lo}(\text{ROI2}) = 0.009$ rad/fs. Even though small deviations from the fit by the fast spectral domain evaluation routine occur, the very good agreement of the results demonstrated that the fast fit routine reliably retrieves the fit parameters, despite the strongly reduced computational effort.

The 2D nanoscopy scan at each spatial pixel in the identical field of view as in Figures 6.10 and 6.13 is evaluated with an automated fit routine. Hence, for every spatial pixel, the nonlinear order N has been retrieved and is employed for calculating the linear response parameters ω_{Lo} and γ_{Lo} from the fit parameters ω'_{Lo} and γ'_{Lo} . Figure 6.15a and b illustrate the spatial distributions of the center frequency ω_{Lo} and the coherence lifetime $\tau_{Lo} = \gamma_{Lo}^{-1}$, respectively. In the gray shaded area the emission yield is below a threshold of 4% and, therefore, is not evaluated. Even though the evaluation of each pixel is performed independently, the obtained results vary only to a small extent within a single emission hot spot. Hence, also within ROI1 and ROI2 the spectral parameters obtained from each pixel are almost homogeneous. In contrast, distinct differences in ω_{Lo} and τ_{Lo} occur between several of the shown spots. The obtained center frequency ranges



between 2.34 rad/fs and 2.38 rad/fs. All visible emission hot spots have ω_{Lo} values close to the center of the excitation spectrum because only those spots couple effectively to the incident laser radiation and generate a strong emission signal, which have a strong overlap with the laser spectrum. This observation does not restrict the possible range of photonic mode frequencies to exactly this spectral region but explains why other modes do not occur in the 2D nanoscopy signal. The local lifetime distribution determined by 2D nanoscopy reveals that indeed the light is trapped for 50 fs to 130 fs in the region of the hot spots. Compared to the averaged lifetime of 70 fs measured by spectral interferometry of the backscattered electric field (see Fig. 6.9) a good accordance of the results of both technique is obvious. No significant correlation between the observed lifetime and the hot spot resonance frequency is visible in Figure 6.15a and b as well as from statistical analysis of a larger field of view. Consequently, ω_{Lo} and τ_{Lo} appear to be independent quantities.

To demonstrate the simultaneous spatial and spectral resolution obtained by 2D nanoscopy with 16 step phase cycling, the electron emission and the center frequency distributions in a smaller area around ROI2 are presented in Figure 6.16. In the PEEM image (Fig. 6.16a) an electron emission pattern with an irregular shape is visible. In addition to the pronounced photoemission peak a local emission maximum is observable which is displaced in vertical direction by approximately 400 nm. From the single PEEM images it is not obvious whether the emission distribution is caused by a single localized photonic mode generating two closely adjacent emission hot spots or whether these hot spots are driven by two distinct localized resonances. The internal structure of the hot spot is clearly distinguishable in the spectral resolved map in Figure 6.16b. Whereas the contour lines still indicate the electron emission yield, the coloring of the pixels indicates the local center frequency ω_{Lo} . Here, the emission pattern is subdivided into two parts with different center frequencies. Within these two parts the center frequency ω_{Lo} is distributed almost homogeneously. The blue line marks the position of the cut through the boundary between both regions shown in Figure 6.16c. Along this cut a steep decent of ω_{Lo} is visible. The blue ribbon shows the 2σ -interval according to the propagated uncertainties originating from fitting the local 2D spectra. On first glance the 2σ -interval appears surprisingly narrow compared to the spectral features that are observed in the 2D nanoscopy spectra (see Figure 6.14). However, this high fit accuracy can be explained by the two-dimensional data, which provides a sufficient number

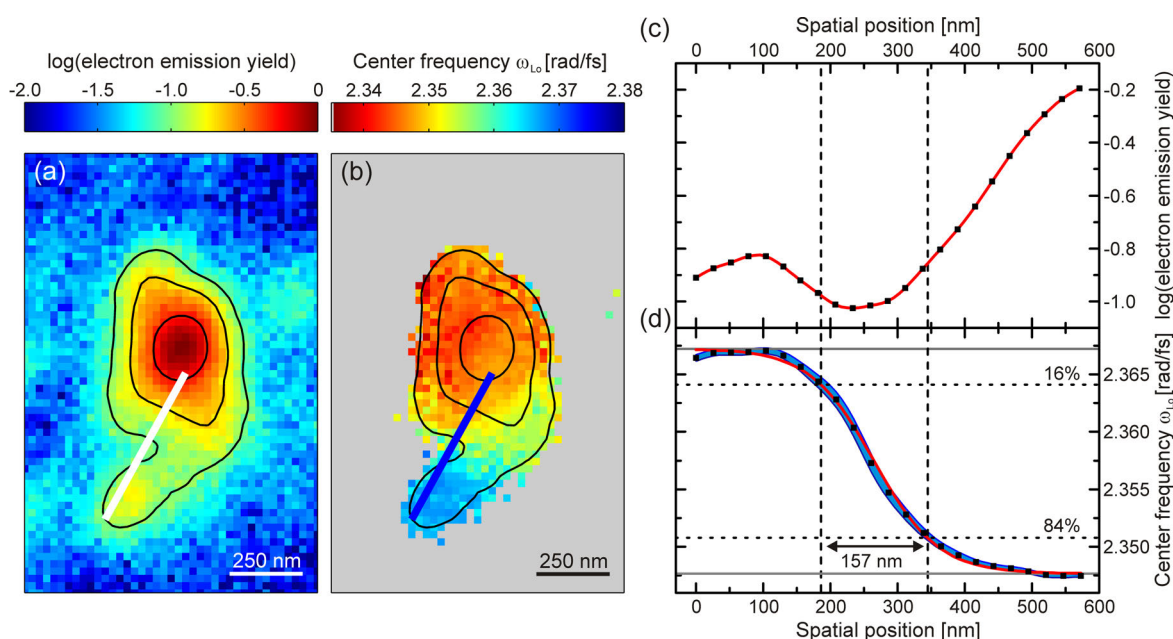


Figure 6.16.: Spatial resolution of 2D nanoscopy. (a) Detail of PEEM image presenting electron emission distribution around ROI 2 acquired with reference pulse illumination. The white line indicates the position of the cut presented in (c). (b) Detail of fitted and rescaled center frequency distribution. The blue line indicates the position of the cut presented in (d). (c) Cut through electron emission distribution. The yield scales logarithmically. The red line is included to guide the eye. (d) Cut through the ω_{Lo} distribution (black squares) with 2σ -interval based on the propagated fit uncertainties of the lineshape function fit (blue). The red line shows the best fit result of a sigmoidal function, which estimates the spatial resolution in the spectral data to be at least 156.8 ± 6.4 nm.

of sampling points. Additionally, the feedback of the fit algorithm is determined by the real and imaginary part of a complex valued signal containing more information than a completely real-valued signal. The spatial resolution along the cut is estimated by fitting the data with a sigmoidal function and determining the width of the 1σ -interval around the position in the middle of the edge. With 156.8 ± 6.4 nm a sub-wavelength spatial resolution in the spectral signal is achieved. Compared to the resolution limit of the PEEM setup demonstrated in Fig. 1.18 this value is considerably larger. However, the investigated sample is not fabricated to approach ideal conditions for are resolution test. In the cut through the PEEM image (Fig. 6.16a) only a low contrast between the minimum yield and the yield of the smaller hot spot is observed. In the interval in which the strongest dynamic of ω_{Lo} is observed (dashed lines) the emission yield varies only by a factor of 1.5 between minimum and maximum value. Consequently, this sample is not suited to test the ultimate limits of the simultaneous spatial and spectral resolution of 2D nanoscopy. Presumably, at a sample with stronger localized emission hot spots at closer spatial distance an even better spatial resolution might be demonstrated with the identical setup. After all, the resolution of 2D nanoscopy is mostly determined by the resolution of the PEEM and the stability of the experimental conditions.

6.4. Conclusion

Thin-film solar cell efficiencies are improved by employing absorber layers with nanotextured interfaces. Especially in the near-infrared regime, in which hydrogenated amorphous silicon exhibits a reduced absorption cross section, an enhancement of the absorption is observed. Spectral interferometry demonstrated that random disorder introduced by nanotexturing of the interfaces significantly increases the decay time of backscattered broadband radiation. Within the area of the focal spot typically several sharp spectral features dominate the obtained spectra. In a lateral scan of the sample position it has been demonstrated that the individual spectral modes originate from regions which are not exceeding the focal spot width.

In 2D nanoscopy experiments a connection between absorption enhancement in nanotextured thin-film solar cells and light trapping in localized photonic modes has been identified. Within the uncertainty of the theoretical modeling the high nonlinear order of the electron emission process ($N = 8$) at localized hot spots is explained with thermionic emission driven by localized photonic modes in the a-Si:H layer. The light trapping efficiency of the localized photonic modes has been estimated to be exceptionally high and, therefore, localization of light has been identified as a dominant mechanism for the absorption enhancement. With 2D nanoscopy it has been proven that indeed the individual emission hot spots exhibit characteristic spectral properties and are associated to distinct localized resonances. The measured local coherence lifetimes of these localized modes in the range of 50–130 fs agree with the far-field spectral interferometry results. Qualitatively, the experimental observations exhibit a strong similarity to the simulations in [378], demonstrating enhanced absorption and localized electric fields in disordered absorber layers, as well as the results of ultrafast SHG microscopy in a random ZnO nanoneedle array [354]. There, spectral narrowing of radiation originating from locally enhanced electric fields was measured. However, the obtained local lifetimes were noticeably shorter than in case of the a-Si:H layer and the optical far-field detection method is diffraction-limited.

2D nanoscopy has been demonstrated to achieve sub-wavelength spatial resolution and a high spectral sensitivity. Fitting the 2D spectra of singular pixels within the emission hot spots with an adapted Lorentz oscillator model determines the center frequency with a typical uncertainty of $\Delta\omega_{Lo} = 1$ mrad/fs ($\Delta\lambda_{Lo} = 0.33$ nm). 2D nanoscopy probing the thermionic electron emission simultaneously gives access on the relevant spectral and spatial properties of the absorber layer and will be a valuable tool in the further optimization of light matter interaction in photovoltaics and disordered scattering systems.

The localized photonic mode enhanced absorption mechanism in nanotextured thin-film solar cells has a broad influence on future light absorber designs. On the one hand, there is a close relation to the absorption enhancement strategies of plasmonic solar cells [25], since scattering of light at nanoscaled surface structures is involved. Therefore, common optimization strategies to enhance the light-scattering abilities of the absorber layer are applicable. On the other other hand, the nanotextured layer can be considered as an agglomeration of randomly distributed localized open resonators. If in such resonators the internal loss processes are equal to the loss via the coupling to external fields, critical coupling conditions are achieved leading to a distinctive boost of the absorption in otherwise weakly absorbing materials [403–407]. Hence, the development of absorber designs that enhance the formation of localized photonic modes in the critical coupling regime further improves the absorption enhancement and might extend the usable spectral bandwidth of the photovoltaic devices. An advantage compared to plasmon

assisted absorption is that the losses are dominated by the absorption within the active material instead of within embedded metal particles. Thus, the charge carriers are directly separated by the internal field within the absorber layer and recombination losses are reduced.

Summary and Outlook

In this thesis the essential experimental aspects for the achievement of ultrafast space- and time-resolved spectroscopy on the nanoscale were investigated: The localization of optical near-fields in nanostructured samples by means of polarization pulse shaping, the space- and time-resolved detection of localized optical excitations on femtosecond time scale and nanometer length scale, and a novel spectroscopic method which retrieves the local spectral information from the incoherent delay-dependent photoemission data. The results of the experiments and simulations emphasize that the combination of TR-PEEM with femtosecond polarization pulse shaping offers unprecedented possibilities in the investigation of ultrafast processes on the nanoscale.

In coherent control experiments the shape and polarization state of femtosecond laser pulses was adapted to generate localized optical near-fields in the vicinity of fabricated nanostructures and at photoemission hot spots of silver films with randomly corrugated surface topography. In Chapter 2 adaptive optimizations utilizing an evolutionary algorithm proved the optimal open-loop scheme for coherent control of near-field switching via the application of an analytically derived control rule [87]. In a two-color two-photon photoemission experiment on gold nanoprisms the local field intensity generated by polarization-shaped laser pulses was measured and a switching between optimal pulse shapes was achieved by introducing an additional relative phase of π to one of the polarization components.

Coherent control was also employed to enhance and manipulate localized optical near-fields at individual photoemission hot spots on a corrugated silver surface (see Chapter 5.2). It was shown that femtosecond polarization pulse shaping enables to selectively excite localized plasmon modes. Hence, ultrafast coherent control of the near-field distribution has applications in improving surface-enhanced Raman spectroscopy on random metal surfaces, e.g. by selectively enhancing the SERS signal at individual spatial positions. The optimal pulse shapes obtained in adaptive optimizations were elongated and complex. This counterintuitive result was checked in systematic scans, which identified the third order dispersion (TOD) as well as the relative phase difference $\Phi(\omega)$ as two independent pulse parameter that determine the local photoemission yield. Here, for separated locations different optimal parameter combinations were found which partially lead to elongated pulse shapes. Thus, first indications of long-living coherences were found suggesting the investigation of the corrugated silver film with time-resolved spectroscopy methods.

In Chapter 3 it was demonstrated that in an incoherent single-color pump-probe experiment the spatiotemporal evolution of optical near-field distributions in nanostructures was determined. In these TR-PEEM measurements an ultrafast switching was detected which was generated by a polarization-shaped laser pulse with two perpendicular polarization directions. It was verified that two distinguished excitation patterns separated by approximately 250 nm in spatial dimension and 200 fs in time have been created. However, the ultimate limit of this technique was not reached. A huge improvement of the temporal resolution is expected if few-cycle laser pulses are utilized [9]. These are available by commercial laser oscillator systems. However, the design

and implementation of a high-bandwidth polarization pulse shaper is challenging. The achievable spatial resolution is dominated by the nanostructure response and the resolution of the PEEM setup. Accordingly, a spatial confinement and detection of the local electric field down to 50 nm or even smaller is feasible. The findings of Chapter 2 and 3 gave the clear experimental evidence that TR-PEEM in combination with polarization pulse shaping provides the complete excitation and detection scheme necessary for nanoscopic ultrafast space-time-resolved spectroscopy [85]. Having demonstrated these essential capabilities of the implemented setup, coherent 2D nanoscopy, a nonlinear spectroscopy method with sub-diffraction spatial resolution, was developed as a complementary experimental technique. The femtosecond pulse shaper was employed to generate excitation sequences with independently adjustable relative delays and phases between the pulses. Instead of optical radiation coherently emitted in a four-wave mixing process, as it is the case of conventional optical 2D spectroscopy, 2D nanoscopy detects electronic populations that are created by the excitation sequence. It was shown by theoretical considerations and in simulations in Chapter 4 that, despite the collinear excitation geometry and the incoherent detection method, unambiguous spectral information are retrieved by phase cycling and two-dimensional Fourier transformation of the delay-dependent photoemission signals. The optical excitation in 2D nanoscopy is still limited by diffraction but the detection of the local photoemission yield drastically improves the spatial resolution. Thus, spectroscopic contrast on length scales considerably smaller than the optical diffraction limit is possible. In this thesis the first experimental demonstrations of 2D nanoscopy were discussed. 2D nanoscopy was employed to investigate localized plasmonic excitations at a corrugated silver surface and of localized photonic modes in a-Si:H thin-film solar cells.

The evaluation of the 2D nanoscopy measurement (see Chapter 5.3) at the corrugated silver surface proved that already with 2×2 phase cycling a subwavelength spatial contrast in the spectroscopic signals was observed. However, since the obtained two-dimensional spectra still contained the contributions of several excitation pathways an unambiguous retrieval of the spectral parameters was not achieved.

A modified two-pulse nanoscopy experiment (see Chapter 5.4) at the identical position on the corrugated silver film showed a distinct beating behavior as well as elongated lifetimes supporting the observations from the coherent control experiments and the 2D nanoscopy measurement. The delay- and phase-dependent photoemission data contained information on the local spectral response function, which was retrieved by simulating the corresponding T - φ_T -plots and fitting spectral lineshapes. Here, two physical models and an unconstrained parametrization were tested. All fits converged to similar spectral response functions, demonstrating that the T - φ_T -plots contain sufficient information to retrieve the spectral response function in the overlap with the excitation spectrum. From the evaluation of the T - φ_T -plots no significant distinction between the physical models was possible as both models reconstructed the measured data with similar accuracy. Nevertheless, the hybridization model describing the coupling of localized plasmonic modes with standing surface plasmon polariton modes is favored because it accounts for the observed long coherence lifetime and the coherent beating in the photoemission yield and explains the nature of the contributing excitations.

Using 2D nanoscopy as a spectroscopy technique with subwavelength resolution, light trapping in localized photonic modes has been identified as the dominant mechanism for absorption enhancement in nanotextured a-Si:H thin-film solar cells. The detected electron emission is

confined to individual hot spots in the literal sense. At these locations the enhancement of the absorption cross section by localized photonic modes leads to a transient heating of the electron gas to $T_{el}^{max} \approx 2500$ K creating a strongly nonlinear thermionic emission of electrons. The 2D nanoscopy signal within the hot spots is to a large extent homogeneous, but between the hot spots no particular spectral correlations were observed. The detected coherence lifetimes of the localized photonic modes varied between 50 fs and 130 fs. The observation of elongated coherence lifetimes agrees with spectral interferometry measurements of backscattered radiation from nanotextured thin-film a-Si:H solar cells.

So far, the localization of light to confined photonic modes has not been the common explanation for the absorption enhancement in thin-film solar cells featuring disordered nanotextured absorber layers. The experimental evidence given by 2D nanoscopy clearly emphasizes that localization of light takes place in functional devices and is crucial for their absorption efficiency. The observations made by 2D nanoscopy are complementary to other investigation techniques and gain their high relevance by the particular excitation and detection scheme of 2D nanoscopy. Without sub-diffraction spatial resolution of spectroscopic signals the identification of individual photonic modes would not be possible. Furthermore, the connection between localized photonic modes and the enhanced absorption becomes obvious from the local nonlinear order of the ultrafast thermionic electron emission which cannot be detected without PEEM. For this reason a distinction between occasional scattering at the nanotextured leading to guided modes propagating in the absorber layer and the localization of light in open photonic resonators was not possible prior to the experiments discussed here.

This thesis discusses the experimental application of 2D nanoscopy on strongly dephasing systems. Nevertheless, 2D nanoscopy investigations of quantum systems with elongated lifetimes such as quantum dots, J-aggregates and the chemical compound Alq3 are currently performed. With these experiments the application of 2D nanoscopy is extended to the measurement of transition dynamics in quantum systems. In a 2D nanoscopy experiment investigating monolayers of Alq3 on cobalt preliminary results indicate that the detected electron yield originates from excited electronic states in Alq3 and exhibits spectroscopic signatures connected to coherent electronic transitions with sharp resonance lineshape.

Even though 2D nanoscopy was proven to simultaneously achieve the spatial and spectral resolved detection of localized optical fields, further improvements of the setup and the development of refined experimental schemes will be able to enhance the performance of this novel spectroscopy technique. For example, 2D nanoscopy would benefit from the implementation of a laser system providing few-cycle pulses and thereby approaching the impulsive limit and broadening the excitation spectrum. In combination with an adapted pulse shaper setup this would allow to vastly broaden the accessible spectral bandwidth and to suppress the influence of the excitation spectrum on the resulting 2D nanospectra. The implementation of a vector field synthesizer [14, 120] for simultaneous shaping of the polarization state, the total phase and the field amplitude would add even more degrees of freedom that could be accessed with 2D nanoscopy. For example, this would allow to probe the tensor character of the local near-field response. Finally, the application of ultrafast coherent control for tailoring the pump and probe near-field distributions generated by the individual laser pulses of the 2D nanoscopy excitation sequences would combine all aspects of ultrafast space- and time-resolved spectroscopy discussed in this thesis. Since the optical near-fields are confined to small spatial regions and the detection is space- and time-resolved,

this method is particularly suited to investigate electronic or plasmonic transfer processes. The application of an appropriate phase cycling scheme, furthermore, guarantees that the photoemission background signals generated only by the local fields at one position are suppressed because they do not interact with all pulses of the excitation sequence.

The publication of 2D nanoscopy has produced large interest and encouraged efforts to reproduce the adaptation of coherent 2D spectroscopy also in other nanooptical techniques, especially SNOM [408]. Detecting optical radiation emitted from nanoscaled systems, this approach is closer related to conventional optical 2D spectroscopy. However, a simultaneous acquisition of spectroscopic data from different sample positions is, in contrast to 2D nanoscopy using TR-PEEM, not possible.

In summary, ultrafast coherent control and 2D nanoscopy provide an unprecedented potential to investigate and manipulate coherent light-matter-interactions on the nanoscale. Even though TR-PEEM is particularly suited to resolve the dynamics of plasmonic excitations, these techniques are not limited to artificially nanostructured plasmonic devices but also achieve outstanding results in the examination of more complex nanophotonic materials such as corrugated silver surfaces and non-metallic systems like thin-film solar cells and will ultimately lead to the spatial-resolved spectroscopy of dynamics in single quantum systems.

A. Laser Pulse Characterization

In Chapter 1.1 it was demonstrated that the temporal properties of femtosecond laser pulses are dependent from the spectral amplitude and phase of two perpendicular polarization components. Whereas the spectral amplitudes are accessible directly via optical spectrometer, the determination of the spectral phase does require special measurement and evaluation techniques. A very good overview over recent pulse characterization methods can be found in [409]. Here, two experimental techniques are discussed. Frequency-resolved optical gating (FROG) experiments (Section A.1.1) involve spectrally resolved nonlinear correlation measurements that allow for a complete reconstruction of amplitude and phase [258–261]. Spectral interferometry with a known reference pulse (Section A.1.2) is a linear detection method [262–264] that enables a complete characterization without iterative evaluation of the data.

In Section A.2 the Jones-matrix formalism is introduced [127], which enables an elegant description of the influence of all components within an optical setup on the polarization state. The Jones matrix states the linear transfer function of the polarization pulse shaper for each frequency and polarization component and is utilized to calculate the pulse shapes for arbitrary LCD voltage settings. A third possibility (Section A.3) to characterize the output of the laser pulse shaper is to determine the Jones matrix by a particular series of FROG and SI measurements. This method is not a direct pulse characterization technique but it enables to predict the generated pulse shapes without the necessity of further measurements once the Jones-matrix is known and as long as the setup is not changed.

A.1. Experimental Pulse Characterization

A.1.1. Second-Harmonic FROG

Frequency-Resolved Optical Gating (FROG) techniques have become an important pulse characterization tool enabling the full reconstruction of the spectral amplitude and phase [258, 410, 411]. The main idea is to combine a nonlinear autocorrelation with spectrally resolved detection. FROG

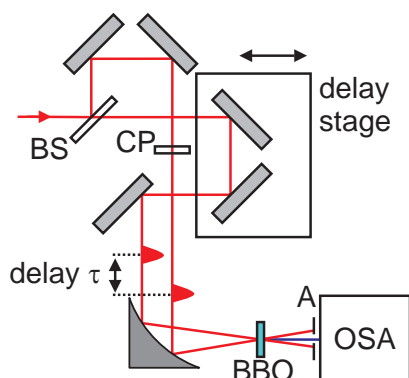


Figure A.1: Second-Harmonic Frequency-Resolved Optical Gating (FROG). The laser pulse is split into two duplicates at a beam splitter (BS). In the reflected arm of the Mach-Zehnder interferometer a chiral compensation plate (CP) balances the dispersion of both beams. The beams are focused by a curved mirror to the same spot in the BBO-crystal (BBO). The SHG signal originating from the superposing electric fields is selected with an aperture (A) on the optical axis and detected with a spectrometer (OSA).

yields a two-dimensional set of data that is proportional to the delay and frequency dependent intensity of a signal field which is created in a nonlinear process involving duplicates of the investigated laser pulse. In general the FROG signal can be written as

$$I_{\text{FROG}}(\tau, \omega) = |E_{\text{sig}}(\tau, \omega)|^2 = |\mathcal{F}\{E_{\text{sig}}(\tau, t)\}|^2 = \left| \int_{-\infty}^{\infty} E_{\text{sig}}(\tau, t) e^{-i\omega t} dt \right|^2. \quad (\text{A.1})$$

A direct reconstruction of the input pulse $E^+(t)$ is not possible, but an iterative FROG algorithm based on the method of generalized projections [412, 413] enables the reconstruction of the spectral intensity and spectral phase except for the absolute phase. Typically, these algorithms are very robust and lead reliably to very similar results. Since no other pulses or additional information are needed, FROG is a self-referencing characterization technique. By now many type of FROG techniques have been developed, giving access to a broad variety of applications [260, 261].

In the following Second-Harmonic FROG (SHG FROG) will be introduced as pulse characterization tool because it was applied in the experiments discussed in this thesis. For the evaluations the FROG 3.2 algorithm from *Femtsoft* was used. In SHG FROG the involved nonlinear process is Second-Harmonic Generation (SHG) by three-wave mixing [259, 414]. A schematic of the setup is presented in Fig. A.1. In a Mach-Zehnder interferometer the input laser pulse is divided into two identical pulses. The optical path difference between both interferometer arms can be adjusted with a mechanical delay stage. The beams are parallel to each other reaching a focusing mirror. Consequently, they are focused to the same focal spot into the BBO-crystal but are coming from different angles. A focusing mirror is advantageous compared to a lens because of the lower introduced dispersion. The SHG signal conserves the momentum of the incoming laser pulses. Additional to the SHG radiation that is emitted along the direction of the fundamental beams, a third beam with doubled carrier frequency $2\omega_0$ appears in the temporal overlap of both pulses. This additional SHG signal is created by the superposing electric fields of both beams. Momentum conservation leads to a momentum vector of the SHG signal which points between the fundamental beams according to

$$\mathbf{k}_{\text{SHG}} = \mathbf{k}_1 + \mathbf{k}_2, \quad (\text{A.2})$$

where \mathbf{k}_1 and \mathbf{k}_2 denote the momentum vectors of the fundamental beams. FROG needs a spectrally resolved detection of the nonlinear signal, therefore, an optical spectrometer records the SHG signal for every delay step yielding $I_{\text{FROG}}(\tau, \omega)$. This is the fundamental difference to an intensity autocorrelator [415, 416], which only detects the integrated intensity $I_{\text{AC}}(\tau)$ as a function of delay.

The SHG FROG technique involves a delay-dependent measurement of the spectral intensity of the frequency doubled beam. Thus, the following relation holds:

$$I_{\text{FROG}}(\tau, \omega) \propto \left| \int_{-\infty}^{\infty} E_1^+(t) E_2^+(t, \tau) e^{-i\omega t} dt \right|^2 = \left| \int_{-\infty}^{\infty} E^+(t) E^+(t - \tau) e^{-i\omega t} dt \right|^2, \quad (\text{A.3})$$

where $E_1^+(t)$ and $E_2^+(t, \tau)$ are the electric fields of the lasers pulse duplicates. Since the two

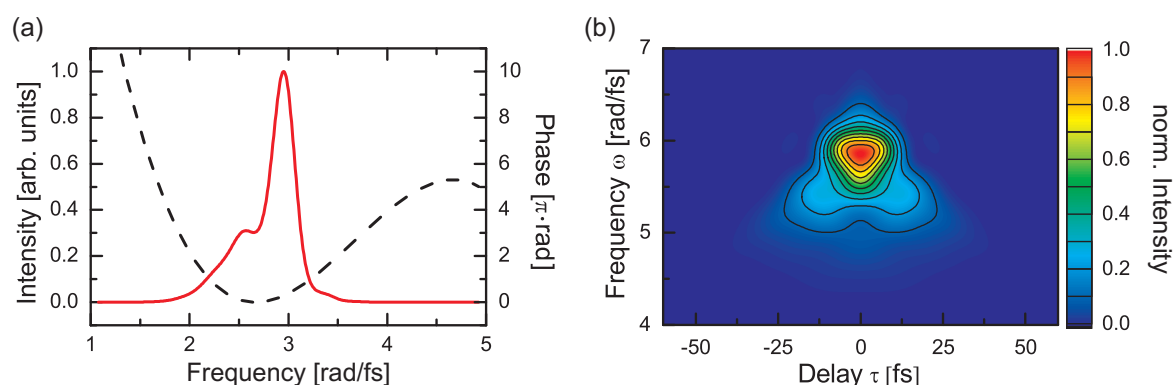


Figure A.2.: Simulation of SHG FROG trace. (a) Input electric field in spectral domain. The modulation of the spectral intensities are created by adding a Gaussian and a sinc^2 intensity profile. The center frequency of the distribution is $\omega_0 = 2.8$ rad/fs. The spectral phase contains quadratic ($25 \text{ fs}^2/\text{rad}^2$) and cubic modulations ($-25 \text{ fs}^3/\text{rad}^3$). (b) Simulated SHG FROG trace $I_{\text{FROG}}(\tau, \omega)$ of the input electric field. The SHG FROG delivers data that is symmetric concerning the delay τ . The signal is detected around twice the fundamental frequency because of the underlying nonlinear process. In the SHG FROG trace it is obvious that the lower frequency components are generated in particular for non-zero delays.

pulses are identical ($E_1^+(t) = E_2^+(t, 0)$), the SHG FROG trace is symmetric concerning the delay

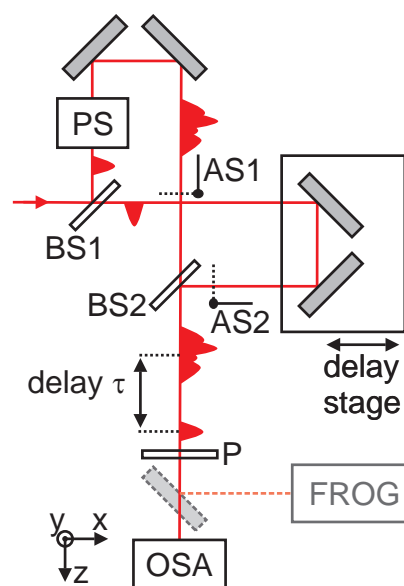
$$I_{\text{FROG}}(\tau, \omega) = I_{\text{FROG}}(-\tau, \omega). \quad (\text{A.4})$$

As a result, two solutions with opposite sign of the phase give equivalent results. A second SHG FROG measurement including a known amount of additional dispersion in the optical path can falsify one of the solutions. Typically, a glass plate with precisely measured dispersion and thickness is inserted as a dispersive element.

A simulated SHG FROG trace is shown in Fig. A.2. The spectral electric field of the laser pulse is modulated as a result of adding a Gaussian and a sinc^2 distribution. The applied phase modulations are ($25 \text{ fs}^2/\text{rad}^2$ and $-25 \text{ fs}^3/\text{rad}^3$). The simulated SHG FROG trace exhibits the enforced delay-symmetry and is located at the doubled fundamental frequency. In the FROG trace the influence of GDD and TOD are visible by a characteristic broadening and bending of the observed feature. For an unambiguous retrieval of the pulse shape, however, a FROG algorithm has to be employed.

The SHG FROG as it is presented above can characterize linearly polarized laser pulses but is not sufficient for polarization-shaped laser pulses. A related technique called tomographic ultrafast retrieval of transverse light E-fields (TURTLE) [417, 418] would allow a reconstruction of nontrivial polarization-shaped laser pulses. However, it involves at least three SHG FROG measurements. Two are necessary for determining the electric fields of the independent polarization components. A third FROG trace is needed for obtaining the relative time delay and relative phase difference. Moreover, FROG suffers from ambiguities in the determination of relative phase differences from temporally isolated subpulses [419]. For 2D Nanoscopy (Sections 4–6) pulse sequences with separated pulses and varying relative phases are essential. Due to these restrictions the SHG FROG is not used for the direct characterization of the polarization pulse shaper output but to characterize the reference pulse for dual-channel spectral interferometry, which is introduced in the next section.

Figure A.3: Spectral interferometry setup for the characterization of polarization shaped laser pulses. The polarization pulse shaper (PS) is located in one arm of the interferometer. The beam splitter (BS1 and BS2) have balanced optical properties. Both interferometer arms can be blocked individually by automatic shutters (AS1 and AS2). The delay stage in the reference arm creates a temporal delay τ between the polarization shaped pulse and the reference pulse. In front of the optical spectrometer (OSA) a polarizer (P) selects the investigated polarization component. A movable mirror permits the characterization of the reference pulse by means of FROG.



A.1.2. Dual-Channel Spectral Interferometry

Spectral interferometry (SI) was first introduced by Froehly [262] in 1973. Several applications have been developed [263, 420]. For a full characterization of the investigated laser pulse a known reference pulse is necessary. TADPOLE [421], a combination of SI with FROG, determines the spectral information of the test pulse by interference with a previously self-referenced laser pulse. The extension of this measurements scheme to polarization-shaped laser pulses is given by POLLIWOG (POLarized Light Interference versus Wavelength of Only a Glint) [422], which employs dual-channel spectral interferometry for a phase retrieval of both polarization components. Spectral interferometry offers a high sensitivity and can investigate signals which are much weaker than necessary for nonlinear characterization techniques such as FROG and SPIDER [421]. SPIDER (spectral phase interferometry for direct electric-field reconstruction) [384–387] is a self-referencing spectral interferometry technique that evaluates the interferogram of two pulse duplicates with fixed delay τ and a spectral shear Ω which is imposed by sum frequency generation with a highly dispersed third copy of the pulse. SPIDER is able to characterize extremely short laser pulses with high precision and consistency [409, 423, 424]. However, here lies a limitation of SPIDER which is not able to detect strong phase modulations that lead to complex-shaped laser pulses with pulse length up to the picosecond regime.

The most important components of the implemented SI setup are presented in Fig. A.3. Basically, the SI setup consists of an optical interferometer with two different arms. The polarization pulse shaper (PS) has to be placed inside one arm of the interferometer to characterize the shaped laser pulses. SI measures the difference in the phases and amplitudes which the two replica of the incident laser pulse acquired during their propagation. Thus, only the optical components between both beam splitters (BS1 and BS2) are responsible for the observed interference signal. The optical path length of the reference pulse can be adjusted with a delay stage to create a temporal delay τ of the shaped laser pulse. A polarizer (P) selects the polarization component that is investigated by the optical spectrometer (OSA). To characterize the complete information of the polarization-shaped laser pulse with a single interferometry measurement, it would be necessary

to detect the interference of both polarization components simultaneously, either by using two spectrometer with single-line detector array or by using one spectrometer with two-dimensional detector. In the experiments discussed in this thesis a single-line spectrometer is employed and the polarization components rotated by 45° and -45° with respect to the horizontally polarized reference pulse are measured consecutively. This procedure is valid because the interferometric stability of the setup is sufficiently high. Furthermore, the interference between both pulses is insensitive to changes of the optical path which is outside the beam splitters (BS1 and BS2), e.g., a rotation of the polarizer. Automatic shutters (AS1 and AS2) are implemented for a fast blocking of the individual beams without the need to remove the covering of the pulse shaper and to manually manipulate the beams introducing disturbances of the interferometric setup. A movable mirror enables to pick the beam before it is coupled into the spectrometer and to measure the reference pulse with the SHG FROG setup discussed in Section A.1.1.

The spectral interference signal of one polarization component measured by the spectrometer (OSA) can be written as

$$I_{SI}(\omega) = |E_{ref}^+(\omega) + E^+(\omega)e^{-i\omega\tau}|^2 = I_{ref}(\omega) + I(\omega) + S(\omega), \quad (\text{A.5})$$

where $E_{ref}^+(\omega)$, $E^+(\omega)$, $I_{ref}(\omega)$ and $I(\omega)$ are the electric fields and intensities of the reference pulse and the polarization shaped pulse, respectively. The additional phase term $e^{-i\omega\tau}$ is caused by the temporal shift of the shaped pulse compared to the reference pulse. $I_{ref}(\omega)$ and $I(\omega)$ can be obtained separately and subtracted from $I_{SI}(\omega)$ to yield the interference term $S(\omega)$, which constitutes as follows

$$S(\omega) = [E_{ref}^+(\omega)]^* E^+(\omega)e^{-i\omega\tau} + E_{ref}^+(\omega)[E^+(\omega)]^* e^{i\omega\tau} \quad (\text{A.6})$$

$$= \sqrt{I_{ref}(\omega)I(\omega)} \cos(\phi_{ref} - \phi - \omega\tau). \quad (\text{A.7})$$

Having determined $\phi_{ref}(\omega)$ by SHG FROG, the only unknown quantity in this equation is the phase of the shaped laser pulse $\phi(\omega)$. In principle a calculation of $\phi(\omega)$ by applying the arccosine function to Eq. (A.7) is possible but can create large phase errors for several reasons [263]. First, the arccosine might create phase jumps because $\cos(\Phi) = \cos(\Phi + 2\pi) = \cos(-\Phi)$. Second, by dividing the interference $S(\omega)$ by the square root of the individual intensities noise can be introduced. Third, when the derivative of the arccosine function around 1 and -1 is huge amplifying small variations in the detected signals to high noise in the phase [263]. A more reliable method involves a filtering of the data by inversely Fourier transforming Eq. (A.6) [263, 264, 425]. The temporal representation of the spectral interference signal $S(t)$ can then be written as

$$S(t) = \frac{1}{\sqrt{2\pi}} \int_{-\infty}^{\infty} [E_{ref}^+(\omega)]^* E^+(\omega) e^{i\omega(t-\tau)} d\omega \quad (\text{A.8})$$

$$+ \frac{1}{\sqrt{2\pi}} \left[\int_{-\infty}^{\infty} [E_{ref}^+(\omega)]^* E^+(\omega) e^{i\omega(-t-\tau)} d\omega \right]^* \quad (\text{A.9})$$

$$= \tilde{S}(t - \tau) + \tilde{S}^*(-t - \tau), \quad (\text{A.10})$$

with

$$\tilde{S}(t) = \frac{1}{\sqrt{2\pi}} \int_{-\infty}^{\infty} [E_{ref}^+(\omega)]^* E^+(\omega) e^{i\omega t} d\omega \quad (\text{A.11})$$

$S(\omega)$ is measured as a real-valued positive quantity. Hence, after the Fourier transformation the resulting signal $S(t)$ is Hermitian and the complete information on the spectral interferometry signal $S(\omega)$ is already included in $S^+(t)$, which contains non-zero values only for positive times t . If the delay τ is sufficiently large, $\tilde{S}(t - \tau)$ and $\tilde{S}^*(-t - \tau)$ are clearly separated and have no contributions around $t = 0$ [263] and $S^+(t)$ is identified as

$$S^+(t) = \tilde{S}(t - \tau) . \quad (\text{A.12})$$

As a result, the complex-valued SI signal restricted to positive frequencies is given by

$$S^+(\omega) = \frac{1}{\sqrt{2\pi}} \int_{-\infty}^{\infty} \tilde{S}(t - \tau) e^{i\omega t} dt \quad (\text{A.13})$$

$$= [E_{ref}^+(\omega)]^* E^+(\omega) e^{-i\omega\tau} \quad (\text{A.14})$$

$$= \sqrt{I_{ref}(\omega) I(\omega)} e^{i(\phi_{ref} - \phi - \omega\tau)} . \quad (\text{A.15})$$

Consequently, the Fourier transformation approach yields instead of Eq. (A.7) a complex function which can be evaluated more reliably. The argument of Eq. (A.15) delivers the following relation

$$\varphi(\omega) + \omega\tau = \varphi_0 - \arg(S^+(t)) . \quad (\text{A.16})$$

To determine the phase modulation of the shaped laser pulse φ the linear phase term $\omega\tau$ has to be removed. If the absolute temporal position with respect to the reference pulse is relevant for further experiments, the delay τ has to be obtained from an individual measurement. If the absolute time scale is not important, a linear fit can remove the complete linear contribution in $\varphi(\omega) + \omega\tau$, eventually canceling out the linear term in $\varphi(\omega)$.

For the investigated polarization component the electric field $E^+(\omega) = \sqrt{I(\omega)} e^{-i\varphi(\omega)}$ can be calculated combining the results of the spectral interference with the measured spectral intensity $I(\omega)$. SI measurements have to be performed for both polarizations directions under interferometric stable conditions to characterize polarization shaped laser pulses because the absolute timing between both components influences the phase difference $\Phi(t) = \varphi_2(t) - \varphi_1(t)$. Already small deviations of the delay are, therefore, associated with severe changes of the polarization state. Furthermore, the delay τ which has to be removed in the evaluation of the individual electric fields has to be set identical for both measurements to chose the same absolute temporal position for zero delay. The coherent superposition of the polarization components finally yields the electric field of the polarization shaped laser pulse in complex representation

$$\mathbf{E}^+(\omega) = \begin{pmatrix} E_1^+(\omega) \\ E_2^+(\omega) \end{pmatrix} = \begin{pmatrix} \sqrt{I_1(\omega)} e^{-i\varphi_1(\omega)} \\ \sqrt{I_2(\omega)} e^{-i\varphi_2(\omega)} \end{pmatrix} . \quad (\text{A.17})$$

In the experimental realization of the spectral interference it has to be considered that a too low value of τ might cause a non-vanishing contributions of $\tilde{S}(t - \tau)$ and $\tilde{S}^*(-t - \tau)$ at time zero,

leading to insufficient separation of both signals. Nevertheless limits the finite spectral resolution of the spectrometer the minimal fringe spacing, which narrows for increasing τ . For the pulse characterization in the experiments the delay was adjusted to a value of $\tau \approx 2.5$ ps to meet both conditions.

In the implementation of spectral interferometry it has to be considered that the optical spectrometer measures the spectral intensity as function of the wavelength λ . Accordingly, a Jacobi transformation would be needed to project the experimental data into frequency space. In order to avoid uncertainties introduced by this procedure the interference signal can also be filtered in the reciprocal wavelength-space [426].

A.2. Jones-Matrix Formalism

The Jones-matrix $J(\omega)$ is a complex 2×2 -matrix [44, 127]. For each frequency component the Jones-Matrix states the effect of a linear optical element, e.g., mirrors, polarizers, and dielectrics, onto the polarization state by the following relation:

$$\mathbf{E}_{out}^+(\omega) = J(\omega)\mathbf{E}_{in}^+(\omega), \quad (\text{A.18})$$

where $\mathbf{E}_{in}^+(\omega)$ and $\mathbf{E}_{out}^+(\omega)$ are the ingoing and outgoing electric fields, respectively. In explicit notation this equation can be written as:

$$\begin{pmatrix} E_{1,out}^+(\omega) \\ E_{2,out}^+(\omega) \end{pmatrix} = \begin{pmatrix} J_{11}(\omega) & J_{21}(\omega) \\ J_{12}(\omega) & J_{22}(\omega) \end{pmatrix} \begin{pmatrix} E_{1,in}^+(\omega) \\ E_{2,in}^+(\omega) \end{pmatrix}. \quad (\text{A.19})$$

When the coordinate systems of the electric field and the Jones-matrix are not identical, coordinate transformations are allowed. The total Jones-Matrix of an optical setup can be calculated from the Jones-Matrices of its n components via multiplication.

$$J(\omega) = J^{(n)}(\omega)J^{(n-1)}(\omega) \dots J^{(2)}(\omega)J^{(1)}(\omega) \quad (\text{A.20})$$

The matrix multiplication is noncommutative. Thus, the ordering of the multiplication has to follow the optical path starting with the Jones-matrix of the first element on the right side. This can be demonstrated in a gedankenexperiment with monochromatic, horizontally polarized light, a polarizer in vertical direction of transmission and a half wave plate at arbitrary angle θ is considered. The coordinate system is chosen with axes in horizontal and vertical direction so that the ingoing horizontally polarized electric field can be written as:

$$\mathbf{E}_{in} = \begin{pmatrix} E_0 \\ 0 \end{pmatrix}. \quad (\text{A.21})$$

The polarizer fully transmits light in vertical polarization direction and completely blocks light in horizontal polarization direction. Thus, the Jones-matrix is given by:

$$J^{(pol)} = \begin{pmatrix} 0 & 0 \\ 0 & 1 \end{pmatrix} \quad (\text{A.22})$$

For calculating the Jones-matrix of the half wave plate the coordinate system of the incoming electric field has to be rotated by the angle θ from horizontal and vertical orientation onto that of

the half wave plate before multiplication and afterwards it has to be rotated back to the original orientation. This is achieved via the rotation matrices:

$$R(\theta) = \begin{pmatrix} \cos \theta & -\sin \theta \\ \sin \theta & \cos \theta \end{pmatrix} \quad \text{and} \quad R^{-1}(\theta) = R(-\theta) = \begin{pmatrix} \cos \theta & \sin \theta \\ -\sin \theta & \cos \theta \end{pmatrix} \quad (\text{A.23})$$

Since the half wave plate shifts the phase of the field component on the slow axis by π the diagonal coefficients have negative signs: $J_{11}^{(\lambda/2)} = -J_{22}^{(\lambda/2)}$.

$$J^{(\lambda/2)}(\theta) = \begin{pmatrix} \cos \theta & -\sin \theta \\ \sin \theta & \cos \theta \end{pmatrix} \begin{pmatrix} 1 & 0 \\ 0 & -1 \end{pmatrix} \begin{pmatrix} \cos \theta & \sin \theta \\ -\sin \theta & \cos \theta \end{pmatrix} \quad (\text{A.24})$$

$$= \begin{pmatrix} \cos 2\theta & \sin 2\theta \\ \sin 2\theta & \cos 2\theta \end{pmatrix} \quad (\text{A.25})$$

In the configuration with half wave plate as first optical element the outgoing field is vertically polarized:

$$\mathbf{E}_{out} = J^{(pol)} J^{(\lambda/2)}(\theta) \mathbf{E}_{in} = \begin{pmatrix} 0 \\ E_0 \sin 2\theta \end{pmatrix}. \quad (\text{A.26})$$

If the polarizer is hit first, there is complete extinction of the beam and no transmission at all

$$\mathbf{E}_{out} = J^{(\lambda/2)} J^{(pol)}(\theta) \mathbf{E}_{in} = \begin{pmatrix} 0 \\ 0 \end{pmatrix} \quad (\text{A.27})$$

The Jones-matrix formalism can be extended to arbitrarily complex system which consists of linear optical components. An example which is important in the context of this thesis is the femtosecond polarization pulse shaper setup and its surrounding optical components. Hence, the Jones-matrix formalism can be utilized to predict the generated pulse shapes for arbitrary settings of the pulse shaper. The determination of the Jones-matrix for the polarization pulse shaper and its application as pulse characterization method is presented in Section A.3.

A.3. Jones-Matrix as Pulse Characterization Tool

The Jones-Matrix $J^{(setup)}$, which describes the influence of the polarization pulse shaper setup on the polarization state of the laser beam, is determined experimentally with a combination of FROG and SI measurements [109, 110]. The Jones-matrix can be separated into three parts. The first matrix $J^{(1)}$ includes the transfer function of all optical elements in front of the liquid crystal display (LCD) of the polarization pulse shaper starting with the beam splitter BS1. The contribution of the LCD is represented in an own Jones-Matrix $J^{(LCD)}$ and afterwards all optical elements in between the display and the experiment are incorporated into $J^{(2)}$.

$$J^{(setup)} = J^{(2)} J^{(LCD)} J^{(1)} \quad (\text{A.28})$$

The LCD is the only element of the setup which is supposed to change during the experiment. The voltages that are applied to the pixels of the LCD determine the phase shift for the individual frequency components. Furthermore, both polarization states can be addressed separately. In

the basis oriented along the LCD layers ($\mathbf{e}_1, \mathbf{e}_2$), the Jones matrix $J^{(LCD)}$ does not contain the rotation matrices (see Eq. (1.34)):

$$J^{(LCD)} = \begin{pmatrix} e^{-i\Delta\varphi_1} & 0 \\ 0 & e^{-i\Delta\varphi_2} \end{pmatrix} \quad (\text{A.29})$$

By partially carrying out the multiplication with the ingoing field \mathbf{E}_{in}^+ , the following relation for the electric field \mathbf{E}_{exp}^+ used in the experiment is found:

$$\mathbf{E}_{exp}^+ = J^{(2)} J^{(LCD)} J^{(1)} \mathbf{E}_{in}^+ \quad (\text{A.30})$$

$$= J^{(2)} J^{(LCD)} \begin{pmatrix} E_{1,in}^+ J_{11} + E_{2,in}^+ J_{12} \\ E_{1,in}^+ J_{21} + E_{2,in}^+ J_{22} \end{pmatrix} \quad (\text{A.31})$$

$$= J^{(2)} \begin{pmatrix} e^{-i\Delta\varphi_1} (E_{1,in}^+ J_{11} + E_{2,in}^+ J_{12}) \\ e^{-i\Delta\varphi_2} (E_{1,in}^+ J_{21} + E_{2,in}^+ J_{22}) \end{pmatrix} \quad (\text{A.32})$$

$$= J^{(2)} \begin{pmatrix} E_{1,in}^+ J_{11} + E_{2,in}^+ J_{12} & 0 \\ 0 & E_{1,in}^+ J_{21} + E_{2,in}^+ J_{22} \end{pmatrix} \begin{pmatrix} e^{-i\Delta\varphi_1} \\ e^{-i\Delta\varphi_2} \end{pmatrix} \quad (\text{A.33})$$

$$= \begin{pmatrix} K_{11} & K_{12} \\ K_{21} & K_{22} \end{pmatrix} \begin{pmatrix} e^{-i\Delta\varphi_1} \\ e^{-i\Delta\varphi_2} \end{pmatrix} = \begin{pmatrix} K_{11}e^{-i\Delta\varphi_1} + K_{12}e^{-i\Delta\varphi_2} \\ K_{21}e^{-i\Delta\varphi_1} + K_{22}e^{-i\Delta\varphi_2} \end{pmatrix}. \quad (\text{A.34})$$

Consequently, the matrix K combines information from the setup surrounding the LCD in the polarization pulse shaper as well as from the incoming electric field. These elements are considered to be passive, i.e. not changing during the experiment. As long as this assumption is valid, K is constant and the pulse shape only depends on the two-dimensional vector containing the phase settings from the LCD. Then, the electric field at the experiment \mathbf{E}_{exp}^+ can easily be calculated by multiplying K with the LCD phase vector.

The determination of K requires an experiment that allows extracting all four complex coefficients K_{11} , K_{12} , K_{21} , and K_{22} in dependence from the frequency from the set of linear equations defined by Eq. (A.34) [109, 110]. This can only be achieved in a series of POLLIWOG measurements in which the phase settings are varied. Two measurements are sufficient, but by sampling over a higher number of tested input pulse shapes the influence of experimental errors can be reduced. The Jones-matrix of each frequency is obtained in an individual least square fit. However, while the POLLIWOG measurements are performed, the interferometric stability of the setup has to be maintained, limiting the number of pulse shapes in the test sample. For the experiments in this thesis eight pulse shapes were used. The first polarization component was fixed to a constant phase $\varphi_1 = 0$, whereas the phase of the second layer was set to the values $\varphi_2 = \{-\frac{3}{2}\pi, -\pi, -\frac{1}{2}\pi, 0, \frac{1}{2}\pi, \pi, \frac{3}{2}\pi, 2\pi\}$. The polarization states which correspond to the respective phase difference $\delta = \varphi_2 - \varphi_1$ are linear in vertical and horizontal direction as well as circular polarized for both senses of rotation. In the optimal case the Jones-matrix is proportional to the identity matrix and these polarization states are obtained after the pulse shaper. Deviations from the pulse shape are caused by intensity transfer from one polarization component to the other via the non-diagonal matrix elements or by unbalanced diagonal elements. If $K_{11} \neq K_{22}$, the transmission of one component is lower or the phase difference δ is changed by different acquired phases.

B. Drift Correction of PEEM Data

Even in a very stable photoemission electron microscope the sample performs small movements with respect to the lens system. Motion on time-scales of the exposure time or faster lead to a blur of the individual image. These movements have to be suppressed already by shielding the PEEM setup against mechanical oscillations. Slow drifts of the sample are caused e.g. by thermal effects such as temperature variations in the laboratory and also by energy transfer to the sample by the light source. These long-term changes in the sample position would still permit the collection of unaffected single photoemission images, but in a series of images the sample slowly drifts in the field of view with typical velocities in the order of one nanometer per minute. An experimental technique comparing the local photoemission yield at a certain spatial position in a series of images has to compensate for this gradual shift of the sample by a drift correction theme. This is the case for coherent control experiments, in which by adaptive optimization the photoemission yield in predefined regions of interest is optimized (Chapter 3, 2 and 5), as well as for time-resolved and spectroscopic measurements (Chapter 3, 5.3 and 6). For example 2D nanoscopy measurements require several ten thousands of PEEM images. This leads to experiment durations of about twelve hours. In this time interval a considerable drift might accumulate. In case of the measurements including predefined variations of parameters the drift correction takes place at an arbitrary time after the measurement before further data processing routines are applied. During adaptive coherent control experiments a fast and robust drift correction is necessary to evaluate the measurement images immediately and create appropriate feedback for the optimization algorithm. In the following, the basic properties of the implemented drift correction mechanisms are discussed. However, during the different experiments presented in this thesis the drift detection and correction algorithms were improved and adapted to the particular task.

The basic idea of the drift correction is presented in Fig. B.1. During the data acquisition process reference PEEM images R_j are recorded in addition to the measurement images M_j of

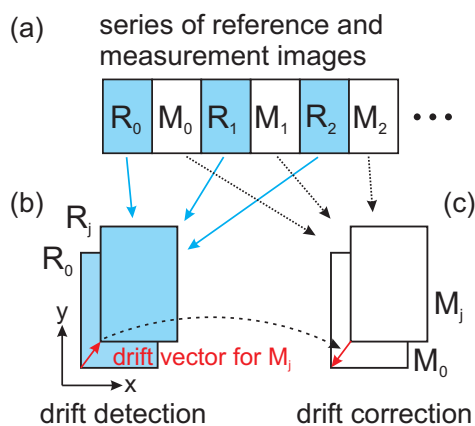


Figure B.1: Scheme for drift detection and correction of PEEM data. (a) Alternately reference images R_j and measurement images M_j are recorded during the experiment. (b) The drift between reference images R_j is evaluated using two-dimensional cross correlation. (c) The obtained drift vector is employed for correcting the repositioning of the measurement images M_j .

the actual experiment (see Fig. B.1a). These reference images R_j have to be taken regularly during the complete measurement or adaptive optimization procedures. Furthermore, they have to be obtained with identical settings of the polarization pulse shaper and other devices of the setup. Otherwise, lateral changes in the photoemission yield which are caused by different pulse shapes might lead to a falsely detected shift of the sample. The drift detection is based on two-dimensional cross-correlation of the reference images (see Fig. B.1b). The resulting drift vector is then used to correct the measurement images M_j (see Fig. B.1c). In order to reduce the total duration of an experiment it is possible to take several measurement images at each position j and correct the according to reference image R_j . This would partially save the acquisition time for the reference images. However, this method is only valid for the assumption that the drift is progressing slowly and evenly in the interval between two successive reference images. Since the photoemission distributions of all R_j are within the experimental restrictions identical except for the spatial drift, the maximum of the cross-correlation

$$XC_j(m, n) = \sum_{x=0}^M \sum_{y=0}^N R_0^*(x, y) R_j(x + m, y + n) = R_0(x, y) \otimes R_j(x, y) \quad (\text{B.1})$$

indicates the drift vector \mathbf{D}_j . In Eq.(B.1) $XC_j(m, n)$ denotes the discrete cross-correlation signal of the first reference image R_0 and the j -th image R_j with $M \times N$ pixels per image. The photoemission yield is a real quantity and, therefore, $R_0^* = R_0$ is fulfilled. Outside the limits of the PEEM image $R_j(x, y)$ is defined to be zero. By determining \mathbf{D}_j always with respect to the initial image R_0 a successive accumulation of deviations from the actual drift is avoided, which is possible in case of comparing consecutive images R_{j-1} and R_j and adding up the drift.

It is advantageous for computational reasons to perform the cross-correlation via the discrete fast Fourier transform (FFT) of the data. The cross-correlation satisfies analogously to the convolution theorem of the Fourier transform:

$$XC_j = \mathcal{F}^{-1} \{ \mathcal{F} \{ R_0 \otimes R_j \} \} = \mathcal{F}^{-1} \{ \mathcal{F} \{ R_0 \} \cdot \mathcal{F} \{ R_j \} \}, \quad (\text{B.2})$$

Since the PEEM images contain discrete data and the cross-correlation according to Eqs. (B.1) and (B.2) is also defined discretely, the pixel size limits the precision of the maximum of $XC_j(m, n)$ as a measure for the drift vector \mathbf{D}_j . However, the maximum of $XC_j(m, n)$ is located in a peak that is several pixels wide. Thus, it is possible to interpolate this area two-dimensionally and by reducing the pixel size to reduce the discretization noise.

In experimental applications it has to be considered that the maximum of the cross-correlation can appear at another position and does not indicate \mathbf{D}_j . One example is a photoemission hot spot with a strong total yield that drifts into the field of view during the experiment. Then, additional strong peaks in $XC_j(m, n)$ might occur and the detected drift vector jumps to the position of the new maximum. One mechanism to avoid such deceptive cross-correlation peaks is to implement masks that select only those parts of the images that deliver unambiguous data. Alternatively, the region in which $XC_j(m, n)$ is evaluated can be restricted to a size large enough to contain all drift vectors of the respective measurement because the false cross-correlation maxima usually appear clearly separated from the peak which is assigned to the best overlap of both images.

To characterize the drift detection scheme, it was tested with simulated data. A total of 100 Gaussian-shaped spots were distributed randomly in an image of 500×500 pixels. The sizes and shapes of the spots were also randomly varied. Fig. B.2a shows the initial image cropped to the

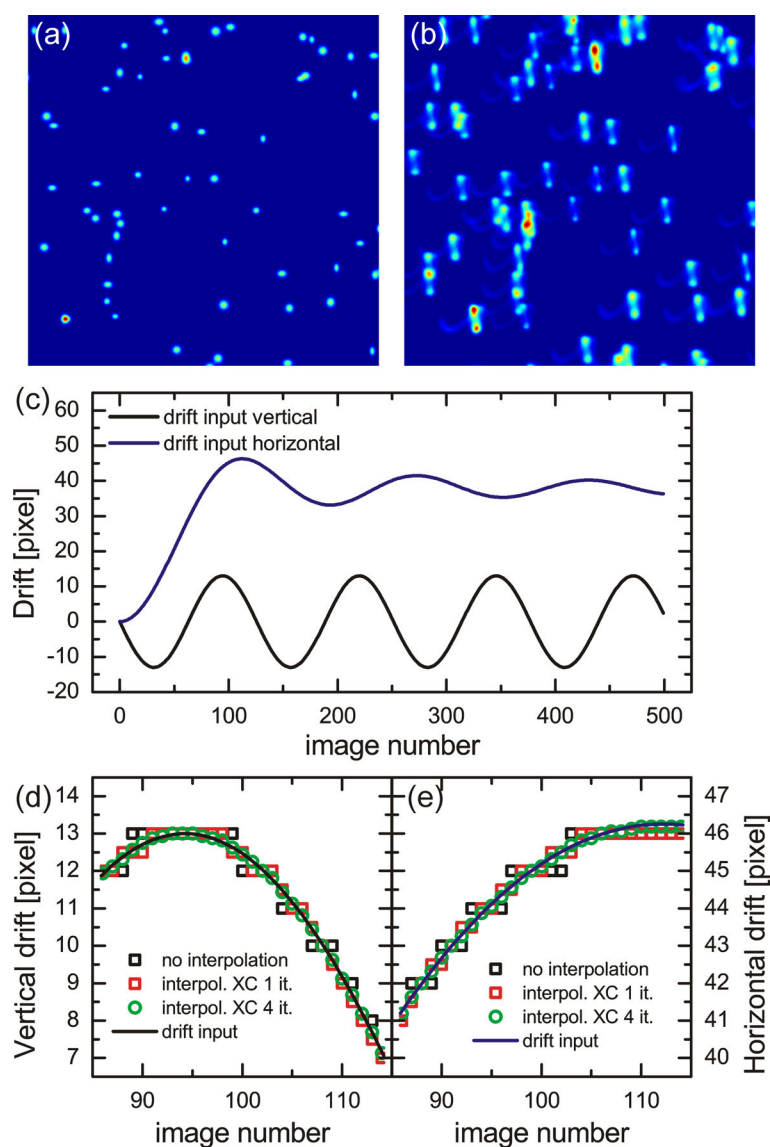


Figure B.2: Drift detection for simulated PEEM data. The position of a random distribution of Gaussian-shaped spots is shifted as a function of simulated time steps (image number). A cross-correlation algorithm based on discrete Fast Fourier transform detects the drift vector with respect to first image. (a) Initial image. (b) Sum over all images without drift correction applied. (c) Input drift vector components for simulation data. The vertical drift vector component is indicated as black line and the horizontal component as blue line. (d) Detail of vertical drift detected by drift detection algorithm for different iterations of bicubic interpolation. (e) Detail of horizontal drift detected by drift detection algorithm for different iterations of bicubic interpolation.

center 400×400 pixels. In a series of 500 images the position of the spot distribution was shifted according to predefined functions horizontally and vertically. The input drift vector components in horizontal and vertical direction are presented in Fig. B.2b. Whereas the vertical drift follows a sinusoidal function, the horizontal position shifts fast during the first 100 simulated time steps and settles at this location performing slowly decaying oscillations. The effect of the drift on the data is demonstrated in Fig. B.2c. Without drift correction the sum over all images is smeared out and all spots are replaced by a pattern that is determined by the input drift vector.

The results of the drift detection are presented in Fig. B.2d and e for details of the vertical and horizontal drift, respectively. In both cases the drift values obtained for non-interpolated and bicubic interpolated cross-correlations match the input values with different accuracies. Without interpolation the detected drift follows the input vector, but it is rounded to the next integer value. With single bicubic interpolation the pixel size is decreased by a factor $1/2$. The drift values are fitting the data more closely. Decreasing the pixel size further by iterative interpolation

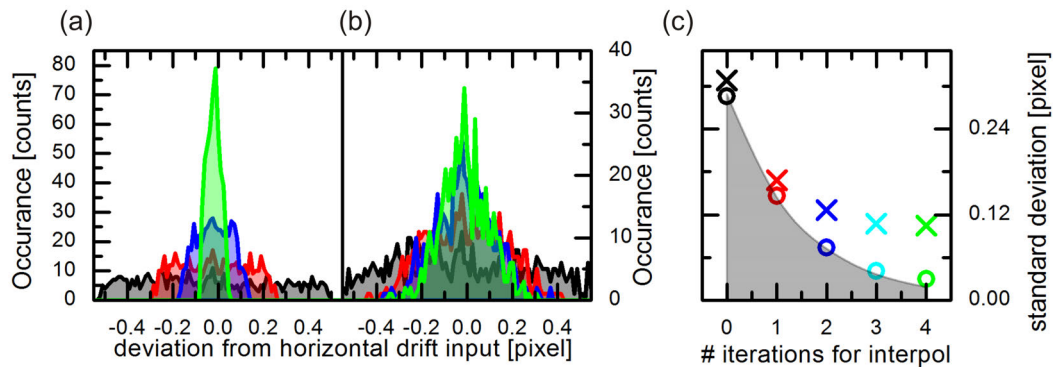


Figure B.3.: Statistical evaluation of drift detection. (a) Histogram of horizontal deviation from input drift vector for different iterations of interpolation. The coloring is identical to (c), i.e. one, two and four bicubic interpolations are indicated by red, blue and green color. (b) Histogram of horizontal deviation from input drift vector for test series data with noise. (c) standard deviation of the displacement histograms (crosses: with noise, circles: without noise) compared to discretization noise level (solid gray) as a function of iterations of interpolation

leads to a very good agreement between the detected \mathbf{D}_j and the input drift vector. For the example of four-fold interpolated data, the width and height of the pixel are reduced to $1/16$ of the initial value.

A statistical evaluation of the drift detection results emphasizes that discretization noise strongly affects the precision of the drift detection. Figure B.3 compares the deviation of the detected horizontal drift component with respect to the input drift. The histograms in Figure B.3a demonstrate that the error of the drift detection is, with an exception in the case of the four-fold interpolated data, almost homogeneously distributed over an interval that corresponds to the pixel size of the according order of interpolation. It is evident that a high interpolation increases the resolution of the drift detection scheme and in principle enables to measure shifts that are in the range of a hundredth of a pixel. The standard deviation of the four-fold interpolated drift data is 0.029 pixels. However, the shape of this distribution is not homogeneous over the interval indicating that the deviations from the input drift are not caused by discretization effects alone. The slight offset in all of the histograms of about -0.02 pixels is in each case within the standard deviation of the distribution.

The same spot distribution and input drift vectors were used to create a second test series. In this case noise was added by jittering the position of each spot with respect to each individual pixel. These displacements randomly varied for every image of the simulated series. In Figure B.3b the histograms show the distribution of the detected drift error for the same iterations of bicubic interpolation as for the noise free data (see Fig. B.3a). Here, the histograms converge faster towards a comparatively broad peak-shaped distribution with a standard deviation of 0.107 pixels. Hence, the implemented noise leads to a position uncertainty in the drift detection that dominates the effects of discretization for at least twice interpolated data.

The standard deviations of the histograms are displayed in Fig. B.3c. They are compared to the standard deviation which is expected for equally distributed random numbers on an interval according to the pixel size of the interpolated data. The noise free data follows closely the theoretical curve. Only the last value is slightly above the limit of the discretization noise. The

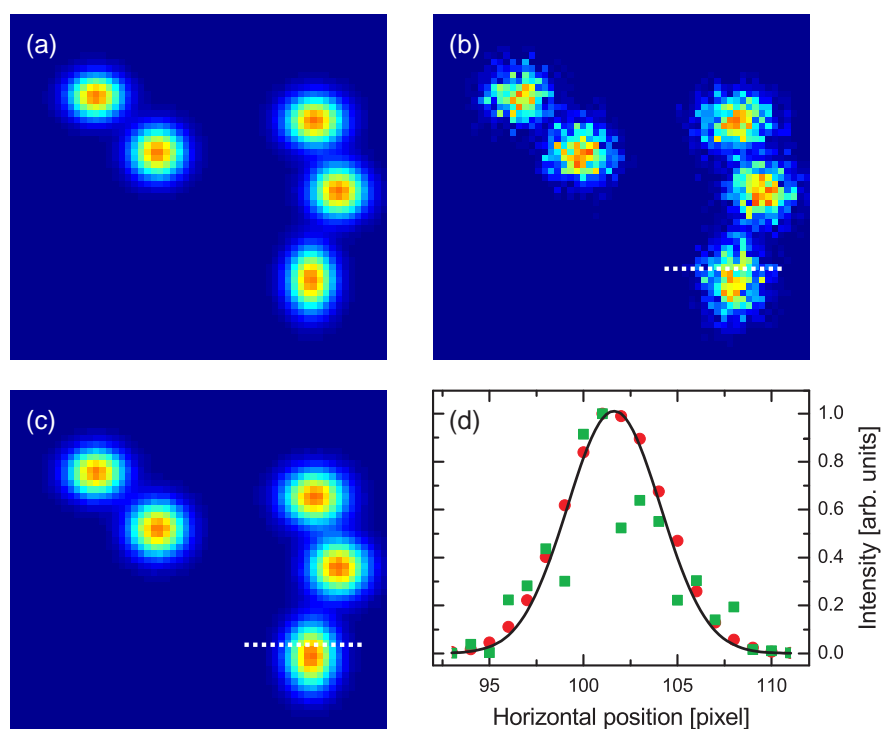


Figure B.4.: Comparison of simulated initial PEEM images and drift corrected image. The white dotted lines in (b) and (c) indicate the data presented in (d). (a) Detail of the initial image without noise. (b) Detail of the initial image with noise. (c) Details of the mean of all drift corrected images. (d) Linecut through images in (b) and (c) in comparison with noise-free initial shape. The averaged drift corrected data (red circles) shows only small deviations from noise-free initial shape (solid black line) compared to the single initial image with noise (green squares).

plot of the simulated images series with noise shows an offset even without interpolation. The separation to the noise limit is even more distinct for reduced pixel size. A further interpolation is not beneficial since most of the position uncertainty is given by the noise within the test images which is uncorrelated to the discretization.

The drift detection scheme as it was presented above is able to resolve spatial drifts which are considerably smaller than a pixel. In a PEEM image with a field of view of $20 \mu\text{m}$ a precision of three percent of a pixel, achieved for noise free data, would lead to a positioning error of smaller than a nanometer. However, noise in the reference images affects the resolution and can lead to a bigger position uncertainty than limited by the discretization.

Having determined the spatial drift of the sample with respect to the PEEM, the drift vector \mathbf{D}_j of the j -th reference image R_j can be utilized to compensate for the drift in the corresponding measurement image M_j . The simplest method to achieve this involves shifting the obtained PEEM images in discrete pixel steps according to the rounded drift vector values. This implies a possible loss of precision, but it is fast and does not need an interpolation of the measured PEEM data. Especially in case of an adaptive optimization this can be advantageous.

An example for a discrete compensation of the drift is presented in Figure B.4. The comparison of the initial images without and with noise in Fig B.4a and b, respectively, demonstrate the

influence of the applied displacement to each pixel. The test series with noise was drift corrected using the 4-fold interpolated drift vector. The average over all drift corrected images (Fig. B.4c) does show any visible noise. Contrary to Figure B.2b there is no distortion of the spot shapes, they resemble strongly those of the undisturbed image. A horizontal linecut through these three images exemplarily underlines that in the averaged, corrected image the shape of the noise free spots is reconstructed to a large extent (Fig. B.4d). A slight broadening of the spot is apparent in the shoulder, which is connected to the uncertainty of the drift correction theme.

C. Excitation Pathways for Single Color Pump-Probe Experiments

The expansion of the term $F(\mathbf{r}, t, t', \tau)$ used in (3.4) leads to the following expression:

$$\begin{aligned}
F(\mathbf{r}, t, t', \tau) = & E_{\alpha,1}^+(\mathbf{r}, t)E_{\alpha,1}^-(\mathbf{r}, t)E_{\alpha,2}^+(\mathbf{r}, t)E_{\alpha,2}^-(\mathbf{r}, t) & * \\
& + E_{\alpha,1}^+(\mathbf{r}, t)E_{\alpha,1}^-(\mathbf{r}, t)E_{\alpha,2}^+(\mathbf{r}, t)E_{\beta,2}^-(\mathbf{r}, t - \tau) \\
& + E_{\alpha,1}^+(\mathbf{r}, t)E_{\alpha,1}^-(\mathbf{r}, t)E_{\beta,2}^+(\mathbf{r}, t - \tau)E_{\alpha,2}^-(\mathbf{r}, t) \\
& + E_{\alpha,1}^+(\mathbf{r}, t)E_{\alpha,1}^-(\mathbf{r}, t)E_{\beta,2}^+(\mathbf{r}, t - \tau)E_{\beta,2}^-(\mathbf{r}, t - \tau) & \# \\
& + E_{\alpha,1}^+(\mathbf{r}, t)E_{\beta,1}^-(\mathbf{r}, t - \tau)E_{\alpha,2}^+(\mathbf{r}, t)E_{\alpha,2}^-(\mathbf{r}, t) \\
& + E_{\alpha,1}^+(\mathbf{r}, t)E_{\beta,1}^-(\mathbf{r}, t - \tau)E_{\alpha,2}^+(\mathbf{r}, t)E_{\beta,2}^-(\mathbf{r}, t - \tau) \\
& + E_{\alpha,1}^+(\mathbf{r}, t)E_{\beta,1}^-(\mathbf{r}, t - \tau)E_{\beta,2}^+(\mathbf{r}, t - \tau)E_{\alpha,2}^-(\mathbf{r}, t) & \# \\
& + E_{\alpha,1}^+(\mathbf{r}, t)E_{\beta,1}^-(\mathbf{r}, t - \tau)E_{\beta,2}^+(\mathbf{r}, t - \tau)E_{\beta,2}^-(\mathbf{r}, t - \tau) \\
& + E_{\beta,1}^+(\mathbf{r}, t - \tau)E_{\alpha,1}^-(\mathbf{r}, t)E_{\alpha,2}^+(\mathbf{r}, t)E_{\alpha,2}^-(\mathbf{r}, t) \\
& + E_{\beta,1}^+(\mathbf{r}, t - \tau)E_{\alpha,1}^-(\mathbf{r}, t)E_{\alpha,2}^+(\mathbf{r}, t)E_{\beta,2}^-(\mathbf{r}, t - \tau) & \# \\
& + E_{\beta,1}^+(\mathbf{r}, t - \tau)E_{\alpha,1}^-(\mathbf{r}, t)E_{\beta,2}^+(\mathbf{r}, t - \tau)E_{\alpha,2}^-(\mathbf{r}, t) \\
& + E_{\beta,1}^+(\mathbf{r}, t - \tau)E_{\alpha,1}^-(\mathbf{r}, t)E_{\beta,2}^+(\mathbf{r}, t - \tau)E_{\beta,2}^-(\mathbf{r}, t - \tau) \\
& + E_{\beta,1}^+(\mathbf{r}, t - \tau)E_{\beta,1}^-(\mathbf{r}, t - \tau)E_{\alpha,2}^+(\mathbf{r}, t)E_{\alpha,2}^-(\mathbf{r}, t) & \# \\
& + E_{\beta,1}^+(\mathbf{r}, t - \tau)E_{\beta,1}^-(\mathbf{r}, t - \tau)E_{\alpha,2}^+(\mathbf{r}, t)E_{\beta,2}^-(\mathbf{r}, t - \tau) \\
& + E_{\beta,1}^+(\mathbf{r}, t - \tau)E_{\beta,1}^-(\mathbf{r}, t - \tau)E_{\beta,2}^+(\mathbf{r}, t - \tau)E_{\alpha,2}^-(\mathbf{r}, t) \\
& + E_{\beta,1}^+(\mathbf{r}, t - \tau)E_{\beta,1}^-(\mathbf{r}, t - \tau)E_{\beta,2}^+(\mathbf{r}, t - \tau)E_{\beta,2}^-(\mathbf{r}, t - \tau) & * \quad (C.1)
\end{aligned}$$

Here * and # mark those terms which do not oscillate in τ because they contain equal numbers of terms $E_{\beta,j}^+$ and $E_{\beta,j}^-$ with positive and negative frequency components, respectively. Ten additional terms oscillate with $\omega_0\tau$ or $2\omega_0\tau$, where the center frequency of the laser pulse is indicated by ω_0 . The fast dither of the probe pulse which is introduced in the experiment averages over constructive and destructive interference of both fields. Only the marked signals persist, as they are stationary or vary slowly with the delay between pump and probe pulse. This is analog to far-field intensity autocorrelation measurements [11]. Consequently, the resulting local cross-correlation signal can be contracted to Eq. (3.5).

In contrast, in 2D nanoscopy (see Chapter 4.2 and Appendix E) excitation pulsed sequences are used in which the relative phases between the individual pulses are defined with high interferometric stability. Accordingly, in this technique also terms analog to those which are omitted here contribute to the photoemission signal.

D. Principles of Optical Coherent 2D Spectroscopy

The description of the principles of optical coherent 2D spectroscopy which is given in the following is based on literature of Mukamel [15, 45], Hamm [427] and Brixner [89]. The properties of a mixed quantum mechanic states, e.g. an ensemble of quantum systems, can be written in the notation of a density matrix. Representations of the density matrix in Hilbert space (Section D.1) and Liouville space (Section D.2) are introduced. The latter allows for an efficient notation of relaxation and dephasing of the system in a response formalism and is also useful for the description of 2D nanoscopy (see Chapter 4.2.1). In the following section the contribution of the excitation pathways to the third order polarization are discussed (Section D.3). Afterwards, the basics of optical coherent 2D spectroscopy experiments are briefly presented (Section D.4).

D.1. Representation of Mixed Quantum Mechanic States with the Density Matrix

In quantum mechanics the solutions $|\psi_n\rangle$ of Schrödinger's equation are energy eigenfunctions. They build a basis of the Hilbert space which contains all pure states the quantum system can reside in. A pure state $|\psi(t)\rangle$ is given by the linear combination of the energy eigenfunctions

$$|\psi(t)\rangle = \sum_n c_n(t) |\psi_n\rangle \quad (\text{D.1})$$

but can also be represented in any other arbitrary basis set. For pure states the density matrix $\rho(t)$, which is also called density operator, is written as:

$$\rho(t) = |\psi(t)\rangle \langle \psi(t)| = \sum_{n,m} c_n(t) c_m^*(t) |\psi_n\rangle \langle \psi_m| = \sum_{n,m} \rho_{nm}(t) |\psi_n\rangle \langle \psi_m| . \quad (\text{D.2})$$

The diagonal matrix elements $\rho_{nn}(t) = \langle \psi_n | \rho(t) | \psi_n \rangle$ denote the probability to find the system in state n associated with the wavefunction $|\psi_n\rangle$. The off-diagonal elements of $\rho(t)$ denote the coherent superposition of two wavefunctions. To comply with Eq. (D.2), pure states have to fulfill the equality $\rho_{nn}(t)\rho_{mm}(t) = |\rho_{nm}(t)|^2$ because $\rho_{nm}(t) = c_n(t)c_m^*(t)$. A normalization of $\rho(t)$ leads to

$$\text{Tr}[\rho(t)] = \sum_n \rho_{nn}(t) = \sum_n c_n(t) c_n^*(t) = 1 . \quad (\text{D.3})$$

The expectation value of an operator is given by $\hat{O}(t) = \langle \psi(t) | \hat{O} | \psi(t) \rangle$, which is connected with the density matrix via

$$\langle \hat{O}(t) \rangle = \sum_{n,m} c_n(t) c_m^*(t) \langle \psi_m | \hat{O} | \psi_n \rangle = \sum_{n,m} \rho_{nm}(t) \hat{O}_{mn} = \text{Tr} [\hat{O} \rho(t)] . \quad (\text{D.4})$$

For normalized pure states also $\text{Tr}\rho^2(t) = 1$ holds.

However, systems can consist of a huge number of single particle quantum systems, e.g. nuclear spins or electronic states in an ensemble of molecules. Furthermore, coupling to external degrees of freedom is possible. Then, a description with pure states is only successful in special cases and a representation with mixed states is necessary. Mixed states are characterized by their probability p_k to obtain a particular pure state $|\psi_k(t)\rangle$ defined via

$$|\psi_k(t)\rangle = \sum_n c_{k,n}(t) |\psi_n\rangle . \quad (\text{D.5})$$

The density matrix of the mixed state is the sum of the density matrices of the pure states.

$$\rho(t) = \sum_k p_k \rho_k(t) = \sum_k p_k |\psi_k(t)\rangle \langle \psi_k(t)| \quad (\text{D.6})$$

Whereas the diagonal elements are real positive values and, therefore, always add up constructively, the off-diagonal elements are complex. Thus, for each off-diagonal position in the density matrix the sum of the off-diagonal elements can be reduced compared to the sum of the absolute values of these elements. This is obvious in the following example treating two identical two-level quantum systems with corresponding wavefunctions $|\psi_1\rangle$ and $|\psi_2\rangle$. The first of the two-level systems ($k = 1$) is in the ground state $|\psi_1\rangle$. Hence, the respective coefficients are $c_{1,1}(t) = 1$ and $c_{1,2}(t) = 0$. System 2 is in a coherent superposition of ground state and excited state with $c_{2,1}(t) = c_{2,2}(t) = \sqrt{1/2}$. The coefficients were chosen time-independent for the sake of simplicity. The density matrices ρ_1 and ρ_2 of the single two-level systems are calculated from Eq. (D.2). The density matrix ρ_{ens} of the combined system is then given by

$$\rho_{ens} = 0.5 \rho_1 + 0.5 \rho_2 = 0.5 \begin{pmatrix} 1 & 0 \\ 0 & 0 \end{pmatrix} + 0.5 \begin{pmatrix} 0.5 & 0.5 \\ 0.5 & 0.5 \end{pmatrix} = \begin{pmatrix} 0.75 & 0.25 \\ 0.25 & 0.25 \end{pmatrix} , \quad (\text{D.7})$$

The resulting density matrix ρ_{ens} was normalized by choosing the sum over all p_k to be one and using normalized density matrices ρ_1 and ρ_2 . Hence, the probability to find the system in any of the possible states is one. Calculation of the trace of ρ_{ens}^2 yields 0.75. Values below one clearly indicate mixed states. This mixed state cannot be expressed as a coherent superposition of wavefunctions, i.e. a pure state, because it violates Eq. (D.2), since $\rho_{11}(t)\rho_{22}(t) > |\rho_{12}(t)|^2$. Another example for a mixed system is the canonical ensemble in thermodynamics. In the canonical ensemble the number of particles and the volume are fixed and the ensemble has a well-defined temperature T due to interaction with an external heat bath [428]. The corresponding density matrix in the basis of energy eigenfunctions is written as

$$\rho_{can}(t) = \frac{\sum_k |\psi_k(t)\rangle e^{-E_k/k_B T} \langle \psi_k(t)|}{\sum_k e^{-E_k/k_B T}} , \quad (\text{D.8})$$

where k_B is the Boltzmann constant [428]. In this equilibrium state no coherences exist. In experiments it is often favorable to start with a population in a single ground state. This is approximatively achieved by cooling the system or by manipulating the energy eigenvalues of the wavefunctions e.g. by applying an external field.

Analog to Eq. (D.4) the expectation value of an operator \hat{O} is given by calculating the trace of the product with the density matrix:

$$\langle \hat{O}(t) \rangle = \text{Tr} [\hat{O}\rho(t)] . \quad (\text{D.9})$$

From Schrödinger's equation the Liouville-Von Neumann equation

$$\frac{\partial \rho}{\partial t} = -\frac{i}{\hbar} [H, \rho] \quad (\text{D.10})$$

can be deduced describing the temporal evolution of the density matrix ρ by the commutator with the Hamiltonian H of the quantum system. For a single element ρ_{nm} of the density matrix Eq. (D.10) is expressed by

$$\frac{\partial \rho_{nm}}{\partial t} = -\frac{i}{\hbar} ((H\rho)_{nm} - (\rho H)_{nm}) . \quad (\text{D.11})$$

The interaction of a quantum system with a weak electric field $E(t)$ is often treated as a time-dependent perturbation that affects the Hamiltonian in Hilbert space notation according to

$$H(t) = H - H_{int}(t) = H - VE(t) , \quad (\text{D.12})$$

where V denotes the time-independent dipole operator, H represents the unperturbed time-independent Hamiltonian and $H_{int}(t)$ denotes the interaction. In the basis of the energy eigenstates the elements of the dipole operator are given by:

$$V = \sum_{a,b} \mu_{ab} |a\rangle \langle b| \quad (\text{D.13})$$

In principle $E(t)$ and the dipole elements μ_{ab} are vectors and have components in all spatial dimensions, but to simplify the following derivations they are treated as scalar quantities, i.e. they are projected onto an arbitrary spatial basis vector. In systems without permanent dipole moment the diagonal elements are zero and only the off-diagonal elements remain. The expectation value of the dipole operator yields the polarization of the quantum system

$$P(t) = \langle V\rho(t) \rangle = \text{Tr}[V\rho(t)]. \quad (\text{D.14})$$

Effectively, the multiplication with the dipole operator projects the polarization onto the diagonal elements and the trace sums up all contributions. The polarization $P(t)$ is identical to the quantity, which is treated by the inhomogeneous wave equation derived from Maxwell's equation (see Eq. (1.19)).

For the example of a two-level quantum system without relaxation effects in which an optical field introduces a dipolar coupling between both states the Hamiltonian

$$H = \begin{pmatrix} \epsilon_1 & 0 \\ 0 & \epsilon_2 \end{pmatrix} - \begin{pmatrix} 0 & \mu_{12} \\ \mu_{21} & 0 \end{pmatrix} E(t) = \begin{pmatrix} \epsilon_1 & V_{12} \\ V_{21} & \epsilon_2 \end{pmatrix} \quad (\text{D.15})$$

contains the eigenenergies ϵ_1 and ϵ_2 on the diagonal. The off-diagonal elements denote the interaction with the electric field via V_{12} and V_{21} . The temporal evolution of the density matrix elements can then be calculated by substitution of H into the Liouville-Von Neumann equation (see Eq. (D.10)).

$$\begin{aligned}
\frac{\partial \rho_{11}}{\partial t} &= -\frac{i}{\hbar} [\rho_{21} V_{12} - \rho_{12} V_{21}] \\
\frac{\partial \rho_{12}}{\partial t} &= -\frac{i}{\hbar} [\rho_{12}(\epsilon_1 - \epsilon_2) + V_{12}(\rho_{11} - \rho_{22})] \\
\frac{\partial \rho_{21}}{\partial t} &= -\frac{i}{\hbar} [\rho_{21}(\epsilon_2 - \epsilon_1) + V_{21}(\rho_{11} - \rho_{22})] \\
\frac{\partial \rho_{22}}{\partial t} &= -\frac{i}{\hbar} [\rho_{12} V_{21} - \rho_{21} V_{12}]
\end{aligned} \tag{D.16}$$

From these equations it can be deduced that in the absence of the dipolar coupling the population states ρ_{11} and ρ_{22} do not evolve at all. The off-diagonal density matrix elements ρ_{12} and ρ_{21} oscillate with a frequency proportional to the difference of the eigenenergies ϵ_1 and ϵ_2 . It is obvious that a direct transition, i.e. a transfer from population, from ρ_{11} into ρ_{22} is not possible. An optically introduced transition, therefore, necessarily involves two interactions with the electric field. The first creates a coherence denoted by the off-diagonal elements and the second transfers the coherence to the excited population state. In Section D.3 optical transitions in quantum systems will be treated more detailed by examining the Liouville pathways for nonlinear orders of the polarization.

D.2. Response Function Formalism in Liouville Space

The representation in Liouville space includes the full information of the density matrix ρ and has the advantage that relaxation and dephasing is applied in a simpler fashion [15]. This is achieved by writing the density matrix of a N level system ρ as a vector $|\rho\rangle\rangle$ with N^2 elements that are addressed by superoperators with $N^2 \times N^2$ elements. The multiplication of $|\rho\rangle\rangle$ with the Liouville operator \mathcal{L} replaces the commutator $[H, \rho]$ in Hilbert space. The Liouville - van Neumann equation (see Eq. (D.10)) then transforms to

$$\frac{\partial |\rho\rangle\rangle}{\partial t} = -\frac{i}{\hbar} \mathcal{L} |\rho\rangle\rangle . \tag{D.17}$$

$$|\rho(t)\rangle\rangle = \exp\left(\frac{-i\mathcal{L}(t-t_0)}{\hbar}\right) |\rho(t_0)\rangle\rangle . \tag{D.18}$$

Accordingly, the Liouville operator is also given by the sum of the unperturbed operator \mathcal{L} and an interaction operator $\mathcal{L}_{int}(t)$.

$$\mathcal{L}(t) = \mathcal{L} + \mathcal{L}_{int}(t) = \mathcal{L} - \mathcal{V}E(t) , \tag{D.19}$$

with \mathcal{V} denoting the time-independent dipole operator in Liouville space. As a result of the perturbation, the density operator is expanded in a series

$$|\rho(t)\rangle\rangle = \sum_n |\rho^{(n)}(t)\rangle\rangle , \tag{D.20}$$

with $|\rho^{(n)}(t)\rangle\rangle$ describing the n -th order contribution to the density matrix. Thus, $|\rho^{(n)}(t)\rangle\rangle$ involves n interactions with the electric field and, therefore, scales with the n -th power of the

electric field. To calculate $|\rho^{(n)}(t)\rangle\rangle$, the temporal propagation is considered for two different situations. The first case is the interaction with the electric field described by the interaction operator $\mathcal{L}_{int}(t)$ and the second is the evolution of the system in the absence of the electric field determined by the Liouville space Greens function $\mathcal{G}(t)$

$$\mathcal{G}(t) = \Theta(t)e^{-\frac{i\mathcal{L}t}{\hbar}} \quad (\text{D.21})$$

The Greens operator $\mathcal{G}(t)$ includes the Liouville operator \mathcal{L} corresponding to the unperturbed Hamiltonian H in Eq. (D.12) and the Heaviside step function $\Theta(t)$. With $\mathcal{L}_{int}(t)$ and $\mathcal{G}(t)$ each contribution $|\rho^{(n)}(t)\rangle\rangle$ to the expansion of $|\rho(t)\rangle\rangle$ is given by

$$\begin{aligned} |\rho^{(n)}(t)\rangle\rangle = & \left(\frac{-i}{\hbar}\right)^n \int_{t_0}^t d\tilde{t}_n \dots \int_{t_0}^{\tilde{t}_2} d\tilde{t}_1 \mathcal{G}(t - \tilde{t}_n) \mathcal{L}_{int}(\tilde{t}_n) \mathcal{G}(\tilde{t}_n - \tilde{t}_{n-1}) \mathcal{L}_{int}(\tilde{t}_{n-1}) \dots \\ & \dots \mathcal{G}(\tilde{t}_2 - \tilde{t}_1) \mathcal{L}_{int}(\tilde{t}_1) \mathcal{G}(\tilde{t}_1 - t_0) |\rho(t_0)\rangle\rangle . \end{aligned} \quad (\text{D.22})$$

Since the system initially is in the equilibrium state $|\rho(t_0)\rangle\rangle$, it does not evolve before the first interaction at temporal position \tilde{t}_1 and the first Greens function has no effect:

$$\mathcal{G}(\tilde{t}_1 - t_0) |\rho(t_0)\rangle\rangle = |\rho(t_0)\rangle\rangle . \quad (\text{D.23})$$

A change of time variables from absolute temporal positions of the interactions \tilde{t}_i to relative delays t_i between the interactions

$$t_1 = \tilde{t}_2 - \tilde{t}_1, \quad t_2 = \tilde{t}_3 - \tilde{t}_2, \quad \dots \quad t_n = t - \tilde{t}_n \quad (\text{D.24})$$

and sending t_0 towards $-\infty$ and substitution of $\mathcal{L}_{int}(t)$ by $-\mathcal{V}E(t)$ allows for rewriting Eq. (D.22) by

$$\begin{aligned} |\rho^{(n)}(t)\rangle\rangle = & \left(\frac{i}{\hbar}\right)^n \int_0^\infty dt_n \int_0^\infty dt_{n-1} \dots \int_0^\infty dt_1 \mathcal{G}(t_n) \mathcal{V} \mathcal{G}(t_{n-1}) \mathcal{V} \dots \mathcal{G}(t_1) \mathcal{V} |\rho(-\infty)\rangle\rangle \\ & \times E(t - t_n) E(t - t_n - t_{n-1}) \dots E(t - t_n - t_{n-1} \dots - t_1) . \end{aligned} \quad (\text{D.25})$$

Substituting the density matrix $|\rho(t)\rangle\rangle$ in Eq. (D.14) by Eq. (D.20), the expansion of the density matrix generates a series of elements $P^{(n)}(t)$ that represent the influence of the n -th order perturbation by the electric field on the polarization $P(t)$. In Liouville notation the expectation value of the dipole operator V is given by the scalar product with the density matrix operator $\rho(t)$ [15]. Accordingly, the elements are given by

$$\begin{aligned} P^{(n)}(t) = & \langle V \rho^{(n)}(t) \rangle = \langle \langle V | \rho^{(n)}(t) \rangle \rangle \\ = & \left(\frac{i}{\hbar}\right)^n \int_0^\infty dt_n \int_0^\infty dt_{n-1} \dots \int_0^\infty dt_1 S^{(n)}(t_n, t_{n-1}, \dots, t_1) \\ & E(t - t_n) E(t - t_n - t_{n-1}) \dots E(t - t_n - t_{n-1} \dots - t_1) , \end{aligned} \quad (\text{D.26})$$

where the n -th order nonlinear response function

$$S^{(n)}(t_n, t_{n-1}, \dots, t_1) = \left(\frac{i}{\hbar}\right)^n \langle\langle V|\mathcal{G}(t_n)\mathcal{V}\mathcal{G}(t_{n-1})\mathcal{V} \dots \mathcal{G}(t_1)\mathcal{V}|\rho(-\infty)\rangle\rangle \quad (\text{D.27})$$

determines the correlations between the n interactions with the electric field at times t_n, t_{n-1}, \dots, t_1 . Already for Equation (D.16) it was obvious that a dipolar coupling cannot lead to a direct transfer of population but connects population states and coherence states. In the nonlinear case a series of such interactions takes place. As a result, complex excitation pathways are found that describe the transfer of population and coherence between the states of the system represented by the density matrix ρ . Section D.3 discusses the Liouville pathways for third order polarization processes in a two-level system and their representations by reduced density matrices and double-sided Feynman diagrams.

D.3. Liouville Pathways for Third Order Polarization

Optical coherent 2D spectroscopy determines the third order response function via measuring the third order polarization. The contribution to the nonlinear response function in third order perturbation theory $S^{(3)}(t_3, t_2, t_1)$ is obtained in Liouville representation by setting $n=3$ in Eq. (D.27).

$$S^{(3)}(t_3, t_2, t_1) = \left(\frac{i}{\hbar}\right)^3 \langle\langle V|\mathcal{G}(t_3)\mathcal{V}\mathcal{G}(t_2)\mathcal{V} \dots \mathcal{G}(t_1)\mathcal{V}|\rho(-\infty)\rangle\rangle \quad (\text{D.28})$$

$S^{(3)}(t_3, t_2, t_1)$ fully describes all processes that are associated with three interactions with the incident electric field separated in time by t_1, t_2 and t_3 . Using the dipole operator in the interaction picture $\mathcal{V}(t)$ (see Eq. (4.8)) and its Hilbert space analogue $V(t)$ the correlation function $S^{(3)}(t_3, t_2, t_1)$ is reshaped towards [15]:

$$S^{(3)}(t_3, t_2, t_1) = \left(\frac{i}{\hbar}\right)^3 \Theta(t_1)\Theta(t_2)\Theta(t_3) \langle\langle V(t_3 + t_2 + t_1)|\mathcal{V}(t_2 + t_1)\mathcal{V}(t_1)\mathcal{V}(0)|\rho(-\infty)\rangle\rangle. \quad (\text{D.29})$$

The notation in Hilbert space is more complex since the Liouville operators have to be replaced by commutators [15]:

$$\begin{aligned} S^{(3)}(t_3, t_2, t_1) &= \left(\frac{i}{\hbar}\right)^3 \Theta(t_1)\Theta(t_2)\Theta(t_3) \\ &\quad \times \langle\langle [[[V(t_3 + t_2 + t_1), V(t_2 + t_1)], V(t_1)] V(0)] \rho(-\infty) \rangle\rangle \\ &= \left(\frac{i}{\hbar}\right)^3 \Theta(t_1)\Theta(t_2)\Theta(t_3) \sum_{\alpha=1}^4 [R_\alpha(t_3, t_2, t_1) - R_\alpha^*(t_3, t_2, t_1)]. \end{aligned} \quad (\text{D.30})$$

Here, the expansion of the commutators was rewritten in a sum over combinations of the dipole operator $V(t)$ for different temporal positions acting on the initial density matrix $\rho(-\infty)$. The terms $R_\alpha(t_3, t_2, t_1)$ ($\alpha=1,2,3,4$) are defined as

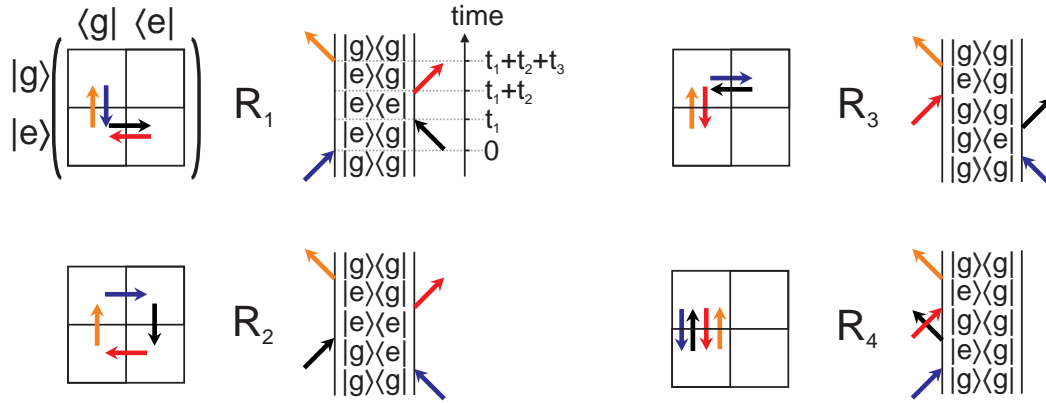


Figure D.1.: Liouville pathways in a coupled two-level system depicted in a reduced density matrix representation and as double-sided Feynman diagrams. The two-level system has ground state $|g\rangle$ and an excited state $|e\rangle$. As emphasized by the parentheses and the bra and ket vectors around the density matrix pictogram for R_1 , the matrix elements are represented by boxes. The first, second and third interaction with the incident electric field are depicted as blue, black and red arrow, respectively. The orange arrow indicates a fourth interaction which is responsible for the detected outgoing wave. In the double-sided Feynman diagrams (right) the time ordering of the interactions is indicated by the vertical position. The initial state is presented at the bottom and with each interaction a step upwards is made. Arrows pointing towards the diagram increase the state on this side, arrows pointing away decrease the state. The four excitation pathways R_α ($\alpha=1,2,3,4$) according to Eq. (D.31) are shown. The respective complex conjugates R_α^* are obtained by inversion of the density matrix representation with respect to the diagonal axes and by inversion of the doubled-sided Feynman diagram at the vertical axes.

$$\begin{aligned}
 R_1(t_3, t_2, t_1) &= \langle V(t_1)V(t_2 + t_1)V(t_3 + t_2 + t_1)V(0)\rho(-\infty) \rangle \\
 R_2(t_3, t_2, t_1) &= \langle V(0)V(t_2 + t_1)V(t_3 + t_2 + t_1)V(t_1)\rho(-\infty) \rangle \\
 R_3(t_3, t_2, t_1) &= \langle V(0)V(t_1)V(t_3 + t_2 + t_1)V(t_2 + t_1)\rho(-\infty) \rangle \\
 R_4(t_3, t_2, t_1) &= \langle V(t_3 + t_2 + t_1)V(t_2 + t_1)V(t_1)V(0)\rho(-\infty) \rangle
 \end{aligned} \tag{D.31}$$

and $R_\alpha^*(t_3, t_2, t_1)$ are the complex conjugates [15]. Each of the R_α and R_α^* is associated with a specific Liouville pathway containing four interactions with the electric field. Whereas the first three interactions are induced by the incident electric field, the fourth interaction is connected with an outgoing wave generated by the polarization of the system after the third interaction. As a consequence of four involved optical waves, processes utilizing the third order polarization are often called four-wave mixing (FWM) processes.

Two types of schematic representations for the Liouville pathways described by R_α are shown in Figure D.1 for the example of a two-level system containing a ground state $|g\rangle$ and an excited state $|e\rangle$ in Hilbert notation. The density matrix representation (left) symbolizes the population states $|g\rangle\langle g|$ and $|e\rangle\langle e|$ as the upper left and lower right box. The coherent states $|g\rangle\langle e|$ and $|e\rangle\langle g|$ are found at the cross diagonal. Arrows indicating transition between the states due to interactions with the electric field. The subsequent interactions have to start from the case that was reached from the previous. The second and third interaction with the incident electric field are depicted as black and red arrow, respectively. The fourth interaction (orange

arrow) is responsible is connected to an outgoing wave which is measured in coherent optical two-dimensional spectroscopy. The arrow representing this last interaction points from $|e\rangle\langle g|$ to $|g\rangle\langle g|$ for R_α . The pathways of the complex conjugate contributions are obtained by inversion of the diagrams so that the last arrow would point from $|g\rangle\langle e|$ to $|g\rangle\langle g|$, i.e. to the left.

The double-sided Feynman diagrams (right) basically contain the same information as the density matrix representation. Here the initial state is written at the bottom of a sequence of obtained states during the excitation process. The interactions with the electric fields are shown as arrows with coloring identical to the density matrix representation. Here, arrows pointing towards the diagram increase the excitation on the respective side. An arrow pointing from the diagram is connected to a decrease of the state. The complex conjugates are obtained by flipping the direction of each arrow and letting them interact with the state on the opposing side of the diagram.

In Figure D.1 a qualitative difference between the excitation pathways R_1 and R_4 compared to R_2 and R_3 is visible. Whereas R_1 and R_4 represent excitation pathways that contain only the coherence term $|e\rangle\langle g|$, which is occupied after the first and third interaction, the first coherent state for R_2 and R_3 is $|g\rangle\langle e|$. The temporal evolution of the phase in this conjugate coherence is opposite to $|e\rangle\langle g|$. Thus, if the time intervals t_1 and t_3 are equal the phase acquired between the first and second interaction is completely compensated for during the interval t_3 between the third and fourth interaction. This behavior is independent of the energy difference between ground and excited state. Hence, in an ensemble of two-level systems with individual resonance frequency each systems shows this rephasing. As a consequence, the superposition of all signals obtained from the ensemble exhibits a so called photon echo, a strong recurrence of the signal for $t_1 = t_3$. During the photon echo all time invariant dephasing effects of affecting the quantum systems are canceled. The loss compared to the initial signal is directly attributed to the loss of coherence in the individual systems. Hence, the homogeneous linewidth Γ_{hom} is accessible. Echo signals are phenomena well known from nuclear magnetic resonance spectroscopy [429]. In contrast to the *rephasing* pathways R_2 and R_3 the pathways represented by R_1 and R_4 lead to *non-rephasing* signals.

D.4. Optical 2D Spectroscopy in Experiments

Coherent optical 2D spectroscopy probes the nonlinear response function of a quantum system via detecting the third order polarization

$$P^{(3)}(\mathbf{r}, t) = \int_0^\infty dt_3 \int_0^\infty dt_2 \int_0^\infty dt_1 S^{(3)}(t_3, t_2, t_1) E(\mathbf{r}, t - t_3) E(\mathbf{r}, t - t_3 - t_2) E(\mathbf{r}, t - t_3 - t_2 - t_1), \quad (\text{D.32})$$

which results from setting $n=3$ in Eq. D.26. Implicitly, the polarization $P^{(3)}(\mathbf{r}, t)$ depends on the temporal structure of the electric field. This is utilized by creating a sequence of femtosecond laser pulses with adjustable pulse delays τ_i . The temporal positions of the interactions with the electric field $t - t_3$, $t - t_3 - t_2$ and $t - t_3 - t_2 - t_1$ are then confined to the temporal overlap with the excitation pulse sequence.

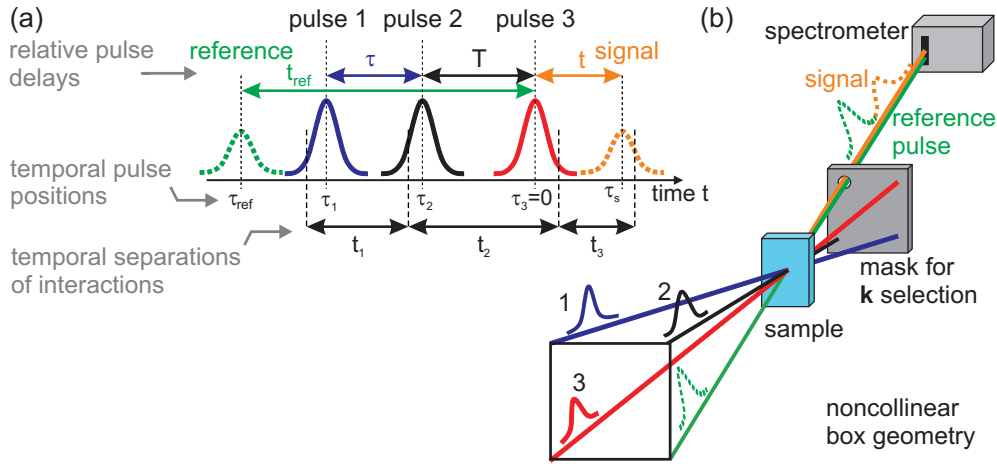


Figure D.2.: (a) Pulse sequence for coherent optical two-dimensional spectroscopy. Three femtosecond laser pulses (full lines) at temporal position τ_1 , τ_2 and τ_3 are used to prepare a third order polarization in the sample. The temporal delays τ and T between the excitation pulses are variable. The induced signal delayed by t compared to the last excitation pulse (orange dashed line) is characterized by spectral interferometry of the signal pulse at τ_s with a reference pulse at a fixed time position τ_{ref} . Without loss of generality pulse 3 is centered at $\tau_3=0$ leading to the equivalence of the absolute time t and the delay between last excitation pulse and signal, which is also denoted as t . Adapted from [89]. (b) Schematic setup for coherent optical two-dimensional spectroscopy in box geometry. The three excitation pulses hit the same position of the sample under different angles given by \mathbf{k}_1 , \mathbf{k}_2 and \mathbf{k}_3 and different temporal positions as depicted in (a). The photon echo signal is emitted in the direction $\mathbf{k}_{PE} = -\mathbf{k}_1 + \mathbf{k}_2 + \mathbf{k}_3$ and is overlapped with the reference pulse and the spectral interference signal is detected with an optical spectrometer. Adapted from [89].

The positive frequency part of the electric field $E^+(\mathbf{r}, t)$ of the laser pulse sequence contains three identical laser pulse fields in complex notation shifted in time by their respective center position τ_l ($l=1,2,3$):

$$E^+(\mathbf{r}, t) = \tilde{E}_1^+(\mathbf{r}, t - \tau_1)e^{i[\omega_L(t-\tau_1)+\mathbf{k}_1\mathbf{r}]} + \tilde{E}_2^+(\mathbf{r}, t - \tau_2)e^{i[\omega_L(t-\tau_2)+\mathbf{k}_2\mathbf{r}]} + \tilde{E}_3^+(\mathbf{r}, t - \tau_3)e^{i[\omega_L(t-\tau_3)+\mathbf{k}_3\mathbf{r}]}, \quad (\text{D.33})$$

where $\tilde{E}_l^+(\mathbf{r}, t)$ denotes the complex temporal envelope of the electric field, ω_L denotes the carrier frequency and \mathbf{k}_l is the wavevector of the respective pulse. To obtain the real valued electric field, the complex conjugate has to be added to Eq. (D.33). The excitation pulse sequence is schematically presented in Figure D.2 as solid lines. The temporal separation between the first (blue) and second (black) laser pulse is called coherence time $\tau = \tau_1 - \tau_2$ because in this time interval the coherence excited by the interaction with the first pulse evolves. The delay $T = \tau_2 - \tau_3$ between second and third pulse (red) is called population time, since during T a two-level system has to be in a population state e.g. $|e\rangle\langle e|$. By setting the temporal position of the third pulse $\tau_3 = 0$ the delay t between last excitation pulse and the obtained signal becomes identical to the time variable t in Eq. (D.32). Since the pulses have finite temporal width, the interactions (vertical dashed black lines) with the electric field do not have to coincide with the center positions τ_l of the field envelope (vertical dotted black lines).

A substitution of $E(t)$ in Eq. (D.32) by Eq. (D.33) plus its complex conjugate does not directly provide a simple expression for $P^{(3)}(\mathbf{r}, t)$. On the contrary, the third order polarization is now

constituted of $6^3=216$ summands because of the 6 summands in the electric field $E(t)$. These summands specify the electric pulses that interact for this specific excitation pathway and the number of interactions within the particular pulse in the sequence. Except for the total number of interactions $n = 3$, in principle no restrictions are made. Thus, also those signals that for example are created by three interactions within a single pulse contribute to $P^{(3)}(\mathbf{r}, t)$.

The difficulties arising from the interplay of various excitation pathways for the third order polarization are solved by employing the different phase matching conditions of the contributing signals. As optical coherent 2D spectroscopy uses far-field illumination which is focused into the sample by means of diffraction-limited optics, e.g. lenses and curved mirrors, to each of the laser pulses in the excitation sequence its corresponding average wavevector \mathbf{k}_l is attributed. The coherent superposition of the local signals generated by the local third order polarization $P^{(3)}(\mathbf{r}, t)$ at all positions within the focal spot yields the emitted signal. According to Eq. (D.32) and Eq. (D.33) the variations of the local polarization are given by the exponential terms $e^{-i\mathbf{k}_l \cdot \mathbf{r}}$ of the excitation pulses, as long as the nonlinear response function does not change over the focal spot. Consequently, phase matching is used to select contributions to $P^{(3)}(\mathbf{r}, t)$ by selection of the propagation direction along the specific wavevector \mathbf{k}_S of the signal [15, 45, 50, 89]. In the box-geometry (see Figure D.2b) only the photon-echo signal with wavevector

$$\mathbf{k}_{PE} = -\mathbf{k}_1 + \mathbf{k}_2 + \mathbf{k}_3 \quad (\text{D.34})$$

can pass the mask and is detected with the spectrometer [45, 89]. The number of summands is therefore reduced to six. The summands are containing the common phase factor $e^{-\omega_L(t-\tau)}$ and phase factors depending on the temporal separations between the interactions. Three types of Liouville pathways ($S_{NR}^{(3)}$, $S_R^{(3)}$ and $S_{DC}^{(3)}$) are able to cancel these additional phase factors and to survive the integration over t_1 , t_2 and t_3 . The contribution of the fast oscillatory terms after integration are neglected in rotating-wave approximation (RWA) [89]. The subscripts *NR* and *R* denote non-rephasing (R_1 and R_4) and rephasing (R_2 and R_3) depicted in Figure D.1. The double-coherence (*DC*) pathway is only possible with systems including at least three energy levels.

Experimentally, the measured signal is an electric field emitted by the oscillating polarization in the direction given by the phase-matching condition. The detection of the electric field via spectral interferometry yields a frequency-domain signal which is connected to the polarization by

$$E_S(\tau, T, \omega_t) \propto \frac{i\omega_t}{n(\omega_t)} P^{(3)}(\tau, T, \omega_t) . \quad (\text{D.35})$$

As the Fourier transformation of the t axes has implicitly already been carried out, a one-dimensional Fourier transformation for the coherence time τ generates the two-dimensional correlation spectrum for the photon-echo signal

$$S_{2D}(\omega_\tau, T, \omega_t) = \int_{-\infty}^{\infty} iP^{(3)}(\tau, T, \omega_t) e^{i\omega_\tau \tau} d\tau \propto \int_{-\infty}^{\infty} \frac{n(\omega_t)}{\omega_t} E_S(\tau, T, \omega_t) e^{i\omega_\tau \tau} d\tau \quad (\text{D.36})$$

The absolute phase of the 2D spectrum has to be retrieved by a *phasing* procedure, which removes uncertainties in the interferometric phase relation between the reference pulse and the excitation pulse sequence [89].

E. 2D Nanoscopy: Mathematical Details

E.1. Local Photoemission Rate for $n = 4$ in Explicit Notation

The momentary photoemission rate $\mathcal{P}_m^{(4)}(\mathbf{r}, t, \tau_1, \tau_3, \varphi_1, \varphi_2, \varphi_3)$ is calculated by substitution of the excitation pulse sequence $E_p(t)$, which is defined in (4.21), into Eq. (4.17).

$$\begin{aligned} \mathcal{P}_m^{(4)} = & \iiint \int dt_1^* \dots dt_4^* \prod_{i=1}^2 A(\mathbf{r}, t_i^*) \left\{ E_L^+(t - t_i + \tau_1) e^{i[w_L(t-t_i)+\varphi_1]} \right. \\ & \left. + E_L^+(t - t_i) e^{i[w_L(t-t_i)+\varphi_2]} + E_L^+(t - t_i - \tau_3) e^{i[w_L(t-t_i)+\varphi_3]} \right\} \\ & \times \prod_{j=3}^4 A(\mathbf{r}, t_j^*) \left\{ E_L^-(t - t_j + \tau_1) e^{-i[w_L(t-t_j)+\varphi_1]} \right. \\ & \left. + E_L^-(t - t_j) e^{-i[w_L(t-t_j)+\varphi_2]} + E_L^-(t - t_j - \tau_3) e^{-i[w_L(t-t_j)+\varphi_3]} \right\} \quad (\text{E.1}) \end{aligned}$$

Replacing $E_L^+(t)$ and $E_L^-(t)$ by $\delta(t)$ and taking out the integral leads to a photoemission rate which is given by

$$\begin{aligned} \mathcal{P}_m^{(4)} = & \left\{ A^+(t + \tau_1) e^{i[-w_L\tau_1+\varphi_1]} + A^+(t) e^{i\varphi_2} + A^+(t - \tau_3) e^{i[w_L\tau_3+\varphi_3]} \right\}^2 \times c.c. \\ = & \left\{ A^+(t + \tau_1) e^{i[-w_L\tau_1+\varphi_1]} A^+(t + \tau_1) e^{i[-w_L\tau_1+\varphi_1]} \right. \\ & + 2A^+(t + \tau_1) e^{i[-w_L\tau_1+\varphi_1]} A^+(t) e^{i\varphi_2} \\ & + 2A^+(t + \tau_1) e^{i[-w_L\tau_1+\varphi_1]} A^+(t - \tau_3) e^{i[w_L\tau_3+\varphi_3]} \\ & + A^+(t) e^{i\varphi_2} A^+(t) e^{i\varphi_2} \\ & + 2A^+(t) e^{i\varphi_2} A^+(t - \tau_3) e^{i[w_L\tau_3+\varphi_3]} \\ & \left. + A^+(t - \tau_3) e^{i[w_L\tau_3+\varphi_3]} A^+(t - \tau_3) e^{i[w_L\tau_3+\varphi_3]} \right\} \times c.c. \quad (\text{E.2}) \end{aligned}$$

Multiplication with the complex conjugate term causes a total number of 36 different contributions to $\mathcal{P}_m^{(4)}(\mathbf{r}, t, \tau_1, \tau_3, \varphi_1, \varphi_2, \varphi_3)$, but several of them are themselves complex conjugates of other contributions. To facilitate the notation, the following substitutions are made:

$$A_1^+ = A^+(t + \tau_1) e^{i[-w_L\tau_1+\varphi_1]} \quad \text{and} \quad A_1^- = A^-(t + \tau_1) e^{-i[-w_L\tau_1+\varphi_1]} \quad (\text{E.3})$$

$$A_2^+ = A^+(t) e^{i\varphi_2} \quad \text{and} \quad A_2^- = A^-(t) e^{-i\varphi_2} \quad (\text{E.4})$$

$$A_3^+ = A^+(t - \tau_3) e^{i[w_L\tau_3+\varphi_3]} \quad \text{and} \quad A_3^- = A^-(t - \tau_3) e^{-i[w_L\tau_3+\varphi_3]} \quad (\text{E.5})$$

Then, the expansion of Equation (E.2) is written as

$$\begin{aligned}
\mathcal{P}_m^{(4)} = & A_1^+ A_1^+ A_1^- A_1^- + 2A_1^+ A_1^+ A_1^- A_2^- + 2A_1^+ A_1^+ A_1^- A_3^- \\
& + A_1^+ A_1^+ A_2^- A_2^- + 2A_1^+ A_1^+ A_2^- A_3^- + A_1^+ A_1^+ A_3^- A_3^- \\
& + 2A_1^+ A_2^+ A_1^- A_1^- + 4A_1^+ A_2^+ A_1^- A_2^- + 4A_1^+ A_2^+ A_1^- A_3^- \\
& + 2A_1^+ A_2^+ A_2^- A_2^- + 4A_1^+ A_2^+ A_2^- A_3^- + 2A_1^+ A_2^+ A_3^- A_3^- \\
& + 2A_1^+ A_3^+ A_1^- A_1^- + 4A_1^+ A_3^+ A_1^- A_2^- + 4A_1^+ A_3^+ A_1^- A_3^- \\
& + 2A_1^+ A_3^+ A_2^- A_2^- + 4A_1^+ A_3^+ A_2^- A_3^- + 2A_1^+ A_3^+ A_3^- A_3^- \\
& + A_2^+ A_2^+ A_1^- A_1^- + 2A_2^+ A_2^+ A_1^- A_2^- + 2A_2^+ A_2^+ A_1^- A_3^- \\
& + A_2^+ A_2^+ A_2^- A_2^- + 2A_2^+ A_2^+ A_2^- A_3^- + A_2^+ A_2^+ A_3^- A_3^- \\
& + 2A_2^+ A_3^+ A_1^- A_1^- + 4A_2^+ A_3^+ A_1^- A_2^- + 4A_2^+ A_3^+ A_1^- A_3^- \\
& + 2A_2^+ A_3^+ A_2^- A_2^- + 4A_2^+ A_3^+ A_2^- A_3^- + 2A_2^+ A_3^+ A_3^- A_3^- \\
& + A_3^+ A_3^+ A_1^- A_1^- + 2A_3^+ A_3^+ A_1^- A_2^- + 2A_3^+ A_3^+ A_1^- A_3^- \\
& + A_3^+ A_3^+ A_2^- A_2^- + 2A_3^+ A_3^+ A_2^- A_3^- + A_3^+ A_3^+ A_3^- A_3^-
\end{aligned} \tag{E.6}$$

A more compact notation for these 36 summands is given by

$$\mathcal{P}_m^{(4)} = \sum_{\substack{\text{Eqs. (E.8)} \\ \text{-(E.10)}}} \frac{4(A_1^+)^{\alpha_+} (A_1^-)^{\alpha_-} (A_2^+)^{\beta_+} (A_2^-)^{\beta_-} (A_3^+)^{\gamma_+} (A_3^-)^{\gamma_-}}{\alpha_+! \beta_+! \gamma_+! \alpha_-! \beta_-! \gamma_-!}, \tag{E.7}$$

where the coefficients α_+ , β_+ , γ_+ , α_- , β_- , and γ_- fulfill the following three conditions

$$\alpha_+ - \alpha_- = \alpha \quad \text{and} \quad \beta_+ - \beta_- = \beta \quad \text{and} \quad \gamma_+ - \gamma_- = \gamma \tag{E.8}$$

$$\alpha_+ + \beta_+ + \gamma_+ = 2 \quad \text{and} \quad \alpha_- + \beta_- + \gamma_- = 2 \tag{E.9}$$

$$\alpha + \beta + \gamma = 0. \tag{E.10}$$

The product of the factorial terms determines the prefactor (1, 2 or 4) of the respective contribution. Replacing

$$(A_1^+)^{\alpha_+} (A_1^-)^{\alpha_-} = B_{\alpha_-}^{\alpha_+}(\mathbf{r}, t, -\tau_1) e^{\alpha \varphi_1} \tag{E.11}$$

$$(A_2^+)^{\beta_+} (A_2^-)^{\beta_-} = B_{\beta_-}^{\beta_+}(\mathbf{r}, t, 0) e^{\beta \varphi_2} \tag{E.12}$$

$$(A_3^+)^{\gamma_+} (A_3^-)^{\gamma_-} = B_{\gamma_-}^{\gamma_+}(\mathbf{r}, t, \tau_3) e^{\gamma \varphi_3} \tag{E.13}$$

$$\text{and} \quad c_{\alpha_-, \beta_-, \gamma_-}^{\alpha_+, \beta_+, \gamma_+} = \frac{2(n/2!)}{\alpha_+! \beta_+! \gamma_+! \alpha_-! \beta_-! \gamma_-!} \tag{E.14}$$

the equation can be further simplified towards

$$\mathcal{P}_m^{(4)} = \sum_{\substack{\text{Eqs. (E.8)} \\ \text{-(E.10)}}} c_{\alpha_-, \beta_-, \gamma_-}^{\alpha_+, \beta_+, \gamma_+} B_{\alpha_-}^{\alpha_+}(\mathbf{r}, t, -\tau_1) B_{\beta_-}^{\beta_+}(\mathbf{r}, t, 0) B_{\gamma_-}^{\gamma_+}(\mathbf{r}, t, \tau_3) e^{\alpha \varphi_1 + \beta \varphi_2 + \gamma \varphi_3} \tag{E.15}$$

which is equivalent to the combination of Eqs. (4.22) and (4.23).

E.2. Partial Photoemission Rate for Lorentz Oscillator Response Function

The partial photoemission rate $\tilde{P}(t, \tau_1, \tau_3, \alpha, \beta, \gamma)$ is calculated by substituting Eq. (4.32) in Eq. (4.23):

$$\tilde{P}(t, \tau_1, \tau_3, \alpha, \beta, \gamma) \propto \Theta(t + \tau_1) e^{i\alpha\omega_{Lo}(t+\tau_1) - |\alpha|\gamma_{Lo}(t+\tau_1)} e^{-i\alpha\omega_L\tau_1} \\ \times \Theta(t) e^{i\beta\omega_{Lo}(t) - |\beta|\gamma_{Lo}(t)} \Theta(t - \tau_3) e^{i\gamma\omega_{Lo}(t-\tau_3) - |\gamma|\gamma_{Lo}(t-\tau_3)} e^{i\gamma\omega_L\tau_3}. \quad (\text{E.16})$$

The exponential functions are combined to two oscillating terms and a decaying term.

$$\tilde{P}(t, \tau_1, \tau_3, \alpha, \beta, \gamma) \propto \Theta(t + \tau_1) \Theta(t) \Theta(t - \tau_3) e^{i\omega_{Lo}[\alpha(t+\tau_1) + \beta t + \gamma(t-\tau_3)]} \\ \times e^{-i\omega_L(\alpha\tau_1 - \gamma\tau_3)} e^{-\gamma_{Lo}[|\alpha|(t+\tau_1) + |\beta|t + |\gamma|(t-\tau_3)]} \quad (\text{E.17})$$

The oscillations with $\pm\omega_{Lo}t$ cancel, whereas the decaying term is separated into a contribution dependent from the delays τ_1 and τ_3 and from the time variable t .

$$\tilde{P}(t, \tau_1, \tau_3, \alpha, \beta, \gamma) \propto \Theta(t + \tau_1) \Theta(t) \Theta(t - \tau_3) e^{i(\omega_{Lo} - \omega_L)[\alpha\tau_1 - \gamma\tau_3]} e^{-\gamma_{Lo}[|\alpha|\tau_1 - |\gamma|\tau_3]} e^{-4t\gamma_{Lo}} \quad (\text{E.18})$$

To calculate the partial photoemission yield $\tilde{Y}^{(4)}(\tau_1, \tau_3, \alpha, \beta, \gamma, \varphi_{21}, \varphi_{31})$ the above equation has to be integrated over t (see Eq. (4.4)). The Heaviside functions adjust the integration boundaries. As the delays τ_1 and τ_3 are defined positive, the lower boundary is determined by τ_3 .

$$\tilde{Y}^{(4)}(\tau_1, \tau_3, \alpha, \beta, \gamma) \propto e^{i(\omega_{Lo} - \omega_L)[\alpha\tau_1 - \gamma\tau_3]} e^{-\gamma_{Lo}[|\alpha|\tau_1 - |\gamma|\tau_3]} \int_{\tau_3}^{\infty} dt e^{-4t\gamma_{Lo}} \quad (\text{E.19})$$

After substituting $\alpha = -(\beta + \gamma)$ and $|\alpha| = 4 - |\beta| - |\gamma|$ and explicitly carrying out the integration, the relation does not contain the variables α and t anymore:

$$\tilde{Y}^{(4)}(\tau_1, \tau_3, \beta, \gamma) \propto e^{i(\omega_{Lo} - \omega_L)[-(\beta + \gamma)\tau_1 - \gamma\tau_3]} e^{-\gamma_{Lo}[(4 - |\beta| - |\gamma|)\tau_1 - |\gamma|\tau_3]} \frac{e^{-4\gamma_{Lo}\tau_3}}{-4\gamma_{Lo}}. \quad (\text{E.20})$$

This equation can be separated into factors depending only on one of the delays. Both delays are defined positive, otherwise the time-ordering within the sequence would be violated. This is expressed explicitly by inserting Heaviside functions and reshape towards

$$\tilde{Y}^{(4)}(\tau_1, \tau_3, \beta, \gamma) \propto \Theta(\tau_1) e^{(-i(\beta + \gamma)(\omega_{Lo} - \omega_L) - (4 - |\beta| - |\gamma|)\gamma_{Lo})\tau_1} \Theta(\tau_3) e^{(-i\gamma(\omega_{Lo} - \omega_L) - (4 - |\gamma|)\gamma_{Lo})\tau_3}, \quad (\text{E.21})$$

where the division by $-4\gamma_{Lo}$ was omitted for simplicity.

F. Lorentz Oscillator

In this thesis a Lorentz oscillator is used in several theoretical considerations as well as for the data evaluation. A Lorentz oscillator is a model system influenced by a restoring force expressed by ω_{Lo} and damping parameter γ_{Lo} via the differential equation

$$\frac{\partial^2 A_{Lo}(t)}{\partial t^2} + 2\gamma_{Lo} \frac{\partial A_{Lo}(t)}{\partial t} + \omega_{Lo}^2 A_{Lo}(t) = E_0(t) , \quad (F.1)$$

which is expressed in frequency domain via

$$-\omega^2 A_{Lo}(\omega) + 2i\omega\gamma_{Lo} A_{Lo}(\omega) + \omega_{Lo}^2 A_{Lo}(\omega) = E_0(\omega) . \quad (F.2)$$

The solution of the differential equation upon impulsive excitation, i.e. with a δ -shaped excitation pulse corresponding to a constant excitation spectrum $E_0(\omega) = 1$, delivers the spectral response function

$$A_{Lo}(\omega) = \frac{1}{\omega_{Lo}^2 - \omega^2 + 2i\gamma_{Lo}\omega} \quad (F.3)$$

If the damping parameter γ_{Lo} approaches the center frequency ω_{Lo} , the oscillator is strongly damped and electric field oscillations are suppressed. If the positive and negative spectral contributions to the Lorentz oscillator response are clearly separated, because the resonance frequency is much larger than the damping parameter ($\omega_{Lo} \gg \gamma_{Lo} > 0$), the Lorentz oscillator is approximated around the resonance frequency i.e. $\omega \approx \omega_{Lo}$ by

$$A_{Lo}^+(\omega) = \frac{1}{\omega_{Lo} - \omega + i\gamma_{Lo}} \quad \text{and} \quad A_{Lo}^-(\omega) = \frac{1}{\omega_{Lo} + \omega - i\gamma_{Lo}} . \quad (F.4)$$

$A_{Lo}^+(\omega)$ reproduces the positive spectral components and $A_{Lo}^-(\omega)$ the negative spectral components. The sum of both contributions has a form which is very similar to the Lorentz oscillator response function:

$$A_{Lo}^+(\omega) + A_{Lo}^-(\omega) = \frac{1}{\omega_{Lo} - \omega + i\gamma_{Lo}} + \frac{1}{\omega_{Lo} + \omega - i\gamma_{Lo}} \quad (F.5)$$

$$= \frac{2\omega_{Lo}}{\underbrace{(\gamma_{Lo}^2 + \omega_{Lo}^2)}_{=(\omega'_{Lo})^2} - \omega^2 + 2i\gamma_{Lo}\omega} \quad (F.6)$$

Under the condition $\omega_{Lo} \gg \gamma_{Lo}$ the influence of the damping on the resonance is weak, i.e. $\omega'_{Lo} \approx \omega_{Lo}$.

In time domain, the approximative Lorentz response exhibits an exponentially decaying oscillation:

$$A_{Lo}^+(t) = \Theta(t)e^{i\omega_{Lo}t - \gamma_{Lo}t} \quad \text{and} \quad A_{Lo}^-(t) = \Theta(t)e^{-i\omega_{Lo}t - \gamma_{Lo}t} \quad (F.7)$$

List of Figures

1.1. Absolute phase in femtosecond laser pulses	6
1.2. Coordinate system for elliptic representation	10
1.3. Polarization pulse shaper setup	14
1.4. Liquid crystal display	15
1.5. Polarization pulse shaping with LCD	16
1.6. Evolutionary algorithm	19
1.7. Basic properties of surface plasmon polaritons (SPP)	21
1.8. Propagating SPP imaged by PEEM	23
1.9. Localized plasmonic resonance in a spherical nanoparticle	24
1.10. Decay processes in localized plasmon resonances	26
1.11. Optical nanoantennas for coupling near-field and far-field	27
1.12. Spatial control of near-fields by local field interference	29
1.13. Spectral phase control by local pulse compression	30
1.14. 1PPE and time-resolved 2PPE excitation schemes	32
1.15. Schematic of photoemission electron microscope (PEEM)	34
1.16. Grazing incidence PEEM and normal incidence PEEM	35
1.17. Geometric conditions at sample for an incidence angle of 65°	36
1.18. Spatial resolution of PEEM setup	38
1.19. Multiphoton photoemission from nanoparticles	39
2.1. Analytic control of plasmonic nanostructures	42
2.2. Concept of optimal open-loop control of plasmonic nanostructures	43
2.3. UV-PEEM image of gold nanostructure used for optimal open-loop control	44
2.4. Setup for optimal open-loop control of plasmonic nanostructures	45
2.5. Dependence of gold nanoprism near-field distribution on wavevector and polarization direction	46
2.6. Distribution of electric field component E_z simulated by FDTD	47
2.7. Adaptive vs. open-loop control of nanoplasmonic excitation	50
3.1. Generation and detection scheme for ultrafast excitation switching	54
3.2. Excitation scheme for two-photon photoemission with single-color pump and probe	55
3.3. Setup for ultrafast excitation switching	59
3.4. SEM, 1PPE and pump and probe 2PPE from Ag-nanosun	60
3.5. Ultrafast excitation switching at silver nanostructure	61
4.1. Comparison of linear and nonlinear optical spectroscopy	64
4.2. Phenomena visible in optical 2D spectra	66
4.3. Comparison between coherent optical 2D spectroscopy and 2D nanoscopy	67
4.4. Spatial resolution of 2D nanoscopy	67

4.5. 2D nanoscopy excitation scheme for a quantum three-level system	68
4.6. 2D nanoscopy excitation scheme in fast dephasing systems	71
4.7. 2D nanoscopy Liouville pathways in a three level quantum system	74
4.8. Absolute and relative time variables	77
4.9. Analytical 2D nanoscopy spectra for a single Lorentz oscillator	82
4.10. Three pulse sequence with second pulse at zero delay position	85
4.11. Simulated temporal local field intensities	87
4.12. Simulated single oscillator 2D nanoscopy time domain signals	89
4.13. Phase cycled single oscillator 2D Nanoscopy time domain signals	91
4.14. Simulated single oscillator 2D nanoscopy spectra	92
4.15. Influence on phase cycling on simulated 2D spectra	93
4.16. Inhomogeneous linewidth in simulated 2D spectrum	95
4.17. 2D nanoscopy spectra in dependence of excitation spectrum and nonlinearity	96
4.18. Rescaling scheme for fitted experimental data	99
4.19. Simulation data point positions and fitted parameters	100
4.20. Simulation and fit parameters for different nonlinear orders	101
5.1. Setup for coherent control and 2D nanoscopy on silver	104
5.2. SEM and AFM images of corrugated topography of silver surface	104
5.3. PEEM image of silver surface and local power law	105
5.4. Near-field control superenhancement	107
5.5. Sub-diffraction control of photoemission hot spots	109
5.6. Reproducibility of coherent control at single hot spot	110
5.7. Two-parameter control scan: PEEM image	111
5.8. Two-parameter control scan: ROIs	112
5.9. Optimal pulses of two-dimensional pulse parameter scans	113
5.10. PEEM reference image for 2D nanoscopy with wide field of view	115
5.11. Spatial lifetime map at photoemission hot spot	116
5.12. Local evaluation of 2D spectra	117
5.13. Pulse sequence for two-pulse nanoscopy experiment and PEEM image with ROIs	119
5.14. Results of two-pulse nanoscopy simulations and experiment	120
5.15. Two-pulse nanoscopy simulations for two oscillators	122
5.16. Hybridization of dark and bright plasmonic modes	124
5.17. Evaluation results for two-pulse nanoscopy scan in ROI1 and ROI2	127
6.1. Light energy conversion in thin-film solar cells	133
6.2. Electronic density of states and absorption of hydrogenated amorphous silicon (a-Si:H)	134
6.3. Photon management strategies in thin-film solar cells	135
6.4. Light trapping and localization in nanostructured systems	135
6.5. Structural properties of investigated thin-film solar cells	137
6.6. Linear absorption spectrum for different thin-film solar cell designs	138
6.7. Spectral interferometry of backscattered radiation from a-Si:H thin-film solar cells	140
6.8. Spatial resolved backscattering spectra	141
6.9. Backscattered electric field from a-Si:H thin-film samples in time domain representation	142

6.10. Spatial distribution of nonlinear order N of emission process	143
6.11. Thermionic emission scheme	144
6.12. Thermionic emission model for a-Si:H.	146
6.13. Absorbed energy density distribution	148
6.14. Experimental local 2D nanoscopy and fit results on a-Si:H	150
6.15. Local response parameter distributions obtained by 2D nanoscopy	152
6.16. Spatial resolution of 2D nanoscopy	153
A.1. Second-Harmonic FROG setup	161
A.2. Simulated SHG FROG trace	163
A.3. Spectral interferometry setup for polarization shaped laser pulses	164
B.1. Drift detection and correction of PEEM data	171
B.2. Drift detection of simulated data	173
B.3. Statistical evaluation of drift detection	174
B.4. Comparison of initial with drift corrected image	175
D.1. Liouville pathways in a coupled two-level system	185
D.2. Pulse sequence and setup for coherent optical 2D spectroscopy	187

Bibliography

- [1] Stephenson, N. T. (1988) *Zodiac*. (Atlantic monthly Press).
- [2] Aeschlimann, M, Bauer, M, Bayer, D, Brixner, T, Cunovic, S, Dimler, F, Fischer, A, Pfeiffer, W, Rohmer, M, Schneider, C, Steeb, F, Strüber, C, & Voronine, D. V. (2010) Spatiotemporal control of nanooptical excitations. *Proceedings of the National Academy of Sciences of the United States of America* **107**, 5329–5333.
- [3] Aeschlimann, M, Brixner, T, Cunovic, S, Fischer, A, Melchior, P, Pfeiffer, W, Rohmer, M, Schneider, C, Strüber, C, Tuchscherer, P, & Voronine, D. V. (2012) Nano-optical control of hot-spot field superenhancement on a corrugated silver surface. *IEEE Journal of Selected Topics in Quantum Electronics* **18**, 275–282.
- [4] Aeschlimann, M, Brixner, T, Fischer, A, Kramer, C, Melchior, P, Pfeiffer, W, Schneider, C, Strüber, C, Tuchscherer, P, & Voronine, D. V. (2011) Coherent two-dimensional nanoscopy. *Science* **333**, 1723–1726.
- [5] Aeschlimann, M, Bauer, M, Bayer, D, Brixner, T, Cunovic, S, Fischer, A, Melchior, P, Pfeiffer, W, Rohmer, M, Schneider, C, Strüber, C, Tuchscherer, P, & Voronine, D. V. (2012) Optimal open-loop near-field control of plasmonic nanostructures. *New Journal of Physics* **14**.
- [6] Aeschlimann, M, Bauer, M, Bayer, D, Brixner, T, Cunovic, S, Dimler, F, Fischer, A, Pfeiffer, W, Rohmer, M, Schneider, C, Steeb, F, Strüber, C, & Voronine, D. V. (2009) in *Ultrafast Phenomena XVI*, Springer Series in Chemical Physics, eds. Corkum, P, Silvestri, S, Nelson, K. A, Riedle, E, & Schoenlein, R. W. (Springer Berlin Heidelberg) No. 92, pp. 705–707.
- [7] Aeschlimann, M, Bauer, M, Bayer, D, Brixner, T, Cunovic, S, Fischer, A, Melchior, P, Pfeiffer, W, Rohmer, W, Schneider, C, Strüber, C, Tuchscherer, P, & Voronine, D. V. (2010) *Deterministic control of subwavelength field localization in plasmonic nanoantennas*, Proc. 17th Int. Conference, Ultrafast Phenomena XVII eds. Chergui, M, Jonas, D. M, Riedle, E, Schoenlein, R. W, & Taylor, A. J. p. 667.
- [8] Aeschlimann, M, Bauer, M, Bayer, D, Brixner, T, Cunovic, S, Fischer, A, Melchior, P, Pfeiffer, W, Rohmer, M, Schneider, C, Strüber, C, Tuchscherer, P, & Voronine, D. V. (2010) *Deterministic Control of Subwavelength Field Localization in Plasmonic Nanoantennas*, OSA Technical Digest (CD). (Optical Society of America), p. WA2.
- [9] Keller, U. (2003) Recent developments in compact ultrafast lasers. *Nature* **424**, 831–838.
- [10] Brabec, T & Krausz, F. (2000) Intense few-cycle laser fields: Frontiers of nonlinear optics. *Reviews of Modern Physics* **72**, 545–591.

- [11] Diels, J.-C & Rudolph, W. (2006) *Ultrashort Laser Pulse Phenomena: Fundamentals, Techniques, and Applications on a Femtosecond Time Scale*. (Academic Press).
- [12] Weiner, A, Leaird, D, Patel, J, & Wullert, J. (1990) Programmable femtosecond pulse shaping by use of a multielement liquid-crystal phase modulator. *Optics Letters* **15**, 326–328.
- [13] Brixner, T & Gerber, G. (2001) Femtosecond polarization pulse shaping. *Opt. Lett.* **26**, 557–559.
- [14] Ninck, M, Galler, A, Feurer, T, & Brixner, T. (2007) Programmable common-path vector field synthesizer for femtosecond pulses. *Optics Letters* **32**, 3379–3381.
- [15] Mukamel, S. (1999) *Principles of Nonlinear Optical Spectroscopy*. (Oxford University Press), New edition.
- [16] Novotny, L & Hecht, B. (2006) *Principles of Nano-Optics*. (Cambridge University Press).
- [17] Maier, S. A. (2007) *Plasmonics: Fundamentals and Applications*. (Springer), 2007 edition.
- [18] Ozbay, E. (2006) Plasmonics: Merging photonics and electronics at nanoscale dimensions. *Science* **311**, 189–193.
- [19] Lin, J, Mueller, J. P. B, Wang, Q, Yuan, G, Antoniou, N, Yuan, X.-C, & Capasso, F. (2013) Polarization-controlled tunable directional coupling of surface plasmon polaritons. *Science* **340**, 331–334.
- [20] Brongersma, M. L & Shalaev, V. M. (2010) The case for plasmonics. *Science* **328**, 440–441.
- [21] Cai, W, White, J. S, & Brongersma, M. L. (2009) Compact, high-speed and power-efficient electrooptic plasmonic modulators. *Nano Letters* **9**, 4403–4411.
- [22] Zia, R, Schuller, J. A, Chandran, A, & Brongersma, M. L. (2006) Plasmonics: the next chip-scale technology. *Materials Today* **9**, 20–27.
- [23] Bergman, D & Stockman, M. (2003) Surface plasmon amplification by stimulated emission of radiation: Quantum generation of coherent surface plasmons in nanosystems. *Phys. Rev. Lett.* **90**, 027402.
- [24] Stockman, M. (2008) Spasers explained. *Nature Photonics* **2**, 327–329.
- [25] Atwater, H. A & Polman, A. (2010) Plasmonics for improved photovoltaic devices. *Nature Materials* **9**, 205–213.
- [26] Mühlischlegel, P, Eisler, H.-J, Martin, O, Hecht, B, & Pohl, D. (2005) Resonant optical antennas. *Science* **308**, 1607–1609.
- [27] Taminiau, T. H, Stefani, F. D, Segerink, F. B, & Van Hulst, N. F. (2008) Optical antennas direct single-molecule emission. *Nature Photonics* **2**, 234–237.
- [28] Novotny, L & van Hulst, N. (2011) Antennas for light. *Nature Photonics* **5**, 83–90.

- [29] Kneipp, K, Wang, Y, Kneipp, H, Perelman, L. T, Itzkan, I, Dasari, R. R, & Feld, M. S. (1997) Single molecule detection using surface-enhanced raman scattering (SERS). *Physical Review Letters* **78**, 1667–1670.
- [30] Nie, S & Emory, S. R. (1997) Probing single molecules and single nanoparticles by surface-enhanced raman scattering. *Science* **275**, 1102–1106.
- [31] Kneipp, K, Haka, A. S, Kneipp, H, Badizadegan, K, Yoshizawa, N, Boone, C, Shafer-Peltier, K. E, Motz, J. T, Dasari, R. R, & Feld, M. S. (2002) Surface-enhanced raman spectroscopy in single living cells using gold nanoparticles. *Applied Spectroscopy* **56**, 150–154.
- [32] Willets, K. A & Van Duyne, R. P. (2007) Localized surface plasmon resonance spectroscopy and sensing. *Annual Review of Physical Chemistry* **58**, 267–297.
- [33] Stiles, P. L, Dieringer, J. A, Shah, N. C, & Van Duyne, R. P. (2008) Surface-enhanced raman spectroscopy. *Annual Review of Analytical Chemistry* **1**, 601–626.
- [34] Wang, Z, Pan, S, Krauss, T. D, Du, H, & Rothberg, L. J. (2003) The structural basis for giant enhancement enabling single-molecule raman scattering. *Proceedings of the National Academy of Sciences* **100**, 8638–8643.
- [35] Rashed, R. (1990) A pioneer in anaclastics: Ibn Sahl on burning mirrors and lenses. *Isis* **81**, 464–491.
- [36] Hooke, R. (1667) *Micrographia: or, Some physiological descriptions of minute bodies made by magnifying glasses. With observations and inquiries thereupon.*
- [37] van Leewenhoek, A. (1677) Observations, communicated to the publisher by mr. antony van leewenhoek, in a dutch letter of the 9th of octob. 1676. here english'd: concerning little animals by him observed in rain-well-sea. and snow water; as also in water wherein pepper had lain infused. *Philosophical Transactions* **12**, 821–831.
- [38] Abbe, E. (1873) Beiträge zur Theorie des Mikroskops und der mikroskopischen Wahrnehmung. *Archiv f. Mikrosk. Anat.* **9**, 413.
- [39] Wollaston, W. H. (1802) A method of examining refractive and dispersive powers, by prismatic reflection. *Philosophical Transactions of the Royal Society of London* **92**, 365–380.
- [40] Fraunhofer, J. (1814–1815) Bestimmung des Brechungs- und des Farben-Zerstreuungs - Vermögens verschiedener Glasarten, in Bezug auf die Vervollkommnung achromatischer Fernrohre. *Denkschriften der Königlichen Akademie der Wissenschaften zu München* **5**, 193–226.
- [41] Udem, T, Holzwarth, R, & Hänsch, T. W. (2002) Optical frequency metrology. *Nature* **416**, 233–237.
- [42] Corkum, P. B & Krausz, F. (2007) Attosecond science. *Nature Physics* **3**, 381–387.
- [43] Brito Cruz, C, Fork, R, Knox, W, & Shank, C. (1986) Spectral hole burning in large molecules probed with 10 fs optical pulses. *Chemical Physics Letters* **132**, 341–344.

- [44] Weiner, A. (2011) *Ultrafast Optics*. (John Wiley & Sons).
- [45] Mukamel, S. (2000) Multidimensional femtosecond correlation spectroscopies of electronic and vibrational excitations. *Annual Review of Physical Chemistry* **51**, 691–729.
- [46] Keusters, D, Tan, H.-S, & Warren. (1999) Role of pulse phase and direction in two-dimensional optical spectroscopy. *The Journal of Physical Chemistry A* **103**, 10369–10380.
- [47] Jonas, D. M. (2003) Two-dimensional femtosecond spectroscopy. *Annual Review of Physical Chemistry* **54**, 425–463.
- [48] Brixner, T, Stenger, J, Vaswani, H. M, Cho, M, Blankenship, R. E, & Fleming, G. R. (2005) Two-dimensional spectroscopy of electronic couplings in photosynthesis. *Nature* **434**, 625–628.
- [49] Tian, P, Keusters, D, Suzuki, Y, & Warren, W. S. (2003) Femtosecond phase-coherent two-dimensional spectroscopy. *Science* **300**, 1553–1555.
- [50] Cho, M. (2008) Coherent two-dimensional optical spectroscopy. *Chemical reviews* **108**, 1331–1418.
- [51] Aue, W. P, Bartholdi, E, & Ernst, R. R. (1976) Two-dimensional spectroscopy. application to nuclear magnetic resonance. *The Journal of Chemical Physics* **64**, 2229–2246.
- [52] Zewail, A. H. (1988) Laser femtochemistry. *Science* **242**, 1645–1653.
- [53] Zewail, A. H. (1993) Femtochemistry. *The Journal of Physical Chemistry* **97**, 12427–12446.
- [54] Warren, W. S, Rabitz, H, & Dahleh, M. (1993) Coherent control of quantum dynamics: The dream is alive. *Science* **259**, 1581–1589.
- [55] Assion, A, Baumert, T, Bergt, M, Brixner, T, Kiefer, B, Seyfried, V, Strehle, M, & Gerber, G. (1998) Control of Chemical Reactions by Feedback-Optimized Phase-Shaped Femtosecond Laser Pulses. *Science* **282**, 919–922.
- [56] Brixner, T, Damrauer, N, Niklaus, P, & Gerber, G. (2001) Photosensitive adaptive femtosecond quantum control in the liquid phase. *Nature* **414**, 57–60.
- [57] Rullière, C. (2004) *Femtosecond Laser Pulses: Principles and Experiments*. (Springer), 2nd edition.
- [58] Brinks, D, Stefani, F. D, Kulzer, F, Hildner, R, Taminiau, T. H, Avlasevich, Y, Müllen, K, & Van Hulst, N. F. (2010) Visualizing and controlling vibrational wave packets of single molecules. *Nature* **465**, 905–908.
- [59] Hildner, R, Brinks, D, & van Hulst, N. F. (2010) Femtosecond coherence and quantum control of single molecules at room temperature. *Nature Physics* **7**, 172–177.
- [60] Hell, S. W. (2007) Far-field optical nanoscopy. *Science* **316**, 1153–1158.
- [61] Hell, S. W & Wichmann, J. (1994) Breaking the diffraction resolution limit by stimulated emission: stimulated-emission-depletion fluorescence microscopy. *Optics Letters* **19**, 780–782.

- [62] Rust, M. J, Bates, M, & Zhuang, X. (2006) Sub-diffraction-limit imaging by stochastic optical reconstruction microscopy (STORM). *Nature Methods* **3**, 793–796.
- [63] Huang, B, Wang, W, Bates, M, & Zhuang, X. (2008) Three-dimensional super-resolution imaging by stochastic optical reconstruction microscopy. *Science* **319**, 810–813.
- [64] Heilemann, M, van de Linde, S, Schüttelpe, M, Kasper, R, Seefeldt, B, Mukherjee, A, Tinnefeld, P, & Sauer, M. (2008) Subdiffraction-resolution fluorescence imaging with conventional fluorescent probes. *Angewandte Chemie International Edition* **47**, 6172–6176.
- [65] Hess, S. T, Girirajan, T. P, & Mason, M. D. (2006) Ultra-high resolution imaging by fluorescence photoactivation localization microscopy. *Biophysical Journal* **91**, 4258–4272.
- [66] Gustafsson, M. G. L. (2005) Nonlinear structured-illumination microscopy: Wide-field fluorescence imaging with theoretically unlimited resolution. *Proceedings of the National Academy of Sciences of the United States of America* **102**, 13081–13086.
- [67] Binnig, G, Rohrer, H, Gerber, C, & Weibel, E. (1982) Tunneling through a controllable vacuum gap. *Applied Physics Letters* **40**, 178–180.
- [68] Binnig, G & Rohrer, H. (1983) Scanning tunneling microscopy. *Surface Science* **126**, 236–244.
- [69] Binnig, G, Quate, C. F, & Gerber, C. (1986) Atomic force microscope. *Physical Review Letters* **56**, 930–933.
- [70] Pohl, D. W, Denk, W, & Lanz, M. (1984) Optical stethoscopy: Image recording with resolution $\lambda/20$. *Applied Physics Letters* **44**, 651–653.
- [71] Pohl, D. W, Fischer, U. C, & Dürig, U. T. (1988) Scanning near-field optical microscopy (SNOM). *Journal of Microscopy* **152**, 853–861.
- [72] Hecht, B, Sick, B, Wild, U. P, Deckert, V, Zenobi, R, Martin, O. J. F, & Pohl, D. W. (2000) Scanning near-field optical microscopy with aperture probes: Fundamentals and applications. *The Journal of Chemical Physics* **112**, 7761–7774.
- [73] Guenther, T, Lienau, C, Elsaesser, T, Glanemann, M, Axt, V. M, Kuhn, T, Eshlaghi, S, & Wieck, A. D. (2002) Coherent nonlinear optical response of single quantum dots studied by ultrafast near-field spectroscopy. *Physical Review Letters* **89**, 057401.
- [74] Balistreri, M. L. M, Gersen, H, Korterik, J. P, Kuipers, L, & Hulst, N. F. v. (2001) Tracking femtosecond laser pulses in space and time. *Science* **294**, 1080–1082.
- [75] Gersen, H, Karle, T. J, Engelen, R. J. P, Bogaerts, W, Korterik, J. P, van Hulst, N. F, Krauss, T. F, & Kuipers, L. (2005) Real-space observation of ultraslow light in photonic crystal waveguides. *Physical Review Letters* **94**, 073903.
- [76] Mulvey, T, Kazan, B, & Hawkes, P. W. (1996) *The growth of electron microscopy*. (Academic Press) Vol. 96.
- [77] Williams, D. B & Carter, C. B. (1996) in *Transmission Electron Microscopy*. (Springer US), pp. 3–17.

- [78] Goldstein, J, Newbury, D. E, Joy, D. C, Lyman, C. E, Echlin, P, Lifshin, E, Sawyer, L, & Michael, J. R. (2003) *Scanning Electron Microscopy and X-ray Microanalysis*. (Springer).
- [79] Gunther, S, Kaulich, B, Gregoratti, L, & Kiskinova, M. (2002) Photoelectron microscopy and applications in surface and materials science. *Progress in Surface Science* **70**, 187–260.
- [80] Feng, J & Scholl, A. (2007) in *Science of Microscopy*, eds. Hawkes, P. W & Spence, J. C. H. (Springer New York), pp. 657–695.
- [81] Cinchetti, M, Gloskovskii, A, Nepjiko, S. A, Schonhense, G, Rochholz, H, & Kreiter, M. (2005) Photoemission electron microscopy as a tool for the investigation of optical near fields. *Phys. Rev. Lett.* **95**, 047601.
- [82] Schmidt, O, Bauer, M, Wiemann, C, Porath, R, Scharte, M, Andreyev, O, Schönhense, G, & Aeschlimann, M. (2002) Time-resolved two photon photoemission electron microscopy. *Applied Physics B* **74**, 223–227.
- [83] Stockman, M, Faleev, S, & Bergman, D. (2002) Coherent control of femtosecond energy localization in nanosystems. *Phys. Rev. Lett.* **88**, 067402.
- [84] Stockman, M, Bergman, D, & Kobayashi, T. (2004) Coherent control of nanoscale localization of ultrafast optical excitation in nanosystems. *Physical Review B* **69**, 54202.
- [85] Brixner, T, Garcia de Abajo, F. J, Schneider, J, & Pfeiffer, W. (2005) Nanoscopic ultrafast space-time-resolved spectroscopy. *Phys. Rev. Lett.* **95**, 093901.
- [86] Brixner, T, García de Abajo, F. J, Schneider, J, Spindler, C, & Pfeiffer, W. (2006) Ultrafast adaptive optical near-field control. *Physical Review B (Condensed Matter and Materials Physics)* **73**, 125437.
- [87] Tuchscherer, P, Rewitz, C, Voronine, D. V, Javier Garcia de Abajo, F, Pfeiffer, W, & Brixner, T. (2009) Analytic coherent control of plasmon propagation in nanostructures. *Opt. Express* **17**, 14235–14259.
- [88] Aeschlimann, M, Bauer, M, Bayer, D, Brixner, T, Garcia de Abajo, F. J, Pfeiffer, W, Rohmer, M, Spindler, C, & Steeb, F. (2007) Adaptive subwavelength control of nano-optical fields. *Nature* **446**, 301–304.
- [89] Brixner, T, Mančal, T, Stiopkin, I. V, & Fleming, G. R. (2004) Phase-stabilized two-dimensional electronic spectroscopy. *The Journal of Chemical Physics* **121**, 4221–4236.
- [90] Carlson, D. E & Wronski, C. R. (1976) Amorphous silicon solar cell. *Applied Physics Letters* **28**, 671–673.
- [91] Street, R. A. (2005) *Hydrogenated amorphous silicon*. (Cambridge University Press).
- [92] Aeschlimann, M, Brixner, T, Differt, D, Hensen, M, Ulrich, H, Kramer, C, Lükermann, F, Melchior, P, Pfeiffer, W, Piecuch, M, Schneider, C, Stiebig, H, Strüber, C, & Thielen, P. (2013) How do thin-film solar cells absorb light? *submitted*.
- [93] Richardson, O. W. O. W. (1921) *The emission of electricity from hot bodies*. (London, New York [etc.] : Longmans, Green and co.).

- [94] Dushman, S. (1923) Electron emission from metals as a function of temperature. *Physical Review* **21**, 623–636.
- [95] Riffe, D. M, Wang, X. Y, Downer, M. C, Fisher, D. L, Tajima, T, Erskine, J. L, & More, R. M. (1993) Femtosecond thermionic emission from metals in the space-charge-limited regime. *Journal of the Optical Society of America B* **10**, 1424–1435.
- [96] Jackson, J. D. (1999) *Classical electrodynamics*. (Wiley, New York), 3 edition.
- [97] Rand, S. C. (2010) *Lectures on light: Nonlinear and quantum optics using the density matrix*. (Oxford University Press).
- [98] Jones, D. J, Diddams, S. A, Ranka, J. K, Stentz, A, Windeler, R. S, Hall, J. L, & Cundiff, S. T. (2000) Carrier-envelope phase control of femtosecond mode-locked lasers and direct optical frequency synthesis. *Science* **288**, 635–639.
- [99] Apolonski, A, Poppe, A, Tempea, G, Spielmann, C, Udem, T, Holzwarth, R, Hänsch, T. W, & Krausz, F. (2000) Controlling the phase evolution of few-cycle light pulses. *Physical Review Letters* **85**, 740–743.
- [100] Hentschel, M, Kienberger, R, Spielmann, C, Reider, G. A, Milosevic, N, Brabec, T, Corkum, P, Heinzmann, U, Drescher, M, & Krausz, F. (2001) Attosecond metrology. *Nature* **414**, 509–513.
- [101] Baltuška, A, Udem, T, Uiberacker, M, Hentschel, M, Goulielmakis, E, Gohle, C, Holzwarth, R, Yakovlev, V. S, Scrinzi, A, Hänsch, T. W, & Krausz, F. (2003) Attosecond control of electronic processes by intense light fields. *Nature* **421**, 611–615.
- [102] Goulielmakis, E, Uiberacker, M, Kienberger, R, Baltuska, A, Yakovlev, V, Scrinzi, A, Westerwalbesloh, T, Kleineberg, U, Heinzmann, U, Drescher, M, & Krausz, F. (2004) Direct measurement of light waves. *Science* **305**, 1267–1269.
- [103] Cavalieri, A. L, Müller, N, Uphues, T, Yakovlev, V. S, Baltuška, A, Horvath, B, Schmidt, B, Blümel, L, Holzwarth, R, Hendel, S, Drescher, M, Kleineberg, U, Echenique, P. M, Kienberger, R, Krausz, F, & Heinzmann, U. (2007) Attosecond spectroscopy in condensed matter. *Nature* **449**, 1029–1032.
- [104] Apolonski, A, Dombi, P, Paulus, G. G, Kakehata, M, Holzwarth, R, Udem, T, Lemell, C, Torizuka, K, Burgdörfer, J, Hänsch, T. W, & Krausz, F. (2004) Observation of light-phase-sensitive photoemission from a metal. *Physical Review Letters* **92**, 073902.
- [105] Krüger, M, Schenk, M, & Hommelhoff, P. (2011) Attosecond control of electrons emitted from a nanoscale metal tip. *Nature* **475**, 78–81.
- [106] Bracewell, R. N & Bracewell, R. (1986) *The Fourier transform and its applications*. (McGraw-Hill New York) Vol. 31999.
- [107] Bronshtein, I. (2007) *Handbook of mathematics*. (Springer).
- [108] Boyd, R. W. (2008) *Nonlinear Optics*. (Academic Press), 3 edition.

- [109] Brixner, T. (2001) Adaptiv femtosecond quantum control (Dissertation, Julius-Maximilians-University Würzburg, Dep. of Physics).
- [110] Brixner, T, Krampert, G, Niklaus, P, & Gerber, G. (2002) Generation and characterization of polarization-shaped femtosecond laser pulses. *Appl. Phys. B* **74**, S133–S144.
- [111] Brixner, T. (2003) Poincaré representation of polarization-shaped femtosecond laser pulses. *Appl. Phys. B* **76**, 531–540.
- [112] Born, M & Wolf, E. (2010) *Principles of optics: electromagnetic theory of propagation, interference and diffraction of light*. (Cambridge Univ. Press, Cambridge).
- [113] Poincaré, H. (1892) *Théorie mathématique de la lumière II. Nouvelles études sur la diffraction.–Théorie de la dispersion de Helmholtz. Leçons professées pendant le premier semestre 1891-1892*. (G. Carré, Paris).
- [114] Herek, J. L, Wohlleben, W, Cogdell, R. J, Zeidler, D, & Motzkus, M. (2002) Quantum control of energy flow in light harvesting. *Nature* **417**, 533–535.
- [115] Köhler, J, Wollenhaupt, M, Bayer, T, Sarpe, C, & Baumert, T. (2011) Zeptosecond precision pulse shaping. *Optics Express* **19**, 11638–11653.
- [116] Heritage, J. P, Weiner, A. M, & Thurston, R. N. (1985) Picosecond pulse shaping by spectral phase and amplitude manipulation. *Optics Letters* **10**, 609–611.
- [117] Weiner, A. M, Heritage, J. P, & Kirschner, E. M. (1988) High-resolution femtosecond pulse shaping. *Journal of the Optical Society of America B* **5**, 1563–1572.
- [118] Weiner, A, Leaird, D, Patel, J, & Wullert, J. (1992) Programmable shaping of femtosecond optical pulses by use of 128-element liquid-crystal phase modulator. *IEEE Journal of Quantum Electronics* **28**, 908–920.
- [119] Weiner, A. (2000) Femtosecond pulse shaping using spatial light modulators. *Rev. Sci. Instrum.* **71**, 1929.
- [120] Weise, F & Lindinger, A. (2009) Full control over the electric field using four liquid crystal arrays. *Optics Letters* **34**, 1258–1260.
- [121] Fechner, T. (2008) Quantenkontrolle im Zeit-Frequenz-Phasenraum (Dissertation, Julius-Maximilians-University Würzburg, Dep. of Physics).
- [122] Gennes, P. G. d & Prost, J. (1995) *The Physics of Liquid Crystals*. (Oxford University Press, USA), 2 edition.
- [123] Collings, P. J & Hird, M. (1997) *Introduction to Liquid Crystals: Chemistry and Physics*. (CRC Press).
- [124] Collings, P. J. (2001) *Liquid Crystals: Nature's Delicate Phase of Matter, Second Edition*. (Princeton University Press), 2 sub edition.
- [125] Fechner, T. (2005) Aufbau eines Polarisationsimpulsformers zur optimalen Kontrolle chemischer Reaktionen (Diploma thesis, Julius-Maximilians-University Würzburg, Dep. of Physics).

- [126] Tuchscherer, P. (2012) A route to optical spectroscopy on the nanoscale (Dissertation, Julius-Maximilians-University Würzburg, Dep. of Physics).
- [127] Jones, R. C. (1948) A new calculus for the treatment of optical systems. vii. properties of the n-matrices. *J. Opt. Soc. Am.* **38**, 671–683.
- [128] Brixner, T, Damrauer, N. H, Kiefer, B, & Gerber, G. (2003) Liquid-phase adaptive femtosecond quantum control: Removing intrinsic intensity dependencies. *The Journal of Chemical Physics* **118**, 3692–3701.
- [129] Uphues, T. (2001) Adaptive femtosecond laser pulse shaping for high harmonic optimization (Diploma thesis, University of Bielefeld, Dep. of Physics).
- [130] Stockman, M. (2008) Ultrafast nanoplasmonics under coherent control. *New Journal of Physics* **10**, 025031 (20pp).
- [131] Volpe, G, Molina-Terriza, G, & Quidant, R. (2010) Deterministic subwavelength control of light confinement in nanostructures. *Physical Review Letters* **105**, 216802.
- [132] Li, X & Stockman, M. (2008) Highly efficient spatiotemporal coherent control in nanoplasmonics on a nanometer-femtosecond scale by time reversal (10 pages). *Physical Review-Section B-Condensed Matter* **77**, 195109–195109.
- [133] Lerosey, G, de Rosny, J, Tourin, A, & Fink, M. (2007) Focusing beyond the diffraction limit with far-field time reversal. *Science* **315**, 1120–1122.
- [134] Goldberg, D. (1993) *Genetic algorithms in search, optimization, and machine learning*. (Addison-Wesley).
- [135] Schwefel, H.-P. (1995) *Evolution and optimum seeking*. (Wiley).
- [136] Hoffmeister, F & Bäck, T. (1991) in *Parallel Problem Solving from Nature*, Lecture Notes in Computer Science, eds. Schwefel, H.-P & Männer, R. (Springer Berlin / Heidelberg) Vol. 496, pp. 455–469.
- [137] Darwin, C & Bynum, W. F. (2009) *The origin of species by means of natural selection: or, the preservation of favored races in the struggle for life*. (AL Burt).
- [138] Fechner, S, Dimler, F, Brixner, T, Gerber, G, & Tannor, D. J. (2007) The von neumann picture: a new representation for ultrashort laser pulses. *Optics Express* **15**, 15387–15401.
- [139] Rützel, S, Kriskche, A, & Brixner, T. (2012) The von neumann representation as a joint time-frequency parameterization for polarization-shaped femtosecond laser pulses. *Applied Physics B* **107**, 1–9.
- [140] Saleh, B & Teich, M. (2007) *Fundamentals of photonics*, Wiley series in pure and applied optics. (Wiley-Interscience).
- [141] Ritchie, R. H. (1957) Plasma losses by fast electrons in thin films. *Phys. Rev.* **106**, 874–881.
- [142] Ritchie, R. (1959) Interaction of charged particles with a degenerate fermi-dirac electron gas. *Phys. Rev.* **114**, 644–654.

- [143] Barnes, W, Dereux, A, & Ebbesen, T. (2003) Surface plasmon subwavelength optics. *Nature* **424**, 824–830.
- [144] Koppens, F. H. L, Chang, D. E, & García de Abajo, F. J. (2011) Graphene plasmonics: A platform for strong Light-Matter interactions. *Nano Letters* **11**, 3370–3377.
- [145] Chen, J, Badioli, M, Alonso-González, P, Thongrattanasiri, S, Huth, F, Osmond, J, Spasenovic, M, Centeno, A, Pesquera, A, Godignon, P, Zurutuza Elorza, A, Camara, N, de Abajo, F. J. G, Hillenbrand, R, & Koppens, F. H. L. (2012) Optical nano-imaging of gate-tunable graphene plasmons. *Nature, advanced online publication*.
- [146] Fei, Z, Rodin, A, Andreev, G, Bao, W, McLeod, A, Wagner, M, Zhang, L, Zhao, Z, Thiemens, M, Dominguez, G, et al. (2012) Gate-tuning of graphene plasmons revealed by infrared nano-imaging. *Nature, advanced online publication*.
- [147] Ordal, M. A, Bell, R. J, Alexander Jr, R, Long, L, Querry, M, et al. (1985) Optical properties of fourteen metals in the infrared and far infrared: Al, co, cu, au, fe, pb, mo, ni, pd, pt, ag, ti, v, and w. *Applied Optics* **24**, 4493–4499.
- [148] Wood, R. W. (1902) On a remarkable case of uneven distribution of light in a diffraction grating spectrum. *Proceedings of the Physical Society of London* **18**, 269.
- [149] Ritchie, R. H, Arakawa, E. T, Cowan, J. J, & Hamm, R. N. (1968) Surface-plasmon resonance effect in grating diffraction. *Physical Review Letters* **21**, 1530–1533.
- [150] Rotenberg, N, Betz, M, & van Driel, H. M. (2008) Ultrafast control of grating-assisted light coupling to surface plasmons. *Optics Letters* **33**, 2137–2139.
- [151] Otto, A. (1968) Excitation of nonradiative surface plasma waves in silver by the method of frustrated total reflection. *Zeitschrift für Physik* **216**, 398–410.
- [152] Kretschmann, E. (1971) Die bestimmung optischer konstanten von metallen durch anregung von oberflächenplasmaschwingungen. *Zeitschrift für Physik* **241**, 313–324.
- [153] Ditlbacher, H, Krenn, J. R, Felidj, N, Lamprecht, B, Schider, G, Salerno, M, Leitner, A, & Aussenegg, F. R. (2002) Fluorescence imaging of surface plasmon fields. *Applied Physics Letters* **80**, 404–406.
- [154] Lemke, C, Schneider, C, Leißner, T, Bayer, D, Radke, J. W, Fischer, A, Melchior, P, Evlyukhin, A. B, Chichkov, B. N, Reinhardt, C, Bauer, M, & Aeschlimann, M. (2013) Spatiotemporal characterization of SPP pulse propagation in two-dimensional plasmonic focusing devices. *Nano Letters* **13**, 1053–1058.
- [155] Buckanie, N, Kirschbaum, P, Sindermann, S, & zu Heringdorf, F. M. (2013) Interaction of light and surface plasmon polaritons in ag islands studied by nonlinear photoemission microscopy. *Ultramicroscopy*.
- [156] Raschke, M. B & Lienau, C. (2003) Apertureless near-field optical microscopy: Tip-sample coupling in elastic light scattering. *Applied Physics Letters* **83**, 5089–5091.

- [157] Olmon, R. L, Krenz, P. M, Jones, A. C, Boreman, G. D, & Raschke, M. B. (2008) Near-field imaging of optical antenna modes in the mid-infrared. *Optics Express* **16**, 20295–20305.
- [158] Kubo, A, Jung, Y. S, Kim, H. K, & Petek, H. (2007) Femtosecond microscopy of localized and propagating surface plasmons in silver gratings. *Journal of Physics B: Atomic, Molecular and Optical Physics* **40**, S259.
- [159] Schneider, C. (2013) Mapping of surface plasmon polariton fields by time-resolved photoemission electron microscopy: experiments, simulations, and applications (Dissertation, University Kaiserslautern, Dep. of Physics).
- [160] Bozhevolnyi, S. I, Volkov, V. S, Devaux, E, Laluet, J.-Y, & Ebbesen, T. W. (2006) Channel plasmon subwavelength waveguide components including interferometers and ring resonators. *Nature* **440**, 508–511.
- [161] Rewitz, C, Keitzl, T, Tuchscherer, P, Huang, J.-S, Geisler, P, Razinskas, G, Hecht, B, & Brixner, T. (2012) Ultrafast plasmon propagation in nanowires characterized by far-field spectral interferometry. *Nano Letters* **12**, 45–49.
- [162] Rewitz, C, Keitzl, T, Tuchscherer, P, Goetz, S, Geisler, P, Razinskas, G, Hecht, B, & Brixner, T. (2012) Spectral-interference microscopy for characterization of functional plasmonic elements. *Optics Express* **20**, 14632–14647.
- [163] Daniel, M.-C & Astruc, D. (2004) Gold nanoparticles: Assembly, supramolecular chemistry, quantum-size-related properties, and applications toward biology, catalysis, and nanotechnology. *Chemical Reviews* **104**, 293–346.
- [164] Faraday, M. (1857) The bakerian lecture: Experimental relations of gold (and other metals) to light. *Philosophical Transactions of the Royal Society of London* **147**, 145–181.
- [165] Kelly, K. L, Coronado, E, Zhao, L. L, & Schatz, G. C. (2003) The optical properties of metal nanoparticles: The influence of size, shape, and dielectric environment. *The Journal of Physical Chemistry B* **107**, 668–677.
- [166] Mie, G. (1908) Beiträge zur Optik trüber Medien, speziell kolloidaler Metallösungen. *Ann. Phys.* **25**, 377.
- [167] Lal, S, Link, S, & Halas, N. J. (2007) Nano-optics from sensing to waveguiding. *Nature Photonics* **1**, 641–648.
- [168] Liu, N, Tang, M. L, Hentschel, M, Giessen, H, & Alivisatos, A. P. (2011) Nanoantenna-enhanced gas sensing in a single tailored nanofocus. *Nature Materials* **10**, 631–636.
- [169] Kim, S, Jin, J, Kim, Y, Park, I, Kim, Y, & Kim, S. (2008) High-harmonic generation by resonant plasmon field enhancement. *Nature* **453**, 757.
- [170] Lükermann, F, Heinzmann, U, & Stiebig, H. (2012) Plasmon enhanced resonant defect absorption in thin a-Si:H n-i-p devices. *Applied Physics Letters* **100**, 253907.
- [171] Kuwata, H, Tamaru, H, Esumi, K, & Miyano, K. (2003) Resonant light scattering from metal nanoparticles: Practical analysis beyond rayleigh approximation. *Applied Physics Letters* **83**, 4625–4627.

- [172] Sönnichsen, C, Franzl, T, Wilk, T, von Plessen, G, & Feldmann, J. (2002) Plasmon resonances in large noble-metal clusters. *New Journal of Physics* **4**, 93.
- [173] Etchegoin, P. G, Le Ru, E. C, & Meyer, M. (2006) An analytic model for the optical properties of gold. *The Journal of Chemical Physics* **125**, 164705.
- [174] Stahrenberg, K, Herrmann, T, Wilmers, K, Esser, N, Richter, W, & Lee, M. J. G. (2001) Optical properties of copper and silver in the energy range 2.5–9.0 eV. *Physical Review B* **64**, 115111.
- [175] Echenique, P, Pitarke, J, Chulkov, E, & Rubio, A. (2000) Theory of inelastic lifetimes of low-energy electrons in metals. *Chem. Phys.* **251**, 1–35.
- [176] Synge, E. H. (1928) A suggested method for extending microscopic resolution into the ultra-microscopic region. *Phil. Mag.* **6**, 356–362.
- [177] Farahani, J, Pohl, D, Eisler, H, & Hecht, B. (2005) Single Quantum Dot Coupled to a Scanning Optical Antenna: A Tunable Superemitter. *Phys. Rev. Lett.* **95**, 17402.
- [178] Bharadwaj, P, Deutsch, B, & Novotny, L. (2009) Optical antennas. *Advances in Optics and Photonics* **1**, 438–483.
- [179] Broers, A. N, Harper, J. M. E, & Molzen, W. W. (1978) 250-Å linewidths with pmma electron resist. *Applied Physics Letters* **33**, 392–394.
- [180] Craighead, H. G, Howard, R. E, Jackel, L. D, & Mankiewich, P. M. (1983) 10-nm linewidth electron beam lithography on GaAs. *Applied Physics Letters* **42**, 38–40.
- [181] Vieu, C, Carcenac, F, Pépin, A, Chen, Y, Mejias, M, Lebib, A, Manin-Ferlazzo, L, Couraud, L, & Launois, H. (2000) Electron beam lithography: resolution limits and applications. *Applied Surface Science* **164**, 111–117.
- [182] Van Dorp, W & Hagen, C. (2008) A critical literature review of focused electron beam induced deposition. *Journal of Applied Physics* **104**, 081301–081301–42.
- [183] Koops, H. W. P, Weiel, R, Kern, D, & Baum, T. (1988) High-resolution electron-beam induced deposition. *Journal of Vacuum Science Technology B: Microelectronics and Nanometer Structures* **6**, 477–481.
- [184] Chou, S, Krauss, P. R, & Renstrom, P. J. (1996) Nanoimprint lithography. *Journal of Vacuum Science Technology B: Microelectronics and Nanometer Structures* **14**, 4129–4133.
- [185] Guo, L. J. (2007) Nanoimprint lithography: Methods and material requirements. *Advanced Materials* **19**, 495–513.
- [186] Veerman, J. A, Otter, A. M, Kuipers, L, & van Hulst, N. (1998) High definition aperture probes for near-field optical microscopy fabricated by focused ion beam milling. *Applied Physics Letters* **72**, 3115–3117.
- [187] Giannuzzi, L & Stevie, F. (1999) A review of focused ion beam milling techniques for TEM specimen preparation. *Micron* **30**, 197–204.

- [188] Farahani, J. N, Eisler, H.-J, Pohl, D. W, Pavius, M, Flückiger, P, Gasser, P, & Hecht, B. (2007) Bow-tie optical antenna probes for single-emitter scanning near-field optical microscopy. *Nanotechnology* **18**, 125506.
- [189] Huang, J.-S, Callegari, V, Geisler, P, Brüning, C, Kern, J, Prangsma, J. C, Wu, X, Feichtner, T, Ziegler, J, Weinmann, P, Kamp, M, Forchel, A, Biagioni, P, Sennhauser, U, & Hecht, B. (2010) Atomically flat single-crystalline gold nanostructures for plasmonic nanocircuitry. *Nature Communications* **1**, 150.
- [190] Kalkbrenner, T, Ramstein, M, Mlynek, J, & Sandoghdar, V. (2001) A single gold particle as a probe for apertureless scanning near-field optical microscopy. *Journal of Microscopy* **202**, 72–76.
- [191] Kühn, S, Håkanson, U, Rogobete, L, & Sandoghdar, V. (2006) Enhancement of single-molecule fluorescence using a gold nanoparticle as an optical nanoantenna. *Physical Review Letters* **97**, 017402.
- [192] Taminiou, T, Stefani, F, & van Hulst, N. (2008) Enhanced directional excitation and emission of single emitters by a nano-optical Yagi-Uda antenna. *Optics Express* **16**, 10858–10866.
- [193] Sukharev, M & Seideman, T. (2006) Phase and polarization control as a route to plasmonic nanodevices. *Nano Letters* **6**, 715–719.
- [194] Sukharev, M & Seideman, T. (2007) Coherent control of light propagation via nanoparticle arrays. *Journal of Physics B: Atomic, Molecular and Optical Physics* **40**, S283.
- [195] Prodan, E, Radloff, C, Halas, N. J, & Nordlander, P. (2003) A hybridization model for the plasmon response of complex nanostructures. *Science* **302**, 419–422.
- [196] Davis, T. J, Gomez, D. E, & Vernon, K. C. (2010) Simple model for the hybridization of surface plasmon resonances in metallic nanoparticles. *Nano Letters* **10**, 2618–2625.
- [197] Zhang, S, Genov, D. A, Wang, Y, Liu, M, & Zhang, X. (2008) Plasmon-induced transparency in metamaterials. *Physical Review Letters* **101**, 047401.
- [198] Liu, N, Langguth, L, Weiss, T, Kästel, J, Fleischhauer, M, Pfau, T, & Giessen, H. (2009) Plasmonic analogue of electromagnetically induced transparency at the drude damping limit. *Nature Materials* **8**, 758–762.
- [199] Luk'yanchuk, B, Zheludev, N. I, Maier, S. A, Halas, N. J, Nordlander, P, Giessen, H, & Chong, C. T. (2010) The fano resonance in plasmonic nanostructures and metamaterials. *Nature Materials* **9**, 707–715.
- [200] Brixner, T, García de Abajo, F, Spindler, C, & Pfeiffer, W. (2006) Adaptive ultrafast nano-optics in a tight focus. *Applied Physics B: Lasers and Optics* **84**, 89–95.
- [201] Fink, M. (1992) Time reversal of ultrasonic fields. i. basic principles. *Ultrasonics, Ferroelectrics and Frequency Control, IEEE Transactions on* **39**, 555–566.

- [202] Wu, F, Thomas, J.-L, & Fink, M. (1992) Time reversal of ultrasonic fields. ii. experimental results. *Ultrasonics, Ferroelectrics and Frequency Control, IEEE Transactions on* **39**, 567–578.
- [203] Brüche, E & Johannson, H. (1933) Elektronenmikroskopische beobachtungen an der barium-aufdampfkathode. *Zeitschrift für Physik* **84**, 56–58.
- [204] Knoll, M & Ruska, E. (1932) Das elektronenmikroskop. *Zeitschrift für Physik* **78**, 318–339.
- [205] Bauer, E. (2012) A brief history of PEEM. *Journal of Electron Spectroscopy and Related Phenomena* **185**, 314–322.
- [206] Könenkamp, R, Word, R. C, Rempfer, G, Dixon, T, Almaraz, L, & Jones, T. (2010) 5.4 nm spatial resolution in biological photoemission electron microscopy. *Ultramicroscopy* **110**, 899–902.
- [207] Tromp, R, Hannon, J, Ellis, A, Wan, W, Berghaus, A, & Schaff, O. (2010) A new aberration-corrected, energy-filtered LEEM/PEEM instrument. i. principles and design. *Ultramicroscopy* **110**, 852–861.
- [208] Tromp, R, Hannon, J, Ellis, A, Wan, W, Berghaus, A, & Schaff, O. (2010) A new aberration-corrected, energy-filtered leem/peem instrument. i. principles and design. *Ultramicroscopy* **110**, 852 – 861.
- [209] Hertz, H. (1887) Über einen Einfluss des ultravioletten Lichtes auf die electriche Entladung. *Annalen der Physik und Chemie* **31**, 983–1000.
- [210] Hallwachs, W. (1883) Über den Einfluss des Lichtes auf elektrostatisch geladene Körper. *Annalen der Physik und Chemie* **33**, 301–312.
- [211] Millikan, R. A. (1916) Einstein's Photoelectric Equation and Contact Electromotive Force. *Phys. Rev.* **7**, 18–32.
- [212] Einstein, A. (1905) Über einen die Erzeugung und Verwandlung des Lichtes betreffenden heuristischen Gesichtspunkt. *Annalen der Physik* **17**, 132–148.
- [213] Planck, M. (1901) Ueber das gesetz der energieverteilung im normalspectrum. *Annalen der Physik* **309**, 553–563.
- [214] Kittel, C & McEuen, P. (1996) *Introduction to solid state physics*. (Wiley New York) Vol. 7.
- [215] Fann, W. S, Storz, R, Tom, H. W. K, & Bokor, J. (1992) Electron thermalization in gold. *Physical Review B* **46**, 13592–13595.
- [216] Seah, M & Dench, W. (1979) Quantitative electron spectroscopy of surfaces: a standard data base for electron inelastic mean free paths in solids. *Surface and interface analysis* **1**, 2–11.
- [217] Göppert-Mayer, M. (1931) Über elementarakte mit zwei quantensprüngen. *Annalen der Physik* **401**, 273–294.

- [218] Fowler, R. H. (1931) The analysis of photoelectric sensitivity curves for clean metals at various temperatures. *Physical Review* **38**, 45–56.
- [219] DuBridge, L. A. (1933) Theory of the energy distribution of photoelectrons. *Physical Review* **43**, 727–741.
- [220] Bechtel, J. H, Lee Smith, W, & Bloembergen, N. (1977) Two-photon photoemission from metals induced by picosecond laser pulses. *Physical Review B* **15**, 4557–4563.
- [221] Schmuttenmaer, C, Aeschlimann, M, Elsayedali, H, Miller, R, Mantell, D, Cao, J, & Time-resolved, Y. (1994) Time-resolved two-photon photoemission from cu(100): Energy dependence of electron relaxation. *Phys. Rev. B* **50**, 8957–8960.
- [222] Petek, H & Ogawa, S. (1997) Femtosecond time-resolved two-photon photoemission studies of electron dynamics in metals. *Prog. Surf. Sci.* **56**, 239–310.
- [223] Aeschlimann, M, Bauer, M, & Pawlik, S. (1996) Competing nonradiative channels for hot electron induced surface photochemistry. *Chem. Phys.* **205**, 127–141.
- [224] Aeschlimann, M, Bauer, M, Pawlik, S, Knorren, R, Bouzerar, G, & Bennemann, K. (2000) Transport and dynamics of optically excited electrons in metals. *Applied Physics A: Materials Science & Processing* **71**, 485–491.
- [225] Merschdorf, M. (2002) Femtodynamics in nanoparticles – the short lives of excited electrons in silver (Dissertation, Julius-Maximilians-University Würzburg, Dep. of Physics).
- [226] Petek, H & Ogawa, S. (1997) Femtosecond time-resolved two-photon photoemission studies of electron dynamics in metals. *Progress in Surface Science* **56**, 239–310.
- [227] Merschdorf, M, Kennerknecht, C, & Pfeiffer, W. (2004) Collective and single-particle dynamics in time-resolved two-photon photoemission. *Phys. Rev. B* **70**, 193401.
- [228] Drescher, M. (2004) Time-resolved ESCA: a novel probe for chemical dynamics. *Zeitschrift für Physikalische Chemie* **218**, 1147–1168.
- [229] Drescher, M, Hentschel, M, Kienberger, R, Uiberacker, M, Yakovlev, V, Scrinzi, A, West-erwalbesloh, T, Kleineberg, U, Heinzmann, U, & Krausz, F. (2002) Time-resolved atomic inner-shell spectroscopy. *Nature* **419**, 803–807.
- [230] Drescher, M, Hentschel, M, Kienberger, R, Tempea, G, Spielmann, C, Reider, G. A, Corkum, P. B, & Krausz, F. (2001) X-ray pulses approaching the attosecond frontier. *Science* **291**, 1923–1927.
- [231] Scherzer, O. (1949) The theoretical resolution limit of the electron microscope. *Journal of Applied Physics* **20**, 20–29.
- [232] Batson, P. E, Dellby, N, & Krivanek, O. L. (2002) Sub-Ångstrom resolution using aberration corrected electron optics. *Nature* **418**, 617–620.

- [233] Krivanek, O. L, Chisholm, M. F, Nicolosi, V, Pennycook, T. J, Corbin, G. J, Dellby, N, Murfitt, M. F, Own, C. S, Szilagy, Z. S, Oxley, M. P, Pantelides, S. T, & Pennycook, S. J. (2010) Atom-by-atom structural and chemical analysis by annular dark-field electron microscopy. *Nature* **464**, 571–574.
- [234] Seiler, H. (1983) Secondary electron emission in the scanning electron microscope. *Journal of Applied Physics* **54**, R1–R18.
- [235] Fecher, G. H, Schmidt, O, Hwu, Y, & Schönhense, G. (2002) Multiphoton photoemission electron microscopy using femtosecond laser radiation. *Journal of Electron Spectroscopy and Related Phenomena* **126**, 77–87.
- [236] Kuch, W, Frömter, R, Gilles, J, Hartmann, D, Ziethen, C, Schneider, C. M, Schönhense, G, Swiech, W, & Kirschner, J. (1998) Element-selective magnetic imaging in exchange-coupled systems by magnetic photoemission microscopy. *Surface Review and Letters* **05**, 1241–1248.
- [237] Cinchetti, M, Oelsner, A, Fecher, G. H, Elmers, H. J, & Schönhense, G. (2003) Observation of cu surface inhomogeneities by multiphoton photoemission spectromicroscopy. *Applied Physics Letters* **83**, 1503–1505.
- [238] Cinchetti, M, Valdaitsev, D, Gloskovskii, A, Oelsner, A, Nepijko, S, & Schönhense, G. (2004) Photoemission time-of-flight spectromicroscopy of ag nanoparticle films on si(1 1 1). *Journal of Electron Spectroscopy and Related Phenomena* **137–140**, 249–257.
- [239] Melchior, P. (2009) Nahfelduntersuchungen an nanooptischen bowtie-antennen (Diploma thesis, University Kaiserslautern, Dep. of Physics).
- [240] Kotsugi, M, Kuch, W, Offi, F, Chelaru, L, & Kirschner, J. (2003) Microspectroscopic two-dimensional fermi surface mapping using a photoelectron emission microscope. *Review of scientific instruments* **74**, 2754–2758.
- [241] Kromker, B, Escher, M, Funnemann, D, Hartung, D, Engelhard, H, & Kirschner, J. (2008) Development of a momentum microscope for time resolved band structure imaging. *Review of Scientific Instruments* **79**, 053702–053702.
- [242] Neuhäusler, U, Oelsner, A, Slieh, J, Brzeska, M, Wonisch, A, Westerwalbesloh, T, Brückl, H, Schicketanz, M, Weber, N, Escher, M, Merkel, M, Schönhense, G, Kleineberg, U, & Heinzmann, U. (2006) High-resolution actinic defect inspection for extreme ultraviolet lithography multilayer mask blanks by photoemission electron microscopy. *Applied Physics Letters* **88**, 053113–053113–3.
- [243] Neuhäusler, U, Lin, J, Oelsner, A, Schicketanz, M, Valdaitsev, D, Slieh, J, Weber, N, Brzeska, M, Wonisch, A, Westerwalbesloh, T, Brechling, A, Brückl, H, Escher, M, Merkel, M, Schönhense, G, Kleineberg, U, & Heinzmann, U. (2006) A new approach for actinic defect inspection of EUVL multilayer mask blanks: Standing wave photoemission electron microscopy. *Microelectronic Engineering* **83**, 680–683.
- [244] Maul, J, Lin, J, Oelsner, A, Valdaitsev, D, Weber, N, Escher, M, Merkel, M, Seitz, H, Heinzmann, U, Kleineberg, U, & Schönhense, G. (2007) Phase defect inspection of

- multilayer masks for 13.5 nm optical lithography using PEEM in a standing wave mode. *Surface Science* **601**, 4758–4763.
- [245] Fischer, A. (2012) Zeit- und orts aufgelöste dynamik und kontrolle plasmonischer systeme (Dissertation, University Kaiserslautern, Dep. of Physics).
- [246] Oelsner, A, Schmidt, O, Schicketanz, M, Klais, M, Schönhense, G, Mergel, V, Jagutzki, O, & Schmidt-Böcking, H. (2001) Microspectroscopy and imaging using a delay line detector in time-of-flight photoemission microscopy. *Review of Scientific Instruments* **72**, 3968–3974.
- [247] Oelsner, A, Rohmer, M, Schneider, C, Bayer, D, Schönhense, G, & Aeschlimann, M. (2010) Time- and energy resolved photoemission electron microscopy-imaging of photoelectron time-of-flight analysis by means of pulsed excitations. *Journal of Electron Spectroscopy and Related Phenomena* **178**, 317–330.
- [248] Friedman, P. G, Cuza, R. A, Fleischman, J. R, Martin, C, Schiminovich, D, & Doyle, D. J. (1996) Multilayer anode with crossed serpentine delay lines for high spatial resolution readout of microchannel plate detectors. *Review of Scientific Instruments* **67**, 596–608.
- [249] Rempfer, G. F, Nadakavukaren, K. K, & Griffith, O. H. (1980) Topographical effects in emission microscopy. *Ultramicroscopy* **5**, 437–448.
- [250] Houle, W. A, Engel, W, Willig, F, Rempfer, G. F, & Griffith, O. (1982) Depth of information in photoelectron microscopy. *Ultramicroscopy* **7**, 371–380.
- [251] Rempfer, G. F & Griffith, O. (1989) The resolution of photoelectron microscopes with UV, x-ray, and synchrotron excitation sources. *Ultramicroscopy* **27**, 273–300.
- [252] Gilbert, B, Andres, R, Perfetti, P, Margaritondo, G, Rempfer, G, & De Stasio, G. (2000) Charging phenomena in PEEM imaging and spectroscopy. *Ultramicroscopy* **83**, 129–139.
- [253] Anders, S, Padmore, H. A, Duarte, R. M, Renner, T, Stammeler, T, Scholl, A, Scheinfein, M. R, Stöhr, J, Séve, L, & Sinkovic, B. (1999) Photoemission electron microscope for the study of magnetic materials. *Review of Scientific Instruments* **70**, 3973–3981.
- [254] Lin, J, Weber, N, Wirth, A, Chew, S. H, Escher, M, Merkel, M, Kling, M. F, Stockman, M. I, Krausz, F, & Kleineberg, U. (2009) Time of flight-photoemission electron microscope for ultrahigh spatiotemporal probing of nanoplasmonic optical fields. *Journal of Physics: Condensed Matter* **21**, 314005.
- [255] Bayer, D, Wiemann, C, Gaier, O, Bauer, M, & Aeschlimann, M. (2008) Time-resolved 2PPE and time-resolved PEEM as a probe of LSPs in silver nanoparticles. *Journal of Nanomaterials* **2008**.
- [256] Kubo, A, Onda, K, Petek, H, Sun, Z, Jung, Y. S, & Kim, H. K. (2005) Femtosecond imaging of surface plasmon dynamics in a nanostructured silver film. *Nano Letters* **5**, 1123–1127.

- [257] Melchior, P, Bayer, D, Schneider, C, Fischer, A, Rohmer, M, Pfeiffer, W, & Aeschlimann, M. (2011) Optical near-field interference in the excitation of a bowtie nanoantenna. *Phys. Rev. B* **83**, 235407.
- [258] Kane, D & Trebino, R. (1993) Characterization of arbitrary femtosecond pulses using Frequency-Resolved Optical Gating. *IEEE Journal of Quantum Electronics* **29**, 571–579.
- [259] DeLong, K. W, Trebino, R, Hunter, J, & White, W. E. (1994) Frequency-resolved optical gating with the use of second-harmonic generation. *J. Opt. Soc. Am. B* **11**, 2206–2215.
- [260] Trebino, R, DeLong, K, Fittinghoff, D, Sweetser, J, Krumbugel, M, Richman, B, & Kane, D. (1997) Measuring ultrashort laser pulses in the time-frequency domain using frequency-resolved optical gating. *Review of Scientific Instruments* **68**, 3277–3295.
- [261] Trebino, R. (2000) *Frequency-Resolved Optical Gating: The Measurement of Ultrashort Laser Pulses*. (Kluwer Academic Publishers).
- [262] Froehly, C, Lacourt, A, & Vienot, J. C. (1973) Notions de réponse impulsionnelle et de fonction de transfert temporelles des pupilles optiques, justifications expérimentales et applications. *J. Opt. (Paris)* **4**, 183–196.
- [263] Lepetit, L, Chériaux, G, & Joffre, M. (1995) Linear techniques of phase measurement by femtosecond spectral interferometry for applications in spectroscopy. *J. Opt. Soc. Am. B* **12**, 2467–2474.
- [264] Dorrer, C, Belabas, N, Likforman, J.-P, & Joffre, M. (2000) Spectral resolution and sampling issues in fourier-transform spectral interferometry. *J. Opt. Soc. Am. B* **17**, 1795–1802.
- [265] Schnell, M, Garcia-Etxarri, A, Huber, A. J, Crozier, K. B, Borisov, A, Aizpurua, J, & Hillenbrand, R. (2010) Amplitude- and phase-resolved near-field mapping of infrared antenna modes by transmission-mode scattering-type near-field microscopy. *The Journal of Physical Chemistry C* **114**, 7341–7345.
- [266] Yee, K. (1966) Numerical solution of initial boundary value problems involving maxwell's equations in isotropic media. *Antennas and Propagation, IEEE Transactions on* **14**, 302–307.
- [267] Taflove, A & Hagness, S. C. (2005) *Computational electrodynamics: the finite-difference time-domain method*. (Artech House, Boston).
- [268] Inan, U. S & Marshall, R. A. (2011) *Numerical electromagnetics: the FDTD method*. (Cambridge University Press, Cambridge; New York).
- [269] Gray, S. K & Kupka, T. (2003) Propagation of light in metallic nanowire arrays: Finite-difference time-domain studies of silver cylinders. *Physical review B* **68**, 045415.
- [270] Taflove, A. (2013) *Advances in FDTD computational electrodynamics: photonics and nanotechnology*. (Artech House, Boston).
- [271] Palik, E. D. (1998) *Handbook of Optical Constants of Solids: Index*. (Access Online via Elsevier) Vol. 3.

- [272] Jelley, E. E. (1936) Spectral absorption and fluorescence of dyes in the molecular state. *Nature* **138**, 1009–1010.
- [273] Bellessa, J, Bonnand, C, Plenet, J. C, & Mugnier, J. (2004) Strong coupling between surface plasmons and excitons in an organic semiconductor. *Physical Review Letters* **93**, 036404.
- [274] Vasa, P, Pomraenke, R, Cirimi, G, De Re, E, Wang, W, Schwieger, S, Leipold, D, Runge, E, Cerullo, G, & Lienau, C. (2010) Ultrafast manipulation of strong coupling in Metal-Molecular aggregate hybrid nanostructures. *ACS Nano* **4**, 7559–7565.
- [275] Vasa, P, Wang, W, Pomraenke, R, Lammers, M, Maiuri, M, Manzoni, C, Cerullo, G, & Lienau, C. (2013) Real-time observation of ultrafast rabi oscillations between excitons and plasmons in metal nanostructures with j-aggregates. *Nature Photonics* **7**, 128–132.
- [276] Arias, D. H, Stone, K. W, Vlaming, S. M, Walker, B. J, Bawendi, M. G, Silbey, R. J, Bulovic, V, & Nelson, K. A. (2013) Thermally-limited exciton delocalization in superradiant molecular aggregates. *The Journal of Physical Chemistry B* **117**, 4553–4559.
- [277] Berera, R, Grondelle, R. v, & Kennis, J. T. M. (2009) Ultrafast transient absorption spectroscopy: principles and application to photosynthetic systems. *Photosynthesis Research* **101**, 105–118.
- [278] Tolles, W. M, Nibler, J. W, McDonald, J. R, & Harvey, A. B. (1977) A review of the theory and application of coherent anti-stokes raman spectroscopy (CARS). *Applied Spectroscopy* **31**, 253–271.
- [279] Druet, S. A & Taran, J.-P. E. (1981) Cars spectroscopy. *Progress in Quantum Electronics* **7**, 1–72.
- [280] Shen, Y. R. (2003) *The principles of nonlinear optics*. (Wiley-Interscience, Hoboken, N.J.).
- [281] Demtröder, W. (2003) *Laser Spectroscopy: Basic Concepts and Instrumentation*. (Springer).
- [282] Götz, T, Buck, M, Dressler, C, Eisert, F, & Träger, F. (1995) Optical second-harmonic generation by supported metal clusters: Size and shape effects. *Applied Physics A* **60**, 607–612.
- [283] Lambrecht, B, Leitner, A, & Aussenegg, F. R. (1997) Femtosecond decay-time measurement of electron-plasma oscillation in nanolithographically designed silver particles. *Applied Physics B* **64**, 269–272.
- [284] Simon, M, Träger, F, Assion, A, Lang, B, Voll, S, & Gerber, G. (1998) Femtosecond time-resolved second-harmonic generation at the surface of alkali metal clusters. *Chemical Physics Letters* **296**, 579–584.
- [285] Lamprecht, B, Krenn, J. R, Leitner, A, & Aussenegg, F. R. (1999) Particle-plasmon decay-time determination by measuring the optical near-field's autocorrelation: influence of inhomogeneous line broadening. *Applied Physics B* **69**, 223–227.

- [286] Lamprecht, B, Leitner, A, & Aussenegg, F. R. (1999) SHG studies of plasmon dephasing in nanoparticles. *Applied Physics B* **68**, 419–423.
- [287] Vartanyan, T, Simon, M, & Träger, F. (1999) Femtosecond optical second harmonic generation by metal clusters: The influence of inhomogeneous line broadening on the dephasing time of surface plasmon excitation. *Applied Physics B* **68**, 425–431.
- [288] Hänsch, T. W, Shahin, I. S, & Schawlow, A. L. (1971) High-resolution saturation spectroscopy of the sodium d lines with a pulsed tunable dye laser. *Physical Review Letters* **27**, 707–710.
- [289] Wieman, C & Hänsch, T. W. (1976) Doppler-free laser polarization spectroscopy. *Physical Review Letters* **36**, 1170–1173.
- [290] Volker, S. (1989) Hole-burning spectroscopy. *Annual Review of Physical Chemistry* **40**, 499–530.
- [291] Rabi, I. I, Zacharias, J. R, Millman, S, & Kusch, P. (1938) A new method of measuring nuclear magnetic moment. *Physical Review* **53**, 318–318.
- [292] Bloch, F, Hansen, W, & Packard, M. (1946) Nuclear induction. *Physical review* **70**, 460–474.
- [293] Bloembergen, N, Purcell, E. M, & Pound, R. V. (1948) Relaxation effects in nuclear magnetic resonance absorption. *Physical Review* **73**, 679.
- [294] Carr, H. Y & Purcell, E. M. (1954) Effects of diffusion on free precession in nuclear magnetic resonance experiments. *Physical Review* **94**, 630.
- [295] Lauterbur, P. C. (1973) Image formation by induced local interactions: Examples employing nuclear magnetic resonance. *Nature* **242**, 190–191.
- [296] Tan, H.-S. (2008) Theory and phase-cycling scheme selection principles of collinear phase coherent multi-dimensional optical spectroscopy. *The Journal of Chemical Physics* **129**, 124501.
- [297] Ekimov, A & Onushchenko, A. (1981) Quantum size effect in three-dimensional microscopic semiconductor crystals. *ZhETF Pis ma Redaktsiiu* **34**, 363.
- [298] Rossetti, R, Nakahara, S, & Brus, L. E. (1983) Quantum size effects in the redox potentials, resonance raman spectra, and electronic spectra of CdS crystallites in aqueous solution. *The Journal of Chemical Physics* **79**, 1086–1088.
- [299] Ekimov, A, Efros, A, & Onushchenko, A. (1985) Quantum size effect in semiconductor microcrystals. *Solid State Communications* **56**, 921–924.
- [300] Reed, M, Randall, J, Aggarwal, R, Matyi, R, Moore, T, & Wetsel, A. (1988) Observation of discrete electronic states in a zero-dimensional semiconductor nanostructure. *Physical Review Letters* **60**, 535–537.
- [301] Leutwyler, W. K, Bürgi, S. L, & Burgli, H. (1996) Semiconductor clusters, nanocrystals, and quantum dots. *Science* **271**, 933.

- [302] Tang, C. W & VanSlyke, S. A. (1987) Organic electroluminescent diodes. *Applied Physics Letters* **51**, 913.
- [303] Tang, C. W, VanSlyke, S. A, & Chen, C. H. (1989) Electroluminescence of doped organic thin films. *Journal of Applied Physics* **65**, 3610.
- [304] DeMasi, A, Piper, L. F. J, Zhang, Y, Reid, I, Wang, S, Smith, K. E, Downes, J. E, Peltekis, N, McGuinness, C, & Matsuura, A. (2008) Electronic structure of the organic semiconductor alq3 (aluminum tris-8-hydroxyquinoline) from soft x-ray spectroscopies and density functional theory calculations. *The Journal of Chemical Physics* **129**, 224705.
- [305] Bisti, F, Stroppa, A, Donarelli, M, Picozzi, S, & Ottaviano, L. (2011) Electronic structure of tris(8-hydroxyquinolato)aluminium(III) revisited using the heyd-scuseria-ernzerhof hybrid functional: Theory and experiments. *Physical Review B* **84**, 195112.
- [306] Steil, S, Großmann, N, Laux, M, Ruffing, A, Steil, D, Wiesenmayer, M, Mathias, S, Monti, O. L. A, Cinchetti, M, & Aeschlimann, M. (2013) Spin-dependent trapping of electrons at spinterfaces. *Nature Physics* **9**, 242–247.
- [307] Stievater, T. H, Li, X, Steel, D. G, Gammon, D, Katzer, D. S, Park, D, Piermarocchi, C, & Sham, L. J. (2001) Rabi oscillations of excitons in single quantum dots. *Physical Review Letters* **87**, 133603.
- [308] Yoshie, T, Scherer, A, Hendrickson, J, Khitrova, G, Gibbs, H. M, Rupper, G, Ell, C, Shchekin, O. B, & Deppe, D. G. (2004) Vacuum rabi splitting with a single quantum dot in a photonic crystal nanocavity. *Nature* **432**, 200–203.
- [309] Stinaff, E. A, Scheibner, M, Bracker, A. S, Ponomarev, I. V, Korenev, V. L, Ware, M. E, Doty, M. F, Reinecke, T. L, & Gammon, D. (2006) Optical signatures of coupled quantum dots. *Science* **311**, 636–639.
- [310] Akimov, A. V, Mukherjee, A, Yu, C. L, Chang, D. E, Zibrov, A. S, Hemmer, P. R, Park, H, & Lukin, M. D. (2007) Generation of single optical plasmons in metallic nanowires coupled to quantum dots. *Nature* **450**, 402–406.
- [311] Engel, G. S, Calhoun, T. R, Read, E. L, Ahn, T.-K, Mancal, T, Cheng, Y.-C, Blankenship, R. E, & Fleming, G. R. (2007) Evidence for wavelike energy transfer through quantum coherence in photosynthetic systems. *Nature* **446**, 782–786.
- [312] Utikal, T, Stockman, M. I, Heberle, A. P, Lippitz, M, & Giessen, H. (2010) All-optical control of the ultrafast dynamics of a hybrid plasmonic system. *Physical Review Letters* **104**, 113903.
- [313] Utikal, T, Zentgraf, T, Paul, T, Rockstuhl, C, Lederer, F, Lippitz, M, & Giessen, H. (2011) Towards the origin of the nonlinear response in hybrid plasmonic systems. *Physical Review Letters* **106**, 133901.
- [314] Shim, S.-H & Zanni, M. T. (2009) How to turn your pump-probe instrument into a multidimensional spectrometer: 2D IR and vis spectroscopies via pulse shaping. *Physical chemistry chemical physics : PCCP* **11**, 748.

- [315] Fulmer, E. C, Mukherjee, P, Krummel, A. T, & Zanni, M. T. (2004) A pulse sequence for directly measuring the anharmonicities of coupled vibrations: Two-quantum two-dimensional infrared spectroscopy. *The Journal of Chemical Physics* **120**, 8067–8078.
- [316] Brown, E. J, Zhang, Q, & Dantus, M. (1999) Femtosecond transient-grating techniques: Population and coherence dynamics involving ground and excited states. *The Journal of Chemical Physics* **110**, 5772–5788.
- [317] Seidner, L, Stock, G, & Domcke, W. (1995) Nonperturbative approach to femtosecond spectroscopy: General theory and application to multidimensional nonadiabatic photoisomerization processes. *The Journal of Chemical Physics* **103**, 3998–4011.
- [318] Meyer, S & Engel, V. (2000) Non-perturbative wave-packet calculations of time-resolved four-wave-mixing signals. *Applied Physics B* **71**, 293–297.
- [319] Siemens, M. E, Moody, G, Li, H, Bristow, A. D, & Cundiff, S. T. (2010) Resonance lineshapes in two-dimensional Fourier transform spectroscopy. *Optics Express* **18**, 17699–17708.
- [320] Lamprecht, B, Krenn, J. R, Leitner, A, & Aussenegg, F. R. (1999) Resonant and off-resonant light-driven plasmons in metal nanoparticles studied by femtosecond-resolution third-harmonic generation. *Physical Review Letters* **83**, 4421–4424.
- [321] Nilius, N, Ernst, N, & Freund, H.-J. (2000) Photon emission spectroscopy of individual oxide-supported silver clusters in a scanning tunneling microscope. *Physical Review Letters* **84**, 3994–3997.
- [322] Hanke, T, Krauss, G, Träutlein, D, Wild, B, Bratschitsch, R, & Leitenstorfer, A. (2009) Efficient nonlinear light emission of single gold optical antennas driven by few-cycle near-infrared pulses. *Physical Review Letters* **103**, 257404.
- [323] Anderson, A, Deryckx, K. S, Xu, X. G, Steinmeyer, G, & Raschke, M. B. (2010) Few-femtosecond plasmon dephasing of a single metallic nanostructure from optical response function reconstruction by interferometric frequency resolved optical gating. *Nano Letters* **10**, 2519–2524.
- [324] Dudovich, N, Dayan, B, Gallagher Faeder, S. M, & Silberberg, Y. (2001) Transform-limited pulses are not optimal for resonant multiphoton transitions. *Physical Review Letters* **86**, 47–50.
- [325] Dicke, R. H. (1954) Coherence in spontaneous radiation processes. *Physical Review* **93**, 99–110.
- [326] Gross, M & Haroche, S. (1982) Superradiance: An essay on the theory of collective spontaneous emission. *Physics Reports* **93**, 301–396.
- [327] Brandes, T. (2005) Coherent and collective quantum optical effects in mesoscopic systems. *Physics Reports* **408**, 315–474.
- [328] Ditlbacher, H, Krenn, J. R, Schider, G, Leitner, A, & Aussenegg, F. R. (2002) Two-dimensional optics with surface plasmon polaritons. *Applied Physics Letters* **81**, 1762–1764.

- [329] Krenn, J. R, Ditlbacher, H, Schider, G, Hohenau, A, Leitner, A, & Aussenegg, F. R. (2003) Surface plasmon micro- and nano-optics. *Journal of Microscopy* **209**, 167–172.
- [330] Raether, H. (1988) *Surface plasmons on smooth surfaces*. (Springer).
- [331] John, S. (1987) Strong localization of photons in certain disordered dielectric superlattices. *Physical Review Letters* **58**, 2486–2489.
- [332] Yablonovitch, E. (1987) Inhibited spontaneous emission in solid-state physics and electronics. *Physical Review Letters* **58**, 2059–2062.
- [333] Joannopoulos, J. D, Villeneuve, P. R, & Fan, S. (1997) Photonic crystals: putting a new twist on light. *Nature* **386**, 143–149.
- [334] Kampfrath, T, Beggs, D. M, White, T. P, Melloni, A, Krauss, T. F, & Kuipers, L. (2010) Ultrafast adiabatic manipulation of slow light in a photonic crystal. *Physical Review A* **81**, 043837.
- [335] Vukusic, P & Sambles, J. R. (2003) Photonic structures in biology. *Nature* **424**, 852–855.
- [336] Kinoshita, S, Yoshioka, S, & Miyazaki, J. (2008) Physics of structural colors. *Reports on Progress in Physics* **71**, 076401.
- [337] Whitney, H. M, Kolle, M, Andrew, P, Chittka, L, Steiner, U, & Glover, B. J. (2009) Floral iridescence, produced by diffractive optics, acts as a cue for animal pollinators. *Science* **323**, 130–133.
- [338] Yin, H, Dong, B, Liu, X, Zhan, T, Shi, L, Zi, J, & Yablonovitch, E. (2012) Amorphous diamond-structured photonic crystal in the feather barbs of the scarlet macaw. *Proceedings of the National Academy of Sciences* **109**, 10798–10801.
- [339] Vukusic, P, Hallam, B, & Noyes, J. (2007) Brilliant whiteness in ultrathin beetle scales. *Science* **315**, 348–348.
- [340] Wiersma, D. S. (2013) Disordered photonics. *Nature Photonics* **7**, 188–196.
- [341] Mosk, A. P, Lagendijk, A, Lerosey, G, & Fink, M. (2012) Controlling waves in space and time for imaging and focusing in complex media. *Nature Photonics* **6**, 283–292.
- [342] Vellekoop, I. M, Lagendijk, A, & Mosk, A. P. (2010) Exploiting disorder for perfect focusing. *Nature Photonics* **4**, 320–322.
- [343] Lerosey, G, Rosny, J. d, Tourin, A, & Fink, M. (2007) Focusing beyond the diffraction limit with far-field time reversal. *Science* **315**, 1120–1122.
- [344] Vellekoop, I. M & Mosk, A. P. (2007) Focusing coherent light through opaque strongly scattering media. *Optics Letters* **32**, 2309–2311.
- [345] Popoff, S, Lerosey, G, Fink, M, Boccaro, A. C, & Gigan, S. (2010) Image transmission through an opaque material. *Nature Communications* **1**, 81.

- [346] Katz, O, Small, E, & Silberberg, Y. (2012) Looking around corners and through thin turbid layers in real time with scattered incoherent light. *Nature Photonics* **6**, 549–553.
- [347] Kim, M, Choi, Y, Yoon, C, Choi, W, Kim, J, Park, Q.-H, & Choi, W. (2012) Maximal energy transport through disordered media with the implementation of transmission eigenchannels. *Nature Photonics* **6**, 581–585.
- [348] Bertolotti, J, Putten, E. G. v, Blum, C, Lagendijk, A, Vos, W. L, & Mosk, A. P. (2012) Non-invasive imaging through opaque scattering layers. *Nature* **491**, 232–234.
- [349] Yaqoob, Z, Psaltis, D, Feld, M. S, & Yang, C. (2008) Optical phase conjugation for turbidity suppression in biological samples. *Nature Photonics* **2**, 110–115.
- [350] Gibson, A. P, Hebden, J. C, & Arridge, S. R. (2005) Recent advances in diffuse optical imaging. *Physics in Medicine and Biology* **50**, R1–R43.
- [351] Anderson, P. W. (1958) Absence of diffusion in certain random lattices. *Physical Review* **109**, 1492–1505.
- [352] Abrahams, E, Anderson, P. W, Licciardello, D. C, & Ramakrishnan, T. V. (1979) Scaling theory of localization: Absence of quantum diffusion in two dimensions. *Physical Review Letters* **42**, 673–676.
- [353] Segev, M, Silberberg, Y, & Christodoulides, D. N. (2013) Anderson localization of light. *Nature Photonics* **7**, 197–204.
- [354] Mascheck, M, Schmidt, S, Silies, M, Yatsui, T, Kitamura, K, Ohtsu, M, Leipold, D, Runge, E, & Lienau, C. (2012) Observing the localization of light in space and time by ultrafast second-harmonic microscopy. *Nature Photonics* **6**, 293–298.
- [355] Zhao, J, Wang, A, Green, M. A, & Ferrazza, F. (1998) 19.8% efficient honeycomb textured multicrystalline and 24.4% monocrystalline silicon solar cells. *Applied Physics Letters* **73**, 1991–1993.
- [356] Shah, A, Torres, P, Tscharnner, R, Wyrsh, N, & Keppner, H. (1999) Photovoltaic technology: The case for thin-film solar cells. *Science* **285**, 692–698.
- [357] O'Regan, B & Grätzel, M. (1991) A low-cost, high-efficiency solar cell based on dye-sensitized colloidal TiO₂ films. *Nature* **353**, 737–740.
- [358] Bach, U, Lupo, D, Comte, P, Moser, J. E, Weissörtel, F, Salbeck, J, Spreitzer, H, & Grätzel, M. (1998) Solid-state dye-sensitized mesoporous TiO₂ solar cells with high photon-to-electron conversion efficiencies. *Nature* **395**, 583–585.
- [359] Hoppe, H & Sariciftci, N. S. (2004) Organic solar cells: An overview. *Journal of Materials Research* **19**, 1924–1945.
- [360] Law, M, Greene, L. E, Johnson, J. C, Saykally, R, & Yang, P. (2005) Nanowire dye-sensitized solar cells. *Nature Materials* **4**, 455–459.
- [361] Hardin, B. E, Snaith, H. J, & McGehee, M. D. (2012) The renaissance of dye-sensitized solar cells. *Nature Photonics* **6**, 162–169.

- [362] Docampo, P, Guldin, S, Stefik, M, Tiwana, P, Orilall, M. C, Hüttner, S, Sai, H, Wiesner, U, Steiner, U, & Snaith, H. J. (2010) Control of solid-state dye-sensitized solar cell performance by block-copolymer-directed TiO₂ synthesis. *Advanced Functional Materials* **20**, 1787–1796.
- [363] Tiedje, T, Cebulka, J. M, Morel, D. L, & Abeles, B. (1981) Evidence for exponential band tails in amorphous silicon hydride. *Physical Review Letters* **46**, 1425–1428.
- [364] Shah, A. V, Schade, H, Vanecek, M, Meier, J, Vallat-Sauvain, E, Wyrsh, N, Kroll, U, Droz, C, & Bailat, J. (2004) Thin-film silicon solar cell technology. *Progress in Photovoltaics: Research and Applications* **12**, 113–142.
- [365] Polman, A & Atwater, H. A. (2012) Photonic design principles for ultrahigh-efficiency photovoltaics. *Nature Materials* **11**, 174–177.
- [366] Zhao, J & Green, M. (1991) Optimized antireflection coatings for high-efficiency silicon solar cells. *IEEE Transactions on Electron Devices* **38**, 1925–1934.
- [367] Ferry, V. E, Verschuuren, M. A, Li, H. B. T, Verhagen, E, Walters, R. J, Schropp, R. E. I, Atwater, H. A, & Polman, A. (2010) Light trapping in ultrathin plasmonic solar cells. *Optics Express* **18**, A237–A245.
- [368] Bermel, P, Luo, C, Zeng, L, Kimerling, L. C, & Joannopoulos, J. D. (2007) Improving thin-film crystalline silicon solar cell efficiencies with photonic crystals. *Optics Express* **15**, 16986–17000.
- [369] Bielawny, A, Rockstuhl, C, Lederer, F, & Wehrspohn, R. B. (2009) Intermediate reflectors for enhanced top cell performance in photovoltaic thin-film tandem cells. *Optics Express* **17**, 8439.
- [370] Basu Mallick, S, Agrawal, M, Wangperawong, A, Barnard, E. S, Singh, K. K, Visser, R. J, Brongersma, M. L, & Peumans, P. (2012) Ultrathin crystalline-silicon solar cells with embedded photonic crystals. *Applied Physics Letters* **100**, 053113.
- [371] Yu, Z, Raman, A, & Fan, S. (2010) Fundamental limit of nanophotonic light trapping in solar cells. *Proc. Natl. Acad. Sci. USA* **107**, 17491–17496.
- [372] Tobías, I, Luque, A, & Martí, A. (2008) Light intensity enhancement by diffracting structures in solar cells. *Journal of Applied Physics* **104**, 034502.
- [373] Franken, R. H, Stolk, R. L, Li, H, van der Werf, C. H. M, Rath, J. K, & Schropp, R. E. I. (2007) Understanding light trapping by light scattering textured back electrodes in thin film n-i-p-type silicon solar cells. *Journal of Applied Physics* **102**, 014503.
- [374] Kluth, O, Rech, B, Houben, L, Wieder, S, Schöpe, G, Beneking, C, Wagner, H, Löffl, A, & Schock, H. (1999) Texture etched ZnO:Al coated glass substrates for silicon based thin film solar cells. *Thin Solid Films* **351**, 247–253.
- [375] Berginski, M, Hüpkens, J, Schulte, M, Schöpe, G, Stiebig, H, Rech, B, & Wuttig, M. (2007) The effect of front ZnO:Al surface texture and optical transparency on efficient light trapping in silicon thin-film solar cells. *Journal of Applied Physics* **101**, 074903.

- [376] Müller, J, Rech, B, Springer, J, & Vanecek, M. (2004) TCO and light trapping in silicon thin film solar cells. *Solar Energy* **77**, 917–930.
- [377] Riboli, F, Barthelemy, P, Vignolini, S, Intonti, F, De Rossi, A, Combrie, S, & Wiersma, D. S. (2011) Anderson localization of near-visible light in two dimensions. *Optics Letters* **36**, 127.
- [378] Vynck, K, Burresti, M, Riboli, F, & Wiersma, D. S. (2012) Photon management in two-dimensional disordered media. *Nature Materials* **11**, 1017–1022.
- [379] Lagendijk, A, Tiggelen, B. v, & Wiersma, D. S. (2009) Fifty years of anderson localization. *Physics Today* **62**, 24–29.
- [380] Yablonovitch, E & Cody, G. (1982) Intensity enhancement in textured optical sheets for solar cells. *IEEE Transactions on Electron Devices* **29**, 300–305.
- [381] Yablonovitch, E. (1982) Statistical ray optics. *Journal of the Optical Society of America* **72**, 899–907.
- [382] Basu Mallick, S, Sergeant, N. P, Agrawal, M, Lee, J.-Y, & Peumans, P. (2011) Coherent light trapping in thin-film photovoltaics. *MRS Bulletin* **36**, 453–460.
- [383] Bozzola, A, Liscidini, M, & Andreani, L. C. (2012) Photonic light-trapping versus lambertian limits in thin film silicon solar cells with 1D and 2D periodic patterns. *Optics Express* **20**, A224.
- [384] Iaconis, C & Walmsley, I. (1998) Spectral phase interferometry for direct electric-field reconstruction of ultrashort optical pulses. *Opt. Lett.* **23**, 792–794.
- [385] Iaconis, C & Walmsley, I. (1999) Self-referencing spectral interferometry for measuring ultrashort optical pulses. *Quantum Electronics, IEEE Journal of* **35**, 501–509.
- [386] Shuman, T, Walmsley, I. A, Waxer, L, Anderson, M, Iaconis, C, & Bromage, J. (1999) Real-time spider: ultrashort pulse characterization at 20 hz. *Opt. Express* **5**, 134–143.
- [387] Takeda, M, Ina, H, & Kobayashi, S. (1982) Fourier-Transform method of fringe-pattern analysis for computer-based topography and interferometry. *J. Opt. Soc. Am.* **72**, 156–160.
- [388] Webb, R. H. (1996) Confocal optical microscopy. *Reports on Progress in Physics* **59**, 427.
- [389] Merschdorf, M, Pfeiffer, W, Thon, A, Voll, S, & Gerber, G. (2000) Photoemission from multiply excited surface plasmons in ag nanoparticles. *Applied Physics A* **71**, 547–552.
- [390] Farkas, G, Toth, C, & Kohazi-Kis, A. (1993) Above-threshold multiphoton photoelectric effect of a gold surface. *Optical Engineering* **32**, 2476–2480.
- [391] Murphy, E. L & Good, R. H. (1956) Thermionic emission, field emission, and the transition region. *Physical Review* **102**, 1464–1473.
- [392] Padovani, F. A & Stratton, R. (1966) Field and thermionic-field emission in schottky barriers. *Solid-State Electronics* **9**, 695–707.

- [393] Crowell, C. R. (1965) The richardson constant for thermionic emission in schottky barrier diodes. *Solid-State Electronics* **8**, 395–399.
- [394] Du, G, Yang, Q, Chen, F, Meng, X, Bian, H, Si, J, & Hou, X. (2013) Ultrafast dynamics of thermionic emission on au film under femtosecond laser excitation. *Applied Physics A* **112**, 479–483.
- [395] Biswas, P, Atta-Fynn, R, & Drabold, D. (2007) Experimentally constrained molecular relaxation: The case of hydrogenated amorphous silicon. *Physical Review B* **76**, 125210.
- [396] Dong, J & Drabold, D. (1998) Atomistic structure of band-tail states in amorphous silicon. *Physical Review Letters* **80**, 1928–1931.
- [397] White, J. O, Cuzeau, S, Hulin, D, & Vanderhaghen, R. (1998) Subpicosecond hot carrier cooling in amorphous silicon. *Journal of Applied Physics* **84**, 4984.
- [398] Chu, S. (1998) Nobel lecture: The manipulation of neutral particles. *Reviews of Modern Physics* **70**, 685–706.
- [399] Cohen-Tannoudji, C. N. (1998) Nobel lecture: Manipulating atoms with photons. *Reviews of Modern Physics* **70**, 707–719.
- [400] Phillips, W. D. (1998) Nobel lecture: Laser cooling and trapping of neutral atoms. *Reviews of Modern Physics* **70**, 721–741.
- [401] Hess, H. F. (1986) Evaporative cooling of magnetically trapped and compressed spin-polarized hydrogen. *Physical Review B* **34**, 3476–3479.
- [402] Tsang, K. H, Kui, H. W, & Chik, K. P. (1993) Calorimetric studies of the heat capacity and relaxation of amorphous si prepared by electron beam evaporation. *Journal of Applied Physics* **74**, 4932.
- [403] Bliokh, K, Bliokh, Y, Freilikher, V, Savel'ev, S, & Nori, F. (2008) Colloquium: Unusual resonators: Plasmonics, metamaterials, and random media. *Reviews of Modern Physics* **80**, 1201–1213.
- [404] Cai, M, Painter, O, & Vahala, K. J. (2000) Observation of critical coupling in a fiber taper to a silica-microsphere whispering-gallery mode system. *Physical Review Letters* **85**, 74–77.
- [405] Shen, J.-T & Fan, S. (2010) Quantum critical coupling conditions for zero single-photon transmission through a coupled atom-resonator-waveguide system. *Physical Review A* **82**, 021802.
- [406] Baker, C, Belacel, C, Andronico, A, Senellart, P, Lemaitre, A, Galopin, E, Ducci, S, Leo, G, & Favero, I. (2011) Critical optical coupling between a GaAs disk and a nanowaveguide suspended on the chip. *Applied Physics Letters* **99**, 151117.
- [407] Manceau, J.-M, Zanotto, S, Sagnes, I, Beaudoin, G, & Colombelli, R. (2013) Optical critical coupling into highly confining metal-insulator-metal resonators. *Applied Physics Letters* **103**, 091110.

- [408] Chen, X.-W, Mohammadi, A, Ghasemi, A. H. B, & Agio, M. (2013) Ultrafast coherent nanoscopy. *Molecular Physics* **111**, 3003–3012.
- [409] Walmsley, I. A & Dorrer, C. (2009) Characterization of ultrashort electromagnetic pulses. *Adv. Opt. Photon.* **1**, 308–437.
- [410] Trebino, R & Kane, D. J. (1993) Using phase retrieval to measure the intensity and phase of ultrashort pulses: frequency-resolved optical gating. *J. Opt. Soc. Am. A* **10**, 1101–1111.
- [411] Kane, D. J & Trebino, R. (1993) Single-shot measurement of the intensity and phase of an arbitrary ultrashort pulse by using frequency-resolved optical gating. *Opt. Lett.* **18**, 823–825.
- [412] DeLong, K. W & Trebino, R. (1994) Improved ultrashort pulse-retrieval algorithm for frequency-resolved optical gating. *J. Opt. Soc. Am. A* **11**, 2429–2437.
- [413] DeLong, K. W, Fittinghoff, D. N, Trebino, R, Kohler, B, & Wilson, K. (1994) Pulse retrieval in frequency-resolved optical gating based on the method of generalized projections. *Opt. Lett.* **19**, 2152–2154.
- [414] Paye, J, Ramaswamy, M, Fujimoto, J. G, & Ippen, E. P. (1993) Measurement of the amplitude and phase of ultrashort light pulses from spectrally resolved autocorrelation. *Opt. Lett.* **18**, 1946–1948.
- [415] Diels, J.-C. M, Fontaine, J. J, McMichael, I. C, & Simoni, F. (1985) Control and measurement of ultrashort pulse shapes (in amplitude and phase) with femtosecond accuracy. *Applied Optics* **24**, 1270–1282.
- [416] Trebino, R, Hayden, C. C, Johnson, A. M, Simpson, W. M, & Levine, A. M. (1990) Chirp and self-phase modulation in induced-grating autocorrelation measurements of ultrashort pulses. *Optics Letters* **15**, 1079–1081.
- [417] Schlup, P, Masihzadeh, O, Xu, L, Trebino, R, & Bartels, R. A. (2008) Tomographic retrieval of the polarization state of an ultrafast laser pulse. *Opt. Lett.* **33**, 267–269.
- [418] Xu, L, Schlup, P, Masihzadeh, O, Bartels, R. A, & Trebino, R. (2009) Analysis of the measurement of polarization-shaped ultrashort laser pulses by tomographic ultrafast retrieval of transverse light e fields. *J. Opt. Soc. Am. B* **26**, 2363–2369.
- [419] Keusters, D, Tan, H.-S, O’Shea, P, Zeek, E, Trebino, R, & Warren, W. S. (2003) Relative-phase ambiguities in measurements of ultrashort pulses with well-separated multiple frequency components. *J. Opt. Soc. Am. B* **20**, 2226–2237.
- [420] Reynaud, F, Salin, F, & Barthelemy, A. (1989) Measurement of phase shifts introduced by nonlinear optical phenomena on subpicosecond pulses. *Opt. Lett.* **14**, 275–277.
- [421] Fittinghoff, D. N, Bowie, J. L, Sweetser, J. N, Jennings, R. T, Krumbüügel, M. A, DeLong, K. W, Trebino, R, & Walmsley, I. A. (1996) Measurement of the intensity and phase of ultraweak, ultrashort laser pulses. *Opt. Lett.* **21**, 884–886.

- [422] Walecki, W. J, Fittinghoff, D. N, Smirl, A. L, & Trebino, R. (1997) Characterization of the polarization state of weak ultrashort coherent signals by dual-channel spectral interferometry. *Opt. Lett.* **22**, 81–83.
- [423] Dorrer, C & Walmsley, I. A. (2002) Accuracy criterion for ultrashort pulse characterization techniques: application to spectral phase interferometry for direct electric field reconstruction. *J. Opt. Soc. Am. B* **19**, 1019–1029.
- [424] Dorrer, C & Walmsley, I. A. (2002) Precision and consistency criteria in spectral phase interferometry for direct electric-field reconstruction. *J. Opt. Soc. Am. B* **19**, 1030–1038.
- [425] Dorrer, C. (1999) Influence of the calibration of the detector on spectral interferometry. *J. Opt. Soc. Am. B* **16**, 1160–1168.
- [426] Dorrer, C, Belabas, N, Likforman, J.-P, & Joffre, M. (2000) Experimental implementation of fourier-transform spectral interferometry and its application to the study of spectrometers. *Appl. Phys. B: Lasers Opt.* **70**, S99–S107.
- [427] Hamm, P. (2005) Principles of nonlinear optical spectroscopy: A practical approach or: Mukamel for dummies.
- [428] Chandler, D. (1987) *Introduction to modern statistical mechanics*. (Oxford University Press, New York).
- [429] Hahn, E. L. (1950) Spin echoes. *Physical Review* **80**, 580–594.

Acknowledgements

I would like to thank Prof. Dr. Walter Pfeiffer for giving me the opportunity to work on this very interesting topic. His confidence and encouragement were as helpful as his rich experience and his accurate guidance.

I would like to thank Prof. Dr. Ulrich Heinzmann for the manifold opportunities to work in exciting and seminal fields of physical research at the department *Physics of Molecules and Surfaces*.

I thank Prof. Dr. Thomas Huser for the interest in our work and his kind willingness to referee this dissertation and to take part in the examination committee.

Matthias Hensen has supported me in many ways. As a master student he quickly proved his brightness and ingenuity while building the f - $2f$ -interferometer for zero-slip CEP stabilization. As my colleague he is the most reliable, helpful and capable person I could wish to work with. Additionally, he is a really nice guy and lets me win once in a while at table tennis.

I would like to express my sincere appreciation to Dr. Stefan Cunvonic. Particularly his commitment in the forefront of and during the experiments was important for this work.

I sincerely thank Dominik Differt for coming up with all these amazing ideas and even more exciting ways to realize them, for his good sense of humor and his skills in handling even complex technical problems with the same easiness with which he boulders.

I want to express my gratitude to Prof. Dr. Helmut Stiebig and Dr. Florian Lükermann for fabricating and characterizing the a-Si:H thin-film solar cells and for the discussion of the experimental results.

Christian Sander, Babak Soleymanzadeh and Michael Birlo have been inspiring colleagues involving me in interesting conversations whenever I needed it.

I sincerely thank Peter Bartz, Fabian Merschjohann and Sergej Neb for their enduring and finally successful work on establishing an attosecond spectroscopy beamline and for their patience and understanding, whenever I had to fix the CEP-stabilized amplifier system or more often the oscillator for them. Seeing the streaking spectra from tungsten was a great relief.

I would like to thank all former and present students of our group, especially Henning Hachmeister, Christoph Neumann, Felix Becker and Stanislaw Nickel, for having so much interest in the field of ultrafast nanooptics, for all their questions and for all their ideas.

I would like to thank all members of the working group *Physics of Molecules and Surfaces* especially Kay Lofthouse for her support in any kind of bureaucratic problems, Christian Meier

for solving most of my computer problems, Dr. Armin Brechling, Dr. Norbert Müller, Dr. Hatem Dachraoui, Andreas Helmstedt and Martin Michelswirth for their good advice in scientific and technical issues. I send my regards to all group members who also drank from the mountain river in the High Tatras.

I sincerely thank Prof. Dr. Martin Aeschlimann, the head of the working group *Ultrafast Phenomena At Surfaces* at the TU Kaiserslautern, for the excellent hospitality and the distinguished conditions of research which we experienced in his department. I also would like to express my appreciation to Dr. Daniela Bayer, Dr. Alexander Fischer, Dr. Felix Steeb, Dr. Martin Rohmer, Dr. Christian Schneider, Pascal Melchior, Philip Thielen and Martin Piecuch for their great personal involvement in the labs, during discussions and the evaluation of the obtained data.

I would like to thank Prof. Dr. Tobias Brixner, head of the chair *Physical Chemistry 1* in Würzburg, for sharing his expertise in 2D spectroscopy and coherent control in fruitful discussions, which were very important for the success of the experiments and the understanding of the results. I would like to express my gratitude to Dr. Philip Tuchscherer and Christian Kramer for their commitment and their helpfulness during the experiments in Kaiserslautern and during the evaluation process.

I sincerely thank Dr. Dmitri D. Voronine for sharing his expertise in multidimensional spectroscopy as well as his enthusiasm and commitment during the experiments and evaluations. Vielen Dank, Dmitri!

I would like to express my sincere appreciation to the *DFG* for founding the *SPP 1391 on Ultrafast Nanooptics*, which has been as successful as we had hoped starting our work. The activities of the SPP1391 have been very inspiring bringing together scientists and students at interesting and beautiful places in Germany.

Most importantly, my great thanks go to my friends, my family and especially to Agathe for their support and encouragement and most of all their love, their patience and their understanding!